Microwave electrometry with Rydberg atoms in thermal atomic vapor

By

Tanim Firdoshi

Enrolment No: PHYS11201604008

National Institute of Science Education and Research,
Bhubaneswar

A thesis submitted to the

Board of Studies in Physical Sciences

In partial fulfillment of requirements

for the Degree of

DOCTOR OF PHILOSOPHY

of

HOMI BHABHA NATIONAL INSTITUTE

September, 2022

Homi Bhabha National Institute[1]

Recommendations of the Viva Voce Committee

As members of the Viva Voce Committee, we certify that we have read the dissertation prepared by **Tanim Firdoshi** entitled **Microwave electrometry with Rydberg atoms in thermal atomic vapor** and recommend that it may be accepted as fulfilling the thesis requirement for the award of Degree of Doctor of Philosophy.

Chairman – Dr. Sanjay K. Swain	Sanjay	13/4/23
Guide / Convener – Dr. Ashok K. Mohapatra	AMohapatra	13/04/2023
Co-guide -		
Examiner – Prof. Rejish Nath		12-04-2023
Member 1- Dr. Ritwick Das	Ritwick Das	13-04-2023
Member 2- Dr. Anamitra Mukherjee		13/04/23
Member 3- Dr. Rajan Jha		13/04/23

Final approval and acceptance of this thesis is contingent upon the candidate's submission of the final copies of the thesis to HBNI.

I/We hereby certify that I/we have read this thesis prepared under my/our direction and recommend that it may be accepted as fulfilling the thesis requirement.

Date: 13/04/2023

Place: NISER

AMohapatra

Dr. Ashok K. Mohapatra

Guide

---

[1] This page is to be included only for final submission after successful completion of viva voce.

STATEMENT BY AUTHOR

This dissertation has been submitted in partial fulfillment of requirements for an advanced degree at Homi Bhabha National Institute (HBNI) and is deposited in the Library to be made available to borrowers under rules of the HBNI.

Brief quotations from this dissertation are allowable without special permission, provided that accurate acknowledgement of source is made. Requests for permission for extended quotation from or reproduction of this manuscript in whole or in part may be granted by the Competent Authority of HBNI when in his or her judgment the proposed use of the material is in the interests of scholarship. In all other instances, however, permission must be obtained from the author.

Tanim Firdoshi

Tanim Firdoshi

DECLARATION

I, hereby declare that the investigation presented in the thesis has been carried out by me. The work is original and has not been submitted earlier as a whole or in part for a degree / diploma at this or any other Institution / University.

Tanim Firdoshi

Tanim Firdoshi

List of Publications arising from the thesis

Journal

- **Published**

    1. “Electromagnetically induced transparency in the strong blockade regime using the four-photon excitation process in thermal rubidium vapor”, **Tanim Firdoshi**, Sujit Garain, Vishu Gupta, Dushmanta Kara, and Ashok K. Mohapatra, Phys. Rev. A, **2021**, 104, 013711.

    2. “Study of microwave field sensing with four-photon excitation to the Rydberg state.”, Suji Garain, **Tanim Firdoshi**, and Ashok K. Mohapatra, http://dx.doi.org/10.1364/FIO.2022.JW5A.91.

    3. “E-Field Strength Measurement using Rydberg Atom Based sensor for Microwave Metrology”, H. S. Rawat, D. Kara, **T. Firdoshi**, S. Garain, S. K. Dubey, A. K. Mohapatra, and V. N. Ojha, 2020 XXXIIIrd General Assembly and Scientific Symposium of the International Union of Radio Science, DOI:10.23919/URSIGASS49373.2020.9232002.

- **Submitted to arXiv** (Communicated)

    1. “Six-wave mixing of optical and microwave fields using Rydberg excitations in thermal atomic vapor”, **Tanim Firdoshi**, Sujit Garain, Suman Mondal, and Ashok K. Mohapatra., arXiv:2207.01835, **2022**.

- **Other journal publications**

    1. ”Imaging of 87Rb atom in cold atomic cloud using four-wave mixing process”, S. Garain, **T. Firdoshi**, S. Mondal, T. Alam, and A. K. Mohapatra, DAE-BRNS National Laser Symposium (NLS 31), https://ila.org.in/nls31.

Conferences

1. “Conference on Optics and Photonics Technology (COPT)”, 2016 @ NISER Bhubaneswar, India.

2. SERB School on “Frontiers in Quantum Optics”, 2017 @ IIT Guwahati, India.

3. International Conference on “Recent Trends in Cold and Ultra-cold Matter”, 2018 @ IIT Guwahati, India.

4. “Topical Meeting on Advances in Photonics (TMAP)”, 2019 @ NISER Bhubaneswar, India.

   Poster presentation: Study of electromagnetically induced transparency (EIT) using four-photon excitation to the Rydberg state in thermal atomic vapor.

5. International conference : “Conference on Lasers and Electro–Optics(CLEO)”, 2020, Virtual conference.

6. Webinar on “Century of Quantum Mechanics and Still Going Strong”, 2020 @ MSUB, India.

7. International conference : “OSA FIO-SLC Student Leadership Conference”, 2020, Virtual conference.

8. International workshop on “Workshop on cold Rydberg chemistry”, 2021, Virtual conference.

9. “Student Conference on Photonics and Quantum Technology (SCPQT)”, 2021 @ NISER Bhubaneswar, India.

   Poster presentation: Electromagnetically induced transparency (EIT) in the strong blockade regime using the four-photon excitation process in thermal rubidium vapor -Bagged second best poster award.

10. International conference : “Photoptics”, 2022, Virtual conference.

    Poster presentation: Six-wave mixing of optical and microwave fields using Rydberg atoms in thermal atomic vapor.

11. SPS Day, 2022, @ NISER Bhubaneswar, India.

    Oral presentation: Six-wave mixing of optical and microwave fields using Rydberg atoms in thermal atomic vapor - Best student talk.

Tanim Firdoshi

Tanim Firdoshi

DEDICATIONS

Dedicated to

.....

My Parents

Sk Kalimulaha

Saukat Ara Begum

.....

My brother

Sk Maseehullah

.....

My grandparents

Md. Sabirul haque

Jahan Ara Begum

Sk Mahebullah

Roshan Ara Bibi

ACKNOWLEDGEMENTS

First, I would like to thank my family, especially my mother, for her unconditional love and support. Without her support, I could not have completed this journey. I want to thank Dr. Ashok K. Mohapatra for his immense support and guidance throughout my Ph.D. I am fortunate to have him as my Ph.D. advisor, and I admire him a lot as a researcher. When things were tough, I had faith in his words. His ′never give up′ attitude taught me how to handle pressure and keep going.

I express my sincere gratitude to my doctoral committee members Prof. Sanjay K. Swain, Dr. Ritwick Das, Dr. Anamitra Mukherjee, and Dr. Rajan Jha, for their valuable feedback and comments on improving my research work.

I am fortunate to have had excellent teachers throughout my career, starting from my mother, Saukat Ara Begum, and my father, Dr. Sk Kalimulaha.

I would also like to thank my lab-mates for every bit of knowledge I have gained from them. They are Dr. Arup Bhowmick, Dr. Sushree S. Sahoo, Dr. Dushmanta Kara, Snigdha S. Pati, Sujit Garain, Soumya R. Mishra, Akshaya Sahoo, Dr. Suman Mondal, Vishu Gupta, Vinit Kumar, Tousif Alam, Nandini Mondal, Nabendu S. Mishra. I also thank Dr. Harish Rawat and Dr. Satyakesh Dubey for discussions. I appreciate the help of Dr. Subhankar Bedanta, Dr. Kartikeswar Senapati, Rohde and Schwarz- India, and Dr. Santosh G. Babu for help regarding microwave signal generators and horn antennas.

Apart from lab, I had fruitful discussions with friends and got motivation from them. Snigdha, Sujit, Prince, Anupa, Purbasha, and Rashmi have been the most significant support. I always had a perfect time with my friends, seniors, and juniors (Dukhi, Subir, Bimalesh, Jagannath, Jamal, Prabhakar, Kalyan, Ashish, Dola, Manoar, Rajesh, Tusaradri, Samapan) here at NISER. Lab-mates and friends always had parties where we cooked a lot of delicious food and enjoyed a lot. We celebrated every festival and occasion together. I thank all for such a warm environment to live in.

I thank my friends Sujit, Prince, Anupa, Soumya, and Akshaya who were my badminton partners, and juniors Lipsa, Pushpendra, Vinit, Indra, Tapas, and others. Vinit trained me during intra-NISER matches, and I had a great time. I thank my workout partner Purbasha who always motivated me, especially for 5 km runs. Badminton and workouts have helped me a lot in my personal growth.

Apart from friends at NISER, some friends have been great support even though they were not always with me Kunu, Snigdha, Babbar, Anubhab, Soumya, Sameer, Rohit, and Abinash. Kunu has provided enormous support in my life for the last 12 years.

Contents

Title page **i**

SUMMARY **xvi**

List of Figures **xviii**

1 Introduction **1**

- 1.1 Atom-based sensors 1
- 1.2 Conventional vs. atom-based E-field sensing 1
- 1.3 Review of Rydberg atom-based E-field sensing 3
- 1.4 Motivation to study microwave field sensing with Rydberg atoms in thermal vapor 4
- 1.5 Contribution of the thesis to the field of microwave field sensing and data communication technology 5
- 1.6 Layout of the thesis 7

2 Basics of coherent Rydberg excitation in rubidium vapor **9**

- 2.1 Rydberg atoms 9
  - 2.1.1 Properties of Rydberg atoms 10
  - 2.1.2 Quantum defect 11
- 2.2 Atom-light interaction and the refractive index 14
  - 2.2.1 Non-interacting two-level atoms in gas density N 14
  - 2.2.2 Dressed state picture 18
  - 2.2.3 Three level system 19

2.2.4 Electromagnetically Induced Transparency (EIT) 22
2.2.5 Adiabatic elimination of the intermediate state: Effective two-level system 24
2.3 Energy levels of rubidium atom 27
2.4 Doppler broadening 28
2.4.1 Doppler effect in a three-level rubidium atomic system 29
2.5 Scaling of hyperfine and fine structure splitting due to wave vector mismatch between the probe and coupling laser fields 30
2.6 Laser frequency stabilization 34
2.6.1 Doppler free absorption spectroscopy 34
2.6.2 Frequency stabilization using EIT locking technique 37

3 Rydberg Electrometry 41
3.1 Theoretical model of four-level system 42
3.2 Experimental set-up for investigation of microwave field sensing using EIT 46
3.3 Observation of AT splitting due to the presence of the microwave field 48
3.4 E-field strength with different microwave power at the signal generator 50
3.5 Effect of microwave detuning on E-field measurement 52
3.6 Communication with Rydberg atoms 55
3.6.1 Analog communication with Rydberg EIT 55
3.6.2 Digital communication with Rydberg EIT 57
3.7 Limitations of microwave field sensing with Rydberg atoms using EIT through two-photon excitation process to the Rydberg state 58
3.8 Conclusion 59

4 Six-wave mixing of optical and microwave fields using Rydberg atoms in thermal atomic vapor 61
4.1 Generation of the new optical field due to six-wave mixing process inside the atomic medium 62
4.2 Theoretical model for six wave-mixing process using four-level system 63

4.2.1 Construction of the master equation 65
4.2.2 Perturbative expansion of the density matrix 66
4.2.3 0^{th} order density matrix equations 66
4.2.4 1^{st} order density matrix equations 68
4.3 Experimental details 70
4.3.1 Optical heterodyne detection 71
4.3.2 Beat signal at δ 73
4.4 Microwave-to-optical conversion efficiency 73
4.5 Strength of the δ beat signal 74
4.6 Wave propagation equations 76
4.7 Observations 77
4.7.1 Beat signal strength as a function of δ 77
4.7.2 Dressed state formation due to strong microwave field 78
4.7.3 Beat strength as a function of Ω_p 79
4.7.4 Beat strength as a function of Δ_μ 80
4.7.5 E-field strength of weak microwave field in free space 81
4.7.6 Dependence of the beat strength on weak microwave power . . 82
4.8 Temporal response of the system 83
4.8.1 Modulation bandwidth 86
4.9 Effect of large coupling Rabi frequency on beat spectrum 88
4.9.1 Investigation in a system with atoms at rest 89
4.9.2 Effect of large coupling Rabi frequency in thermal system . . . 90
4.10 Conclusion 92

5 Study of electromagnetically induced transparency (EIT) using four-photon excitation to the Rydberg state in thermal atomic vapor 93

5.1 Five-level atomic model for four-photon excitation to the Rydberg state 94
5.2 Construction of the master equation 96
5.3 Optical Bloch equations 97
5.4 EIT in a four-photon excitation process 98

5.4.1 Geometry of the laser beams 98

5.4.2 Energy level scheme for EIT 99

5.4.3 Doppler averaging 100

5.5 Variation of EIT peak transmission with k_c 104

5.6 Reduction of five-level system to an effective three-level system: Adiabatic elimination method 105

5.6.1 Formation of the effective three-level system 105

5.6.2 Optical Bloch equations 109

5.7 Experimental proposal 110

5.8 Elimination of the residual wave vector using suitable beam geometry 111

5.9 Conclusion 112

6 Outlook: Microwave field sensing using four-photon excitation to the Rydberg state in thermal rubidium vapor 115

6.1 Theoretical model for microwave field sensing with four-photon excitation process 116

6.2 Effect of a microwave field on four-photon EIT 118

6.3 Microwave field sensing with two-photon Rydberg EIT system 119

6.4 Microwave field sensing with four-photon Rydberg EIT system 121

6.5 Achieving a narrow EIT line-width 122

6.6 Sensitivity of electric field 124

6.7 Experimental plan 125

6.7.1 Beam geometry 125

6.7.2 Using a microwave waveguide 125

6.7.3 Design of the vacuum chamber for four-photon excitation experiment 126

6.8 Conclusion 128

A Electromagnetically induced transparency (EIT) in the strong blockade regime using four-photon excitation to the Rydberg state in

thermal atomic vapor **129**
A.1 Development of two-atom model 130
A.1.1 Optical Bloch equations 132
A.1.2 Monte Carlo simulation technique 137
A.2 Comparison of non-interacting two-atom system with a single-atom system 138
A.3 Observation of Rydberg blockade phenomenon 139
A.3.1 Dependence of Rydberg blockade on k_c 140
A.3.2 Variation of Rydberg blockade with super-atom dephasing . . 141
A.3.3 Effect of Δ_{int} on Rydberg blockade 142

References **144**

SUMMARY

The radio frequency to the far-infrared regime of the electromagnetic spectrum plays a crucial role in developing technologies for communication, the environment, healthcare, astronomy, and entertainment industries. Conventional electric field sensing involves calibrated dipole probes and antennas for electric field measurements. There are resonantly enhanced detectors which also need to be calibrated. Hence, the need for calibration and the inability to detect fields smaller than mV/cm range with calibration free detectors limits the use of these electromagnetic probes in modern technologies. On the other hand, the atom-based sensors are self-calibrated owing to their universal properties and can detect a field of the order of μV/cm.

This thesis aims to explore microwave field sensing with Rydberg atoms in thermal rubidium vapor. Transitions between Rydberg states span from less than a MHz to THz, allowing a wide operating frequency range. Large dipole moments and large polarizability makes the Rydberg atoms prone to even weak external electric fields. The usual all optical detection of Rydberg states is achieved through electromagnetically induced transparency (EIT). When the applied microwave field is strong enough to dress the Rydberg state, splitting in the EIT peak is observed. The extent of the splitting gives a measure of the strength of the electric field experienced by the atoms. The modulation bandwidth in these systems is limited to a few MHz. This limitation is because of the optical pumping rate to the EIT dark state. The six-wave mixing of optical and microwave fields in thermal atomic vapor leads to the parametric generation of a new optical field, which is expected to be an instantaneous process, limited by the available coupling Rabi frequency.. The generated field is along the direction of the probe field, resulting in an interference beat signal. The generation bandwidth has an FWHM $\sim$ 17 MHz. The temporal response of the system is investigated by amplitude modulation of the generated field, and it is observed that the bandwidth of the modulation spectrum matches perfectly with the beat spectrum bandwidth, both limited by available coupling Rabi frequency. The modulation spectrum bandwidth determines the temporal response of the system. Hence, the effect of coupling Rabi frequency on the beat spectrum bandwidth is explored theoretically. With increased coupling Rabi frequency, the bandwidth of the beat spectrum increases for off-resonance conditions. The sensitivity of the detected electric field is given $\frac{E_{min}}{\sqrt{Hz}}$, where E_{min} is the minimum detectable electric field dictated by the linewidth of the EIT signal, which is nearly 3-4 MHz for the two-photon EIT process. A theoretical study is performed for four-photon excitation to the Rydberg state. The motion-induced dephasing can be eliminated in such a system. It is observed that an EIT transparency of nearly 100% is achieved with zero residual wave-vector. It is not easy to achieve this condition using two-photon excitation processes in alkali atoms. Whereas the Doppler-free condition can be achieved under suitable conditions and beam geometry for the four-photon excitation process. An experiment is proposed with rubidium to study the four-photon excitation to the Rydberg state. The laser beams are arranged such that they make small angles with respect to the horizontal axis of the rubidium vapor cell to reduce the residual wave vector to zero. This leads to the elimination of the motion-induced dephasing in the system. The microwave field sensing using two-photon Rydberg EIT is compared with the field sensing through a four-photon excitation process by evaluating the minimum detectable field for both cases with similar parameters. For optimal parameters and laser geometry, a narrow EIT linewidth of 230 kHz can be achieved, resulting in the total sensitivity of microwave field detection to be $\sim$ 55 nV cm^{-1} $Hz^{1/2}$. Lastly, an experimental design is proposed to perform microwave field sensing using the four-photon excitation process.

List of Figures

2.1 Energy levels of ^{85}Rb up to $n = 100$. The figure is obtained using ARC documentation [58]. 12

2.2 Quantum defect values for ^{85}Rb for $l = 0 - 3$. The figure is obtained using ARC documentation [58]. 13

2.3 Schematic of energy levels of a two-level system where $|g\rangle$ and $|e\rangle$ represent the ground state and the excited state respectively. 14

2.4 For a two level-system with atoms at rest: (a) Real ($\Re(\chi)$) and imaginary ($\Im(\chi)$) part of the susceptibility are given by red closed circles and cyan closed circles respectively and (b) probe transmission. $\Re(\chi)$ provides an estimate of the dispersion induced by the atomic light interaction in the medium and $\Im(\chi)$ estimates the absorption of the input light while propagating through the atomic medium. Laser parameters are: $\Omega_p = 0.1$ MHz, $\Gamma_{eg} = 6$ MHz and density of the atoms (N) is 10^{10} cm^{-3}. 17

2.5 Schematic of energy levels of a three-level system in ladder configuration. $|g\rangle$, $|e\rangle$ and $|r\rangle$ represent the ground, intermediate and the excited state respectively. 19

2.6 Probe transmission as a function of probe detuning (Δ_p) in the absence (olive open circles) and presence (red closed circles) of coupling field. Laser parameters used in the model are $\Omega_p = 100$ kHz, $\Omega_c = 5$ MHz, $\Gamma_{eg} = 6$ MHz, $\Gamma_{re} = 10$ kHz, $\Gamma_{rg} = 100$ kHz and $\Delta_c = 0$. Density of the atoms (N) is 1.7×10^{10} cm^{-3}. 23

2.7 Schematic of energy levels of (a) three-level system and (b) effective two-level system. 24

2.8 Comparison of an effective two level system (open olive circles) with a three level system (red solid line) at large probe detuning $\Delta_p = 600$ MHz. Other parameters used in the model are $\Omega_p = 50$ MHz, $\Omega_c = 5$ MHz, $\Gamma_{eg} = 6$ MHz, $\Gamma_{re} = 10$ kHz and $\Gamma_{rg} = 100$ kHz. Density of the atoms (N) is 1.7×10^{10} cm^{-3}. 26

2.9 Energy levels of rubidium. D1 and D2 lines for (a) ^{87}Rb and (b) ^{85}Rb 27

2.10 Two dimensional density plots for probe transmission as a function of detuning of the laser field and atomic velocity for the ladder configuration where $k_p = 1.28166 \times 10^6$ m^{-1} and $k_c = 2.08333 \times 10^6$. Other parameters used are $\Omega_p = 500$ kHz, $\Omega_c = 5$ MHz, $\Gamma_{eg} = 6$ MHz, $\Gamma_{re} = 10$ kHz, and $\Gamma_{rg} = 100$ kHz. The density of the atoms is 1.7×10^{10} cm^{-3}. 29

2.11 Energy level scheme where $|g\rangle$ represents the ground state, and $|r\rangle$ represents the Rydberg state: (a) for hyperfine states $|e\rangle$ and $|e'\rangle$ and (b) for fine structure states $|r\rangle$ and $|r'\rangle$. Δ_{hf} and Δ_f represent the hyperfine and fine structure splitting, respectively. 31

2.12 Two-dimensional density plots for probe transmission as a function of laser field detuning and atomic velocity representing two hyperfine resonances: (a) Δ_p scan and (c) Δ_c scan. Doppler averaged probe transmission for the same: (b) Δ_p scan and (d) Δ_c scan. Here, Δ_{hf} is taken to be 100 MHz, just as an example. This value of Δ_{hf} is not specific to rubidium. 32

2.13 Two-dimensional density plots for probe transmission as a function of laser field detuning and atomic velocity representing two fine structure resonances: (a) Δ_p scan and (c) Δ_c scan. Doppler averaged probe transmission for: (b) Δ_p scan and (d) Δ_c scan. Here, Δ_f is taken to be 100 MHz, just as an example. This value of Δ_f is not specific to rubidium. 33

2.14 Optical set up for Doppler-free absorption spectroscopy. HWP: Half-wave plate, PBS: Polarizing beam splitter, M: Mirror, QWP: Quarter wave plate, ND: Neutral Density Filter, L: Lens, and DET: Detector. 34

2.15 (A) represents SAS data for rubidium D2 line where (a) represents the ^{87}Rb $5S_{\frac{1}{2}}F = 2 \rightarrow 5P_{\frac{3}{2}}F'(1,2,3)$ transition , (b) represents the ^{85}Rb $5S_{\frac{1}{2}}F = 3 \rightarrow 5P_{\frac{3}{2}}F'(2,3,4)$ transition, (c) represents the ^{85}Rb $5S_{\frac{1}{2}}F = 2 \rightarrow 5P_{\frac{3}{2}}F'(1,2,3)$ transition and (d) represents the ^{87}Rb $5S_{\frac{1}{2}}F = 1 \rightarrow 5P_{\frac{3}{2}}F'(0,1,2)$ transition. (B) and (C) represent the zoomed view of the first two transitions (a) and (b), respectively. . . . 35

2.16 Optical set up for frequency stabilization using EIT locking technique. HWP: Half-wave plate, PBS: Polarizing beam splitter, EOM: Electro-optic modulator, M: Mirror, QWP: Quarter wave plate, L: Lens, D.M.: Dichroic mirror, and DET: Detector. 37

2.17 EIT signal: (a) without modulation and (b) after frequency modulation with side bands at the modulation frequency. 38

2.18 Generated error signal from the EIT signal. 39

3.1 Schematic of energy levels of a four-level system in a ladder configuration. $|g\rangle$, $|e\rangle$, $|r\rangle$ and $|r'\rangle$ represent the ground state, intermediate state, first Rydberg state and the second Rydberg state respectively. . 42

3.2 Probe transmission as a function of Δ_c. The solid red line represents the EIT peak in the absence of the microwave field ($\Omega_\mu = 0$), and the solid cyan line represents the splitting in the EIT peak due to the presence of the microwave field ($\Omega_\mu = 5$ MHz). Other parameters are $\Omega_p = 500$ kHz, $\Omega_c = 4$ MHz, $\Gamma_{eg} = 6$ MHz, $\Gamma_{re} = 10$ kHz, $\Gamma_{rg} = 100$ kHz, $\Gamma_{r'g} = 100$ kHz, $\Gamma_{r'r} = 10$ kHz, $\Delta_p = 0$ and $\Delta_\mu = 0$. The density of the atoms is 1.7×10^{10} cm^{-3}. 45

3.3 Optical set up for microwave electric field sensing. The set up consists of two parts: one for probe frequency stabilization (SAS) and the other part for experiment. HWP: Half wave-plate, PBS: Polarizing beam splitter, M: Mirror, QWP: Quarter wave-plate, L: Lens, DM: Dichroic mirror, DET: Detector. 47

3.4 Microwave electrometry with Rydberg atoms: (a) Energy level scheme where $|g\rangle = 5S_{\frac{1}{2}}$, $|e\rangle = 5P_{\frac{3}{2}}$, $|r\rangle = 62S_{\frac{1}{2}}$, and $|r'\rangle = 61P_{\frac{3}{2}}$. (b) EIT signal when the microwave is off and on with microwave power $P_{\mu W} = 1$ dBm at the signal generator. 48

3.5 Splitting of the EIT signal for different microwave source power at the signal generator. 50

3.6 Measured value of E-field strength for given microwave source power. 51

3.7 (a) Energy level scheme where $|g\rangle = 5S_{\frac{1}{2}}$, $|e\rangle = 5P_{\frac{3}{2}}$, $|r\rangle = 45D_{\frac{5}{2}}$, and $|r'\rangle = 46P_{\frac{3}{2}}$. (b) EIT signal when the microwave is off and on with microwave power $P_{\mu W} = -9$ dBm at the signal generator applied on-resonance to the transition. 52

3.8 Comparison of AT splitting of the EIT signal for off-resonant microwave fields ($f_{\mu,0} \pm \Delta_\mu$) with resonant microwave field splitting ($f_{\mu,0}$) for fixed power of the microwave field ($P_{\mu W} = -9$ dBm) and with $\Delta_\mu = 30$ MHz. 53

3.9 Separation between the AT split peaks at finite detuning (Δf_{Δ_μ}) as a function of Δ_μ for $P_{\mu W} = -9$ dBm. 54

3.10 (a) Energy level scheme and (b) experimental set-up. 56

3.11 Input audio signal (top) to the microwave signal generator and retrieved audio signal (bottom) at the photodetector. 57

4.1 Schematic of energy levels in the ladder configuration where $|g\rangle$ represents the ground state, $|e\rangle$ represents the intermediate state, $|r\rangle$ represents the Rydberg state, and $|r'\rangle$ represents the second nearby Rydberg state. A probe field (ω_p) couples the transition $|g\rangle \rightarrow |e\rangle$, and a coupling field ($\omega_c$) couples the transition $|e\rangle \rightarrow |r\rangle$. Two microwave fields, ω_μ and $(\omega_\mu + \delta)$, are applied between the two Rydberg states $|r\rangle$ and $|r'\rangle$. 62

4.2 Comparison of (a) Real and (b) Imaginary part of $(\rho^{(0)}_{eg})_D$ calculated from 0^{th} order equations with $(\rho^{(0)}_{eg})_D$ calculated from a four-level system. Other parameters are $\Omega_p = 500$ KHz, $\Omega_c = 4$ MHz, $\Omega_\mu = 5$ MHz, $\Gamma_{eg} = 6$ MHz, $\Gamma_{re} = 10$ KHz, $\Gamma_{rg} = 100$ KHz, $\Gamma_{r'g} = 10$ KHz, $\Gamma_{r'r} = 100$ KHz, $\Delta_p = 0$ and $\Delta_\mu = 0$. The density of the atoms is 1.7×10^{10} cm^{-3}. 68

4.3 (a) Schematic of energy levels of rubidium. (b) Experimental set-up. HWP: Half-wave plate, PBS: Polarizing beam splitter, QWP: Quarter-wave plate, M: Mirror, L: Lens, DM: Dichroic mirror, AOM: Acousto-optic modulator, L.O.: Local oscillator, and DET: Photodetector. 70

4.4 Spectrum analyzer signal showing 40 MHz beat signal along with two side bands for $\delta = 2$ MHz. 72

4.5 Beat signal at the spectrum analyzer for $\delta = 2$ MHz. 73

4.6 Microwave-to-optical conversion efficiency for different δ. 74

4.7 Beat signal amplitude with varying δ. Experimental parameters used are: $\Omega_p = 283$ MHz, $\Omega_c = 2$ MHz, $\Omega_{\mu_1} = 80$ MHz and $\Omega_{\mu_2} = 40$ MHz, $\Delta_p = 1.2$ GHz, $\Delta_c = -1.2$ GHz and $\Delta_\mu = 0$. 78

4.8 Schematic of dressed state picture due to the strong microwave field (ω_μ) with Rabi frequency Ω_{μ_1}. 79

4.9 Beat signal amplitude with varying Ω_p for fixed $\delta = 10$ MHz. Blue open circles are the experimental data and red line is a fit to the polynomial $y = a_1x + a_2x^3 + a_3x^5$ with $a_1 = 0.18 \pm 0.11$, $a_2 = 5.07E-5 \pm 4.85E-6$, and $a_3 = -4.56E-10 \pm 4.69E-11$. Other experimental parameters used are: $\Omega_p = 283$ MHz, $\Omega_c = 2$ MHz, $\Omega_{\mu_1} = 80$ MHz and $\Omega_{\mu_2} = 40$ MHz, $\Delta_p = 1.2$ GHz, $\Delta_c = -1.2$ GHz, and $\Delta_\mu = 0$. . . 80

4.10 Beat signal amplitude with varying Δ_μ for fixed $\delta = 5$ MHz. Other experimental parameters used are: $\Omega_p = 283$ MHz, $\Omega_c = 2$ MHz, $\Omega_{\mu_1} = 80$ MHz and $\Omega_{\mu_2} = 40$ MHz, $\Delta_p = 1.2$ GHz, and $\Delta_c = -1.2$ GHz. 81

4.11 Beat signal amplitude with increasing weak microwave field strength at $\delta = 10$ MHz. Other experimental parameters used are: $\Omega_p = 283$ MHz, $\Omega_c = 2$ MHz, $\Omega_{\mu_1} = 80$ MHz, $\Delta_p = 1.2$ GHz, $\Delta_c = -1.2$ GHz and $\Delta_\mu = 0$. 83

4.12 Amplitude modulated signal with side bands for $\delta = 2$ MHz and $\nu = 70$ kHz. Other experimental parameters are: $\Omega_p = 283$ MHz, $\Omega_c = 2$ MHz, $\Omega_{\mu_1} = 80$ MHz and $\Omega_{\mu_2} = 40$ MHz, $\Delta_p = 1.2$ GHz, $\Delta_c = -1.2$ GHz, and $\Delta_\mu = 0$. 84

4.13 m with varying modulation frequency ν at $\delta = 2$ MHz for the upper sideband at $(\delta + \nu)$ and lower sideband at $(\delta - \nu)$. The experimental parameters are: $\Omega_p = 283$ MHz, $\Omega_c = 2$ MHz, $\Omega_{\mu_1} = 80$ MHz and $\Omega_{\mu_2} = 40$ MHz, $\Delta_p = 1.2$ GHz, $\Delta_c = -1.2$ GHz and $\Delta_\mu = 0$. 86

4.14 Comparison of the modulation spectrum with the normalized beat spectrum due to the six-wave mixing process. Cyan open circles represent the beat spectrum given by Fig. 4.7. Blue and red open circles represent m for the upper and lower sideband of the modulated signal, respectively, at $\delta = 2$ MHz. The other experimental parameters are: $\Omega_p = 283$ MHz, $\Omega_c = 2$ MHz, $\Omega_{\mu_1} = 80$ MHz and $\Omega_{\mu_2} = 40$ MHz, $\Delta_p = 1.2$ GHz, $\Delta_c = -1.2$ GHz, and $\Delta_\mu = 0$. 87

4.15 Theoretically generated spectrum for A' as a function of δ for (a) $\Omega_c = 2$ MHz and (b) $\Omega_c = 50, 100$ MHz. Other parameters used are: $\Omega_p = 300$ MHz, $\Omega_{\mu_1} = 80$ MHz and $\Omega_{\mu_2} = 1$ MHz, $\Delta_p = 1.2$ GHz, $\Delta_c = -1.2$ GHz and $\Delta_\mu = 0$. 88

4.16 Schematic of energy levels: (a) for off-resonant condition with two-photon detuning $\delta_1 = 0.6$ GHz and three-photon detuning $\delta_2 = 0.8$ GHz and (b) weak microwave transitions (yellow lines) corresponding to the two peaks at $\delta = 0.6$ GHz and $\delta = 0.8$ GHz. 89

4.17 Theoretically generated spectrum for A' with atoms at rest as a function of δ for: (a) $\Omega_p = 300$ MHz, $\Omega_c = 2$ MHz, $\Omega_{\mu_1} = 80$ MHz and $\Omega_{\mu_2} = 1$ MHz. Inset shows the spectrum for $\Omega_p = 10$ MHz, $\Omega_c = 2$ MHz, $\Omega_{\mu_1} = 10$ MHz and $\Omega_{\mu_2} = 1$ MHz. (b) $\Omega_p = 300$ MHz, $\Omega_c = 100$ MHz, $\Omega_{\mu_1} = 80$ MHz and $\Omega_{\mu_2} = 1$ MHz. Other parameters used are: $\Delta_p = 1.2$ GHz, $\Delta_c = -0.6$ GHz and $\Delta_\mu = 0.2$ GHz. 90

4.18 Theoretically generated spectrum for A' as a function of δ for (a) $\Omega_c = 2$ MHz and (b) $\Omega_c = 10, 50, 100$ MHz. Other parameters used are: $\Omega_p = 300$ MHz, $\Omega_{\mu_1} = 80$ MHz and $\Omega_{\mu_2} = 1$ MHz, $\Delta_p = 1.2$ GHz, $\Delta_c = -0.6$ GHz and $\Delta_\mu = 0.2$ GHz. 91

5.1 Energy level scheme of a five-level system in the ladder configuration. 94

5.2 Schematic of the laser geometry through a Rb vapor cell consisting of four laser fields of frequencies ω_1, ω_2, ω_3, and ω_4. 99

5.3 Energy level scheme of the five-level system representing the conditions to satisfy EIT. 100

5.4 Up: Two-dimensional density plots for probe transmission as a function of Δ_2 and velocity for $\Delta k = 0$. Down: Doppler averaged probe transmission for the same. 101

5.5 Up: Two-dimensional density plots for probe transmission as a function of Δ_2 and velocity for $\Delta k = 0.043 \times 10^6$ m^{-1}. Down: Doppler averaged probe transmission for the same. 102

5.6 Probe transmission in the absence of the coupling fields while scanning Δ_2 (cyan open circles) and in the presence of the coupling fields (solid red line) for (a) $\Delta k = 0$ and for (b) $\Delta k = 0.023 \times 10^6$ m^{-1}. The laser parameters used in the model are $\Omega_1 = 10$ MHz, $\Omega_2 = 110$ MHz, $\Omega_3 = 25$ MHz, $\Omega_4 = 160$ MHz, $\Delta_1 = 1200$ MHz, $\Delta_3 = 1000$ MHz and Δ_4 is adjusted around Δ_3 to make the transmission symmetric. Here, the value of the effective probe transition wave vector is taken to be $k_p = 0.007 \times 10^6$ m^{-1}. 103

5.7 EIT transmission peak height as a function of k_c. The laser parameters used in the model are $\Omega_1 = 10$ MHz, $\Omega_2 = 110$ MHz, $\Omega_3 = 25$ MHz, $\Omega_4 = 160$ MHz, $\Delta_1 = 1200$ MHz, $\Delta_3 = 1000$ MHz and Δ_4 is adjusted around Δ_3 to make the transmission symmetric. 104

5.8 Schematic of reduction of a five-level system (left) to an effective three-level system (right). 106

5.9 Comparison of probe transmission of effective three-level system with a five-level system. 109

5.10 Rubidium energy levels in ladder configuration for four-photon excitation to the Rydberg state. 111

5.11 Laser beam geometry through rubidium vapor cell. 112

6.1 Schematic of energy levels in ladder configuration. 116

6.2 Probe transmission: (a) in absence of microwave field ($\Omega_\mu = 0$) and (b) in presence of microwave field ($\Omega_\mu = 1$ MHz). $k_p = k_c = 0.007 \times 10^6$ m^{-1} and $k_\mu = 0.00005 \times 10^6$ m^{-1}. The laser parameters used in the model are $\Omega_1 = 10$ MHz, $\Omega_2 = 110$ MHz, $\Omega_3 = 25$ MHz, $\Omega_4 = 160$ MHz, $\Delta_1 = 1200$ MHz, $\Delta_3 = 1000$ MHz, $\Delta_\mu = 0$ and Δ_4 is adjusted around Δ_3 to make the transmission symmetric. 119

6.3 (a) Schematic of a four-level system for microwave field sensing with a two-photon excitation process. (b) Probe transmission as a function of Δ_c and Δ_μ in the absence ($\Omega_\mu = 0$) and presence of microwave field ($\Omega_\mu = 3$ MHz). The laser parameters are: $\Omega_p = 0.5$ MHz, $\Omega_c = 2$ MHz, $\Delta_p = 0$, $\Gamma_{eg} = 6$ MHz, $\Gamma_{re} = 1$ kHz, $\Gamma_{r'r} = 0.5$ kHz, $\Gamma_{rg} = 0.2$ MHz, $\Gamma_{r'g} = 0.2$ MHz, $k_p = 1.28166 \times 10^6$ m^{-1}, $k_c = 2.08333 \times 10^6$ m^{-1} and $k_\mu = 0.00005 \times 10^6$ m^{-1}. 120

6.4 Percentage of reduction in probe transmission as a function of microwave E-field strength. The laser parameters are: $\Omega_p = 0.5$ MHz, $\Omega_c = 2$ MHz, $\Delta_p = 0$, $\Delta_c = 0$, $\Gamma_{eg} = 6$ MHz, $\Gamma_{re} = 1$ kHz, $\Gamma_{r'r} = 0.5$ kHz, $\Gamma_{rg} = 0.2$ MHz, $\Gamma_{r'g} = 0.2$ MHz, $k_p = 1.28166 \times 10^6$ m^{-1}, $k_c = 2.08333 \times 10^6$ m^{-1} and $k_\mu = 0.00005 \times 10^6$ m^{-1}. 121

6.5 Percentage of reduction in probe transmission with varying microwave E-field strength. $k_p = k_c = 0.007 \times 10^6$ m^{-1} and $k_\mu = 0.00005 \times 10^6$ m^{-1}. The laser parameters used in the model are $\Omega_1 = 10$ MHz, $\Omega_2 = 110$ MHz, $\Omega_3 = 25$ MHz, $\Omega_4 = 160$ MHz, $\Delta_1 = 1200$ MHz, $\Delta_3 = 1000$ MHz, $\Delta_\mu = 0$ and Δ_4 is adjusted around Δ_3 to make the transmission symmetric. 122

6.6 Probe transmission: (a) in the absence of microwave field ($\Omega_\mu = 0$) and (b) in presence of microwave field ($\Omega_\mu = 0.2$ MHz). $k_p = k_c = k_\mu = 0.00005 \times 10^6$ m^{-1}. The laser parameters used in the model are $\Omega_1 = 1$ MHz, $\Omega_2 = 30$ MHz, $\Omega_3 = 20$ MHz, $\Omega_4 = 50$ MHz, $\Delta_1 = 1200$ MHz, $\Delta_3 = 1000$ MHz, $\Delta_\mu = 0$ and Δ_4 is adjusted around Δ_3 to make the transmission symmetric. 123

6.7 Percentage of reduction in probe transmission with varying microwave E-field strength. $k_p = k_c = k_\mu = 0.00005 \times 10^6$ m^{-1}. The laser parameters used in the model are $\Omega_1 = 1$ MHz, $\Omega_2 = 30$ MHz, $\Omega_3 = 20$ MHz, $\Omega_4 = 50$ MHz, $\Delta_1 = 1200$ MHz, $\Delta_3 = 1000$ MHz, $\Delta_\mu = 0$ and Δ_4 is adjusted around Δ_3 to make the transmission symmetric. 124

6.8 Microwave wave-guide. 126

6.9 Design of vacuum chamber for four-photon experiment. 127

6.10 63 CF flange design for mounting the wave-guide. 128

A.1 Energy level scheme for the two-atom system. Each atom is in an effective three-level system in a ladder configuration. 130

A.2 Gaussian distribution of random numbers. 138

A.3 Comparison of probe transmission calculated using single-atom system (solid black line) and non-interacting two-atom system (open red circles) for $\Delta k = 0$. Here, $k_p = 0.007 \times 10^6$ m^{-1}. The laser parameters used in the model are $\Omega_1 = 25$ MHz, $\Omega_2 = 110$ MHz, $\Omega_3 = 25$ MHz and $\Omega_4 = 160$ MHz, $\Delta_1 = 1200$ MHz, $\Delta_3 = 1000$ MHz and Δ_4 is adjusted around Δ_3 such that the transmission is symmetric. . . . 139

A.4 Comparison of probe transmission calculated for non-interacting two-atom system (open red circles) and interacting two-atom system with $\Delta_{int} = 100$ MHz (open black circles) for (a) $\Delta k = 0$ and (b) $\Delta k = 0.013 \times 10^6$ m^{-1}. Here, $k_p = 0.007 \times 10^6$ m^{-1}. The laser parameters used in the model are $\Omega_1 = 25$ MHz, $\Omega_2 = 110$ MHz, $\Omega_3 = 25$ MHz and $\Omega_4 = 160$ MHz, $\Delta_1 = 1200$ MHz, $\Delta_3 = 1000$ MHz and Δ_4 is adjusted around Δ_3 such that the transmission is symmetric. 140

A.5 Normalized blockaded transmission as a function of k_c with $k_p = 0.007 \times 10^6$ m^{-1} for $\Delta_{int} = 100$ MHz. The laser parameters used in the model are $\Omega_1 = 25$ MHz, $\Omega_2 = 110$ MHz, $\Omega_3 = 25$ MHz and $\Omega_4 = 160$ MHz, $\Delta_1 = 1200$ MHz, $\Delta_3 = 1000$ MHz and Δ_4 is adjusted around Δ_3 such that the transmission is symmetric. 141

Chapter 1

Introduction

1.1 Atom-based sensors

Atomic spectroscopy lays the foundation for many precise measurements of physical quantities. Due to the invariance of the atomic properties over time, they act as an accurate detection method for various applications. The spectroscopic signals of atomic transitions are affected due to external perturbations such as the presence of electromagnetic fields. Atom-based measurements are being used to set the time and frequency standards [1–5], length standards [6], measure electric fields [7–12], magnetic fields [13–18], and gravity [19], inertia and rotation. These sensors can either be prepared by using room temperature atoms in a vapor cell [7], or laser cooled atoms through optical and magnetic fields [17]. The room temperature vapor cell experiments are comparatively easier to realize and implement for quantum device purposes.

1.2 Conventional vs. atom-based E-field sensing

Many scientific queries in communication technology, healthcare, weather, astronomy, electronic devices, etc., need to be answered over a wide frequency range from radio frequency (RF) to far-infrared (FI) regime. This requires precise measurement of the electric field strength. The conventional electric field sensing method involves using dipole antennas or electromagnetic probes [20–22]. The probe can be visualized as a diode placed across a dipole antenna. Calibrating these probes is difficult as they need to be placed in a known field. In order to have a known field, a calibrated probe is necessary. The uncertainties in the measurement of the known field are nearly 5 % [23]. The probes are used below the resonant frequency of the dipole to avoid the issues of perturbation and variations in the response at resonance. The size of the probe is limited by the electronics and the size of the dipole antenna. There are various limitations to using such probes, such as:

- The probes need to be calibrated over time.
- The metallic nature of the probe can perturb the measurement of the electric field.
- The sensitivity of the measured electric field depends on the length of the dipole used as long as no resonant enhancement is used.
- The minimum detectable field is of the order of 1 mV/cm, which limits the sensitivity [24].

The research community targeted to make the measurements directly traceable to SI units and fundamental physical constants to avoid discrepancy [23, 25]. From the atomic transition frequencies, the frequency of the electromagnetic field interacting with the atoms can be determined precisely and accurately. Frequency can be related to other physical quantities through fundamental constants. Hence, the atom-based methods can provide a precise measurement of the physical quantities. The advantages of atom-based sensing methods over the conventional techniques are listed below:

- The atomic systems are self-calibrating; do not need to be calibrated as the atomic properties do not change over time.
- The perturbation is very little as the probe is very small compared to the wavelength of the electromagnetic field.

- The atom-based measurements link the different physical quantities to each other through fundamental constants and can be traced to SI units.
- The sensitivity is very high with low field strengths of the order of 1 μV/cm [26].
- The atomic systems provide the advantage of measuring fields over a wide frequency range from MHz to THz.

1.3 Review of Rydberg atom-based E-field sensing

Rydberg atom-based microwave field sensing was realized using highly excited Rydberg atoms contained in a vapor cell [7]. These highly excited Rydberg atoms [27] allow a wide range of transition frequencies which can be achieved using diode lasers. Electromagnetically induced transparency (EIT) [28, 29] provides a non-destructive approach to detect these Rydberg states [30]. EIT results in probe transmission around resonance, rather than absorption, within a narrow frequency range. This happens due to destructive interference of the excitation pathways: (a) direct probe absorption and (b) probe absorption along with the coherent excitation and de-excitation by the coupling beam. Several studies have been performed to develop an atomic probe for sensing electric fields using Rydberg EIT. With their large atomic dipole moment, the Rydberg atoms allow free space efficient coupling of microwave and THz fields to optical fields [7, 8, 31] without the need for any optical cavity. In contrast, most systems need cavities to enhance the coupling of microwave fields to optical fields [32–34]. The coupling of microwave and THz fields to optical fields leads to various applications such as sub-wavelength imaging [35, 36], detection of millimeter waves [37], storing quantum information [38], transfer of quantum states from microwave to optical domain [39], THz imaging [31], etc. Presence of the microwave field leads to the splitting of the EIT peak or absorption within the transmission window, which is also a quantum interference process. As frequencies can be measured precisely through atomic transitions, measuring the splitting of the EIT peak provides an accurate measurement of the electric field strength of the microwave field. The minimum detectable field amplitude with Rydberg EIT, using a two-photon excitation process, is 8 μV/cm with a sensitivity of 30 $\mu\text{Vcm}^{-1}\text{Hz}^{-1/2}$ [7]. This sensitivity was improved to 5 $\mu\text{Vcm}^{-1}\text{Hz}^{-1/2}$ with the minimum detectable field of 1 μV/cm using a homodyne detection method [26].

1.4 Motivation to study microwave field sensing with Rydberg atoms in thermal vapor

The field of microwave sensing using Rydberg atoms has developed exponentially over the decade and offers vast prospects for data communication technology. Several companies have been founded to make use of these methods. Usual microwave field sensing involves the usual two-photon excitation process to the Rydberg state with a probe and coupling field to achieve EIT. The Rydberg state is then coupled to another nearby Rydberg state with a microwave field. Two major limitations exist in the RF electric field sensing using the two-photon Rydberg-EIT method. The first one is that the signal bandwidth or the modulation bandwidth determined from amplitude/frequency/phase modulation of the microwave field is limited to only a few MHz [40–42]. This limitation is set by the optical pumping rate to the EIT dark state, which depends on the coupling field Rabi frequency and natural line-width of the intermediate state, which is 6 MHz for rubidium. The other limitation is that the sensitivity of the detected electric field is limited by the linewidth of the EIT signal, which is typically a few MHz [43], let's say about 3-4 MHz, for the two-photon Rydberg excitation process. The modulation bandwidth helps to determine the temporal response a system. The limitation in the signal bandwidth served as a motivation to develop a plan which can have a larger bandwidth and hence, a faster data transfer rate. Also, the need to create a system with higher sensitivity to detect electric fields provided an investigation direction for the thesis. Also, the thermal vapor systems are easier to execute for application purposes than the cold atomic systems with bulky metallic setups which can perturb the microwave fields. Hence, electric field sensing in thermal vapor system are beneficial for practical applications.

1.5 Contribution of the thesis to the field of microwave field sensing and data communication technology

This thesis work is focused on sensing microwave fields using Rydberg atoms in thermal atomic vapor.
(A) As an introduction to this research field, this thesis provides an overview of the study of microwave field sensing with Rydberg atoms in thermal atomic vapor using a two-photon Rydberg EIT system.

- Experiments have been performed to demonstrate the field sensing using two-photon excitation processes, and a theoretical model has been provided.
- Analog communication has been demonstrated using the two-photon Rydberg EIT system.

(B) The thesis also presents a six-wave mixing of optical and microwave fields in thermal atomic vapor.

- The demonstrated six-wave mixing process leads to a parametric generation of a new optical field with a generation bandwidth of 17 MHz.
- A theoretical model is provided to understand the experimental results. The optical Bloch equations are solved using a perturbative expansion of the density matrix, and also, the wave propagation equations are solved for the generated field.

- The temporal response of the system is explored through amplitude modulation of the generated fields. The system shows a modulation bandwidth, same as the signal generation bandwidth, limited by the available coupling Rabi frequency rather than any fundamental limitation.
- A theoretical study is performed to understand that the bandwidth can be increased significantly with the increase in coupling Rabi frequency without compromising the efficiency of the sensor.
- This system offers a huge technological advantage of faster data transfer rate for communication technology. Also, it is a thermal vapor system. Executing such systems to quantum devices is much easier compared to complex ultra-cold atomic systems.

(C) Further studies in the thesis involve the theoretical study of the four-photon excitation process to the Rydberg state.

- A theoretical model of four-photon excitation to the Rydberg state is provided.
- The elimination of motion-induced dephasing is achieved through the use of lasers of suitable wavelength and arranging the laser fields properly through the atomic vapor cell.
- The four-photon process helps to achieve a narrow electromagnetically induced transparency (EIT) signal with transparency of ~ 0.9 by eliminating the motion-induced dephasing in the system.
- An experimental proposal is provided for performing the four-photon excitation to the Rydberg state in thermal rubidium vapor.

(D) A theoretical study on microwave field sensing is performed using the four-photon excitation process to the Rydberg state.

- With suitable parameters, the four-photon process helps achieve a narrow line-width electromagnetically induced transparency (EIT) signal with a bandwidth of 230 kHz.

- It provides a higher sensitivity of detected electric field, which is of the order of ~ 55 nVcm^{-1}Hz$^{-1/2}$.

- Designing of the experiment is discussed briefly.

1.6 Layout of the thesis

The thesis consists of six chapters, including the introduction chapter and excluding the appendix section. The layout of the thesis is provided below.

- **Chapter 2** gives an introduction to a special class of atoms known as Rydberg atoms and its various properties. It includes the basics of atom-light interaction, where the atomic model of two-level and three-level systems is discussed. The three-level system is used to explain the phenomenon of EIT. Since the experiments in the thesis involve the use of the rubidium atomic system, the energy levels of the rubidium system are discussed. Finally, the techniques to stabilize the frequency of the probe and coupling laser fields are presented.

- **Chapter 3** provides an introduction to Rydberg electrometry, where microwave field sensing is investigated using EIT in a two-photon excitation process. As an application, analog communication with Rydberg atoms is demonstrated using this system. Finally, the limitations of field sensing with a two-photon EIT system are discussed, which provided the motivation for further investigations.

- **Chapter 4** discusses the six-wave mixing phenomenon of optical and microwave fields in thermal atomic vapor using Rydberg atoms. The generation of a new optical field due to the six-wave mixing process is studied, and the temporal response of the system is investigated using amplitude modulation of the generated field. A theoretical model is provided for a four-level system, and the wave propagation equations are solved for the generated fields to explain the experimental observations. Finally, a theoretical study is performed to understand the effect of coupling Rabi frequency on the signal bandwidth.

- **Chapter 5** provides a theoretical study on EIT using four-photon excitation to the Rydberg state in a thermal atomic medium. It describes an atomic model of a five-level system to achieve EIT with a four-photon excitation process where the motion-induced dephasing is eliminated. The effect of residual wave-vector on peak EIT transmission is studied. The method of adiabatic elimination is discussed to reduce the complex-five level system to an effective three-level system. Finally, an experimental proposal is discussed to realize the system with rubidium atomic vapor.

- As an outlook to the thesis, **Chapter 6** provides a theoretical study on microwave field sensing using a four-photon excitation process to the Rydberg state in thermal atomic vapor. An atomic model is provided to observe EIT and study the effect of a microwave field on EIT with four-photon excitation to the Rydberg state. A comparison is provided between the field sensing using the two-photon and four-photon excitation process, and the sensitivity of the detected electric field for the four-photon excitation system is estimated. Finally, a brief experimental plan is provided, which includes some designing using SOLIDWORKS.

The thesis focuses on microwave field sensing with thermal Rydberg atoms. However, a theoretical study of EIT in the strong blockade regime using the four-photon excitation process has also been performed, which does not fit into the focus of the thesis. Hence, it has been included in the appendix. The **Appendix** discusses the study of EIT in the strong blockade regime using the four-photon excitation process in thermal rubidium vapor.

Chapter 2

Basics of coherent Rydberg excitation in rubidium vapor

Atom-light interaction lays the foundation for research in atomic and molecular physics. This chapter introduces Rydberg atoms [27] and their properties followed by a scaling law of these properties with the principal quantum number (n). The chapter also describes atom-light interaction using a simple two-level and three-level system [44]. The concept of the three-level system is further used to explain the phenomenon of electromagnetically induced transparency (EIT) [28, 29, 45]. Since the experiments in the thesis involve the use of the rubidium atom, the properties of the rubidium atomic system are described. Finally, a discussion on the techniques to stabilize the frequency of the laser fields to a particular atomic transition is presented, which involves Doppler-free absorption spectroscopy and frequency stabilization using EIT locking technique [46].

2.1 Rydberg atoms

Atoms in which the valence electron is excited to a very high principal quantum number (n) state are known as Rydberg atoms [27]. The interest in exploring Rydberg atoms draws long back to the time of the discovery of the Balmer series of spectral lines for Hydrogen atoms in 1885. Later, in 1888, the entire spectral series of the Hydrogen atom was explained by J. Rydberg, and he provided the Rydberg formula for deriving the energy levels of the highly excited atoms, which helped in explaining atomic spectroscopy. The unique properties of Rydberg atoms fueled the interest to explore such atoms.

2.1.1 Properties of Rydberg atoms

Two crucial motivations led to the investigation of Rydberg atoms. First, all the properties of Rydberg atoms show regular n dependence, allowing researchers to verify the measurements accurately and consistently. Second, atoms in the Rydberg state offered an opportunity to use their exaggerated properties, which was not possible in the case of ground state atoms. As the highly excited valence electron in a Rydberg atom is loosely bound to the ionic core, it exhibits high sensitivity to even a small external electric field compared to any normal atom, which provides a promising scope for DC electric field sensing [47]. Also, Rydberg atoms can be used for quantum information processing because of the strong long-range interaction between them [48, 49]. The controllable strong interaction results in a phenomenon called the Rydberg blockade [50–52], which enables manipulation of qubits.

2.1.1.1 Scaling laws of Rydberg atom properties

The various properties of Rydberg atoms can be scaled with the principal quantum number (n), which is presented in Table. 2.1. The size of the Rydberg atom, given by the orbital radius, goes as n^2. Compared to the ground state, let's say n=5, the atom in the Rydberg state with n=60 has a size larger by 144 times. The larger size results in a strong dipole moment (μ), which also goes as n^2. The lifetime of the Rydberg states goes as n^3, which means that high n Rydberg states are long-lived. Hence, such states have narrow natural linewidth. The energy difference between the Rydberg states $\Delta E_n \propto n^{-3}$. This suggests that the energy difference between Rydberg states decreases with increasing n. So the high n Rydberg states are continuum states above the ionization limit. The field needed to ionize the Rydberg atoms goes as n^{-4}. The ionization field is a million times smaller than the field needed to ionize the Hydrogen atom in the ground state. Field ionization is also a technique that has been used to detect the highly excited Rydberg states [53]. The polarizability of the Rydberg atoms given by $\frac{\mu^2}{\Delta E_n}$ goes as n^7, which has been exploited to measure d.c. electric fields [30]. The polarizability and the dipole moment increase strongly for states with high n, which exaggerates the sensitivity of the Rydberg states to external electric fields [54]. The strong van der Waals Rydberg-Rydberg interaction [55] depends on n^{11} which is the reason for the Rydberg blockade phenomenon and many-body effects observed for interacting Rydberg atoms [56, 57].

Table 2.1: Scaling laws with n

No	Properties	n scaling
1	Orbital radius	n^2
2	Dipole moment	n^2
3	Binding energy	n^{-2}
4	Energy between adjacent n states	n^{-3}
5	Radiative Lifetime	n^3
6	Ionization field	n^{-4}
7	Polarizability	n^7
8	van der Waals interaction	n^{11}

2.1.2 Quantum defect

Using the quantum defect approach, for a single valence electron atom such as the H atom as a special case, the energy levels of Rydberg atoms are calculated. The Rydberg states of an alkali atom are similar to that of an H atom. Considering an alkali atom such as Rubidium (Rb), Rb^+ core has a +1 charge, with the core having 37protons and 36 electrons. The Rydberg electron spends most of its time far from the core and at the highly excited n state. There is a very nominal difference between the H atom and the Rb atom at such a state. So, the properties of Rydberg atoms are expected to be similar to the H atom. But if the Rydberg electron approaches the Rb^+ core, it polarizes and penetrates the Rb^+ core which changes the wave functions

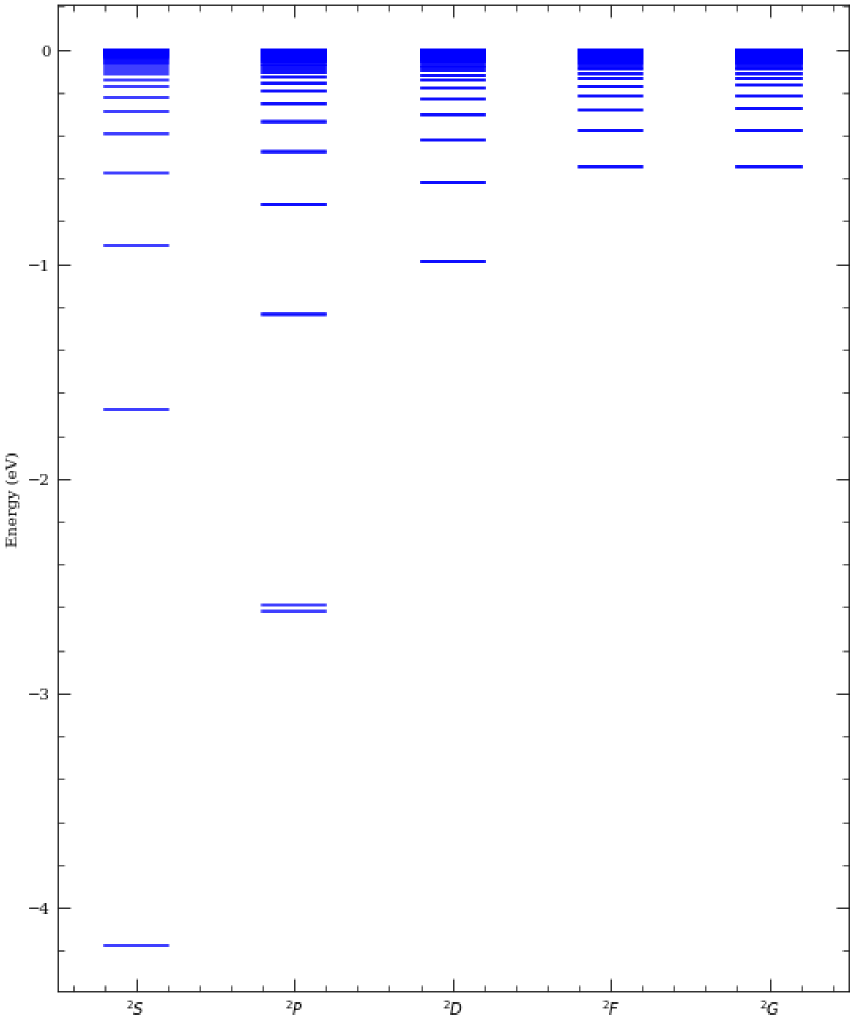

Figure 2.1: Energy levels of ^{85}Rb up to $n = 100$. The figure is obtained using ARC documentation [58].

and energies of the Rb Rydberg state from the H atom. If the atoms are in a higher orbital angular momentum state (l), the Rydberg electron cannot penetrate the Rb$^+$ core or the penetration is almost zero. So, the differences between H and Rb are insignificant. But for low-lying l states, the core polarization and penetration reduce the energies of the low l states. The high l states of Rb and the H levels are observed to be degenerate, but there is a difference in energy for low-lying l states. The formula for the energy of the low l Rydberg states is given by

$$E_{nl} = -\frac{Ry}{2(n - \delta_{nl})^2} \tag{2.1}$$

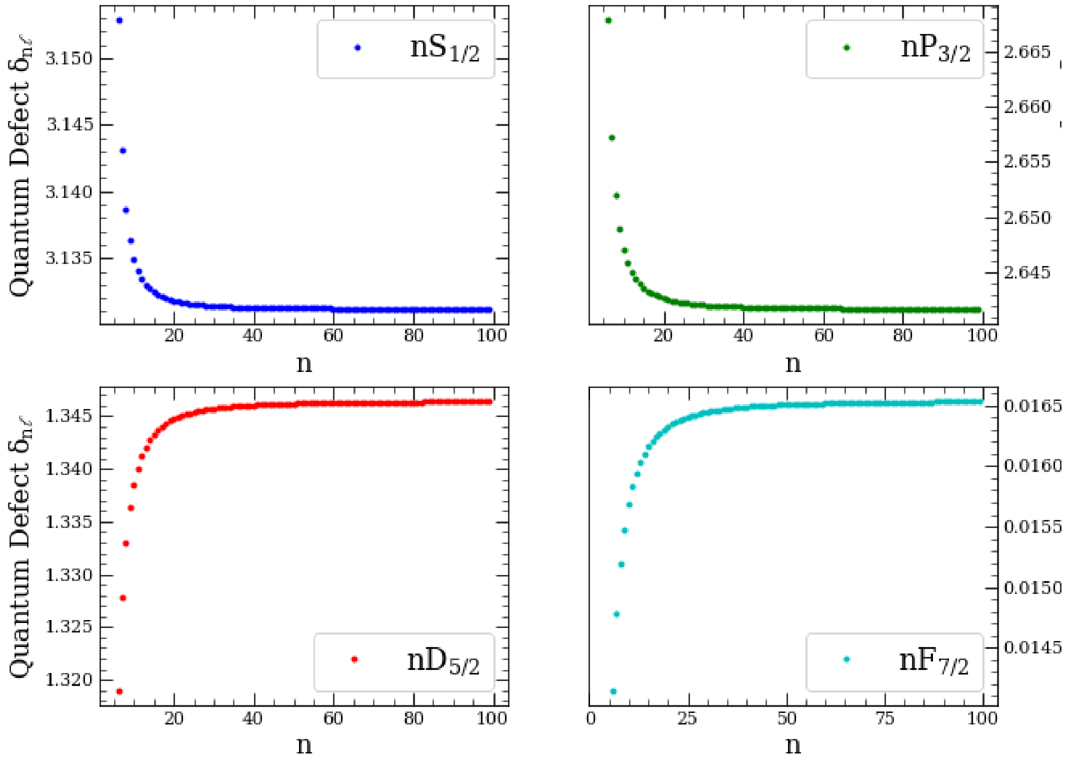

Figure 2.2: Quantum defect values for ^{85}Rb for $l = 0 - 3$. The figure is obtained using ARC documentation [58].

where δ_{nl} is the observed quantum defect for states with orbital angular momentum l and Ry is the Rydberg constant given by $Ry = 109721.6$ cm^{-1}. The energy levels for such atoms can be categorized into different series, with each series corresponding to a different value of l as shown in Fig. 2.1. δ_{nl} is a slowly varying function of n for a given l, so it can be considered to be nearly independent of n. It has been found experimentally that Eqn.(2.1) is suitable for alkali atoms with one electron outside the closed shell configuration. Quantum defects for different alkali atoms for the first few angular momentum states are listed in Table. 2.2 [59, 60]. It can be seen

Table 2.2: Quantum defect values for alkali atoms at different l states.

l	Li	Na	K	Rb	Cs
s	0.40	1.35	2.19	3.13	4.06
p	0.04	0.85	1.71	2.66	3.59
d	0.00	0.01	0.25	1.34	2.46
f	0.00	0.00	0.00	0.01	0.02

that the value of δ_{nl} decreases drastically for higher values of l. This indicates that the energy of high l lying states are nearly degenerate with H atom. δ_{nl} is depicted as a function of n for different l states in Fig. 2.2 for ^{85}Rb.

2.2 Atom-light interaction and the refractive index

The interaction of monochromatic optical fields with the atomic system can be understood by solving the optical Bloch equations for the system using a semi-classical model [44]. Here, the laser field is considered a classical electromagnetic field, whereas the atomic system is treated with a quantum mechanical approach. This section discusses the basics of atom-light interaction using the two-level and three-level systems coupled with monochromatic optical fields in the ladder configuration.

2.2.1 Non-interacting two-level atoms in gas density N

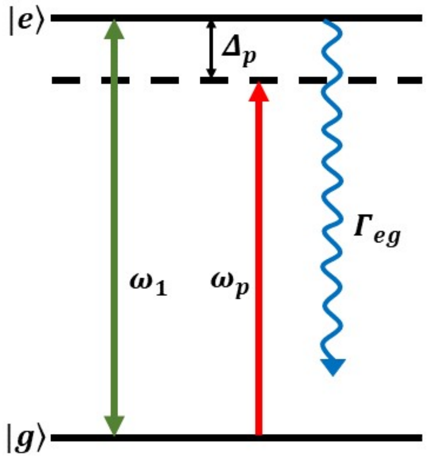

Figure 2.3: Schematic of energy levels of a two-level system where $|g\rangle$ and $|e\rangle$ represent the ground state and the excited state respectively.

The two-level system is the simplest configuration to study the atom-light interaction. It consists of a ground state $|g\rangle$ and an excited state $|e\rangle$ coupled by a monochromatic probe field of frequency ω_p as shown in Fig. 2.3. The energy difference between the states is given by $E_e - E_g = \hbar\omega_1 - 0 = \hbar\omega_1$ with ω_1 being the atomic resonance frequency. The detuning of the probe beam from the atomic resonance is given by $\Delta_p = \omega_p - \omega_1$. The probe field is represented by $\vec{E'}_p = \vec{E}_p e^{-i\omega_p t} + c.c.$ The Rabi frequency of the probe is given by $\Omega_p = \frac{2\mu_{ge}E_p}{\hbar}$ where μ_{ge}, E_p denote the transition dipole moment and electric field amplitude corresponding to the probe field respectively. The bare atomic Hamiltonian for the two-level system is written as $H_0 = \hbar\omega_1 |e\rangle\langle e|$. The interaction Hamiltonian between the optical field and the atomic system is $H_{int} = -\vec{\mu}\cdot\vec{E} = -(E_p e^{-i\omega_p t} + c.c)(\mu_{ge}|g\rangle\langle e| + \mu_{eg}|e\rangle\langle g|)$. The total Hamiltonian for the system is given as

$$\tilde{H} = H_0 + H_{int} = \begin{pmatrix} 0 & -(E_p e^{-i\omega_p t} + c.c)\mu_{ge} \\ -(E_p e^{-i\omega_p t} + c.c)\mu_{eg} & \hbar\omega_1 \end{pmatrix}.$$

This Hamiltonian is time-dependent. Using a unitary operation, the frame of reference can be transformed to a rotational frame of reference where the Hamiltonian becomes time independent. In such a case, the rapidly oscillating terms are neglected. This approximation holds for the case when the applied laser field is near the resonance. The unitary operator used for the two-level system is

$$U = \begin{pmatrix} 1 & 0 \\ 0 & e^{-i\omega_p t} \end{pmatrix}.$$

The Hamiltonian in the rotating frame is given by the operation $H = U^\dagger \tilde{H} U - i\hbar U^\dagger \frac{dU}{dt}$ such that

$$H = \begin{pmatrix} 0 & -(E_p + E_p^* e^{-2i\omega_p t})\mu_{ge} \\ -(E_p^* + E_p e^{2i\omega_p t})\mu_{eg} & \hbar(\omega_1 - \omega_p) \end{pmatrix}.$$

After the use of rotating wave approximation, the rapidly oscillating terms with frequency $2\omega_p$ are neglected to find the total time-independent Hamiltonian as

$$H = -\frac{\hbar}{2}\begin{pmatrix} 0 & \Omega_p \\ \Omega_p^* & 2\Delta_p \end{pmatrix}.$$

The system is understood by studying the optical Bloch equation or the master equation, which is written as

$$\dot{\rho} = \frac{i}{\hbar}[\rho, H] + \mathcal{L}_{\mathcal{D}}(\rho). \tag{2.2}$$

Here, ρ is the density matrix of the system defined by the 2×2 matrix as

$$\rho = \begin{pmatrix} \rho_{gg} & \rho_{ge} \\ \rho_{eg} & \rho_{ee} \end{pmatrix}$$

and $\mathcal{L}_{\mathcal{D}}(\rho)$, the Lindblad operator [61], constituting the decay and decoherence processes occurring in the system, is given by

$$\mathcal{L}_{\mathcal{D}}(\rho) = \begin{pmatrix} \Gamma_{eg}\rho_{ee} & -\frac{1}{2}\Gamma_{eg}\rho_{ge} \\ -\frac{1}{2}\Gamma_{eg}\rho_{eg} & -\Gamma_{eg}\rho_{ee} \end{pmatrix}.$$

Here, ρ_{gg} and ρ_{ee} represent the population in the ground and excited states, respectively. ρ_{eg} represents the coherence between the states $|g\rangle$ and $|e\rangle$ created by the probe laser field. Γ_{eg} is the population decay from the excited state to the ground state, which is the inverse of the lifetime of the state. For a closed system, $\rho_{gg}+\rho_{ee} = 1$, $\rho_{eg} = \rho_{ge}^*$ and for stationary states $\dot{\rho_{ij}} = 0$. The optical Bloch equations for the steady state are written as

$$\frac{i}{2}[2\Delta_p\rho_{ge} - 2\Omega_p\rho_{ee} + \Omega_p] - \frac{\Gamma_{eg}}{2}\rho_{ge} = 0 \tag{2.3}$$

$$\frac{i}{2}[\Omega_p^*\rho_{ge} - \Omega_p\rho_{eg}] + \Gamma_{eg}\rho_{ee} = 0 \tag{2.4}$$

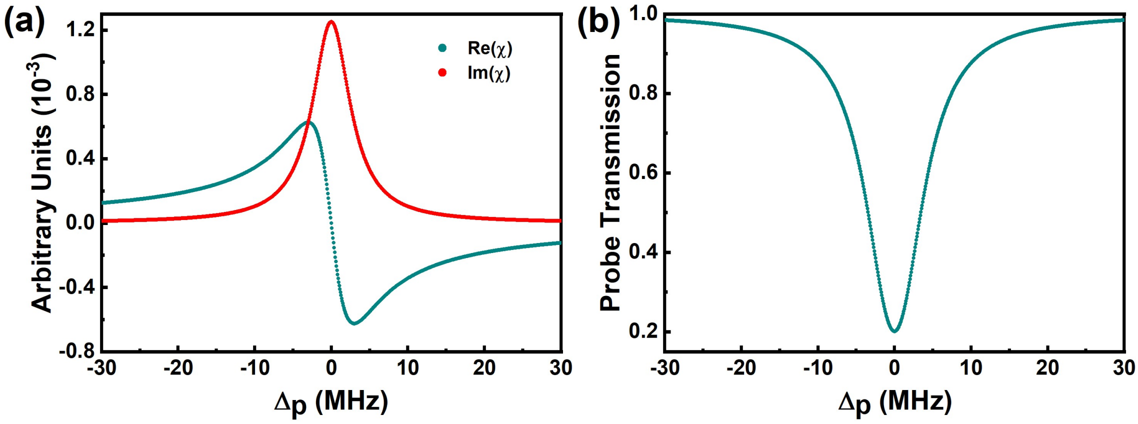

Figure 2.4: For a two level-system with atoms at rest: (a) Real ($\Re(\chi)$) and imaginary ($\Im(\chi)$) part of the susceptibility are given by red closed circles and cyan closed circles respectively and (b) probe transmission. $\Re(\chi)$ provides an estimate of the dispersion induced by the atomic light interaction in the medium and $\Im(\chi)$ estimates the absorption of the input light while propagating through the atomic medium. Laser parameters are: $\Omega_p = 0.1$ MHz, $\Gamma_{eg} = 6$ MHz and density of the atoms (N) is 10^{10} cm^{-3}.

The above Bloch equations are solved to find out ρ_{ee} and ρ_{eg} as

$$\rho_{ee} = \frac{\Omega_p^2}{2\Omega_p^2 + 4\Delta_p^2 + \Gamma_{eg}^2} \tag{2.5}$$

$$\rho_{eg} = \frac{\Omega_p(-i\Gamma_{eg} - 2\Delta_p)}{2\Omega_p^2 + 4\Delta_p^2 + \Gamma_{eg}^2} \tag{2.6}$$

The susceptibility of the probe field coupling the $|g\rangle \rightarrow |e\rangle$ transition is

$$\chi(\omega_p) = \frac{2N|\ \mu_{ge}\ |^2}{\hbar\epsilon_0\Omega_p}\rho_{eg} \tag{2.7}$$

where N is the density of the atoms inside the atomic medium. The refractive index is given by

$$n = \sqrt{1+\chi} = (1 + \frac{\chi}{2}) = (1 + \frac{\Re(\chi)}{2}) + i\frac{\Im(\chi)}{2} = \Re(n) + i\Im(n). \tag{2.8}$$

$\Re(\chi)$ represents the dispersion of the laser field due to the atomic medium, whereas $\Im(\chi)$ is the measure of absorption of the laser field by the medium, represented in

Fig. 2.4(a). The transmission of the probe through the atomic medium is

$$T = (\frac{I}{I_0}) = e^{(-\alpha l)} \tag{2.9}$$

where $\alpha = \Im(\chi) k_p l$ is the absorption coefficient and l is the path length of the laser field through the atomic medium. The transmission of the probe for the two-level system with atoms at rest is represented by Fig. 2.4(b). The situation will be different in the case of a three-level system where the presence of a second laser field changes the response of the atomic medium as compared to that in a two-level system.

2.2.2 Dressed state picture

The atomic wave function for the two-level system is represented as $|\psi\rangle = C_g(t)|g\rangle + C_e(t)|e\rangle$ where $C_g(t)$ and $C_e(t)$ represent the probability amplitude at time t for the atom to be in state $|g\rangle$ and $|e\rangle$ respectively. The two-level Hamiltonian eigenvalues are found by solving the characteristic eigenvalue equation $|H - \Lambda I| = 0$. The diagonalization of the matrix using the eigenvalue equation gives

$$\left| -\frac{\hbar}{2} \begin{pmatrix} 0 & \Omega_p \\ \Omega_p^* & 2\Delta_p \end{pmatrix} - \Lambda \begin{pmatrix} 1 & 0 \\ 0 & 1 \end{pmatrix} \right| = 0 \tag{2.10}$$

$$\implies \Lambda = -\frac{\hbar}{2}\big(\Delta_p \pm \sqrt{\Delta_p^2 + \mid \Omega_p \mid^2}\big) = -\frac{\hbar}{2}\big(\Delta_p \pm \Omega'\big). \tag{2.11}$$

$\Omega' = \sqrt{\Delta_p^2 + \mid \Omega_p \mid^2}$ is defined as the generalized Rabi frequency.

The eigenstates for the given eigenvalues are found as

$$|\psi_+\rangle = \sin\frac{\theta}{2}|g\rangle + \cos\frac{\theta}{2}|e\rangle \tag{2.12}$$

$$|\psi_-\rangle = \cos\frac{\theta}{2}|g\rangle - \sin\frac{\theta}{2}|e\rangle \tag{2.13}$$

where we define $\mid \Omega_p \mid = \Omega' \sin\theta$, $\Delta_p = \Omega' \cos\theta$ and $\tan\theta = \frac{|\Omega_p|}{\Delta_p}$. $|\psi_+\rangle$ and $|\psi_-\rangle$ are the energy eigenstates known as the dressed states.

When $\Delta_p = 0$:

When the applied field is on resonance to the atomic transition, i.e., $\Delta_p = 0$, then $\Omega' =\mid \Omega_p \mid$. The energy eigenvalues are given by $\Lambda_\pm = \mp\frac{\hbar}{2} \mid \Omega_p \mid$. The dressed states have equal energy and are equally separated from the unperturbed atomic bare states but in opposite directions.

When $\Delta_p \gg\mid \Omega_p \mid$:

When the applied field is such that $\Delta_p \gg\mid \Omega_p \mid$, then the energy eigenvalues are $\Lambda_+ = -\hbar\Delta_p - \frac{\hbar|\Omega_p|^2}{4\Delta_p}$ and $\Lambda_- = \frac{\hbar|\Omega_p|^2}{4\Delta_p}$. The dressed states are separated from the bare atomic states by a factor of $\frac{|\Omega_p|^2}{4\Delta_p}$ and in the opposite direction. The difference between the energy eigenvalues gives the separation between the dressed states to be $-\hbar\Delta_p - \frac{\hbar|\Omega_p|^2}{2\Delta_p}$. The factor $\frac{|\Omega_p|^2}{4\Delta_p}$ is the light shift factor that is introduced into the system because of the strong applied laser field. The formation of the dressed states depends on the detuning and Rabi frequency of the laser field.

2.2.3 Three level system

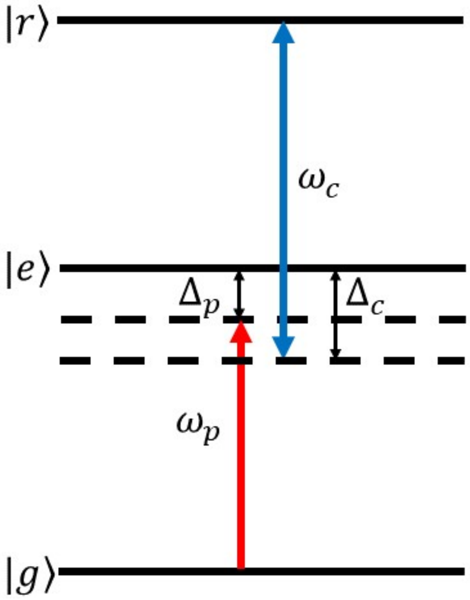

Figure 2.5: Schematic of energy levels of a three-level system in ladder configuration. $|g\rangle$, $|e\rangle$ and $|r\rangle$ represent the ground, intermediate and the excited state respectively.

Consider a three level system in ladder configuration consisting of states $|g\rangle$, $|e\rangle$ and $|r\rangle$, as shown in Fig. 2.5, where the atomic resonance frequency between states $|g\rangle$ and $|e\rangle$, $|e\rangle$ and $|r\rangle$ is given by ω_1 and ω_2 respectively. Excitation from $|g\rangle \rightarrow |e\rangle$ and $|e\rangle \rightarrow |r\rangle$ are dipole allowed whereas the excitation from $|g\rangle \rightarrow |r\rangle$ is dipole forbidden. The coherence between $|g\rangle$ and $|e\rangle$ ($|e\rangle$ and $|r\rangle$) is created by probe (coupling) field of frequency ω_p (ω_c) given by $\vec{E'}_p = \vec{E}_p e^{-i\omega_p t} + c.c$ ($\vec{E'}_c = \vec{E}_c e^{-i\omega_c t} + c.c$). The detuning of the probe (coupling) field from the atomic resonance is given by $\Delta_p = \omega_p - \omega_1$ ($\Delta_c = \omega_c - \omega_2$). The two photon detuning is defined by $\delta = (\Delta_p + \Delta_c)$. The Rabi frequency of the probe and coupling field is given by $\Omega_p = \frac{2\mu_{ge}E_p}{\hbar}$ and $\Omega_c = \frac{2\mu_{er}E_c}{\hbar}$ respectively. μ_{ge} (μ_{er}) and E_p (E_c) denote respectively the transition dipole moment and electric field amplitude corresponding to the probe (coupling) field.

The total Hamiltonian for the system is written as $\tilde{H} = H_0 + H_{int}$ where $H_0 = \hbar\omega_1|e\rangle\langle e| + \hbar(\omega_1 + \omega_2)|r\rangle\langle r|$ is the bare atomic Hamiltonian and $H_{int} = -\vec{\mu} \cdot \vec{E} = -E_p(\mu_{ge}|g\rangle\langle e| + \mu_{eg}|e\rangle\langle g|) - E_c(\mu_{er}|e\rangle\langle r| + \mu_{re}|r\rangle\langle e|)$ is the interaction Hamiltonian that represents the interaction between optical fields and atomic medium. After the use of rotating wave approximation, the time-independent total H is found to be

$$H = -\frac{\hbar}{2}\begin{pmatrix} 0 & \Omega_p & 0 \\ \Omega_p^* & 2\Delta_p & \Omega_c \\ 0 & \Omega_c^* & 2(\Delta_p + \Delta_c) \end{pmatrix}.$$

The optical Bloch equation or the master equation is given by

$$\dot{\rho} = \frac{i}{\hbar}[\rho, H] + \mathcal{L}_{\mathcal{D}}(\rho) \tag{2.14}$$

where ρ is the 3×3 density matrix of the three-level system. $\mathcal{L}_{\mathcal{D}}(\rho)$ is the Lindblad operator, represented as

$$\mathcal{L}_{\mathcal{D}}(\rho) = \sum_{if} \Gamma_{if}\Big[C_{if}\rho C_{if}^{\dagger} - \frac{1}{2}\{C_{if}^{\dagger}C_{if}, \rho\}\Big]. \tag{2.15}$$

C_{if} is defined as $C_{if} = |f\rangle\langle i|$ where $|f\rangle$ is the final state and $|i\rangle$ is the initial state. Lindblad operator matrix is written as

$$\mathcal{L}_{\mathcal{D}}(\rho) = \begin{pmatrix} \Gamma_{eg}\rho_{ee} + \Gamma_{rg}\rho_{rr} & -\frac{1}{2}\Gamma_{eg}\rho_{ge} & -\frac{1}{2}(\Gamma_{rg} + \Gamma_{re})\rho_{gr} \\ -\frac{1}{2}\Gamma_{eg}\rho_{eg} & \Gamma_{re}\rho_{rr} - \Gamma_{eg}\rho_{ee} & -\frac{1}{2}(\Gamma_{rg} + \Gamma_{re} + \Gamma_{eg})\rho_{er} \\ -\frac{1}{2}(\Gamma_{rg} + \Gamma_{re})\rho_{rg} & -\frac{1}{2}(\Gamma_{rg} + \Gamma_{re} + \Gamma_{eg})\rho_{re} & -(\Gamma_{rg} + \Gamma_{re})\rho_{rr} \end{pmatrix}.$$

The population decay rates from state $|e\rangle \rightarrow |g\rangle$ and $|r\rangle \rightarrow |e\rangle$ are represented by Γ_{eg} and Γ_{re} respectively. Decay from $|r\rangle \rightarrow |g\rangle$ is forbidden as the excitation is not dipole allowed. But there is a transit time decay Γ_{rg} from $|r\rangle \rightarrow |g\rangle$ due to the transverse motion of the atoms through the cross-section of the beam. As the system is a closed system $\rho_{gg} + \rho_{ee} + \rho_{rr} = 1$. Also, for stationary states $\dot{\rho_{ij}} = 0$. The optical Bloch equations for the steady state are

$$\frac{i}{2}[-2\Delta_p\rho_{ge} + \Omega_p(2\rho_{ee} + \rho_{rr}) - \Omega_p - \Omega_c^*\rho_{gr}] - \frac{\Gamma_{eg}}{2}\rho_{ge} = 0 \tag{2.16}$$

$$\frac{i}{2}[-2\delta\rho_{gr} + \Omega_p\rho_{er} - \Omega_c\rho_{ge}] - \frac{(\Gamma_{rg} + \Gamma_{re})}{2}\rho_{gr} = 0 \tag{2.17}$$

$$\frac{i}{2}[\Omega_p^*\rho_{ge} - \Omega_p\rho_{eg} + \Omega_c\rho_{re} - \Omega_c^*\rho_{er}] + \Gamma_{re}\rho_{rr} - \Gamma_{eg}\rho_{ee} = 0 \tag{2.18}$$

$$\frac{i}{2}[\Omega_p^*\rho_{gr} - 2\Delta_c\rho_{er} + \Omega_c(\rho_{rr} - \rho_{ee})] - \frac{(\Gamma_{rg} + \Gamma_{re} + \Gamma_{eg})}{2}\rho_{er} = 0 \tag{2.19}$$

$$\frac{i}{2}[\Omega_c^*\rho_{er} - \Omega_c\rho_{re}] - (\Gamma_{rg} + \Gamma_{re})\rho_{rr} = 0 \tag{2.20}$$

The system is solved for the steady state to find ρ_{eg}. The susceptibility of the probe, coupling the ground state $|g\rangle$ to the excited state $|e\rangle$, is given by

$$\chi(\omega_p) = \frac{2N|\ \mu_{ge}\ |^2}{\hbar\epsilon_0\Omega_p}\rho_{eg} \tag{2.21}$$

where N is the density of the atoms inside the atomic medium. $\Re(\chi)$ and $\Im(\chi)$ express the dispersion and absorption of the probe, respectively. The transmission of the probe beam is given as

$$T = (\frac{I}{I_0}) = e^{(-\alpha l)} \tag{2.22}$$

where $\alpha = \Im(\chi)k_p l$ is the absorption coefficient. l is the optical path length through the atomic medium.

2.2.4 Electromagnetically Induced Transparency (EIT)

Electromagnetically induced transparency (EIT) [29, 62] is an efficient and non-destructive technique to probe the atoms in the Rydberg states [45]. EIT makes the medium transparent to the probe light within a narrow frequency window. The narrow frequency regime, called the transparency regime, shows enhanced nonlinear response. EIT abruptly changes the absorption and dispersion of the probe beam within the narrow transparency regime [63]. The phenomenon of EIT was termed by Harris and his coworkers, who first demonstrated EIT in optically thick strontium vapor in 1991 [28]. Later in 1991, they also demonstrated EIT for pressure broadened lead vapor [64]. Since then, several studies have been performed to utilize EIT for different applications. The significant applications are compression of light pulses inside the atomic medium or the 'slow light' [65], development of quantum memory through control of the storage and retrieval of light pulses [66]. All these applications are possible because the group index can be controlled efficiently within the narrow EIT regime, and a large group index of the order of 10^6 can be achieved with EIT [63].

2.2.4.1 EIT in a three-level system

EIT can be observed in a three-level ladder system with weak probe and strong coupling fields. The strong probe field dresses the intermediate state and leads to the formation of two dressed states. There can be excitation from both the dressed states to the Rydberg state. Quantum destructive interference between the excitation

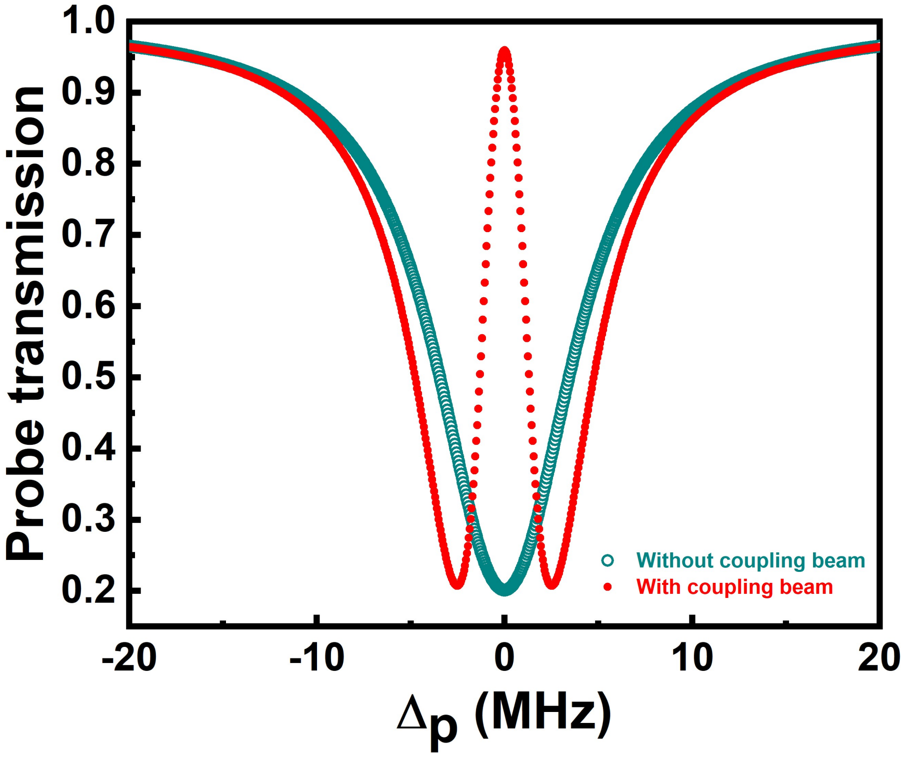

Figure 2.6: Probe transmission as a function of probe detuning (Δ_p) in the absence (olive open circles) and presence (red closed circles) of coupling field. Laser parameters used in the model are Ω_p = 100 kHz, Ω_c = 5 MHz, Γ_{eg} = 6 MHz, Γ_{re} = 10 kHz, Γ_{rg} = 100 kHz and $\Delta_c = 0$. Density of the atoms (N) is 1.7× 10^{10} cm^{-3}.

pathways changes the absorption of the probe field to otherwise transmission within a narrow frequency regime around the resonance. This leads to the modification of the response of the optical system to the atomic medium and gives rise to large optical nonlinearity.

The three-level system has been discussed in detail in the previous section. The optical Bloch equation of a three-level system for the steady state, in the weak probe limit, i.e., $\Omega_p \ll \Omega_c$, are

$$\frac{i}{2}[-2\Delta_p\rho_{ge} - \Omega_p - \Omega_c^*\rho_{gr}] - \frac{\Gamma_{eg}}{2}\rho_{ge} = 0 \tag{2.23}$$

$$\frac{i}{2}[-2\delta\rho_{gr} - \Omega_c\rho_{ge}] - \frac{(\Gamma_{rg} + \Gamma_{re})}{2}\rho_{gr} = 0 \tag{2.24}$$

The above equations are solved numerically to find ρ_{eg}. The susceptibility of the probe and the transmission is calculated as discussed in Sec. 2.2.3. The probe transmission in the EIT regime is shown in Fig. 2.6. In the absence of the coupling beam, the probe is absorbed as expected. In the presence of the coupling beam, we observe transparency around the resonance instead of absorption of the probe beam.

2.2.5 Adiabatic elimination of the intermediate state: Effective two-level system

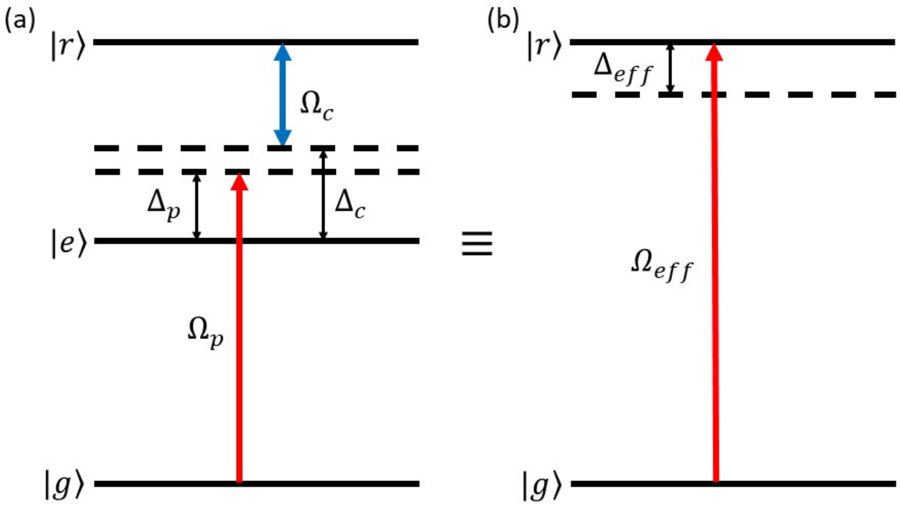

Figure 2.7: Schematic of energy levels of (a) three-level system and (b) effective two-level system.

A three-level system can be treated like an effective two-level system by elimination of the intermediate state under certain conditions, i.e., $\Delta_p \gg \Omega_p, \Gamma_{eg}$. This process of reducing a system to an effective system with effective parameters by eliminating the intermediate state is known as the adiabatic elimination process [67]. Under the conditions of adiabatic elimination, if the initial population in the intermediate state $|e\rangle$ is zero, then it will not get populated further and hence, can be neglected or eliminated. The schematic of the effective two-level system obtained from a three-level system is represented in Fig. 2.7. It consists of two states $|g\rangle$ and $|r\rangle$ with effective Rabi frequency (detuning) given by $\Omega_{eff}(\Delta_{eff})$. Performing a translation operation $H \rightarrow H' = H + \frac{\hbar}{2}\delta I$ gives

$$H' = -\frac{\hbar}{2}\begin{pmatrix} -\delta & \Omega_p & 0 \\ \Omega_p^* & 2\Delta_p - \delta & \Omega_c \\ 0 & -\Omega_c^* & \delta \end{pmatrix}.$$

The time-dependent Schrödinger equation is represented as $i\hbar\frac{\partial}{\partial t}|\psi(t)\rangle = H'|\psi(t)\rangle$, where $|\psi(t)\rangle = C_g(t)|g\rangle + C_e(t)|e\rangle + C_r(t)|r\rangle$ is written in terms of the orthonormal basis states. The equations for the complex coefficients are derived as

$$2i\frac{\partial}{\partial t}C_g(t) = \delta C_g(t) - \Omega_p C_e(t) \tag{2.25}$$

$$2i\frac{\partial}{\partial t}C_e(t) = -\Omega_p^* C_g(t) + (\delta - 2\Delta_p)C_e(t) + \Omega_c C_r(t) \tag{2.26}$$

$$2i\frac{\partial}{\partial t}C_r(t) = -\delta C_r(t) - \Omega_c^* C_e(t) \tag{2.27}$$

Under conditions of adiabatic elimination, $\frac{\partial}{\partial t}C_e(t) = 0$. Hence, $C_e(t)$ is found as $C_e(t) = -\frac{\Omega_p^* C_g(t)}{(\Delta_p - \Delta_c)} - \frac{\Omega_c C_r(t)}{(\Delta_p - \Delta_c)}$. Substituting the value of $C_e(t)$ in the other two equations, the Hamiltonian for the effective two-level system is derived as

$$H_{eff} = \frac{\hbar}{2}\begin{pmatrix} \delta + \frac{|\Omega_p|^2}{(\Delta_p - \Delta_c)} & \frac{\Omega_p \Omega_c}{(\Delta_p - \Delta_c)} \\ \frac{\Omega_p^* \Omega_c^*}{(\Delta_p - \Delta_c)} & \frac{|\Omega_c|^2}{(\Delta_p - \Delta_c)} - \delta \end{pmatrix}.$$

The effective Hamiltonian is similar to the Hamiltonian of a two-level system $H_{2level} = \frac{\hbar}{2}\Omega|g\rangle\langle r| + \frac{\hbar}{2}\Omega|r\rangle\langle g| + \hbar\Delta|r\rangle\langle r|$ with Rabi frequency Ω and detuning Δ. By comparing the effective two-level system with a simple two-level system, the effective Rabi frequency is found out to be $\Omega_{eff} = \frac{\Omega_p \Omega_c}{(\Delta_p - \Delta_c)}$ and the effective detuning is $\Delta_{eff} = \delta + \frac{|\Omega_p|^2}{2(\Delta_p - \Delta_c)} - \frac{|\Omega_c|^2}{2(\Delta_p - \Delta_c)}$. The density matrix ρ for the effective system is given by a 2×2 matrix. The decay from $|e\rangle \rightarrow |g\rangle$ is faster than $|r\rangle \rightarrow |e\rangle$, i.e. $\Gamma_{eg} \gg \Gamma_{re}$. Hence, the atoms in state $|r\rangle$ can be considered to decay directly into state $|g\rangle$. The effective decay, including the transit time decay, is written as $\gamma_{rg} \approx \Gamma_{rg} + \Gamma_{re}$. ρ_{rg} and ρ_{rr} are found by solving the optical Bloch equations in the

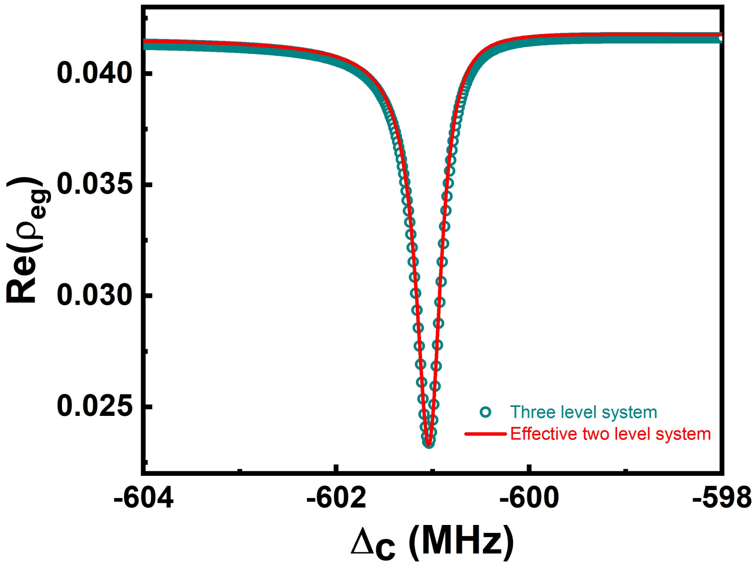

Figure 2.8: Comparison of an effective two level system (open olive circles) with a three level system (red solid line) at large probe detuning Δ_p = 600 MHz. Other parameters used in the model are Ω_p = 50 MHz, Ω_c = 5 MHz, Γ_{eg} = 6 MHz, Γ_{re} = 10 kHz and Γ_{rg} = 100 kHz. Density of the atoms (N) is 1.7× 10^{10} cm^{-3}.

steady state:

$$\frac{i}{2}[\Omega^*_{eff}\rho_{gr} - \Omega_{eff}\rho_{rg}] + \gamma_{rg}\rho_{rr} = 0 \tag{2.28}$$

$$\frac{i}{2}[\Omega_{eff}(1-2\rho_{rr}) - 2\Delta_{eff}\rho_{gr}] - \frac{\gamma_{rg}}{2}\rho_{gr} = 0 \tag{2.29}$$

The above equations are solved numerically to find ρ_{eg}, in terms of ρ_{rg} and ρ_{rr}, from the three-level system [68] as

$$\rho_{eg} = \frac{\Omega_p(\rho_{rr}-1) - \Omega_c\rho_{rg}}{2\Delta_p + i\Gamma_{eg}}. \tag{2.30}$$

A comparison of the effective two-level system with the three-level system at large probe detuning, i.e., under conditions of adiabatic elimination, shows a good agreement between the two, as shown in Fig.2.8. The figure shows $\Re(\rho_{eg})$ for the two systems at large probe detuning. The adiabatic elimination process is helpful in studying a complex system with a larger number of atomic levels, such as a five-level system where it can be reduced to simpler, effective system. This will be discussed in the forthcoming chapters.

2.3 Energy levels of rubidium atom

Alkali atoms are popular in atomic physics as their excitation frequency from the ground to the first excited state falls in the visible and infrared region. Hence, light can be easily generated for the optical transition. Also, due to their considerable vapor pressure at low temperatures, alkali metal atoms can be readily made available for manipulation by laser beams by heating. They have one valence electron in the outermost shell and behave like Hydrogen-like atoms. The study in this thesis is based on optical excitation with rubidium atomic medium. Rubidium has ground state electronic configuration of $1s^2\ 2s^2\ 2p^6\ 3s^2\ 3d^{10}\ 4s^2\ 4p^6\ 5s^1$ with atomic number 37. It has two naturally occurring isotopes ^{85}Rb and ^{87}Rb with a relative abundance of 72.2% and 27.8%, respectively.

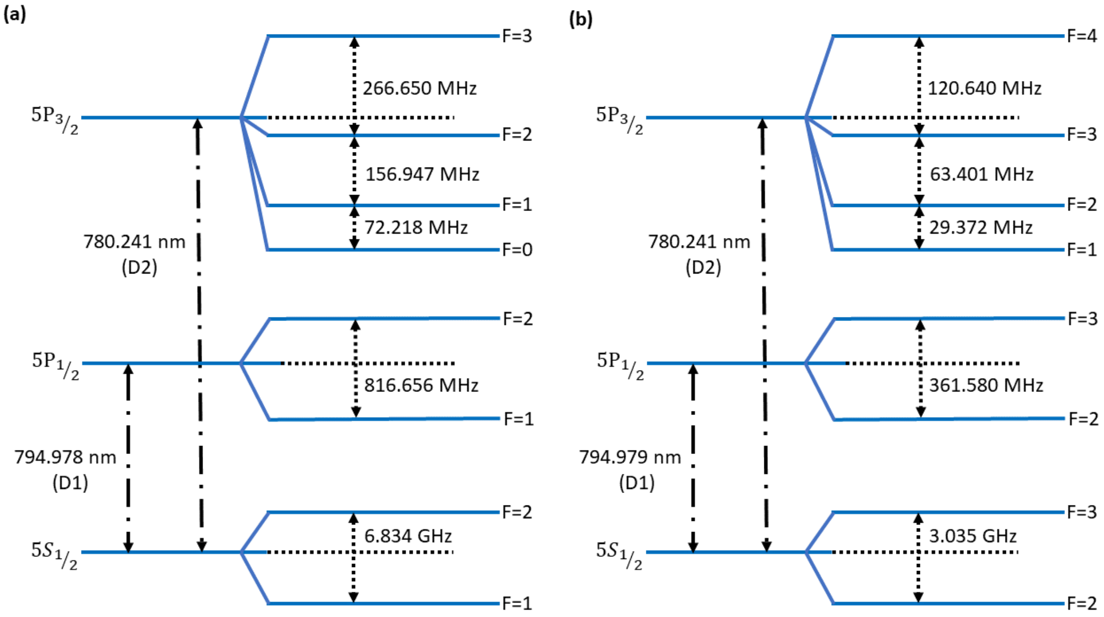
(a)
5P3/2
5P1/2
5S1/2
F=3
266.650 MHz
F=2
156.947 MHz
F=1
72.218 MHz
F=0
780.241 nm
(D2)
F=2
816.656 MHz
F=1
794.978 nm
(D1)
F=2
6.834 GHz
F=1
(b)
5P3/2
5P1/2
5S1/2
F=4
120.640 MHz
F=3
63.401 MHz
F=2
29.372 MHz
F=1
780.241 nm
(D2)
F=3
361.580 MHz
F=2
794.979 nm
(D1)
F=3
3.035 GHz
F=2

Figure 2.9: Energy levels of rubidium. D1 and D2 lines for (a) ^{87}Rb and (b) ^{85}Rb

The alkali metal atoms have a closed shell configuration with one valence electron; hence, the core does not contribute to the orbital angular momentum L. The valence electron contributes to the orbital angular momentum. The orbital angular momentum L and the spin angular momentum S provide the total angular momentum J. It is expressed as $\vec{J} = \vec{L} + \vec{S}$ with $\mid L - S \mid \leq J \leq \mid L + S \mid$. For rubidium, ground state valence electron configuration is $5S^1$ with $L = 0$ and $S = \frac{1}{2}$ and hence, its ground state is written as $5S_{\frac{1}{2}}$ with $J = \frac{1}{2}$. The excited state $5P$ can have $J = \frac{1}{2}$ or $J = \frac{3}{2}$ as $L = 1$ and are represented as $5P_{\frac{1}{2}}$ and $5P_{\frac{3}{2}}$. These are called the fine structure states. The interaction of the total angular momentum J with the nuclear angular momentum I is given by $\vec{F} = \vec{J} + \vec{I}$ with $\mid I - J \mid \leq F \leq \mid I + J \mid$. This leads to the formation of hyper-fine states. For ^{87}Rb with $I = \frac{3}{2}$, the ground state $5S_{\frac{1}{2}}$ splits into hyper-fine states given by $F = 1, 2$, the excited state $5P_{\frac{1}{2}}$ splits into hyper-fine states given by $F = 1, 2$, and the excited state $5P_{\frac{3}{2}}$ splits into hyper-fine states given by $F = 0, 1, 2, 3$. For ^{85}Rb with $I = \frac{5}{2}$, the ground state $5S_{\frac{1}{2}}$ splits into hyper-fine states given by $F = 2, 3$, the excited state $5P_{\frac{1}{2}}$ splits into hyper-fine states given by $F = 2, 3$, and the excited state $5P_{\frac{3}{2}}$ splits into hyper-fine states given by $F = 1, 2, 3, 4$. The transition from $5S_{\frac{1}{2}} \rightarrow 5P_{\frac{1}{2}}$ is called the D1 line and from $5S_{\frac{1}{2}} \rightarrow 5P_{\frac{3}{2}}$ is called the D2 line. The states of rubidium are represented in Fig. 2.9 for ^{85}Rb and ^{87}Rb. The work in this thesis is related to the D2 line of rubidium.

2.4 Doppler broadening

Due to the thermal motion of the absorbing or emitting atoms, their absorbing or emitting frequencies are Doppler-shifted. As different atoms have different velocities, the Doppler shift broadens the spectral lines of the gases at low pressure. The Lorentzian line profile of the spectral lines is concealed by various broadening effects from which the significant contribution comes from the Doppler broadening. If the atom moves with velocity v, the atom moving towards the light source experiences a blue shift in the frequency, and the atom moving away from the light source experiences a redshift. The Doppler shifted frequency given by $\omega = \omega_0 + \vec{k} \cdot \vec{v}$, where ω is the frequency of laser beam experienced by the atom due to its motion, ω_o is the frequency of the laser beam in the rest frame of the atom, $\vec{k}$ is the wave vector of the laser beam, and $\vec{v}$ is the velocity of the atom in consideration.

In thermal atomic ensemble, the atoms follow a Maxwell Boltzmann velocity distribution, which in 1D, is given by the function $f(v)dv = \frac{1}{\sqrt{\pi}v_p}e^{-\frac{v^2}{v_p^2}}dv$. $v_p = \sqrt{\frac{2k_bT}{m}}$ is the most probable velocity of the atoms, k_b is the Boltzmann constant, m is the mass of the atom, and T is the average temperature of the ensemble of atoms. While working with a thermal atomic ensemble, the different physical quantities need to be averaged over the velocities of the atoms to take into account the effect of Doppler broadening.

2.4.1 Doppler effect in a three-level rubidium atomic system

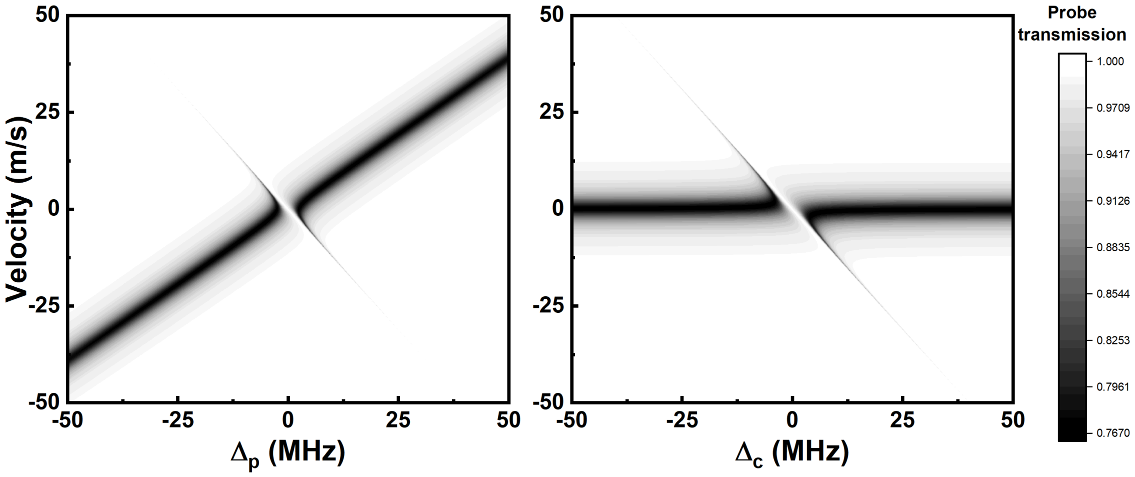

Figure 2.10: Two dimensional density plots for probe transmission as a function of detuning of the laser field and atomic velocity for the ladder configuration where $k_p = 1.28166 \times 10^6$ m^{-1} and $k_c = 2.08333 \times 10^6$. Other parameters used are $\Omega_p = 500$ kHz, $\Omega_c = 5$ MHz, $\Gamma_{eg} = 6$ MHz, $\Gamma_{re} = 10$ kHz, and $\Gamma_{rg} = 100$ kHz. The density of the atoms is 1.7×10^{10} cm^{-3}.

The atom-light interaction in a three-level ladder system has been discussed in Sec. 2.2.3, which can be used to excite the atoms to the Rydberg state. The two-photon excitation to the Rydberg state in a rubidium atomic medium is realized with a probe field (ω_p) at 780 nm and a coupling field (ω_c) at 480 nm having wave vectors k_p and k_c respectively. The laser fields are taken to be in a counter-propagating configuration to reduce the wave-vector mismatch. The analytical solution for the ground state to excited state coherence under the conditions of EIT, i.e., in the weak probe limit, is calculated to be

$$\rho_{eg} = \frac{i}{2}\Omega_p \frac{(\Delta_p + \Delta_c - i\frac{\Gamma_{31}+\Gamma_{32}}{2})}{(-i\Delta_p - \frac{\Gamma_{21}}{2})(\Delta_p + \Delta_c - i\frac{\Gamma_{31}+\Gamma_{32}}{2}) + i\frac{\Omega_c^2}{4}} \tag{2.31}$$

For the same velocity class of atoms in thermal vapor, the detuning of the fields are modified as $\Delta_p \rightarrow \Delta_p - k_p v$ and $\Delta_c \rightarrow \Delta_c + k_c v$. The susceptibility of the probe field coupling the transition from $|g\rangle \rightarrow |e\rangle$ is calculated as

$$\chi(\Delta_i, v)f(v)dv = \frac{2N|\ \mu_{ge}\ |^2}{\hbar\epsilon_0\Omega_p}\frac{1}{\sqrt{\pi}v_p}\rho_{eg}(\Delta_i, v)e^{-\frac{v^2}{v_p^2}}dv \tag{2.32}$$

where $i = p, c$. The probe transmission is calculated using Eqn. (2.22). The transmission components in the two-dimensional display are presented in Fig. 2.10, where the left and the right figure represent the transmission with probe field scan and coupling field scan, respectively. The different velocity groups contribute to the transmission components across the Doppler profile. Drawing a horizontal line on the plots represents the same velocity class of atoms, and the intersection of the horizontal line with the colored curves represents the laser field detuning corresponding to the transmission components for the particular velocity class of atoms. A vertical line on the plots represents a particular laser detuning, and its intersection with the curves corresponds to the different velocity groups of atoms contributing to the transmission components. For the zero velocity group of atoms, the transmission is maximum around the resonance, which corresponds to the maximum EIT transparency.

2.5 Scaling of hyperfine and fine structure splitting due to wave vector mismatch between the probe and coupling laser fields

In the case of two hyperfine states and fine structure states, the frequency axis is calibrated differently for the hyperfine splitting and fine structure splitting. This is

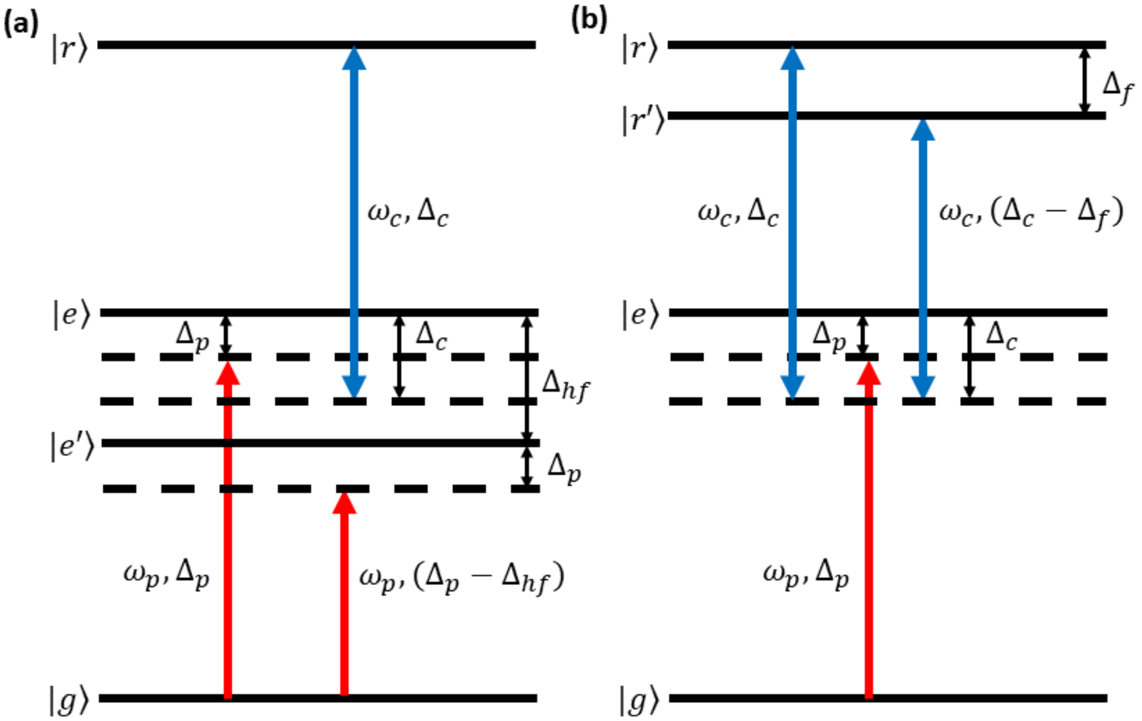
(a)
$|r\rangle$
ω_c, Δ_c
$|e\rangle$
Δ_p
Δ_c
Δ_{hf}
$|e'\rangle$
Δ_p
ω_p, Δ_p
$\omega_p, (\Delta_p - \Delta_{hf})$
$|g\rangle$
(b)
$|r\rangle$
Δ_f
$|r'\rangle$
ω_c, Δ_c
$\omega_c, (\Delta_c - \Delta_f)$
$|e\rangle$
Δ_p
Δ_c
ω_p, Δ_p
$|g\rangle$

Figure 2.11: Energy level scheme where $|g\rangle$ represents the ground state, and $|r\rangle$ represents the Rydberg state: (a) for hyperfine states $|e\rangle$ and $|e'\rangle$ and (b) for fine structure states $|r\rangle$ and $|r'\rangle$. Δ_{hf} and Δ_f represent the hyperfine and fine structure splitting, respectively.

due to the Doppler mismatch between probe and coupling laser fields. The hyperfine splitting is scaled by a factor of $1 - \frac{k_p}{k_c}$ and fine structure splitting by $\frac{k_p}{k_c}$, when the probe field is scanned. For coupling field scan, the hyperfine splitting is scaled as $\frac{k_c}{k_p} - 1$ and fine structure splitting by 1. The energy level scheme for the system is represented by 2.11. This scaling is derived by solving the optical Bloch equations for the above systems in the weak probe limit.

The analytical solution for the ground state to excited state coherence corresponding to the hyperfine states, in the weak probe limit, is found to be $\rho_{eg} + \rho_{e'g}$.

$$\rho_{e'g} = \frac{Num}{den} \tag{2.33}$$

where $Num = -\Omega_p(2(\Delta_p + \Delta_c) - i(\Gamma_{31} + 2\Gamma_{32}))(2\Delta_p - i\Gamma_{21})$;
$den = (2\Delta_p - i\Gamma_{21})(2(\Delta_p + \Delta_c) - i(\Gamma_{31} + 2\Gamma_{32}))(2(\Delta_p - \Delta_{hf}) - i\Gamma_{21}) - \Omega_c^2(2(\Delta_p -$

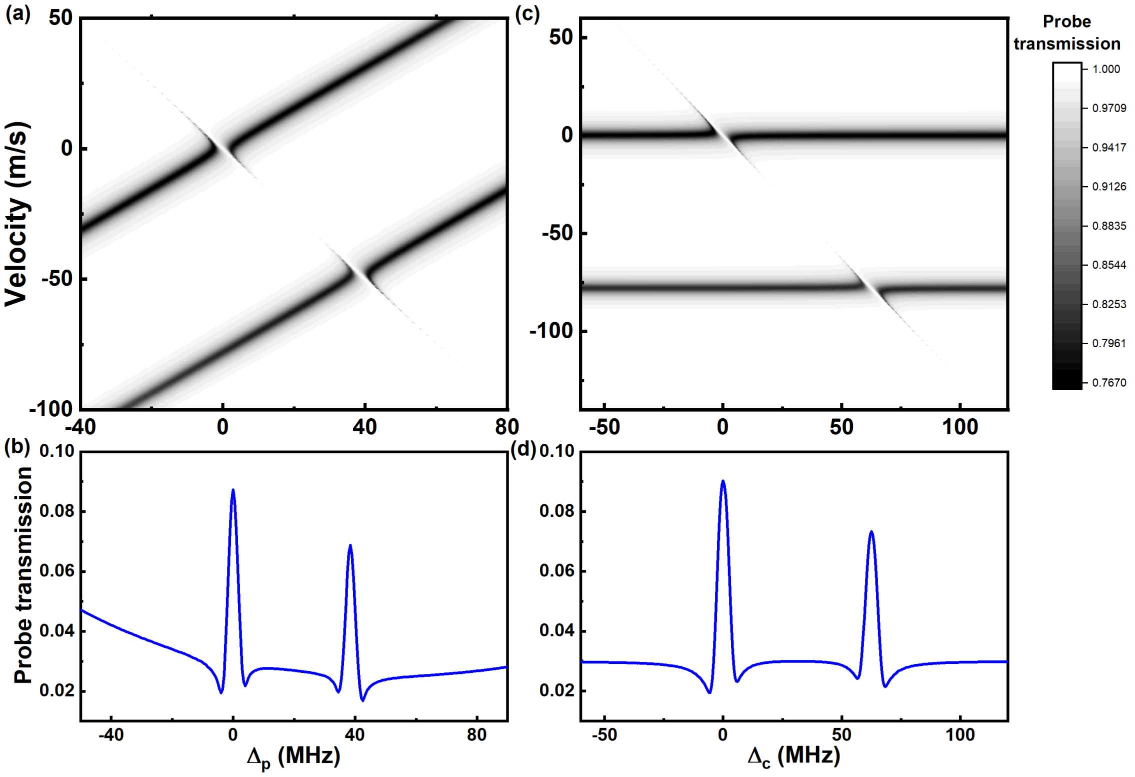

Figure 2.12: Two-dimensional density plots for probe transmission as a function of laser field detuning and atomic velocity representing two hyperfine resonances: (a) Δ_p scan and (c) Δ_c scan. Doppler averaged probe transmission for the same: (b) Δ_p scan and (d) Δ_c scan. Here, Δ_{hf} is taken to be 100 MHz, just as an example. This value of Δ_{hf} is not specific to rubidium.

$\Delta_{hf}) - i\Gamma_{21}) - \Omega_c^2(2\Delta_p - i\Gamma_{21})$.

$$\rho_{eg} = \frac{(2(\Delta_p - \Delta_{hf}) - i\Gamma_{21})}{(2\Delta_p - i\Gamma_{21})}\rho_{e'g}. \tag{2.34}$$

For the thermal vapor system, the detunings are modified as $\Delta_p \to \Delta_p - k_p v$ and $\Delta_c \to \Delta_c + k_c v$. When the probe field is scanned, the coupling field is considered to be on atomic resonance, i.e., $\Delta_c = 0$. While scanning the coupling field, the probe field is considered to be on atomic resonance, i.e., $\Delta_p = 0$. Fig. 2.12 shows the probe transmission for the case of two hyperfine resonances, where the hyperfine splitting is scaled by the factors discussed above.

For the case of fine structure states, in the weak probe limit, the analytical so-

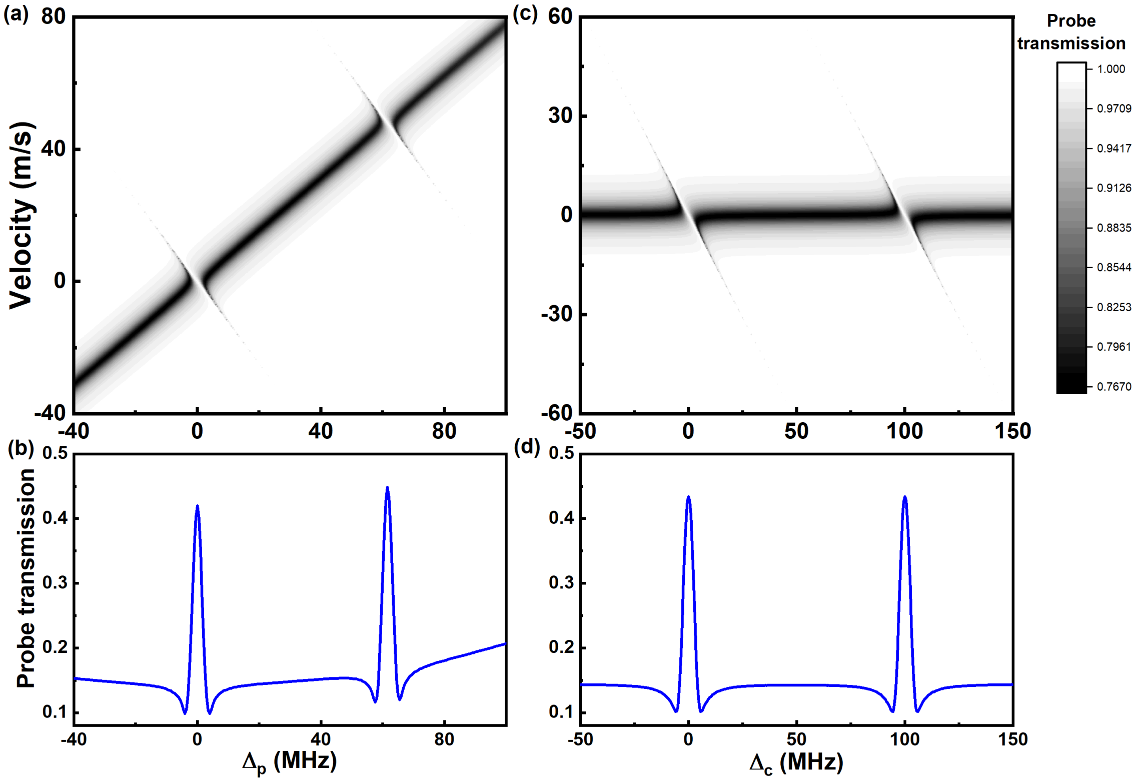

Figure 2.13: Two-dimensional density plots for probe transmission as a function of laser field detuning and atomic velocity representing two fine structure resonances: (a) Δ_p scan and (c) Δ_c scan. Doppler averaged probe transmission for: (b) Δ_p scan and (d) Δ_c scan. Here, Δ_f is taken to be 100 MHz, just as an example. This value of Δ_f is not specific to rubidium.

lution for the ground to excited state coherence is

$$\rho_{eg} = \frac{Num_f}{den_f} \tag{2.35}$$

where $Num_f = -\Omega_p(2(\Delta_p + \Delta_c) - i(\Gamma_{31} + \Gamma_{32}))(2(\Delta_p + \Delta_c - \Delta_f) - i(\Gamma_{31} + \Gamma_{32}))$; $den_f = (2\Delta_p - i\Gamma_{21})(2(\Delta_p + \Delta_c) - i(\Gamma_{31} + \Gamma_{32}))(2(\Delta_p + \Delta_c - \Delta_f) - i(\Gamma_{31} + \Gamma_{32})) - \Omega_c^2(2(\Delta_p + \Delta_c) - i(\Gamma_{31} + \Gamma_{32})) - \Omega_c^2(2(\Delta_p + \Delta_c - \Delta_f) - i(\Gamma_{31} + \Gamma_{32}))$.

Fig. 2.13 shows the probe transmission for the case of two fine structure states. As can be observed from the plots, the frequency difference between the fine structure states is scaled by the factors discussed above.

2.6 Laser frequency stabilization

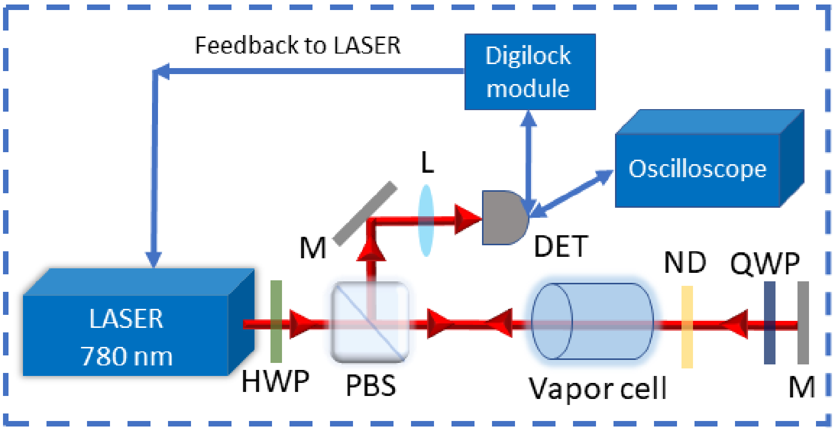

Figure 2.14: Optical set up for Doppler-free absorption spectroscopy. HWP: Half-wave plate, PBS: Polarizing beam splitter, M: Mirror, QWP: Quarter wave plate, ND: Neutral Density Filter, L: Lens, and DET: Detector.

Laser frequency stabilization requires precise determination of the excitation frequency from the ground state to the excited state. The determination of the exact frequency is limited by the lifetime of the state, whose inverse gives us the spectral width of the excitation. However, the spectral width of room temperature atoms is concealed due to Doppler broadening effect, and the precise transition frequencies cannot be distinguished within the broad absorption spectrum of the rubidium atom. Special techniques are needed to stabilize the laser frequency precisely. The frequency of the laser beam can be stabilized using various methods such as providing a feedback loop to the laser, Doppler-free absorption spectroscopy, generating an error signal through frequency modulation of the beam, etc. This section will discuss the two frequency locking techniques for stabilizing the laser frequencies.

2.6.1 Doppler free absorption spectroscopy

Doppler-free absorption spectroscopy, also known as saturated absorption spectroscopy (SAS), is a technique to precisely determine the atomic transition frequency without requiring the cooling of an atomic medium where the Doppler broadening

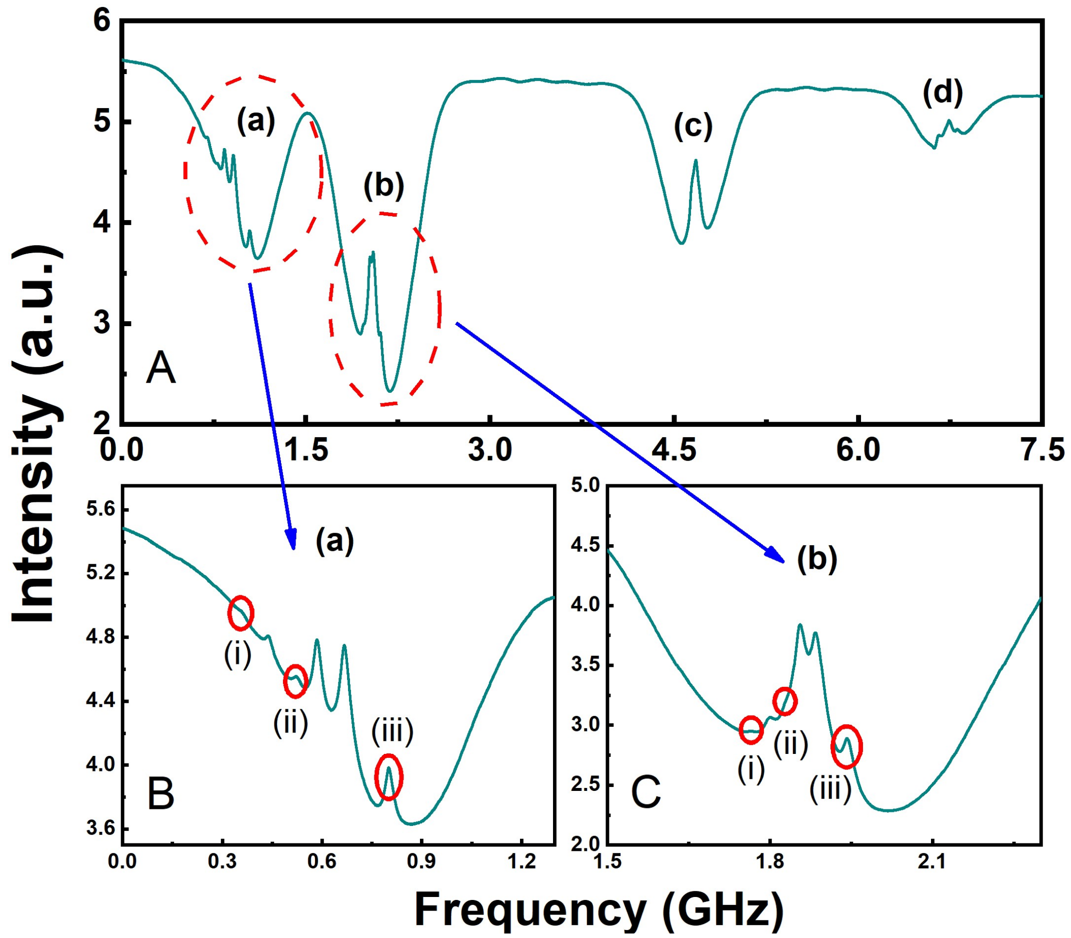

Figure 2.15: (A) represents SAS data for rubidium D2 line where (a) represents the $^{87}Rb\ 5S_{\frac{1}{2}}F = 2 \rightarrow 5P_{\frac{3}{2}}F'(1,2,3)$ transition , (b) represents the $^{85}Rb\ 5S_{\frac{1}{2}}F = 3 \rightarrow 5P_{\frac{3}{2}}F'(2,3,4)$ transition, (c) represents the $^{85}Rb\ 5S_{\frac{1}{2}}F = 2 \rightarrow 5P_{\frac{3}{2}}F'(1,2,3)$ transition and (d) represents the $^{87}Rb\ 5S_{\frac{1}{2}}F = 1 \rightarrow 5P_{\frac{3}{2}}F'(0,1,2)$ transition. (B) and (C) represent the zoomed view of the first two transitions (a) and (b), respectively.

no longer plays a significant role. It is used to frequency lock the probe laser to an excited state with the help of hyper-fine transition of the atomic medium, which is a room temperature rubidium atomic system for our case. This technique uses a counter-propagating pump and probe scheme in a simple two-level system. The optical setup for achieving SAS is shown in Fig. 2.14. An external cavity diode laser (ECDL) at 780 nm is used to derive the optical beam. The beam is made to pass through the rubidium atomic vapor cell. A half-wave plate (HWP) and a polarizing beam splitter (PBS) are used to control the power of the light passing through the vapor cell. This acts as the pump beam, which is of a higher power. It is made to pass through the quarter-wave plate (QWP) after passing through the vapor cell and reflected from a mirror. A neutral density filter is used to reduce the power of the reflected beam. The reflected beam is orthogonally polarized to the pump beam and called the probe beam. The probe is weak compared to the pump beam; after passing through the vapor cell, it is reflected from the PBS. The probe beam is focused using a lens to a photo-detector to study the absorption signal. The photodiode signal is fed into a TOPTICA digilock module of the ECDL for frequency locking. The photodiode signal is also observed at the oscilloscope to identify the different hyperfine transitions as shown in Fig. 2.15.

If the laser is in resonance to the atomic transition, the pump and the probe beam interact with the atoms with velocity perpendicular to the direction of the propagation of the laser beam. Using the two-level picture, the strong pump beam excites the atoms from the ground state to the excited state such that the excited state is saturated, i.e., the excited state and ground state has an almost equal number of atoms. When the counter-propagating probe beam encounters the exited atoms, they undergo stimulated emission, giving rise to a dip in the absorption spectrum (or a peak in the transmission spectrum) at each hyperfine resonance. If there is more than one hyperfine transition within a broad absorption spectrum having the same ground state, then some cross-over peaks occur. These peaks occur at frequencies exactly halfway between the two hyperfine transitions.

Fig. 2.15(A) shows the different transitions falling in the D2 line of rubidium. The experiments in this thesis, involve the use of $^{87}Rb\ 5S_{\frac{1}{2}}F = 2 \rightarrow 5P_{\frac{3}{2}}F'(1,2,3)$ and $^{85}Rb\ 5S_{\frac{1}{2}}F = 3 \rightarrow 5P_{\frac{3}{2}}F'(2,3,4)$ transitions and the lower figures (B) and (C) show the zoomed view of those transitions. In Fig. 2.15(B), (i),(ii) and (iii) represent respectively the hyper-fine transitions with $F' = 1,2,3$ and other peaks represent the cross over resonances. Similarly, in Fig. 2.15(c), (i),(ii) and (iii) represent respectively the hyper-fine transitions with $F' = 2,3,4$ and other peaks are the cross over resonances. The strength of the cross-over resonances can be larger than the hyper-fine resonances.

2.6.2 Frequency stabilization using EIT locking technique

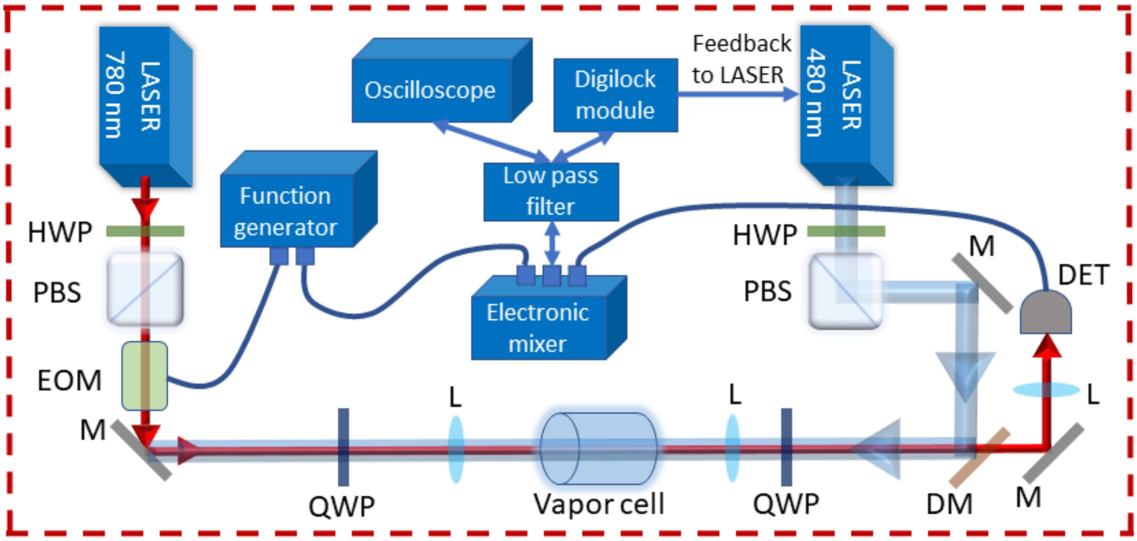
LASER
780 nm
Oscilloscope
Digilock
module
Feedback
to LASER
LASER
480 nm
Function
generator
Low pass
filter
HWP
PBS
EOM
M
Electronic
mixer
HWP
PBS
M
DET
L
L
L
QWP
Vapor cell
QWP
DM
M

Figure 2.16: Optical set up for frequency stabilization using EIT locking technique. HWP: Half-wave plate, PBS: Polarizing beam splitter, EOM: Electro-optic modulator, M: Mirror, QWP: Quarter wave plate, L: Lens, D.M.: Dichroic mirror, and DET: Detector.

EIT locking technique is used to stabilize the frequency of the coupling laser to a highly excited state such as the Rydberg state [46]. This technique utilizes the concept of EIT, where the probe and coupling laser fields are in counter-propagate each other and satisfy the ladder configuration to excite the atoms to the Rydberg state. The probe frequency is stabilized at the resonance of a hyper-fine transition using SAS, as discussed in the previous section. The frequency of the coupling laser is stabilized at the EIT resonance by generating an error signal from the EIT signal, which is explained below.

The experimental setup is shown in Fig. 2.16. Here, an ECDL at 780 nm generates the probe beam, and a frequency doubling cavity laser generates the coupling beam at 480 nm. The probe beam is used to couple the ground state of rubidium $5S_{\frac{1}{2}}$ to the excited state $5P_{\frac{3}{2}}$, and the coupling beam excites the atoms from the excited state to the Rydberg state. When the system satisfies the condition of EIT, we observe the EIT signal in the photodiode as shown in Fig. 2.17(a).

Generation of sidebands due to frequency modulation of the probe beam

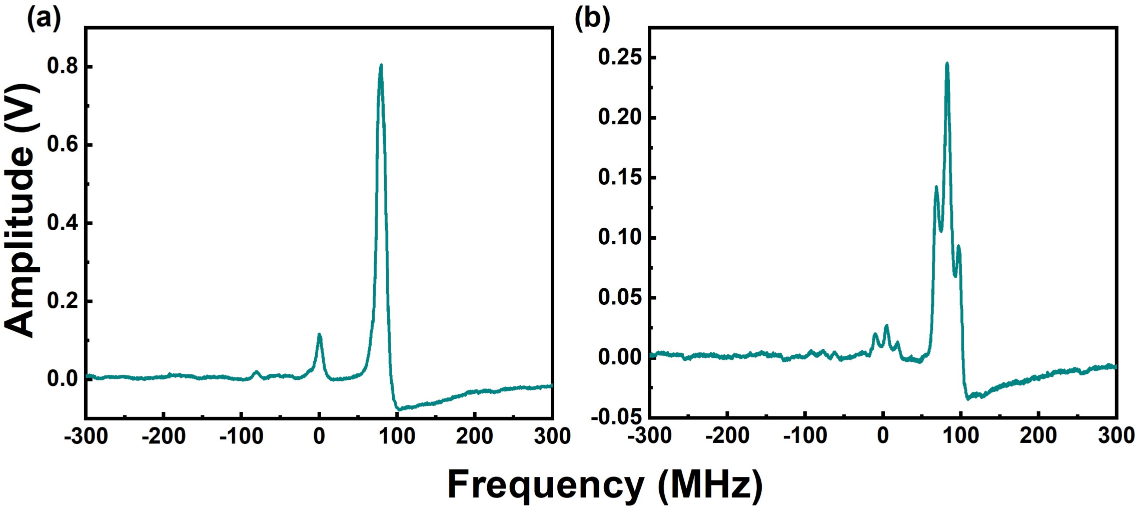

Figure 2.17: EIT signal: (a) without modulation and (b) after frequency modulation with side bands at the modulation frequency.

The phase of the probe beam is modulated using an electro-optic modulator (EOM). The probe beam is represented by $E(t) = E_0 e^{i\omega_p t}$. In order to drive the EOM, an rf signal is used from a function generator which introduces the phase change, which can be written as $\phi(t) = \delta\phi \sin(\omega_e t)$ where ω_e is the frequency of the modulation signal and $\delta\phi$ is the very small phase change. The phase modulated probe beam is written as $E(t) = E_0 e^{i\omega_p t + i\delta\phi \sin(\omega_e t)}$. Phase modulation results in frequency modulation as given by $\delta\phi = \frac{\delta\omega}{\omega_e}$. Using the Taylor's expansion for $e^{i\delta\phi \sin(\omega_e t)}$, the frequency modulated signal is written as $E(t) = E_0 e^{i\omega_p t}(1 + i\delta\phi \sin(\omega_e t))$. This expression can be simplified as

$$E(t) = E_0(e^{i\omega_p t} + \frac{\delta\phi}{2} e^{i(\omega_p + \omega_e)t} - \frac{\delta\phi}{2} e^{i(\omega_p - \omega_e)t}). \tag{2.36}$$

Here, the first term is the carrier wave which is the probe field, and the subsequent two terms are the sidebands generated at frequencies $(\omega_p + \omega_e)$ and $(\omega_p - \omega_e)$. This can be seen in Fig. 2.17(b), where we observe the sidebands being generated for the EIT signal due to the frequency modulation of the probe.

Generation of the error signal from the EIT signal

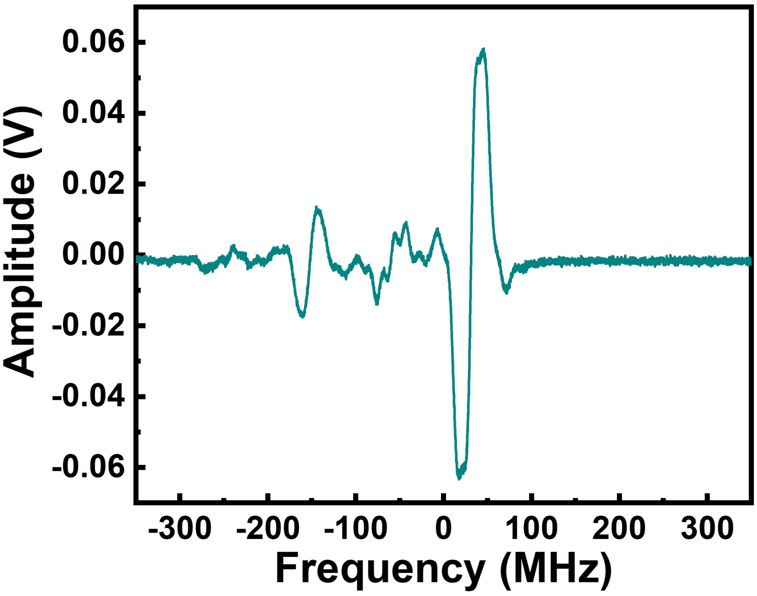

Figure 2.18: Generated error signal from the EIT signal.

The photodiode receives an intensity of light $I \propto \mid E \mid^2$, which depends on the instantaneous frequency. The instantaneous frequency is equal to the time derivative of $\omega_p t + \delta\phi \sin(\omega_e t)$, i.e. $\omega_i = \omega_p + \omega_e \delta\phi \cos(\omega_e t) = \omega_p + \delta\omega \cos(\omega_e t)$. Hence, $I(\omega) = I(\omega_p + \delta\omega \cos(\omega_e t))$. Using Taylor's expansion $I(\omega) = I(\omega_p) + \delta\omega \cos(\omega_e t)\frac{\partial I}{\partial \omega} + ..$. The signal from the photodiode is multiplied with a local oscillator (L.O.) signal $A_0 \sin(\omega_e t + \phi)$ with the help of an R.F. mixer to understand the changes in the laser frequency. This L.O. signal is generated from the same function generator, which drives the EOM at the same frequency as the modulation signal but with an extra phase factor ϕ. This results in intensity given by

$$\begin{aligned}
I(\omega) * A_0 \sin(\omega_e t + \phi) &= [E_0^2 \sin^2(\omega_p t) + \delta\omega \cos(\omega_e t)\tfrac{\partial I}{\partial \omega}] A_0 \sin(\omega_e t + \phi) \\
&= [\tfrac{E_0^2}{2}(1 - \cos(2\omega_p t)) + \delta\omega \cos(\omega_e t)\tfrac{\partial I}{\partial \omega}] A_0 \sin(\omega_e t + \phi) \\
&= \tfrac{A_0 E_0^2}{2} \sin(\omega_e t + \phi) - \tfrac{A_0 E_0^2}{2} \cos(2\omega_p t) \sin(\omega_e t + \phi) + A_0 \delta\omega \cos(\omega_e t)\tfrac{\partial I}{\partial \omega} \sin(\omega_e t + \phi) \\
&= \tfrac{A_0 E_0^2}{2} \sin(\omega_e t + \phi) - \tfrac{A_0 E_0^2}{4}[\sin(2\omega_p t + \omega_e t + \phi) - \sin(2\omega_p t - \omega_e t - \phi)] + \\
&\quad \tfrac{A_0 \delta\omega}{2} \tfrac{\partial I}{\partial \omega} \sin(2\omega_e t + \phi) + \tfrac{A_0 \delta\omega}{2} \tfrac{\partial I}{\partial \omega} \sin\phi
\end{aligned}$$

Using a low pass filter, the high-frequency terms are filtered out, and the remaining term is the last term which gives the error signal. The error signal is the derivative of the EIT signal, as shown in Fig. 2.18. The error signal is fed into the TOPTICA digilock module to lock the frequency of the coupling beam at the slope of the error signal.

This technique is used for experiments involving EIT, which require both the probe and the coupling beam frequency to be stabilized on resonance to the atomic transition.

Chapter 3

Rydberg Electrometry

Large atomic polarizability and strong transition dipole moments make Rydberg atoms suitable candidates for sensing extremely small electric fields [47, 69, 70]. Due to the wide range of optical transitions from MHz to GHz, Rydberg atoms make accessing the RF-FI regime possible [27]. DC field electrometry has also been performed while observing the motional stark shifts with thermal Rydberg atoms [71]. The cold atom experiments utilize the stark effect to compensate for the electric fields inside the vacuum chambers. Atom-based E-field sensing [7, 8, 12] utilizes EIT as a detection scheme for electric fields in the RF-FI regime where EIT is achieved using a two-photon excitation process to the Rydberg state [23, 72, 73]. Sensing of microwave electric fields with EIT using Rydberg atoms is understood with the help of a four-level system [74]. The Rydberg atomic excitation is carried out using a three-level system coupled with the probe and coupling fields. A third field, a microwave field, couples the Rydberg state to another neighboring Rydberg state. Electric field sensing with Rydberg atoms leads to various applications such as THz imaging [31, 75], sub-wavelength imaging [35, 36], millimeter wave detection [37], etc. Also, the Rydberg atomic sensors have grown over time to become an efficient technology for data communication [40, 41, 76]. This chapter discusses the theoretical model of a four-level system for E-field sensing. Also, it provides an overview of some experimental studies which have been performed in the lab to understand the basics of electric field sensing with the Rydberg EIT medium [74]. As an application to microwave electrometry, analog data communication with Rydberg atoms is demonstrated. The Rydberg EIT-based sensing methods with a two-photon excitation process have various limitations, which are also discussed towards the end of this chapter.

3.1 Theoretical model of four-level system

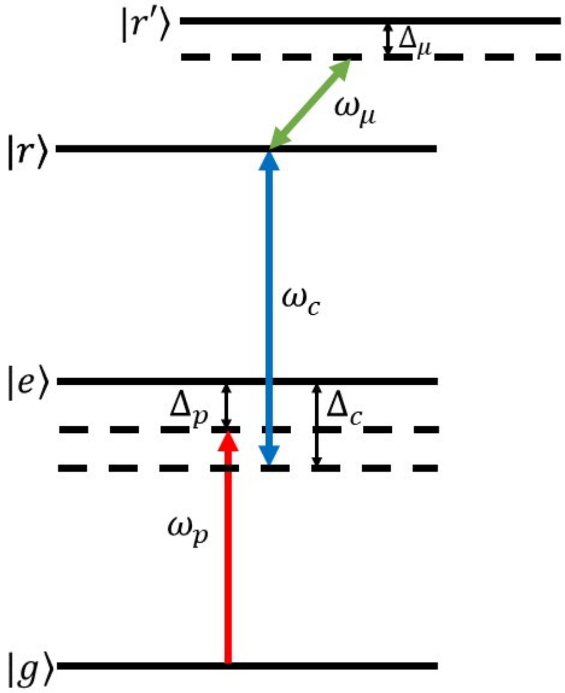

Figure 3.1: Schematic of energy levels of a four-level system in a ladder configuration. $|g\rangle$, $|e\rangle$, $|r\rangle$ and $|r'\rangle$ represent the ground state, intermediate state, first Rydberg state and the second Rydberg state respectively.

Consider a four-level system in ladder configuration consisting of states $|g\rangle$, $|e\rangle$, $|r\rangle$ and $|r'\rangle$, as shown in Fig. 3.1, where the corresponding atomic resonance frequencies between states are ω_1, ω_2 and ω_3 respectively. Excitation from $|g\rangle \rightarrow |e\rangle$, $|e\rangle \rightarrow |r\rangle$ and $|r\rangle \rightarrow |r'\rangle$ are dipole allowed whereas the excitation from $|g\rangle \rightarrow |r\rangle$ and $|g\rangle \rightarrow |r'\rangle$ are dipole forbidden. The transitions $|g\rangle \rightarrow |e\rangle$, $|e\rangle \rightarrow |r\rangle$ and $|r\rangle \rightarrow |r'\rangle$ are coupled by the probe, coupling and microwave fields of frequency ω_p, ω_c and

ω_μ respectively. The fields are given by $\vec{E'}_p = \vec{E}_p e^{-i\omega_p t} + c.c$, $\vec{E'}_c = \vec{E}_c e^{-i\omega_c t} + c.c$ and $\vec{E'}_\mu = \vec{E}_\mu e^{-i\omega_\mu t} + c.c.$ The detuning of the probe, coupling, and microwave field from the respective atomic resonances are given by $\Delta_p = \omega_p - \omega_1$, $\Delta_c = \omega_c - \omega_2$ and $\Delta_\mu = \omega_\mu - \omega_3$. The two-photon and three-photon detuning are defined by $\delta_1 = (\Delta_p + \Delta_c)$ and $\delta_2 = (\Delta_p + \Delta_c + \Delta_\mu)$ respectively and also $\delta_3 = (\Delta_c + \Delta_\mu)$. The Rabi frequencies of the probe, coupling and microwave fields are given by $\Omega_p = \frac{2\mu_{ge}E_p}{\hbar}$, $\Omega_c = \frac{2\mu_{er}E_c}{\hbar}$ and $\Omega_\mu = \frac{2\mu_{rr'}E_\mu}{\hbar}$ respectively. μ_{ge}, μ_{er}, $\mu_{rr'}$ denote the transition dipole moment and E_p, E_c, E_μ denote the electric field amplitude corresponding to the probe, coupling and microwave fields respectively.

The Hamiltonian of the four-level system is written as $\tilde{H} = H_0 + H_{int}$ where $H_0 = \hbar\omega_1|e\rangle\langle e| + \hbar(\omega_1+\omega_2)|r\rangle\langle r| + \hbar(\omega_1+\omega_2+\omega_3)|r'\rangle\langle r'|$ is the bare atomic Hamiltonian and $H_{int} = -\vec{\mu}\cdot\vec{E} = -E_p(\mu_{ge}|g\rangle\langle e| + \mu_{eg}|e\rangle\langle g|) - E_c(\mu_{er}|e\rangle\langle r| + \mu_{re}|r\rangle\langle e|) - E_\mu(\mu_{rr'}|r\rangle\langle r'| + \mu_{r'r}|r'\rangle\langle r|)$ is the interaction Hamiltonian that represents the interaction between optical fields and atomic medium. After the use of rotating wave approximation, the time-independent total Hamiltonian H is written as

$$H = -\frac{\hbar}{2}\begin{pmatrix} 0 & \Omega_p & 0 & 0 \\ \Omega_p^* & 2\Delta_p & \Omega_c & 0 \\ 0 & \Omega_c^* & 2(\Delta_p + \Delta_c) & \Omega_\mu \\ 0 & 0 & \Omega_\mu^* & 2(\Delta_p + \Delta_c + \Delta_\mu) \end{pmatrix}.$$

As discussed in section. 2.2.3, the optical Bloch equation is given by

$$\dot{\rho} = \frac{i}{\hbar}[\rho, H] + \mathcal{L}_{\mathcal{D}}(\rho). \tag{3.1}$$

The density matrix for the four-level system is a 4×4 matrix ρ_{ij} with $i, j = g, e, r, r'$. Γ_{eg}, Γ_{re}, $\Gamma_{r'r}$ denote the population decay between the states. Decay from $|r\rangle \rightarrow |g\rangle$ and $|r'\rangle \rightarrow |g\rangle$ are dipole forbidden. Still, there is decay between these states, known as the transit time decay, due to the atoms' transverse velocity through the beam's cross-section. The transit time decays, which occur between the the ground state and the Rydberg excited state, are denoted by Γ_{rg} and $\Gamma_{r'g}$. The Lindblad operator for this system is given by

$$\mathcal{L}_{\mathcal{D}}(\rho) = \begin{pmatrix} \Gamma_{eg}\rho_{ee} + \Gamma_{rg}\rho_{rr} + \Gamma_{r'g}\rho_{r'r'} & -\frac{\Gamma_{eg}}{2}\rho_{ge} & -\frac{\gamma_1}{2}\rho_{gr} & -\frac{\gamma_2}{2}\rho_{gr'} \\ -\frac{\Gamma_{eg}}{2}\rho_{eg} & \Gamma_{re}\rho_{rr} - \Gamma_{eg}\rho_{ee} & -\frac{\gamma_3}{2}\rho_{er} & -\frac{(\Gamma_{eg}+\gamma_2)}{2}\rho_{er'} \\ -\frac{\gamma_1}{2}\rho_{rg} & -\frac{\gamma_3}{2}\rho_{re} & \Gamma_{r'r}\rho_{r'r'} - \gamma_1\rho_{rr} & -\frac{(\gamma_1+\gamma_2)}{2}\rho_{rr'} \\ -\frac{\gamma_2}{2}\rho_{r'g} & -\frac{(\Gamma_{eg}+\gamma_2)}{2}\rho_{r'e} & -\frac{(\gamma_1+\gamma_2)}{2}\rho_{r'r} & -\gamma_2\rho_{r'r'} \end{pmatrix}$$

where $\gamma_1 = \Gamma_{rg} + \Gamma_{re}$, $\gamma_2 = \Gamma_{r'g} + \Gamma_{r'r}$ and $\gamma_3 = \Gamma_{rg} + \Gamma_{re} + \Gamma_{eg}$.

For the closed system, $\rho_{gg} + \rho_{ee} + \rho_{rr} + \rho_{r'r'} = 1$ and $\dot{\rho_{ij}} = 0$ for the steady state system. Hence, the optical Bloch equations for the steady state are written as

$$\frac{i}{2}(\Omega_p\rho_{eg} - \Omega_p^*\rho_{ge}) + \Gamma_{eg}\rho_{ee} + \Gamma_{rg}\rho_{rr} + \Gamma_{r'g}\rho_{r'r'} = 0 \tag{3.2}$$

$$\frac{i}{2}[-2\Delta_p\rho_{ge} + \Omega_p(2\rho_{ee} + \rho_{rr} + \rho_{r'r'}) - \Omega_p - \Omega_c^*\rho_{gr}] - \frac{\Gamma_{eg}}{2}\rho_{ge} = 0 \tag{3.3}$$

$$\frac{i}{2}[-2\delta_1\rho_{gr} - \Omega_\mu^*\rho_{gr'} + \Omega_p\rho_{er} - \Omega_c\rho_{ge}] - \frac{\gamma_1}{2}\rho_{gr} = 0 \tag{3.4}$$

$$\frac{i}{2}[-2\delta_2\rho_{gr'} - \Omega_\mu\rho_{gr} + \Omega_p\rho_{er'}] - \frac{\gamma_2}{2}\rho_{gr'} = 0 \tag{3.5}$$

$$\frac{i}{2}[2\Delta_p\rho_{ge} - \Omega_p^*(2\rho_{ee} + \rho_{rr} + \rho_{r'r'}) + \Omega_p^* + \Omega_c\rho_{rg}] - \frac{\Gamma_{eg}}{2}\rho_{eg} = 0 \tag{3.6}$$

$$\frac{i}{2}[\Omega_p^*\rho_{ge} - \Omega_p\rho_{eg} + \Omega_c\rho_{re} - \Omega_c^*\rho_{er}] + \Gamma_{re}\rho_{rr} + \Gamma_{r'e}\rho_{r'r'} - \Gamma_{eg}\rho_{ee} = 0 \tag{3.7}$$

$$\frac{i}{2}[\Omega_p^*\rho_{gr} - 2\Delta_c\rho_{er} - \Omega_\mu^*\rho_{er'} + \Omega_c(\rho_{rr} - \rho_{ee})] - \frac{\gamma_3}{2}\rho_{er} = 0 \tag{3.8}$$

$$\frac{i}{2}[-2\delta_3\rho_{er'} - \Omega_\mu\rho_{er} + \Omega_p^*\rho_{gr'} + \Omega_c\rho_{rr'}] - \frac{(\Gamma_{eg} + \gamma_2)}{2}\rho_{er'} = 0 \tag{3.9}$$

$$\frac{i}{2}[2\delta_1\rho_{rg} + \Omega_\mu\rho_{r'g} - \Omega_p^*\rho_{re} + \Omega_c^*\rho_{eg}] - \frac{\gamma_1}{2}\rho_{rg} = 0 \tag{3.10}$$

$$\frac{i}{2}[-\Omega_p\rho_{rg} + 2\Delta_c\rho_{re} + \Omega_\mu\rho_{r'e} + \Omega_c^*(\rho_{ee} - \rho_{rr})] - \frac{\gamma_3}{2}\rho_{re} = 0 \tag{3.11}$$

$$\frac{i}{2}[\Omega_c^*\rho_{er} - \Omega_c\rho_{re} + \Omega_\mu\rho_{r'r} - \Omega_\mu^*\rho_{rr'}] - \gamma_1\rho_{rr} + \Gamma_{r'r}\rho_{r'r'} = 0 \tag{3.12}$$

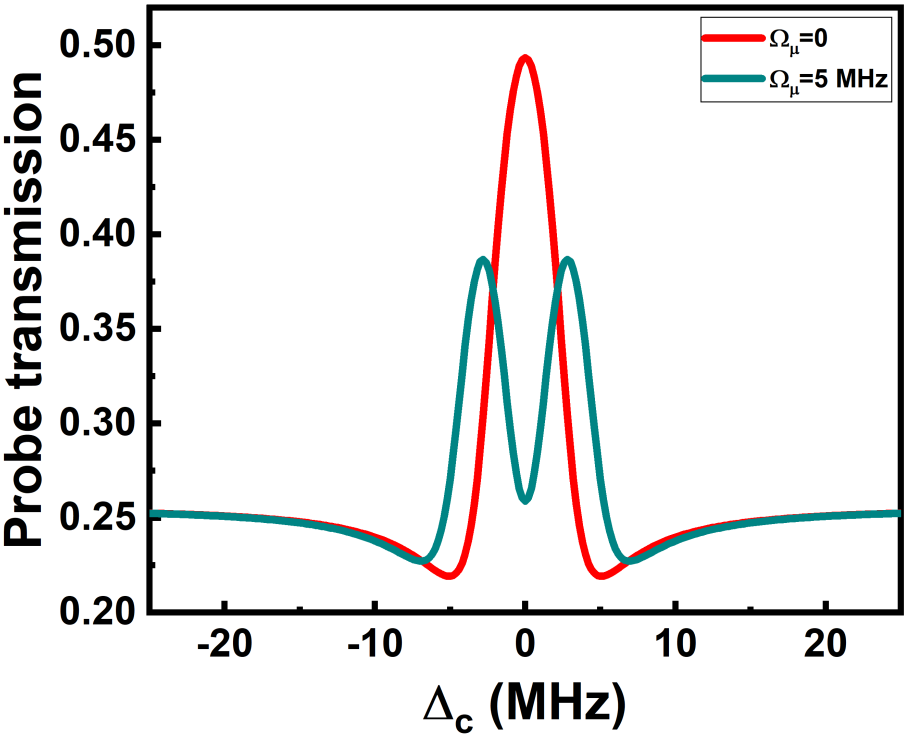

Figure 3.2: Probe transmission as a function of Δ_c. The solid red line represents the EIT peak in the absence of the microwave field ($\Omega_\mu = 0$), and the solid cyan line represents the splitting in the EIT peak due to the presence of the microwave field ($\Omega_\mu = 5$ MHz). Other parameters are $\Omega_p = 500$ kHz, $\Omega_c = 4$ MHz, $\Gamma_{eg} = 6$ MHz, $\Gamma_{re} = 10$ kHz, $\Gamma_{rg} = 100$ kHz, $\Gamma_{r'g} = 100$ kHz, $\Gamma_{r'r} = 10$ kHz, $\Delta_p = 0$ and $\Delta_\mu = 0$. The density of the atoms is 1.7×10^{10} cm^{-3}.

$$\frac{i}{2}[\Omega_c^* \rho_{er'} - 2\Delta_\mu \rho_{rr'} - \Omega_\mu(\rho_{rr} - \rho_{r'r'})] - \frac{(\gamma_1 + \gamma_2)}{2}\rho_{rr'} = 0 \tag{3.13}$$

$$\frac{i}{2}[2\delta_2 \rho_{r'g} + \Omega_\mu^* \rho_{rg} - \Omega_p^* \rho_{r'e}] - \frac{\gamma_2}{2}\rho_{r'g} = 0 \tag{3.14}$$

$$\frac{i}{2}[2\delta_3 \rho_{r'e} + \Omega_\mu^* \rho_{re} - \Omega_p \rho_{r'g} - \Omega_c^* \rho_{r'r}] - \frac{(\Gamma_{eg} + \gamma_2)}{2}\rho_{r'e} = 0 \tag{3.15}$$

$$\frac{i}{2}[-\Omega_c \rho_{r'e} + 2\Delta_\mu \rho_{r'r} + \Omega_\mu^*(\rho_{rr} - \rho_{r'r'})] - \frac{(\gamma_1 + \gamma_2)}{2}\rho_{r'r} = 0 \tag{3.16}$$

$$\frac{i}{2}[\Omega_\mu^* \rho_{rr'} - \Omega_\mu \rho_{r'r}] - \gamma_2 \rho_{r'r'} = 0 \tag{3.17}$$

The above equations are solved numerically to find the ground state to the excited state coherence ρ_{eg}. For the same velocity class of atoms in thermal atomic vapor, the detuning of the fields are modified as $\Delta_p \to \Delta_p - k_p v$, $\Delta_c \to \Delta_c + k_c v$ and

$\Delta_\mu \rightarrow \Delta_\mu - k_\mu v$. k_p, k_c, and k_μ are the wave-vectors of the probe, coupling, and microwave field, respectively, and v is the velocity of the atoms.

For the thermal atomic medium, the susceptibility of the probe is found out as

$$\chi(\omega_p) = \frac{2N|\ \mu_{ge}\ |^2}{\hbar\epsilon_0\Omega_p}\frac{1}{\sqrt{\pi}v_p}\int_{-\infty}^{\infty}\rho_{eg}e^{-\frac{v^2}{v_p^2}}dv \tag{3.18}$$

The probe transmission is calculated using Eqn. (2.22). The probe transmission for the four-level system is represented by Fig. 3.2. The plot with a solid red line represents the EIT peak as a function of coupling detuning Δ_c in the absence of the third field, i.e., microwave field (Ω_μ). The plot with a solid cyan line represents the splitting in the EIT peak or the absorption feature within the transparency window due to the presence of the microwave field. This splitting is also known as the Autler-Townes (AT) splitting.

3.2 Experimental set-up for investigation of microwave field sensing using EIT

The experimental set-up for microwave electric field sensing using EIT is shown in Fig. 3.3. An external cavity diode laser (ECDL) TOPTICA DL PRO of wavelength 780 nm is used to derive the probe beam (ω_p). The experimental set-up shows that saturated absorption spectroscopy (SAS) is used to frequency stabilize the probe laser. The probe beam carries out the atomic excitation from the ground state $|g\rangle$ to the excited state $|e\rangle$ and the probe frequency is locked to the ^{87}Rb $5S_{\frac{1}{2}}F = 2 \rightarrow 5P_{\frac{3}{2}}F' = 3$ transition. The coupling beam (ω_c) is derived from a frequency doubling cavity laser (TOPTICA TA-SHG PRO) at a wavelength of 480 nm. The coupling beam excites the atoms from the excited state $|e\rangle$ to the Rydberg state $|r\rangle$. The probe and the coupling beams counter propagate each other through the cylindrical rubidium vapor cell length of 5 cm and diameter of 2.5 cm. The probe and the coupling beam are focused at the center of the vapor cell where $\frac{1}{e}$ radii of

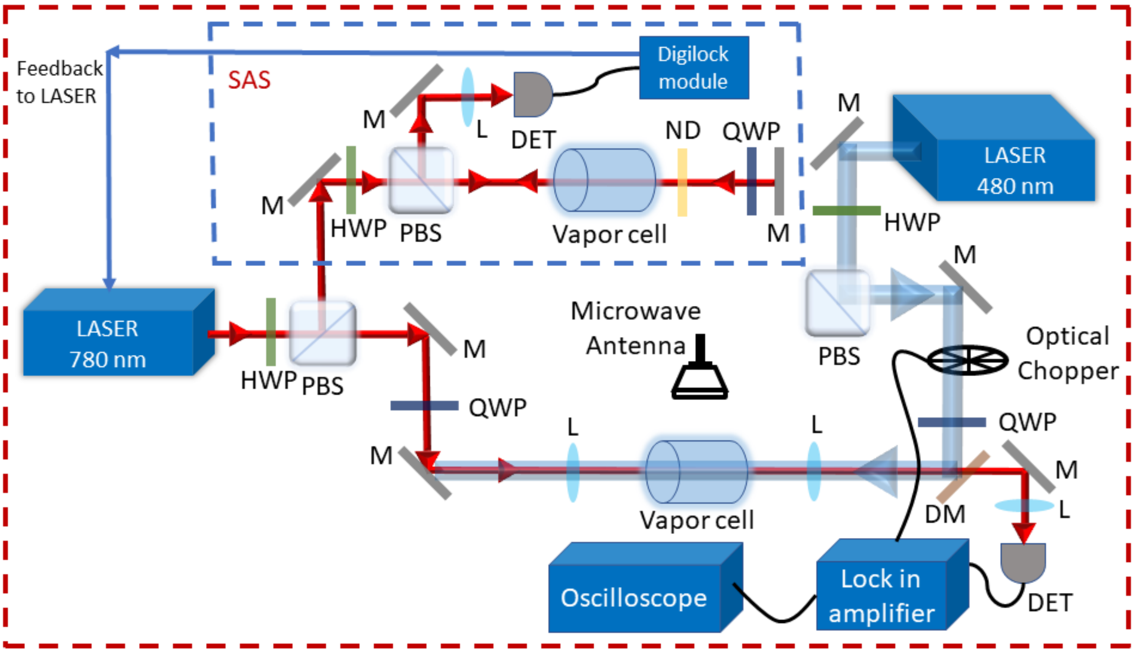
Feedback to LASER
SAS
Digilock module
M
L
DET
ND
QWP
M
HWP
PBS
Vapor cell
M
M
LASER 480 nm
HWP
M
LASER 780 nm
HWP
PBS
M
Microwave Antenna
PBS
Optical Chopper
QWP
QWP
L
L
M
M
Vapor cell
DM
L
Oscilloscope
Lock in amplifier
DET

Figure 3.3: Optical set up for microwave electric field sensing. The set up consists of two parts: one for probe frequency stabilization (SAS) and the other part for experiment. HWP: Half wave-plate, PBS: Polarizing beam splitter, M: Mirror, QWP: Quarter wave-plate, L: Lens, DM: Dichroic mirror, DET: Detector.

the probe and coupling beams are 0.4 mm and 0.7 mm, respectively. The power of the probe and coupling beams are approximately 1μW and 100 mW, respectively. The probe and the coupling beams are circularly polarized but orthogonal. The probe beam is detected using a photodetector. A lock-in detection is performed to have an enhanced signal-to-noise ratio (SNR). The detector signal is fed into a lock-in amplifier. The reference to the lock-in amplifier is provided from an optical chopper used to modulate the coupling beam intensity. It is operated at a frequency of 5 kHz. The output of the lock-in amplifier is observed using an oscilloscope. A microwave signal generator is used as the source which radiates the microwave field in the free space using a horn antenna. As shown in the experimental set-up, the horn antenna is placed at a distance of approximately 38 cm from the center of the vapor cell along the radial direction. The microwave field couples the Rydberg state $|r\rangle$ to another nearby Rydberg state $|r'\rangle$. The effect of the presence of microwave field is studied by observing the EIT signal using an oscilloscope.

3.3 Observation of AT splitting due to the presence of the microwave field

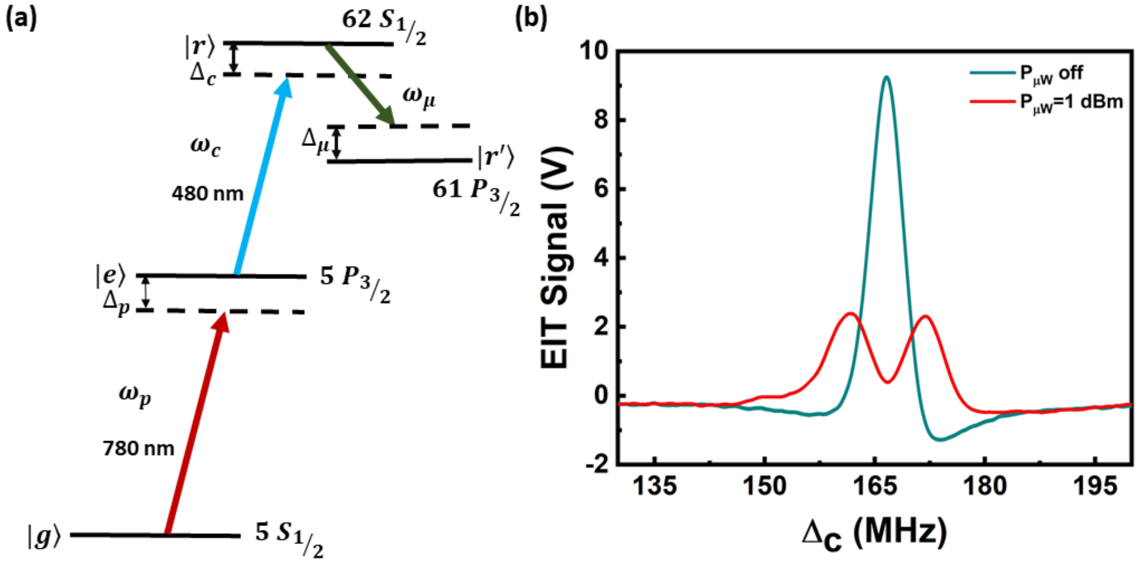

Figure 3.4: Microwave electrometry with Rydberg atoms: (a) Energy level scheme where $|g\rangle = 5S_{\frac{1}{2}}$, $|e\rangle = 5P_{\frac{3}{2}}$, $|r\rangle = 62S_{\frac{1}{2}}$, and $|r'\rangle = 61P_{\frac{3}{2}}$. (b) EIT signal when the microwave is off and on with microwave power $P_{\mu W} = 1$ dBm at the signal generator.

The schematic of the energy level is shown in Fig. 3.4(a). The different states of the system are $|g\rangle = 5S_{\frac{1}{2}}$, $|e\rangle = 5P_{\frac{3}{2}}$, $|r\rangle = 62S_{\frac{1}{2}}$, and $|r'\rangle = 61P_{\frac{3}{2}}$. The probe and coupling field wavelengths corresponding to the transitions are 780.241 nm and 479.786 nm, respectively. When the probe beam is on resonance (i.e., $\Delta_p = 0$) and the coupling beam is scanned to satisfy the conditions of EIT, we observe the EIT signal as a function of Δ_c shown in Fig. 3.4(b). The resonance frequency of the microwave field for the given transition from $|r\rangle \rightarrow |r'\rangle$ is $f_{\mu,0} = 15.17375$ GHz. The horn antenna is placed at a distance of 38 cm from the center of the vapor cell. Application of the microwave field on resonance to the atomic transition (i.e., $\Delta_\mu = 0$) results in the splitting of the EIT peak. This splitting is called the Autler-Townes (AT) splitting. The presence of the microwave field leads to the formation of the dressed states. The Rydberg state is split into two dressed states leading to the splitting of the EIT signal into two AT peaks as shown in Fig. 3.4(b). Here, the total microwave power used is $P_{\mu W} = 1$ dBm. This power shown at the signal generator is not the same power or field experienced by the Rydberg atoms. There are losses from the cables, horn antenna, and also during propagation. The cross-sectional interacting area of the optical beam and the vapor cell is 0.5 cm^2, considering a beam of around 1 mm diameter. The electric field reaching the interacting area is nearly 0.08 V/m. There are also electric fields due to reflections from the metallic optical table, vapor cell walls, etc.

The microwave power or electric field strength experienced by the atoms is provided from the measure of the splitting of the EIT signal. The frequency difference between the two peaks determines the Rabi frequency of the microwave field (Ω_μ). The field strength of the microwave field is calculated from the relation

$$\mid E \mid = 2\pi \frac{\hbar}{d_\mu} \Omega_\mu = 2\pi \frac{\hbar}{d_\mu} \Delta f_0 = 2\pi \frac{\hbar}{d_\mu} D \Delta f_m \tag{3.19}$$

where $\Delta f_0 = D\Delta f_m$, Δf_m is the measured splitting of the EIT peak, d_μ is the dipole moment of the microwave coupled transition, and D is a scaling factor which takes into consideration the Doppler mismatch of the probe and coupling laser. If the probe laser is scanned, then $D = \frac{\lambda_p}{\lambda_c}$ where λ_p and λ_c are the wavelengths of the probe and coupling laser, respectively. If the coupling laser is scanned, then $D = 1$. For the given parameters discussed in this section and for $P_{\mu W} = 1$ dBm, the microwave Rabi frequency is found to be $\Omega_\mu = \Delta f_0 = 10.2$ MHz and the electric field strength is calculated to be $\mid E \mid = 0.37$ V/m. The lock-in amplifier parameters used in the measurement are time constant=300 μs and sensitivity=1 mV. The lock-in amplifier gain is 10000. The dipole moment for the microwave transition is given by $d_\mu = RAea_0$ where e is the elementary charge and a_0 is the Bohr radius. R and A are the radial and angular parts of the dipole moment, respectively. These values are calculated from [58]. The dipole moment considered here is 2146.98 ea_0.

In a typical experiment, the vapor cell is heated to 60°C to increase the density of atoms inside the vapor cell to 5×10^{11} cm^{-3}. The geometry of the atomic vapor cell also affects the E-field measurement, which has been discussed in [77]. In these results, the effect of vapor cell geometry has been ignored during the measurements as the vapor cell is kept fixed, and the measurements are taken at a fixed point, i.e., at the center of the vapor cell. The effect of the reflections from the surface of the optical table is also ignored in the measurements.

3.4 E-field strength with different microwave power at the signal generator

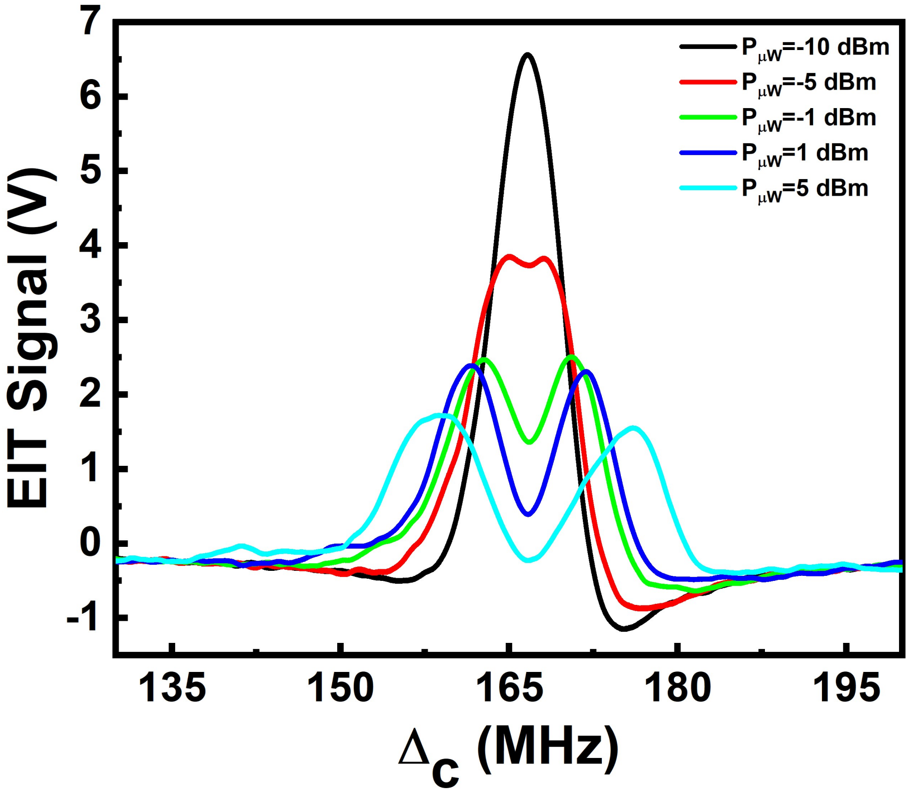

Figure 3.5: Splitting of the EIT signal for different microwave source power at the signal generator.

For the above-discussed transitions, the E-field observed by the Rydberg atoms for different power levels of the microwave signal generator is also studied. Different power levels of the signal generator lead to different splitting of the EIT signal, as shown in Fig. 3.5. As discussed in the earlier section, the strength of the E-field experienced by the atoms is measured from AT splitting of the EIT peaks using Eqn. 3.19. It is observed that the AT splitting increases linearly with the square root of microwave source power, and hence, the measured E-field strength increases linearly with the square root of microwave source power as shown in Fig. 3.6. The behavior follows a linear fit with a slope of 0.41±0.01 v/m$\sqrt{mW}$. There can be statistical and systematic uncertainties in the experimental measurement method. From Eqn. 3.19, it is known that there is a linear relationship between measured AT splitting and E-field. When the EIT line-width is comparable to or larger than the measured splitting of the EIT peak, the linear relationship breaks down [25]. The EIT line-width is a function of the Rabi frequencies of the probe and coupling beams [78], and various other factors [79].

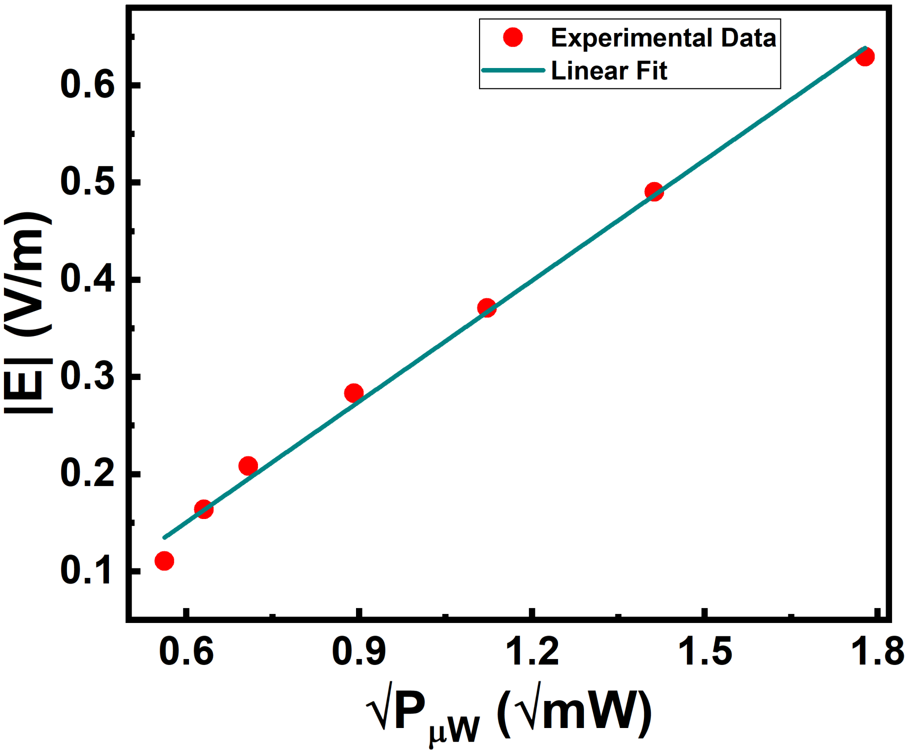

Figure 3.6: Measured value of E-field strength for given microwave source power.

3.5 Effect of microwave detuning on E-field measurement

The above section measures the on-resonant microwave field strengths and their dependence on the source power. When the microwave field is weak, it is difficult to measure the splitting with on resonant microwave field. Such can be the case while detecting weak microwave fields in the upper millimeter wave and sub-THz bands. Determination of AT splitting becomes difficult in these high frequencies for two reasons. One is the weak power of the electric field, and another one is the small dipole moment due to the use of low n states for detecting such high frequencies. The detection of the E-field can be improved for weak microwave fields by detuning the microwave field away from the resonance, i.e., using off-resonant fields [80]. In this section, an example is presented which shows how off-resonant fields help to improve the sensitivity of E-field measurement.

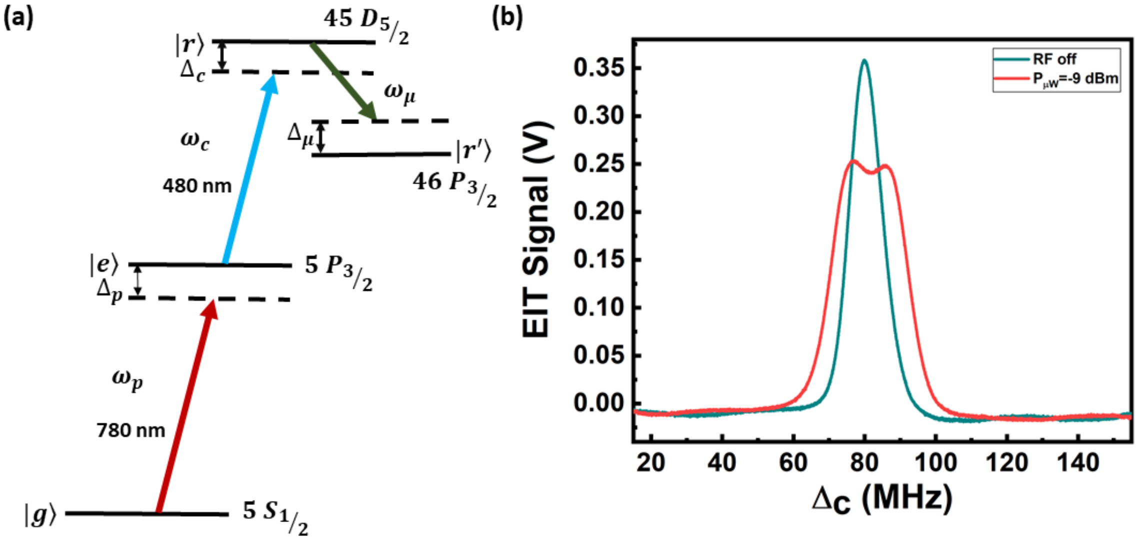

Figure 3.7: (a) Energy level scheme where $|g\rangle = 5S_{\frac{1}{2}}$, $|e\rangle = 5P_{\frac{3}{2}}$, $|r\rangle = 45D_{\frac{5}{2}}$, and $|r'\rangle = 46P_{\frac{3}{2}}$. (b) EIT signal when the microwave is off and on with microwave power $P_{\mu W} = -9$ dBm at the signal generator applied on-resonance to the transition.

The schematic of the energy level scheme is shown in Fig. 3.7(a). The different states of the system are $|g\rangle = 5S_{\frac{1}{2}}$, $|e\rangle = 5P_{\frac{3}{2}}$, $|r\rangle = 45D_{\frac{5}{2}}$, and $|r'\rangle = 46P_{\frac{3}{2}}$. The probe and coupling field wavelengths corresponding to the transitions are 780.241 nm and 480.38 nm, respectively. The power of the probe and coupling beam is nearly 2μW and 120 mW, respectively. The $\frac{1}{e}$ probe and coupling radius are around 0.4 mm and 0.7 mm, respectively. The EIT signal as a function of Δ_c is shown in Fig. 3.7(b). For the given transition, the resonance frequency of the microwave field is $f_{\mu,0} = 25.7747$ GHz. The horn antenna is placed at a distance of 20 cm from the center of the vapor cell. When the microwave field is applied at $\Delta_\mu = 0$, the splitting of the EIT peak is observed, as discussed earlier. For the parameters discussed in this section and for $P_{\mu W} = -9$ dBm, the microwave Rabi frequency is found to be $\Omega_\mu = \Delta f_0 = 9.04$ MHz and electric field strength to be $\mid E \mid = 0.43$ V/m. The transition dipole moment is 1637.11 ea_0. The lock-in amplifier parameters used in the measurement are time constant=1 ms and sensitivity=500 mV. The lock-in amplifier gain is 20. The vapor cell is heated to 60°C to increase the density of atoms inside the vapor cell to 5×10^{11} cm^{-3}.

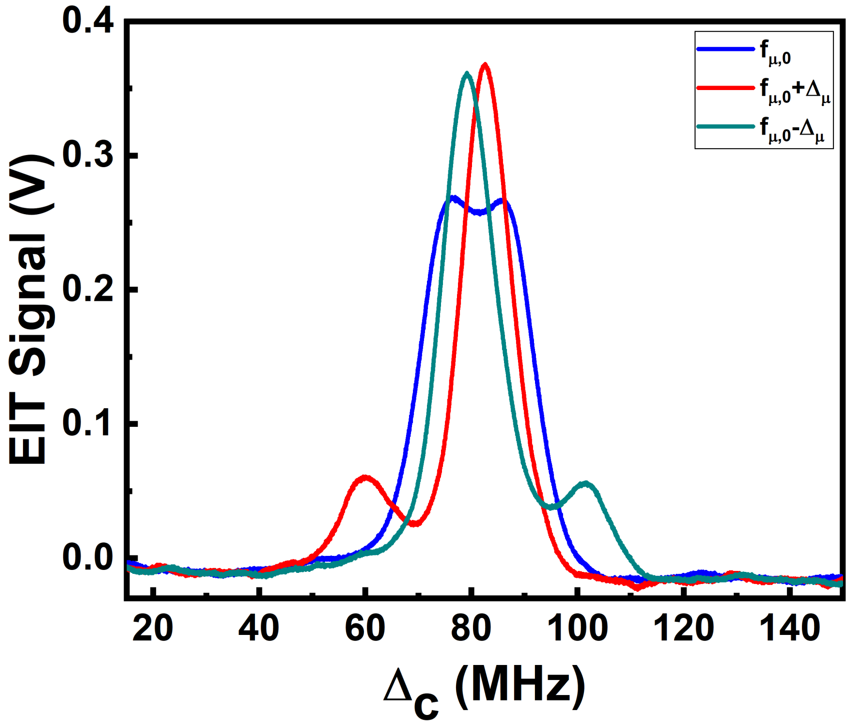

Figure 3.8: Comparison of AT splitting of the EIT signal for off-resonant microwave fields ($f_{\mu,0} \pm \Delta_\mu$) with resonant microwave field splitting ($f_{\mu,0}$) for fixed power of the microwave field ($P_{\mu W} = -9$ dBm) and with $\Delta_\mu = 30$ MHz.

Fig. 3.8 shows the splitting of the EIT signal for the off-resonant microwave fields (f_{μ,Δ_μ}) as compared to the on-resonant case ($f_{\mu,0}$) where $f_{\mu,\Delta_\mu} = f_{\mu,0} \pm \Delta_\mu$ and Δ_μ represents the detuning of the microwave from the atomic resonance. As it is seen from the figure, the off-resonant field leads to AT splitting, which can be differentiated better than the on-resonant AT splitting for a fixed power level of the microwave source. The off-resonant microwave field leads to non-symmetric splitting of the EIT peak, which is observed in the above figure. For $f_{\mu,\Delta_\mu} < f_{\mu,0}$, the left side peak is smaller than the right, and for $f_{\mu,\Delta_\mu} > f_{\mu,0}$, the right side peak is smaller than the left peak. Also, the increase in microwave detuning leads to an increased separation between the two peaks. The power level of the microwave source is fixed at $P_{\mu W} = -9$ dBm, and the dependence of the measured AT splitting on Δ_μ is studied as shown in Fig. 3.9.

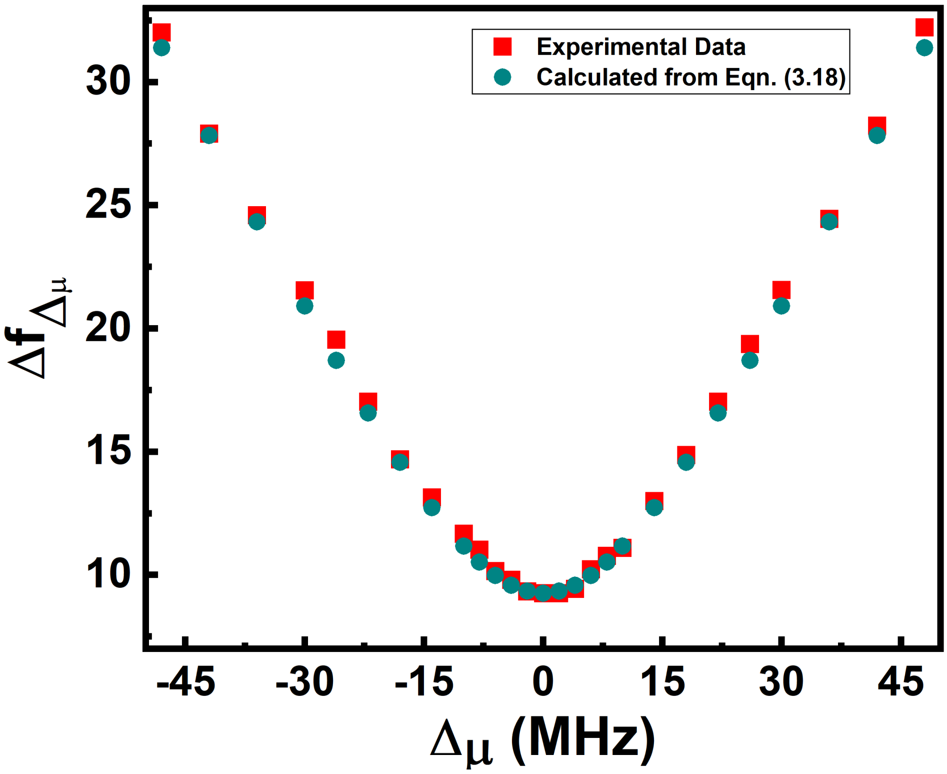

Figure 3.9: Separation between the AT split peaks at finite detuning (Δf_{Δ_μ}) as a function of Δ_μ for $P_{\mu W} = -9$ dBm.

The separation between the AT split peaks is given by

$$\Delta f_{\Delta_\mu} = \sqrt{(\Delta_\mu)^2 + (\Delta f_0)^2} \tag{3.20}$$

The AT splitting is increased by more than three times for a fixed weak microwave field when the microwave is detuned away from the atomic resonance. The calculated values from Eqn. (3.20) show a good agreement with experimentally found values. There is a limit up to which the microwave can be detuned to observe the improvement in E-field detection [80]. Fitting the Eqn. (3.20) to the data obtained in the experiment, it helps to determine the resonance frequency of the microwave transition for cases when the resonance frequency is not known.

3.6 Communication with Rydberg atoms

Communication technology with the Rydberg EIT system involves modulation/demodulation of a baseband signal onto an electromagnetic carrier signal [42]. This modulation is carried out using amplitude modulation or frequency modulation for analog communication purposes and phase or frequency shift keying for digital communication. All the studies involve the use of EIT in a two-photon excitation process to the Rydberg state where the microwave field (carrier wave) is modulated.

3.6.1 Analog communication with Rydberg EIT

The microwave electric field sensing technique can be utilized for analog data communication with Rydberg atoms [76, 81]. This sensing technique can make Rydberg atoms act as an antenna/receiver for message signals encoded into microwave radiation (carrier wave). This has led physicists to term the system as **atom-radio**. The system can be used to record and play a message signal (an audio signal in our case) in real time. This system uses the concept of amplitude modulation of the carrier signal to deliver the message signal (modulating signal) to the Rydberg

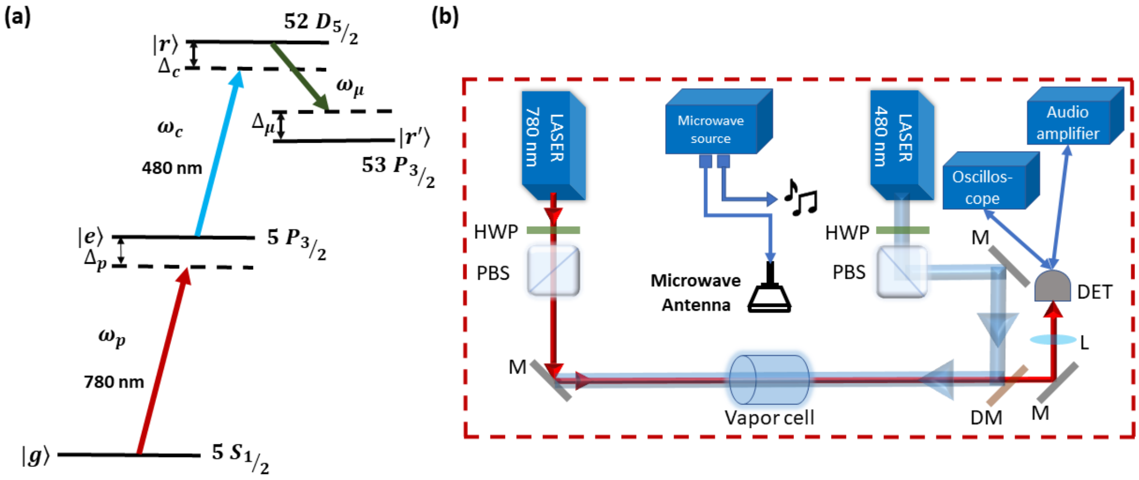
(a)
$|r\rangle$
Δ_c
$52\,D_{5/2}$
ω_μ
ω_c
480 nm
Δ_μ
$|r'\rangle$
$53\,P_{3/2}$
$|e\rangle$
Δ_p
$5\,P_{3/2}$
ω_p
780 nm
$|g\rangle$
$5\,S_{1/2}$
(b)
LASER 780 nm
Microwave source
LASER 480 nm
Audio amplifier
Oscillos-cope
HWP
PBS
Microwave Antenna
HWP
PBS
M
DET
L
M
Vapor cell
DM
M

Figure 3.10: (a) Energy level scheme and (b) experimental set-up.

atoms. This message signal can be retrieved from the probe beam and detected at the photo-diode without the need for any demodulation circuit.

The energy level scheme and the experimental set-up are shown in Fig. 3.10. The set-up utilizes a counter-propagating probe and coupling scheme to achieve the conditions of EIT with the Rydberg atoms, as discussed in the previous sections. The probe frequency is stabilized at $^{87}Rb\ 5S_{\frac{1}{2}}F = 2 \rightarrow 5P_{\frac{3}{2}}F' = 3$ resonance using SAS technique, and the coupling frequency is stabilized at the resonance of the EIT using the technique discussed in Sec. 2.5.2. Microwave field is radiated through the horn antenna to interact with the $52D_{\frac{5}{2}} \rightarrow 53P_{\frac{3}{2}}$ transition. Here, the modulation input of the microwave signal generator is fed with a message signal. The microwave field acts as a carrier of the message signal, and the process is like an amplitude modulation of the microwave field. The modulated microwave field interacts with the Rydberg atoms and transfers the message signal to the probe beam. The probe beam is detected using a photodetector, and the detector output is fed to the oscilloscope. The output voltage observed is proportional to the modulating signal. A direct read-out of the audio signal can be observed without the need for any demodulation circuit. The output is anti-correlated to the input message signal with reduced amplitude, as shown in Fig. 3.11. It is also observed that when the detector output is fed directly to an audio amplifier, we hear the same output audio signal as the

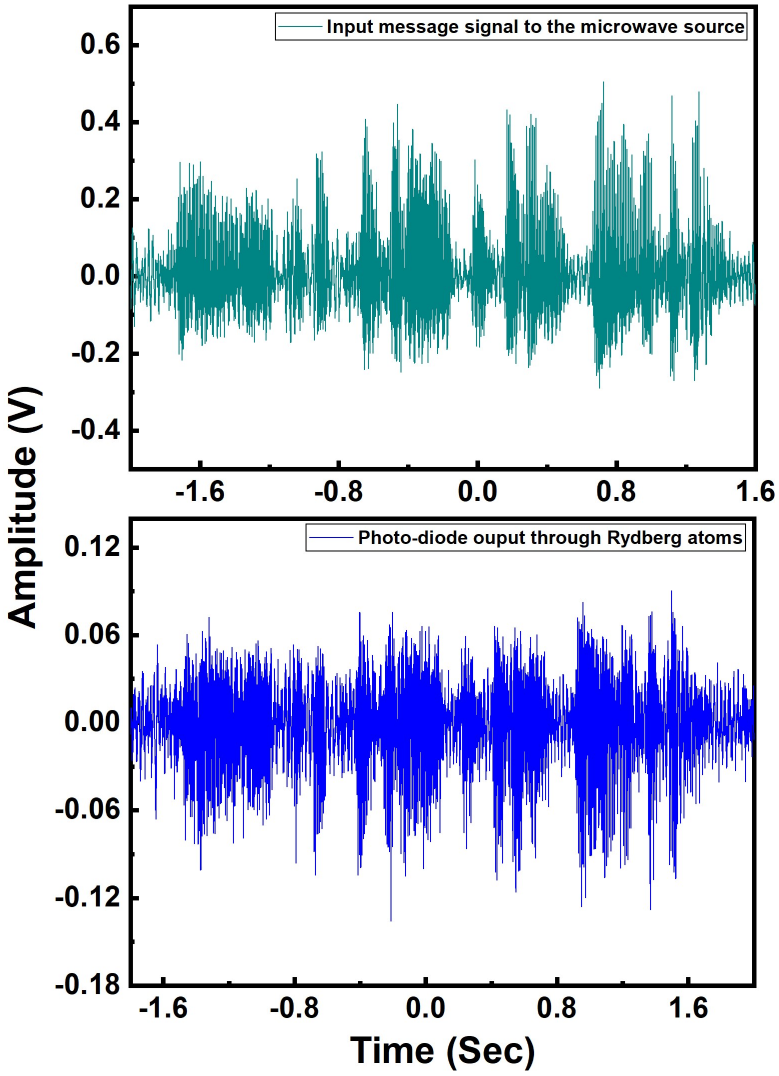

Figure 3.11: Input audio signal (top) to the microwave signal generator and retrieved audio signal (bottom) at the photodetector.

input to the modulation port of the microwave signal generator but with reduced strength.

3.6.2 Digital communication with Rydberg EIT

Rydberg EIT field sensing techniques have also been exploited for digital communication purposes [40, 41]. This involved using frequency or phase shift keying to investigate the data transfer rate in the two-photon Rydberg EIT system. The major aim behind this investigation is to develop a system that has a faster data transfer rate, and the bandwidth of the modulation spectrum determines the data transfer rate. It has been demonstrated that the two-photon Rydberg EIT system can have a data transfer rate of 8.2 Mbit/s with a signal bandwidth of nearly 1 MHz [40].

3.7 Limitations of microwave field sensing with Rydberg atoms using EIT through two-photon excitation process to the Rydberg state

• The data transfer rate in the two-photon Rydberg EIT system is limited to a few Mbit/s as the modulation bandwidth is limited to only a few MHz. This limitation is because of the optical pumping rate to the EIT dark state, which is given by $\Omega_{EIT} = \frac{\Omega_c^2}{2\Gamma}$ where Ω_c is the Rabi frequency of the coupling beam and Γ is the natural line-width of the intermediate state which is 6 MHz for rubidium. To have a faster data transfer rate, a system with larger modulation bandwidth is necessary.

• The sensitivity of measured electric field is given by $\frac{E_{min}}{\sqrt{Hz}} = \frac{h}{\mu\sqrt{T_2 N}}$, where E_{min} is the minimum detectable electric field, T_2 is the dephasing time of the EIT process and N is the number of atoms participating in the detection process [12]. The electric field that causes an AT splitting similar to the line-width of the EIT signal is the minimum detectable field and is given by the relation $E_{min} = 2\pi \frac{\hbar}{d_\mu}\gamma_{EIT}$ [43]. The minimum electric field detected using Rydberg EIT systems is limited by the line-width of the EIT spectrum γ_{EIT}. In the two-photon Rydberg system discussed in this chapter, the line-width of the EIT signal is $\gamma_{EIT} \sim 4$ MHz. For such an EIT line-width, the minimum detectable field using AT splitting is around 2 mV/cm for d_μ =1637.11 ea_0. As the minimum detectable field depends on the EIT line width, narrowing the EIT line width can result in better sensitivity of the detected electric field.

3.8 Conclusion

The Rydberg atoms act as accurate and precise sensors for microwave electric fields due to their significant dipole moment and large polarizability. The system utilizes the splitting of the two-photon EIT signal to determine the electric field strength of the microwave field. As discussed in this chapter, Rydberg atoms can also be used for communication technology. But the data transfer rate with a two-photon Rydberg EIT system is limited by the optical pumping rate to the dark state, and also, the sensitivity of the measured electric field is limited by the EIT linewidth.

Chapter 4

Six-wave mixing of optical and microwave fields using Rydberg atoms in thermal atomic vapor

The six-wave mixing process of optical and microwave fields has been studied for coherent microwave-to-optical conversion in a cold atomic system using Rydberg atoms [82, 83]. The system utilizes EIT for better conversion efficiency but has a limited conversion bandwidth of a few MHz. Rydberg atoms facilitate the efficient free space microwave-to-optical conversion due to their large dipole moment in a wide operating frequency range varying from MHz to THz [27]. The limited bandwidth of the Rydberg EIT system restricts the data transfer rate to only a few MHz. This chapter demonstrates the six-wave mixing of optical and microwave fields in thermal atomic vapor using Rydberg atoms [84]. The six-wave mixing process leads to the parametric generation of a new optical field. Due to the parametric nature of the process, the system is expected to respond faster, and the available coupling Rabi frequency limits the response. This chapter describes a theoretical model of a four-level system, and the wave propagation equations are solved for the generated field to model the experimental results. The temporal response of the system is investigated through amplitude modulation of the generated field. Finally, a theoretical study is performed to understand the effect of coupling rabi frequency on the modulation bandwidth.

4.1 Generation of the new optical field due to six-wave mixing process inside the atomic medium

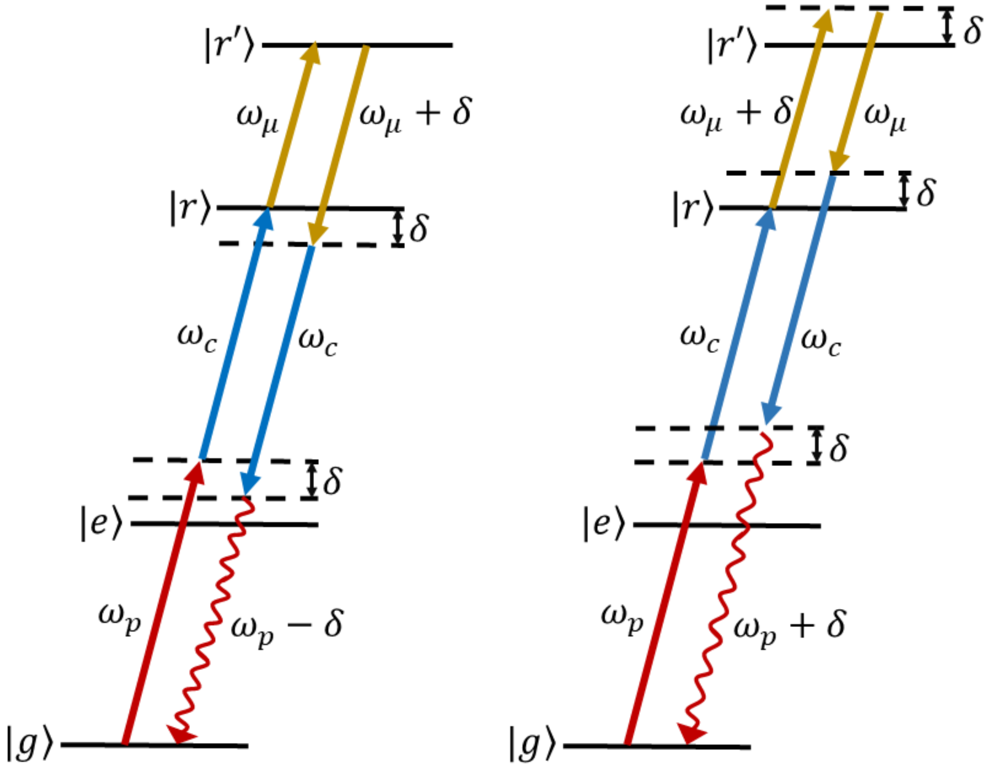
$|r'\rangle$
ω_μ
$\omega_\mu + \delta$
$|r\rangle$
δ
ω_c
ω_c
δ
$|e\rangle$
ω_p
$\omega_p - \delta$
$|g\rangle$
$|r'\rangle$
δ
$\omega_\mu + \delta$
ω_μ
$|r\rangle$
δ
ω_c
ω_c
δ
$|e\rangle$
ω_p
$\omega_p + \delta$
$|g\rangle$

Figure 4.1: Schematic of energy levels in the ladder configuration where $|g\rangle$ represents the ground state, $|e\rangle$ represents the intermediate state, $|r\rangle$ represents the Rydberg state, and $|r'\rangle$ represents the second nearby Rydberg state. A probe field (ω_p) couples the transition $|g\rangle \rightarrow |e\rangle$, and a coupling field ($\omega_c$) couples the transition $|e\rangle \rightarrow |r\rangle$. Two microwave fields, ω_μ and ($\omega_\mu + \delta$), are applied between the two Rydberg states $|r\rangle$ and $|r'\rangle$.

The energy level scheme for the six-wave mixing process is shown in Fig. 4.1. The six-wave mixing of optical and microwave fields inside the atomic medium results in the generation of the new optical field. It is a parametric generation process and hence, is an instantaneous process. The limitation is set by the available coupling

Rabi frequency. The phenomenon of parametric six-wave mixing is understood as follows: absorption of a probe photon of frequency ω_p, absorption of a coupling photon of frequency ω_c, absorption of a microwave photon of frequency ω_μ $(\omega_\mu + \delta)$, emission of a microwave photon of frequency $\omega_\mu + \delta$ (ω_μ), emission of a coupling photon of frequency ω_c, leading to the generation of new optical field at frequency $\omega_p - \delta$ $(\omega_p + \delta)$.

The frequency of the generated optical field is given by $\omega_p \pm \delta = \omega_p + \omega_c + \omega_\mu + \delta(\omega_\mu) - \omega_\mu(\omega_\mu + \delta) - \omega_c$. The generated optical field has a direction derived from the phase matching condition as: $\vec{k}_{p'} = \vec{k}_p + \vec{k}_c - \vec{k}_{\mu_1} + \vec{k}_{\mu_2} - \vec{k}_c$. $\vec{k}_p$ and $\vec{k}_c$ are the wave vectors of the probe and coupling field. $\vec{k}_{\mu_1}$ and $\vec{k}_{\mu_2}$ are the wave vectors of the two microwave fields. $\vec{k}_{p'}$ is the wave vector of the generated optical field. The magnitude of the wave-vectors of the microwave field is negligible compared to the magnitude of the wave-vectors of the optical fields. The microwave wave-vectors cancel out each other as one of the microwave photon is emitted, and the other one is absorbed. From the phase matching condition, it is found that the direction of the generated optical field is along the direction of the applied probe field.

4.2 Theoretical model for six wave-mixing process using four-level system

The theoretical model needed to explain the six-wave mixing phenomenon is a four-level system, as shown in 4.1. As mentioned in the caption, the system consists of states $|g\rangle$, $|e\rangle$, $|r\rangle$ and $|r'\rangle$ in ladder configuration and laser fields coupling the transitions are ω_p, ω_c, ω_μ, and $\omega_\mu + \delta$. δ is the frequency difference between the two microwave fields. The second microwave field $(\omega_\mu + \delta)$ is considered to be very weak as compared to the first microwave field ω_μ. The detuning of the probe, coupling, and first microwave field from the corresponding atomic transitions are Δ_p, Δ_c, and Δ_μ, respectively. The two-photon and three-photon detuning are defined as $\delta_1 = (\Delta_p + \Delta_c)$, and $\delta_2 = (\Delta_p + \Delta_c + \Delta_\mu)$ respectively and $\delta_3 = (\Delta_c + \Delta_\mu)$. The bare atomic Hamiltonian of the system is $H_0 = \hbar\omega_{ge}|e\rangle\langle e| + \hbar(\omega_{ge}+\omega_{er})|r\rangle\langle r| + \hbar(\omega_{ge} + \omega_{er}+\omega_{rr'})|r'\rangle\langle r'|$. The laser fields are expressed as

$$\vec{E'}_p = \vec{E}_p e^{-i\omega_p t} + c.c \tag{4.1}$$

$$\vec{E'}_c = \vec{E}_c e^{-i\omega_c t} + c.c \tag{4.2}$$

$$\vec{E'}_{\mu_1} = \vec{E}_{\mu_1} e^{-i\omega_\mu t} + c.c \tag{4.3}$$

$$\vec{E'}_{\mu_2} = \vec{E}_{\mu_2} e^{-i(\omega_\mu+\delta)t} + c.c \tag{4.4}$$

where E_p, E_c, E_{μ_1} and E_{μ_2} are the amplitudes of the electric fields. The total microwave electric field is written as

$$\vec{E'}_\mu = \vec{E'}_{\mu_1} + \vec{E'}_{\mu_2} = \vec{E}_{\mu_1} e^{-i\omega_\mu t} + \vec{E}_{\mu_2} e^{-i(\omega_\mu+\delta)t} = \vec{E}_\mu e^{-i\omega_\mu t} \tag{4.5}$$

where $\vec{E}_\mu = \vec{E}_{\mu_1} + \vec{E}_{\mu_2} e^{-i\delta t}$. The Hamiltonian due to the interaction of the optical field with the atomic medium is $H_{int} = -\vec{\mu}\cdot\vec{E} = -E_p(\mu_{ge}|g\rangle\langle e| + \mu_{eg}|e\rangle\langle g|) - E_c(\mu_{er}|e\rangle\langle r| + \mu_{re}|r\rangle\langle e|) - E_\mu(\mu_{rr'}|r\rangle\langle r'| + \mu_{r'r}|r'\rangle\langle r|)$. The Rabi frequency of the probe, coupling and the two microwave fields is given by $\Omega_p = \frac{2\mu_{ge}E_p}{\hbar}$, $\Omega_c = \frac{2\mu_{er}E_c}{\hbar}$, $\Omega_{\mu_1} = \frac{2\mu_{er}E_{\mu_1}}{\hbar}$ and $\Omega_{\mu_2} = \frac{2\mu_{er}E_{\mu_2}}{\hbar}$ respectively. Without the loss of generality, all the Rabi frequencies are considered to be real.

The total Hamiltonian of the system is given by $\tilde{H} = H_0 + H_{int}$. After the use of rotating wave approximation and in a suitable rotating frame, the Hamiltonian is expressed as

$$H = -\frac{\hbar}{2}\begin{pmatrix} 0 & \Omega_p & 0 & 0 \\ \Omega_p^* & 2\Delta_p & \Omega_c & 0 \\ 0 & \Omega_c^* & 2(\Delta_p+\Delta_c) & \Omega_{\mu_1} + e^{-i\delta t}\Omega_{\mu_2} \\ 0 & 0 & \Omega_{\mu_1}^* + e^{i\delta t}\Omega_{\mu_2}^* & 2(\Delta_p+\Delta_c+\Delta_\mu) \end{pmatrix}.$$

The Hamiltonian acquired for the system is a time-dependent Hamiltonian even after suitable unitary operations.

4.2.1 Construction of the master equation

The master equation is written as:

$$\dot{\rho} = \frac{i}{\hbar}[\rho, H] + \mathcal{L}_{\mathcal{D}}(\rho). \tag{4.6}$$

The density matrix ρ is a 4×4 matrix and is written as $\rho_{i,j}$ with $i, j = g, e, r, r'$ and the Lindblad operator is

$$\mathcal{L}_{\mathcal{D}}(\rho) = \begin{pmatrix} \Gamma_{eg}\rho_{ee} + \Gamma_{rg}\rho_{rr} + \Gamma_{r'g}\rho_{r'r'} & -\frac{\Gamma_{eg}}{2}\rho_{ge} & -\frac{\gamma_1}{2}\rho_{gr} & -\frac{\gamma_2}{2}\rho_{gr'} \\ -\frac{\Gamma_{eg}}{2}\rho_{eg} & \Gamma_{re}\rho_{rr} - \Gamma_{eg}\rho_{ee} & -\frac{\gamma_3}{2}\rho_{er} & -\frac{(\Gamma_{eg}+\gamma_2)}{2}\rho_{er'} \\ -\frac{\gamma_1}{2}\rho_{rg} & -\frac{\gamma_3}{2}\rho_{re} & \Gamma_{r'r}\rho_{r'r'} - \gamma_1\rho_{rr} & -\frac{(\gamma_1+\gamma_2)}{2}\rho_{rr'} \\ -\frac{\gamma_2}{2}\rho_{r'g} & -\frac{(\Gamma_{eg}+\gamma_2)}{2}\rho_{r'e} & -\frac{(\gamma_1+\gamma_2)}{2}\rho_{r'r} & -\gamma_2\rho_{r'r'} \end{pmatrix}$$

where $\gamma_1 = \Gamma_{rg} + \Gamma_{re}$, $\gamma_2 = \Gamma_{r'g} + \Gamma_{r'r}$ and $\gamma_3 = \Gamma_{rg} + \Gamma_{re} + \Gamma_{eg}$.

Decay from $|r\rangle \rightarrow |g\rangle$ and $|r'\rangle \rightarrow |g\rangle$ is not allowed as the transitions are dipole forbidden. Γ_{eg}, Γ_{re}, $\Gamma_{r'r}$ denote the population decay between the dipole allowed transitions. If an atom in the excited state goes out of the beam, then a new atom enters the ground state. A decay process occurs due to the motion of the atoms through the finite size of the beam, known as transit time decay. The transit time decays are denoted by Γ_{rg} and $\Gamma_{r'g}$, which is taken to be 4.2 MHz. The decay values are $\Gamma_{eg} = 6$ MHz, $\Gamma_{re} = \Gamma_{r'r} = 0.01$ MHz.

In a thermal atomic medium, the atoms move with velocity governed by Maxwell-Boltzmann velocity distribution depending on the temperature of the system. For the same velocity class of atoms and for counter-propagating configuration of the probe and coupling fields, the detuning of the fields are modified as $\Delta_p \rightarrow \Delta_p - k_p v$, $\Delta_c \rightarrow \Delta_c + k_c v$ and $\Delta_\mu \rightarrow \Delta_\mu - k_\mu v$. k_p, k_c, and k_μ are the wave-vectors of the probe, coupling, and microwave field, respectively, and v is the velocity of the atoms. For the closed system, the sum of the population of the states $\rho_{gg} + \rho_{ee} + \rho_{rr} + \rho_{r'r'} = 1$ and for the steady state system $\dot{\rho}_{ij} = 0$.

4.2.2 Perturbative expansion of the density matrix

The Hamiltonian for the system is a time-dependent Hamiltonian that cannot be solved exactly. Hence, a method of perturbative expansion of the density matrix is used to get to the solutions similar to the four-wave mixing process in a two-level system, as discussed in [85]. The density matrix is expanded as

$$\rho_{ij} = \rho_{ij}^{(0)} + \rho_{ij}^{(1)} e^{-i\delta t} + \rho_{ij}^{(-1)} e^{i\delta t} + ... \tag{4.7}$$

$\forall\ i,j$. Here, $\rho_{ij}^{(0)}$ are the 0^{th} order density matrix elements similar to that of a simple four-level system with a probe field, a coupling field, and only the strong microwave field. $\rho_{ij}^{(1)}$ and $\rho_{ij}^{(-1)}$ are the 1^{st} order density matrix elements that come into the picture because of the presence of the second weak microwave field. The higher order terms are neglected. Polarization of the probe field is $P(\omega_p) \propto \rho_{ij}^{(0)}$ whereas the polarization of generated fields $P(\omega_p \pm \delta) \propto \rho_{ij}^{(\pm 1)}$.

As the density matrix is hermitian, $\rho_{ij}^* = \rho_{ji}$. $\implies (\rho_{ij}^* - \rho_{ji}) = 0$
$\implies (\rho_{ij}^{(0)*} - \rho_{ji}^{(0)}) + (\rho_{ij}^{(-1)*} - \rho_{ji}^{(1)})e^{-i\delta t} + (\rho_{ij}^{(1)*} - \rho_{ji}^{(-1)})e^{i\delta t} = 0$,
neglecting the higher order terms. A complete set of orthonormal basis is formed given by [1,$e^{\pm i\delta t}$]. As the basis states are linearly independent, $\rho_{ij}^{(0)*} = \rho_{ji}^{(0)}$, $\rho_{ij}^{(1)*} = \rho_{ji}^{(-1)}$ and $\rho_{ij}^{(-1)*} = \rho_{ji}^{(1)}$. The diagonal elements of the unperturbed density matrix represent the population of the respective states and hence are real. This implies $\rho_{ii}^* = \rho_{ii} \implies \rho_{ii}^{(0)*} = \rho_{ii}^{(0)}$, $\rho_{ii}^{(1)*} = \rho_{ii}^{(-1)}$ and $\rho_{ii}^{(-1)*} = \rho_{ii}^{(1)}$. The diagonal elements for 0^{th} order density matrix are all real, but 1^{st} order diagonal density matrix elements need not be strictly real.

4.2.3 0^{th} order density matrix equations

The optical Bloch equations are written in terms of the expanded density matrix given by Eqn. 4.7. The 0^{th} order optical Bloch equations are derived by equating the coefficients of $e^{-i\delta t}$ with $\delta = 0$ as:

$$\frac{i}{2}(\Omega_p\rho_{eg}^{(0)} - \Omega_p^*\rho_{ge}^{(0)}) + \Gamma_{eg}\rho_{ee}^{(0)} + \Gamma_{rg}\rho_{rr}^{(0)} + \Gamma_{r'g}\rho_{r'r'}^{(0)} = 0 \tag{4.8}$$

$$\frac{i}{2}[-2\Delta_p\rho_{ge}^{(0)} + \Omega_p(2\rho_{ee}^{(0)} + \rho_{rr}^{(0)} + \rho_{r'r'}^{(0)}) - \Omega_p - \Omega_c^*\rho_{gr}^{(0)}] - \frac{\Gamma_{eg}}{2}\rho_{ge}^{(0)} = 0 \tag{4.9}$$

$$\frac{i}{2}[-2\delta_1\rho_{gr}^{(0)} - \Omega_{\mu_1}^*\rho_{gr'}^{(0)} - \Omega_{\mu_2}^*\rho_{gr'}^{(1)} + \Omega_p\rho_{er}^{(0)} - \Omega_c\rho_{ge}^{(0)}] - \frac{\gamma_1}{2}\rho_{gr}^{(0)} = 0 \tag{4.10}$$

$$\frac{i}{2}[-2\delta_2\rho_{gr'}^{(0)} - \Omega_{\mu_1}\rho_{gr}^{(0)} - \Omega_{\mu_2}\rho_{gr}^{(-1)} + \Omega_p\rho_{er'}^{(0)}] - \frac{\gamma_2}{2}\rho_{gr'}^{(0)} = 0 \tag{4.11}$$

$$\frac{i}{2}[\Omega_p^*\rho_{ge}^{(0)} - \Omega_p\rho_{eg}^{(0)} + \Omega_c\rho_{re}^{(0)} - \Omega_c^*\rho_{er}^{(0)}] + \Gamma_{re}\rho_{rr}^{(0)} + \Gamma_{r'e}\rho_{r'r'}^{(0)} - \Gamma_{eg}\rho_{ee}^{(0)} = 0 \tag{4.12}$$

$$\frac{i}{2}[\Omega_p^*\rho_{gr}^{(0)} - 2\Delta_c\rho_{er}^{(0)} - \Omega_{\mu_1}^*\rho_{er'}^{(0)} - \Omega_{\mu_2}^*\rho_{er'}^{(1)} + \Omega_c(\rho_{rr}^{(0)} - \rho_{ee}^{(0)})] - \frac{\gamma_3}{2}\rho_{er}^{(0)} = 0 \tag{4.13}$$

$$\frac{i}{2}[-2\delta_3\rho_{er'}^{(0)} - \Omega_{\mu_1}\rho_{er}^{(0)} - \Omega_{\mu_2}\rho_{er}^{(-1)} + \Omega_p^*\rho_{gr'}^{(0)} + \Omega_c\rho_{rr'}^{(0)}] - \frac{(\Gamma_{eg} + \gamma_2)}{2}\rho_{er'}^{(0)} = 0 \tag{4.14}$$

$$\frac{i}{2}[\Omega_c^*\rho_{er}^{(0)} - \Omega_c\rho_{re}^{(0)} + \Omega_{\mu_1}\rho_{r'r}^{(0)} - \Omega_{\mu_1}^*\rho_{rr'}^{(0)} + \Omega_{\mu_2}\rho_{r'r}^{(-1)} - \Omega_{\mu_2}^*\rho_{rr'}^{(1)}] - \gamma_1\rho_{rr}^{(0)} + \Gamma_{r'r}\rho_{r'r'}^{(0)} = 0 \tag{4.15}$$

$$\frac{i}{2}[\Omega_c^*\rho_{er'}^{(0)} - 2\Delta_\mu\rho_{rr'}^{(0)} - \Omega_{\mu_1}(\rho_{rr}^{(0)} - \rho_{r'r'}^{(0)}) - \Omega_{\mu_2}(\rho_{rr}^{(-1)} - \rho_{r'r'}^{(-1)})] - \frac{(\gamma_1 + \gamma_2)}{2}\rho_{rr'}^{(0)} = 0 \tag{4.16}$$

$$\frac{i}{2}[\Omega_{\mu_1}^*\rho_{rr'}^{(0)} - \Omega_{\mu_1}\rho_{r'r}^{(0)} + \Omega_{\mu_2}^*\rho_{rr'}^{(1)} - \Omega_{\mu_2}\rho_{r'r}^{(-1)}] - \gamma_2\rho_{r'r'}^{(0)} = 0 \tag{4.17}$$

There are some higher order terms such as $\Omega_{\mu_2}^*\rho_{gr'}^{(1)}$, $\Omega_{\mu_2}\rho_{gr}^{(-1)}$, $\Omega_{\mu_2}^*\rho_{er'}^{(1)}$, $\Omega_{\mu_2}\rho_{er}^{(-1)}$, $\Omega_{\mu_2}\rho_{r'r}^{(-1)}$, $\Omega_{\mu_2}^*\rho_{rr'}^{(1)}$, $\Omega_{\mu_2}\rho_{rr}^{(-1)}$, $\Omega_{\mu_2}\rho_{r'r'}^{(-1)}$, $\Omega_{\mu_2}^*\rho_{rr'}^{(1)}$, $\Omega_{\mu_2}\rho_{r'r}^{(-1)}$ which are very small and hence, are neglected. Numerical methods are used to solve the 0^{th} order equations for the strong microwave field to get the ground to excited state coherence. The ground to excited state coherence $\rho_{eg}^{(0)}$ for the thermal atomic medium is computed using Maxwell-Boltzmann velocity distribution as

$$(\rho_{eg}^{(0)})_D = \frac{1}{\sqrt{\pi}v_p}\int_{-\infty}^{+\infty}\rho_{eg}^{(0)}e^{-v^2/v_p^2}dv \tag{4.18}$$

where v_p represents the most probable speed of the atoms. The 0^{th} order optical Bloch equations are the same as the Bloch equations of a simple four-level system with a probe field, a coupling field, and a microwave field. Fig. 4.2 shows the comparison of $(\rho_{eg}^{(0)})_D$ derived from 0^{th} order equations with that from a four-level

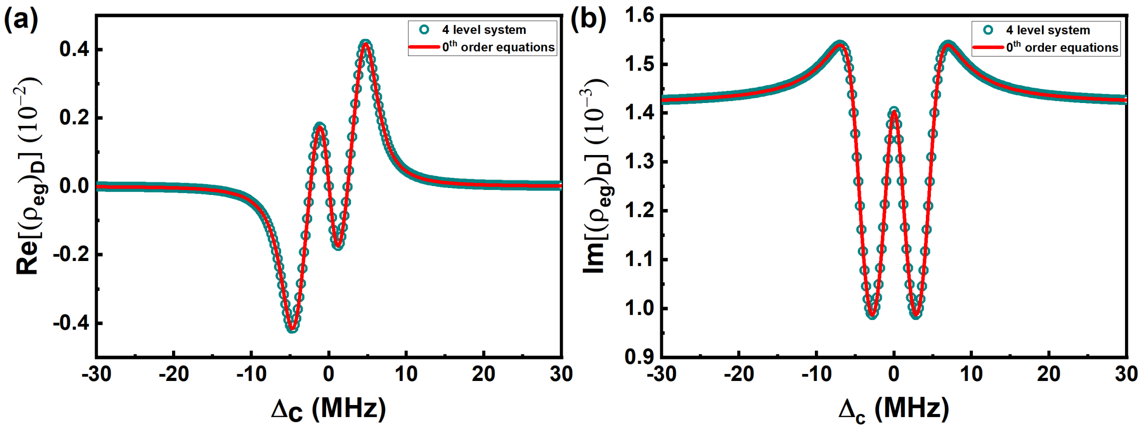

Figure 4.2: Comparison of (a) Real and (b) Imaginary part of $(\rho_{eg}^{(0)})_D$ calculated from 0^{th} order equations with $(\rho_{eg}^{(0)})_D$ calculated from a four-level system. Other parameters are $\Omega_p = 500$ KHz, $\Omega_c = 4$ MHz, $\Omega_\mu = 5$ MHz, $\Gamma_{eg} = 6$ MHz, $\Gamma_{re} = 10$ KHz, $\Gamma_{rg} = 100$ KHz, $\Gamma_{r'g} = 10$ KHz, $\Gamma_{r'r} = 100$ KHz, $\Delta_p = 0$ and $\Delta_\mu = 0$. The density of the atoms is 1.7×10^{10} cm^{-3}.

system where it is observed that the real and imaginary parts of $(\rho_{eg}^{(0)})_D$ match perfectly for both the systems.

4.2.4 1^{st} order density matrix equations

The 1^{st} order optical Bloch equations are derived from the coefficients of $e^{-i\delta t}$ and $e^{i\delta t}$. Here, the first set of equations is derived from the coefficients of $e^{-i\delta t}$ and are represented as:

$$\begin{aligned}\frac{i}{2}(\Omega_p\rho_{eg}^{(+1)} - \Omega_p^*\rho_{ge}^{(+1)}) + \Gamma_{eg}\rho_{ee}^{(+1)} + \Gamma_{rg}\rho_{rr}^{(+1)} + \Gamma_{r'g}\rho_{r'r'}^{(+1)} = \\ i\delta(\rho_{ee}^{(+1)} + \rho_{rr}^{(+1)} + \rho_{r'r'}^{(+1)})\end{aligned} \tag{4.19}$$

$$\frac{i}{2}[-2\Delta_p\rho_{ge}^{(+1)} + \Omega_p(2\rho_{ee}^{(+1)} + \rho_{rr}^{(+1)} + \rho_{r'r'}^{(+1)}) - \Omega_c^*\rho_{gr}^{(+1)}] - \frac{\Gamma_{eg}}{2}\rho_{ge}^{(+1)} = -i\delta\rho_{ge}^{(+1)} \tag{4.20}$$

$$\frac{i}{2}[-2\delta_1\rho_{gr}^{(+1)} - \Omega_{\mu_1}^*\rho_{gr'}^{(+1)} + \Omega_p\rho_{er}^{(+1)} - \Omega_c\rho_{ge}^{(+1)}] - \frac{\gamma_1}{2}\rho_{gr}^{(+1)} = -i\delta\rho_{gr}^{(+1)} \tag{4.21}$$

$$\frac{i}{2}[-2\delta_2\rho_{gr'}^{(+1)} - \Omega_{\mu_1}\rho_{gr}^{(+1)} - \Omega_{\mu_2}\rho_{gr}^{(0)} + \Omega_p\rho_{er'}^{(+1)}] - \frac{\gamma_2}{2}\rho_{gr'}^{(+1)} = -i\delta\rho_{gr'}^{(+1)} \tag{4.22}$$

$$\frac{i}{2}[2\Delta_p\rho_{ge}^{(+1)} - \Omega_p^*(2\rho_{ee}^{(+1)} + \rho_{rr}^{(+1)} + \rho_{r'r'}^{(+1)}) + \Omega_c\rho_{rg}^{(+1)}] - \frac{\Gamma_{eg}}{2}\rho_{eg}^{(+1)} = -i\delta\rho_{eg}^{(+1)} \tag{4.23}$$

$$\frac{i}{2}[\Omega_p^*\rho_{ge}^{(+1)} - \Omega_p\rho_{eg}^{(+1)} + \Omega_c\rho_{re}^{(+1)} - \Omega_c^*\rho_{er}^{(+1)}] + \Gamma_{re}\rho_{rr}^{(+1)} + \Gamma_{r'e}\rho_{r'r'}^{(+1)} - \Gamma_{eg}\rho_{ee}^{(+1)} = -i\delta\rho_{ee}^{(+1)} \tag{4.24}$$

$$\frac{i}{2}[\Omega_p^*\rho_{gr}^{(+1)} - 2\Delta_c\rho_{er}^{(+1)} - \Omega_{\mu_1}^*\rho_{er'}^{(+1)} + \Omega_c(\rho_{rr}^{(+1)} - \rho_{ee}^{(+1)})] - \frac{\gamma_3}{2}\rho_{er}^{(+1)} = -i\delta\rho_{er}^{(+1)} \tag{4.25}$$

$$\frac{i}{2}[-2\delta_3\rho_{er'}^{(+1)} - \Omega_{\mu_1}\rho_{er}^{(+1)} - \Omega_{\mu_2}\rho_{er}^{(0)} + \Omega_p^*\rho_{gr'}^{(+1)} + \Omega_c\rho_{rr'}^{(+1)}] - \frac{(\Gamma_{eg}+\gamma_2)}{2}\rho_{er'}^{(+1)} = -i\delta\rho_{er'}^{(+1)} \tag{4.26}$$

$$\frac{i}{2}[2\delta_1\rho_{rg}^{(+1)} + \Omega_{\mu_1}\rho_{r'g}^{(+1)} + \Omega_{\mu_2}\rho_{r'g}^{(0)} - \Omega_p^*\rho_{re}^{(+1)} + \Omega_c^*\rho_{eg}^{(+1)}] - \frac{\gamma_1}{2}\rho_{rg}^{(+1)} = -i\delta\rho_{rg}^{(+1)} \tag{4.27}$$

$$\frac{i}{2}[-\Omega_p\rho_{rg}^{(+1)} + 2\Delta_c\rho_{re}^{(+1)} + \Omega_{\mu_1}\rho_{r'e}^{(+1)} + \Omega_{\mu_2}\rho_{r'e}^{(0)} + \Omega_c^*(\rho_{ee}^{(+1)} - \rho_{rr}^{(+1)})] - \frac{\gamma_3}{2}\rho_{re}^{(+1)} = -i\delta\rho_{re}^{(+1)} \tag{4.28}$$

$$\frac{i}{2}[\Omega_c^*\rho_{er}^{(+1)} - \Omega_c\rho_{re}^{(+1)} + \Omega_{\mu_1}\rho_{r'r}^{(+1)} - \Omega_{\mu_1}^*\rho_{rr'}^{(+1)} + \Omega_{\mu_2}\rho_{r'r}^{(0)}] - \gamma_1\rho_{rr}^{(+1)} + \Gamma_{r'r}\rho_{r'r'}^{(+1)} = -i\delta\rho_{rr}^{(+1)} \tag{4.29}$$

$$\frac{i}{2}[\Omega_c^*\rho_{er'}^{(+1)} - 2\Delta_\mu\rho_{rr'}^{(+1)} - \Omega_{\mu_1}(\rho_{rr}^{(+1)} - \rho_{r'r'}^{(+1)}) - \Omega_{\mu_2}(\rho_{rr}^{(0)} - \rho_{r'r'}^{(0)})] - \frac{(\gamma_1+\gamma_2)}{2}\rho_{rr'}^{(+1)} = -i\delta\rho_{rr'}^{(+1)} \tag{4.30}$$

$$\frac{i}{2}[2\delta_2\rho_{r'g}^{(+1)} + \Omega_{\mu_1}^*\rho_{rg}^{(+1)} - \Omega_p^*\rho_{r'e}^{(+1)}] - \frac{\gamma_2}{2}\rho_{r'g}^{(+1)} = -i\delta\rho_{r'g}^{(+1)} \tag{4.31}$$

$$\frac{i}{2}[2\delta_3\rho_{r'e}^{(+1)} + \Omega_{\mu_1}^*\rho_{re}^{(+1)} - \Omega_p\rho_{r'g}^{(+1)} - \Omega_c^*\rho_{r'r}^{(+1)}] - \frac{(\Gamma_{eg}+\gamma_2)}{2}\rho_{r'e}^{(+1)} = -i\delta\rho_{r'e}^{(+1)} \tag{4.32}$$

$$\frac{i}{2}[-\Omega_c\rho_{r'e}^{(+1)} + 2\Delta_\mu\rho_{r'r}^{(+1)} + \Omega_{\mu_1}^*(\rho_{rr}^{(+1)} - \rho_{r'r'}^{(+1)})] - \frac{(\gamma_1+\gamma_2)}{2}\rho_{r'r}^{(+1)} = -i\delta\rho_{r'r}^{(+1)} \tag{4.33}$$

$$\frac{i}{2}[\Omega_{\mu_1}^*\rho_{rr'}^{(+1)} - \Omega_{\mu_1}\rho_{r'r}^{(+1)} - \Omega_{\mu_2}\rho_{r'r}^{(0)}] - \gamma_2\rho_{r'r'}^{(+1)} = -i\delta\rho_{r'r'}^{(+1)} \tag{4.34}$$

In a similar manner, the coefficients of $e^{i\delta t}$ provide the other set of equations. First, the zeroth order equations are solved for atoms at rest. The solutions of the zeroth order equations are substituted into the first order equations, which are then solved numerically for atoms at rest. The first order ground to excited state coherence $\rho_{eg}^{(+1)}$ and $\rho_{eg}^{(-1)}$ correspond to the fields generated at $(\omega_p + \delta)$ and $(\omega_p - \delta)$ respectively.

$\rho_{eg}^{(\pm1)}$ is used to find the Doppler averaged susceptibility of the probe for the thermal atoms as

$$\chi^{(5)}_{eff}(\omega_p \pm \delta) = \frac{N \mid \mu_{ge} \mid}{\epsilon_0 E_p E_c^2 E_{\mu_1} E_{\mu_2} \sqrt{2\pi} v_p} \int_{-\infty}^{+\infty} \rho_{eg}^{(\pm1)} e^{-v^2/2v_p^2} dv \tag{4.35}$$

where N is the vapor density.

4.3 Experimental details

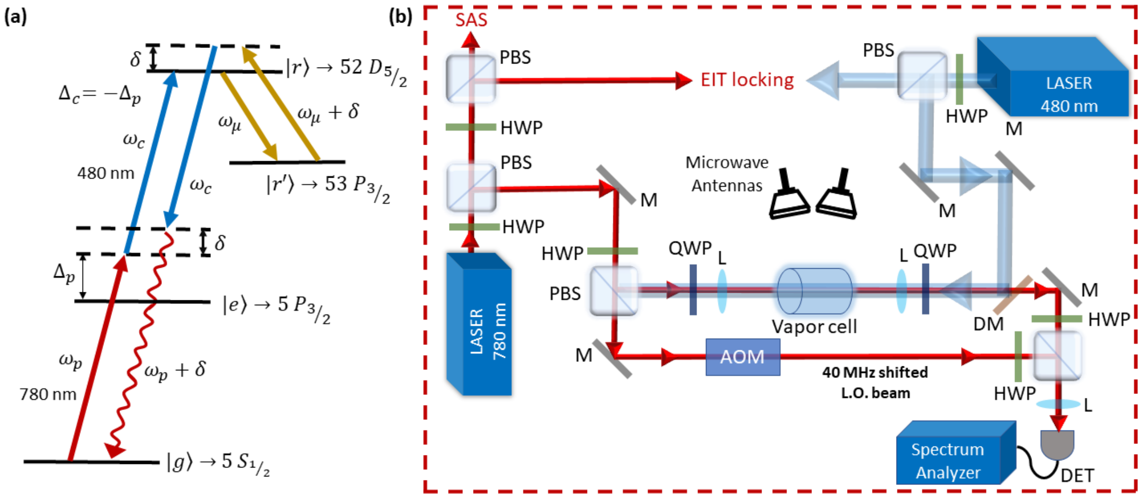
(a)
(b)
δ
$\Delta_c = -\Delta_p$
ω_c
480 nm
ω_μ
$\omega_\mu + \delta$
ω_c
$|r\rangle \rightarrow 52\,D_{5/2}$
$|r'\rangle \rightarrow 53\,P_{3/2}$
δ
Δ_p
$|e\rangle \rightarrow 5\,P_{3/2}$
ω_p
780 nm
$\omega_p + \delta$
$|g\rangle \rightarrow 5\,S_{1/2}$
SAS
PBS
EIT locking
PBS
LASER 480 nm
HWP
M
HWP
PBS
Microwave Antennas
M
M
HWP
HWP
QWP
L
L
QWP
PBS
M
LASER 780 nm
Vapor cell
DM
HWP
M
AOM
40 MHz shifted L.O. beam
HWP
L
Spectrum Analyzer
DET

Figure 4.3: (a) Schematic of energy levels of rubidium. (b) Experimental set-up. HWP: Half-wave plate, PBS: Polarizing beam splitter, QWP: Quarter-wave plate, M: Mirror, L: Lens, DM: Dichroic mirror, AOM: Acousto-optic modulator, L.O.: Local oscillator, and DET: Photo-detector.

Fig. 4.3(a) shows the schematic of energy levels of rubidium used for the experiment and (b) shows the optical set-up for the experiment. An ECDL (TOPTICA DL PRO) at 780 nm is used to derive the probe beam (ω_p). The probe laser frequency is stabilized using the SAS frequency locking technique discussed in Sec. 2.6.1. The probe frequency is detuned by 1.2 GHz from the $^{85}Rb\ 5S_{\frac{1}{2}} F = 3 \rightarrow 5P_{\frac{3}{2}}$ transition ($\Delta_p = 1.2$ GHz). As the probe is largely detuned away from resonance, the probe absorption is considered to be negligible. The probe beam has $\frac{1}{e}$ radius of w_p=32.3 μm, and the rabi frequency of the probe is calculated to be $\Omega_p = \Gamma_{eg}\sqrt{\frac{I_p}{2I_{sat}}} = 283$

MHz. I_p is the intensity of the probe field, and $I_{sat} = 1.67$ mW/cm^2 is the saturation intensity for circularly polarized light. A frequency doubling cavity laser (TOPTICA TA-SHG PRO) is used to generate the coupling beam (ω_c) at 480 nm. The coupling laser frequency is stabilized using the EIT locking technique discussed in Sec. 2.6.2. The coupling beam has $\frac{1}{e}$ radius of w_c=63.2 μm, and the rabi frequency is calculated to be $\Omega_c = \Gamma_{re}\sqrt{\frac{I_c}{2I_{sat}}} = 2$ MHz where I_c is the intensity of the coupling field. A dichroic mirror is used to reflect the coupling beam and transmit the probe to make the coupling beam counter propagate the probe beam. The probe and coupling beam is focused at the center of the rubidium vapor cell, of length l, through lenses of a focal length of 10 cm. The probe and coupling field satisfy the two-photon resonance condition to the Rydberg state $|r\rangle$ while scanning the coupling frequency. The probe beam is made right circularly polarized, and the coupling beam is made left circularly polarized using quarter-wave plates for efficient coupling to the Rydberg state. The probe beam is detected using a photodetector. Two synchronized microwave signal generators are used for the two microwave fields. The microwave fields are applied through two horn antennas placed at a distance of 32 cm from the center of the vapor cell. The microwave fields travel along the horizontal plane through the center of the vapor cell, and these fields are linearly polarized. The first microwave field (ω_μ) is applied at a resonance frequency of 15.0895 GHz, which couples the Rydberg state $|r\rangle$ to another nearby Rydberg state $|r'\rangle$. The second microwave field ($\omega_\mu + \delta$) is applied between the same Rydberg states where δ is the frequency difference between the two microwave fields, also called the beat frequency. The first microwave field is a strong field and the second microwave field is weak as compared to the first microwave field, i.e., $\Omega_{\mu_2} \ll \Omega_{\mu_1}$. The vapor cell is heated to 100 °C to maintain the atomic density at 6 × 10^{12} cm^{-3}.

4.3.1 Optical heterodyne detection

The generation of a new optical field due to the six-wave mixing process is observed through the optical heterodyne detection technique (OHDT). For OHDT, an addi-

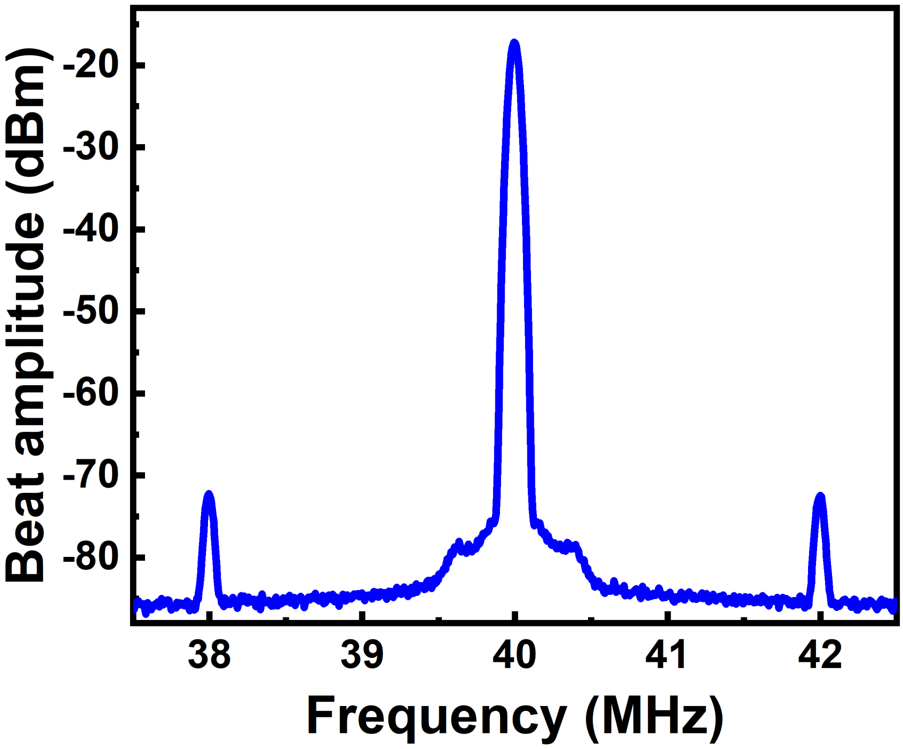

Figure 4.4: Spectrum analyzer signal showing 40 MHz beat signal along with two side bands for $\delta = 2$ MHz.

tional field is used, which is derived from the probe beam. The derived beam is shifted by 40 MHz using acousto-optic modulators (AOM), as shown in Fig. 4.3(b), and is called the local oscillator (L.O.) field. The L.O. field has a frequency $\omega_p + 40$ MHz. A PBS is used to interfere the L.O. field with the probe field. A polarizer is used to optimize the interference of the fields. The two fields interfere to generate a beat signal at 40 MHz. Since the fields generated due to the six-wave mixing phenomenon at $(\omega_p \pm \delta)$ travel along the same direction as the probe field (ω_p), they also interfere with the L.O. field. This interference results in beat signal at (40 MHz + δ) and (40 MHz - δ). Fig. 4.4 shows the spectrum analyzer signal with 40 MHz beat signal and beat signals at 38 MHz and 42 MHz for $\delta = 2$ MHz. Thus, we have two frequency components generated at $(\omega_p + \delta)$ and $(\omega_p - \delta)$ which correspond to coherence terms $\rho_{eg}^{(+1)}$ and $\rho_{eg}^{(-1)}$ respectively. The experimental parameters are: $\Omega_p = 283$ MHz, $\Omega_c = 2$ MHz, $\Omega_{\mu_1} = 80$ MHz and $\Omega_{\mu_2} = 40$ MHz, $\Delta_p = 1.2$ GHz, $\Delta_c = -1.2$ GHz, and $\Delta_\mu = 0$.

4.3.2 Beat signal at δ

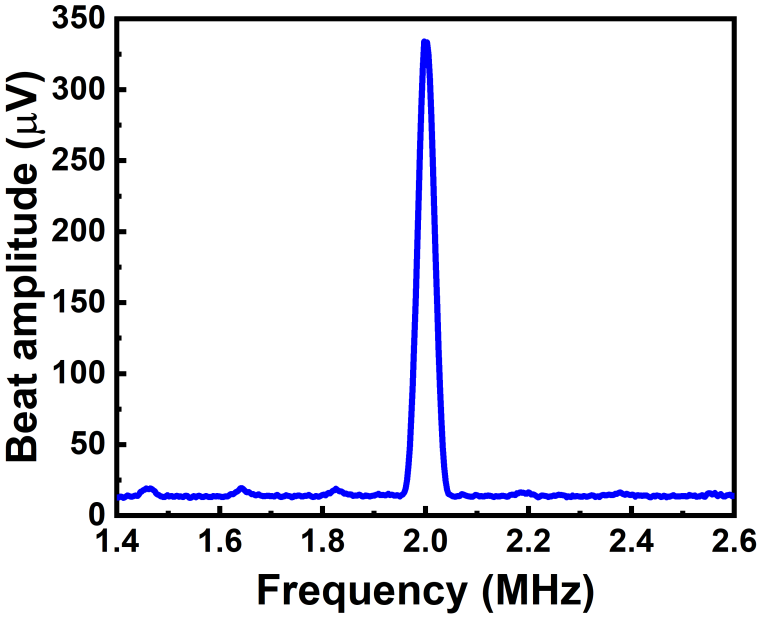

Figure 4.5: Beat signal at the spectrum analyzer for $\delta = 2$ MHz.

It is understood that the generated optical field $(\omega_p \pm \delta)$ interferes with the probe field (ω_p). The interference of $(\omega_p + \delta)$ with ω_p and $(\omega_p - \delta)$ with ω_p, both contribute to the interference signal or beat signal at frequency δ. For the rest of the experiment, the L.O. field is switched off, and the beat signal at δ is observed, which is shown in Fig. 4.5.

4.4 Microwave-to-optical conversion efficiency

The microwave-to-optical conversion efficiency is calculated from the formula [82] given below:

$$\eta = \frac{P_{(\omega_p \pm \delta)}/\hbar(\omega_p \pm \delta)}{I_{(\omega_\mu + \delta)} S/\hbar(\omega_\mu + \delta)}. \tag{4.36}$$

$P_{(\omega_p \pm \delta)}$ is the measured power of the generated optical field due to the six-wave mixing process. $I_{(\omega_\mu + \delta)}$ is the intensity of the microwave field which is being experienced by the atoms. S is the interacting area of the microwave field and atomic medium given by $S = l \times 2w_p$. $P_{(\omega_p \pm \delta)}$ is calculated from the heterodyne signal observed in Fig. 4.4 and is found to be 74.75×10^{-5} μW for $\delta = 2$ MHz. The microwave field strength experienced by the atoms, measured by observing the splitting of the EIT signal, is measured experimentally to be 0.94 V/m. It is then used to calculate $I_{(\omega_\mu + \delta)} = 11.8 \times 10^{-4}$ W/m^2. The microwave-to-optical conversion efficiency is found to be $\eta \sim 7.5 \times 10^{-6}$ for $\delta = 2$ MHz. Fig. 4.6 shows the microwave-to-optical conversion efficiency for three different δ.

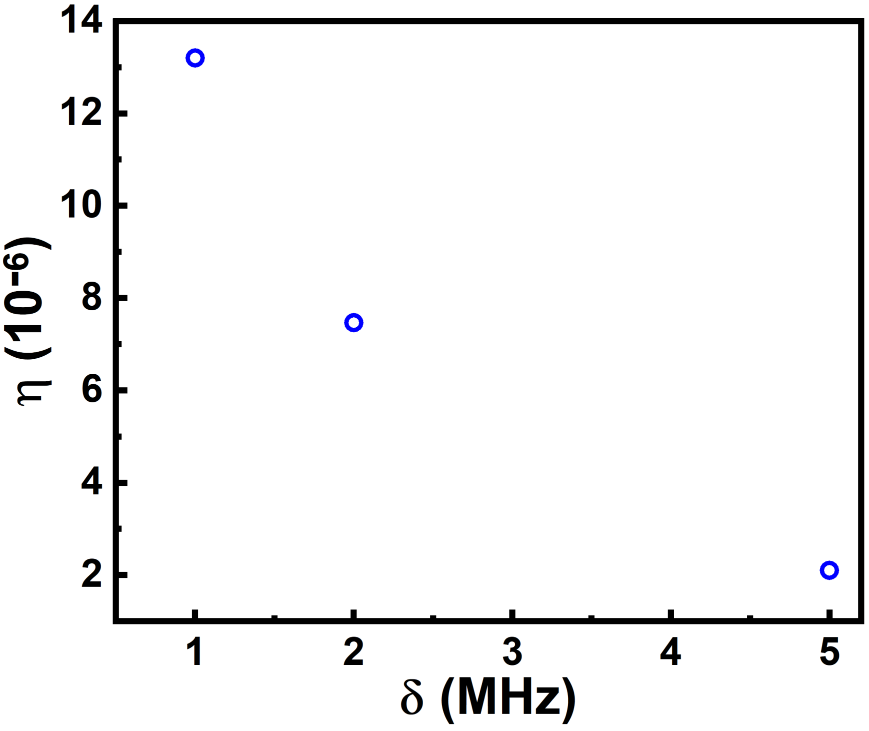

Figure 4.6: Microwave-to-optical conversion efficiency for different δ.

4.5 Strength of the δ beat signal

Both the frequency components at $(\omega_p + \delta)$ and $(\omega_p - \delta)$ constructively contribute to the δ beat signal, whose strength is found by looking at the electric fields of the probe and the generated fields. As discussed earlier, the probe field is expressed as

$$E'_p = E_p e^{-i\omega_p t} \tag{4.37}$$

and the generated fields are similarly expressed as

$$E_{p'}^{+} = E_{+1}e^{-i((\omega_p+\delta)t+\phi_1)} \tag{4.38}$$

$$E_{p'}^{-} = E_{-1}e^{-i((\omega_p-\delta)t+\phi_2)} \tag{4.39}$$

where $E_{\pm 1}$ are the complex amplitudes of the generated fields. ϕ_1 and ϕ_2 are the phase acquired by the generated fields due to the six-wave mixing process, which are very small. The light intensity resulting from the interference of the probe field with the generated fields is given by

$$\begin{aligned}(E_pe^{-i\omega_pt} + E_{+1}e^{-i((\omega_p+\delta)t+\phi_1)} + E_{-1}e^{-i((\omega_p-\delta)t+\phi_2)})(E_pe^{-i\omega_pt}+\\ E_{+1}e^{-i((\omega_p+\delta)t+\phi_1)} + E_{-1}e^{-i((\omega_p-\delta)t+\phi_2)})^*\\ = |E_p|^2 + |E_{+1}|^2 + |E_{-1}|^2 + 2E_pE_{+1}\cos(\delta t+\phi_1)\\ +2E_pE_{-1}\cos(\delta t-\phi_2) + 2E_{+1}E_{-1}\cos(2\delta t+\phi_1-\phi_2)\end{aligned} \tag{4.40}$$

The first three terms are d.c. intensity terms where the first term is due to the probe field, and the second and third terms are due to the generated field. The fourth and fifth terms represent the intensity due to interference of the probe field with the generated field. The last term is the higher harmonics term, which occurs due to the interference of the generated fields. The beat signal is represented as $A_0\cos(\delta t+\phi)$. If $A_0\cos(\delta t+\phi)$ is compared with the terms containing the interference of the probe and the generated field, i.e., $2E_pE_{+1}\cos(\delta t+\phi_1) + 2E_pE_{-1}\cos(\delta t-\phi_2)$, it is found that

$$A_0 = \frac{2E_pE_{+1}\sin(\phi_1+\phi_2)}{\sin(\phi+\phi_2)} = \frac{2E_pE_{-1}\sin(\phi_1+\phi_2)}{\sin(\phi_1-\phi)}; \tag{4.41}$$

$$\phi = \frac{E_{+1}\phi_1 - E_{-1}\phi_2}{E_{+1}+E_{-1}}. \tag{4.42}$$

The strength of the beat signal is directly proportional to the electric field amplitude of the probe and the generated fields. They also depend on the phases acquired by the generated fields due to the $\chi^{(5)}$ process.

4.6 Wave propagation equations

To model the experimental results, the wave propagation equations [85] are solved for the generated fields. The system is studied under conditions of perfect phase matching, i.e., $\Delta k = 0$. The slowly varying amplitudes $E_{\pm 1}$ follow the equations as given below:

$$\frac{dE_{\pm 1}}{dz} = -\alpha_{\pm 1} E_{\pm 1} + \kappa_{\pm 1}. \tag{4.43}$$

Here, the non-linear absorption in the medium is given by

$$\alpha_{\pm 1} = -\frac{k_{\pm 1}}{2} Im(\chi^{(1)}) \tag{4.44}$$

and the non-linear coupling coefficients are

$$\kappa_{\pm 1} = -i \frac{3}{2} \frac{k_{\pm 1}}{n_{\pm 1}^2} \chi_{eff}^{(5)}(\omega_p \pm \delta) E_p E_c^2 E_{\mu_1} E_{\mu_2}. \tag{4.45}$$

The non-linear coupling coefficients corresponding to the generated frequencies contain the susceptibility due to the six-wave mixing process. E_p, E_c, E_{μ_1} and E_{μ_2} denote the complex electric field amplitudes of the probe field, coupling field, strong microwave field, and weak microwave field respectively which are kept constant during the experiment. $k_{\pm 1}$ denotes the propagation constant of the generated fields, and $n_{\pm 1}$ denotes the real part of the refractive index experienced by these fields. As the probe is largely detuned from resonance, i.e., $\Delta_p = 1.2$ GHz, the probe absorption and hence, the absorption of the generated field is negligible. $\chi^{(1)}$ represents the effective linear susceptibility, and $\chi_{eff}^{(5)}$ represents the effective fifth-order susceptibility due to the six-wave mixing process.

The wave propagation equations for the generated fields are solved to find out the solution as

$$E_{\pm 1} = \frac{\kappa_{\pm 1}}{\alpha_{\pm 1}} (1 - e^{-\alpha_{\pm 1} l}). \tag{4.46}$$

Since the probe is far detuned (1.2 GHz) away from resonance, the absorption of the probe and generated field can be neglected, i.e., $\alpha_{\pm1} = 0$. Using Taylor's expansion of $e^{-\alpha_{\pm1}l}$ and keeping the first order terms, the solution is given as

$$E_{\pm1} = \kappa_{\pm1} l \tag{4.47}$$

where l is the length of the vapor cell. From the above equation, it is obvious that the amplitude of the generated field is directly proportional to $\kappa_{\pm1}$. The total amplitude of the beat signal is given by Eqn. 4.41, which is used to model the experimental results.

4.7 Observations

4.7.1 Beat signal strength as a function of δ

The beat spectrum due to interference of the generated optical field with the probe field is studied as a function of δ. With the strong microwave field (ω_μ) on resonance, i.e., $\Delta_\mu = 0$, the beat frequency is varied by scanning the weak microwave field ($\omega_\mu + \delta$). It is observed that the strength of the generated beat signal is maximum when the weak microwave field is near the resonance ($\delta \sim 0$). The beat strength decreases as the weak microwave field is scanned away from resonance. The generation spectrum is shown in Fig. 4.7 with FWHM of $\sim$ 17 MHz. A qualitative agreement is observed between the experimental results and the theoretical model. The theoretically generated spectrum is symmetric around the resonance. But the experimental plot is broader along the left side of the spectrum. This is attributed to the fact that there is the contribution from another nearby Rydberg state or the fine structure state $|52D_{\frac{3}{2}}\rangle$ which is lying at around 80 MHz away from $|52D_{\frac{5}{2}}\rangle$ state. This is not taken into account in the theoretical model. Also, there are small features at $\delta = \pm 80$ MHz around the main peak. This is due to the formation of dressed states by the strong microwave field with Rabi frequency $\Omega_{\mu_2} = 80$ MHz, which is discussed in detail in the next section. The bandwidth of the generation

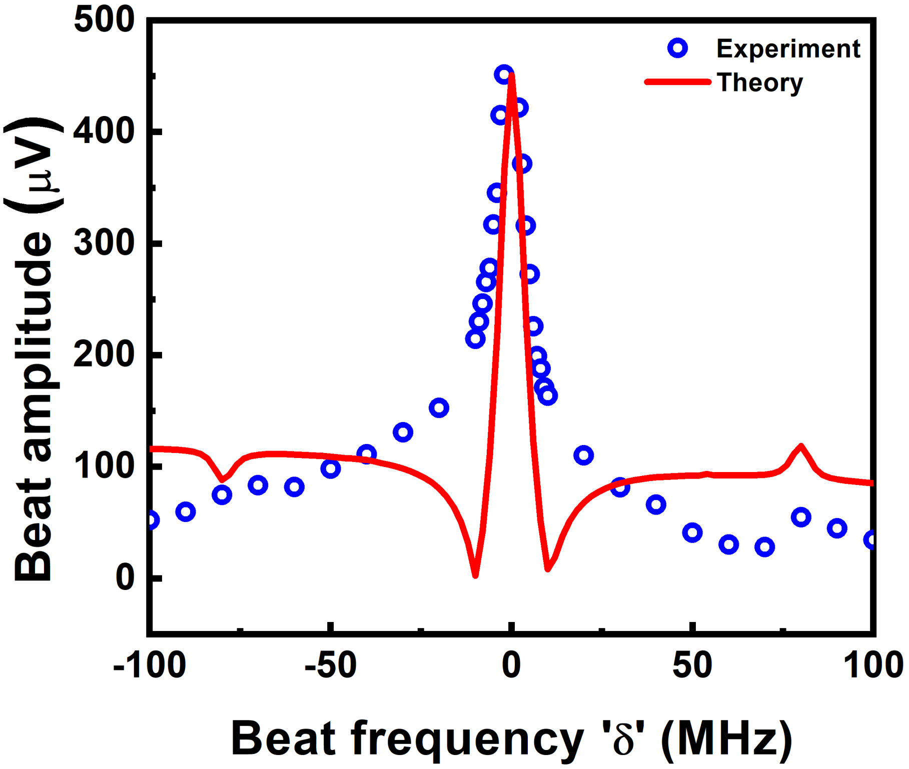

Figure 4.7: Beat signal amplitude with varying δ. Experimental parameters used are: $\Omega_p = 283$ MHz, $\Omega_c = 2$ MHz, $\Omega_{\mu_1} = 80$ MHz and $\Omega_{\mu_2} = 40$ MHz, $\Delta_p = 1.2$ GHz, $\Delta_c = -1.2$ GHz and $\Delta_\mu = 0$.

spectrum and the strength of the generated optical field are not fundamentally limited. Instead, it is limited by the available coupling power. With a larger available coupling Rabi frequency, larger bandwidth can be achieved, which will be discussed in the later sections.

4.7.2 Dressed state formation due to strong microwave field

The formation of two small features at $\delta = \pm$ 80 MHz can be explained with a dressed state picture as discussed in Sec. 2.2.2. When the strong dressing microwave field is on resonance, the frequency difference between the dressed states is equal to the Rabi frequency of the dressing field, and the dressed states are equally spaced away from the resonance. The formation of the dressed states depends on the Rabi frequency of the strong microwave field, which is $\Omega_{\mu_1} = 80$ MHz. As shown in Fig.

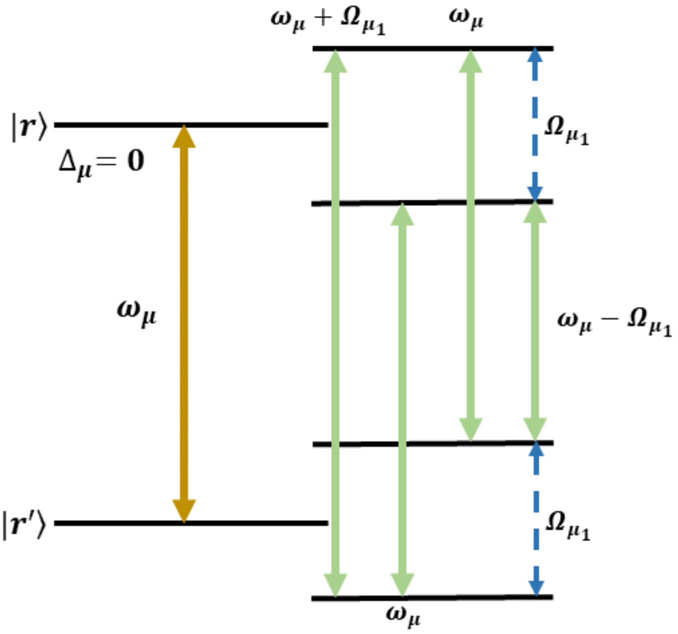

Figure 4.8: Schematic of dressed state picture due to the strong microwave field (ω_μ) with Rabi frequency Ω_{μ_1}.

4.8, the strong microwave field splits the states such that we have four probabilities. When the weak microwave field is scanned, we observe three peaks. Two possible transitions correspond to strong microwave field frequency ω_{μ_1}. They give rise to the main peak at around $\delta = 0$. The transition corresponding to frequency $(\omega_\mu + \Omega_{\mu_1})$ gives rise to the small feature at $\delta = 80$ MHz and the transition corresponding to frequency $(\omega_\mu - \Omega_{\mu_1})$ gives rise to the feature at $\delta = -80$ MHz.

4.7.3 Beat strength as a function of Ω_p

The generated optical field increases with an increase in the Rabi frequency of the probe field, as shown in Fig. 4.9. It shows the beat signal amplitude's dependence on the probe field's power.The x-axis in the plot is the peak Rabi frequency at the center of the cell. The observed beat amplitude corresponding to each peak Rabi frequency is an average effect due to the different Rabi frequencies over the length of the cell. Hence, instead of using the model to fit the data a polynomial function is used. It follows the polynomial function $y = a_1x + a_2x^3 + a_3x^5 + ...$ which is represented

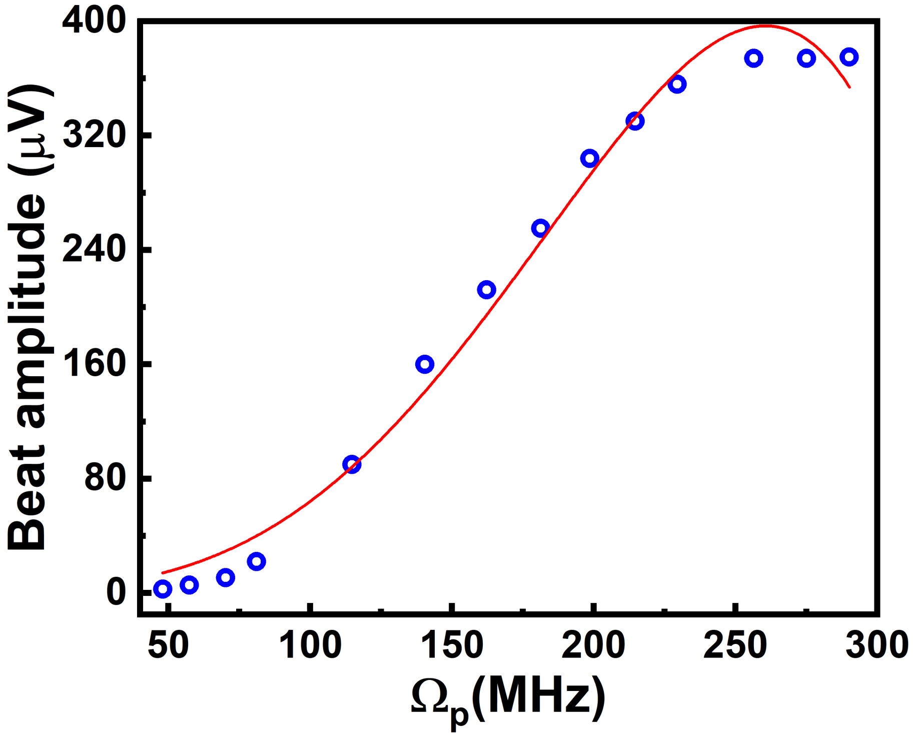

Figure 4.9: Beat signal amplitude with varying Ω_p for fixed $\delta = 10$ MHz. Blue open circles are the experimental data and red line is a fit to the polynomial $y = a_1x + a_2x^3 + a_3x^5$ with $a_1 = 0.18 \pm 0.11$, $a_2 = 5.07E - 5 \pm 4.85E - 6$, and $a_3 = -4.56E - 10 \pm 4.69E - 11$. Other experimental parameters used are: $\Omega_p = 283$ MHz, $\Omega_c = 2$ MHz, $\Omega_{\mu_1} = 80$ MHz and $\Omega_{\mu_2} = 40$ MHz, $\Delta_p = 1.2$ GHz, $\Delta_c = -1.2$ GHz, and $\Delta_\mu = 0$.

by red line. a_1 corresponds to the contribution due to the $\chi^{(5)}$ process, whereas a_3 and a_5 are contribution due to the higher order $\chi^{(7)}$ and $\chi^{(9)}$ processes respectively. After certain values of Ω_p, the beat amplitude does not increase with the increase in probe power; it saturates due to the higher order nonlinear processes. For the rest of the experiment, the probe power is fixed at the value where the maximum beat strength is observed.

4.7.4 Beat strength as a function of Δ_μ

We also study the newly generated optical field as a function of the detuning of the microwave fields from the atomic resonance. We detune the microwave fields away from the atomic resonance by varying Δ_μ and keep the frequency difference

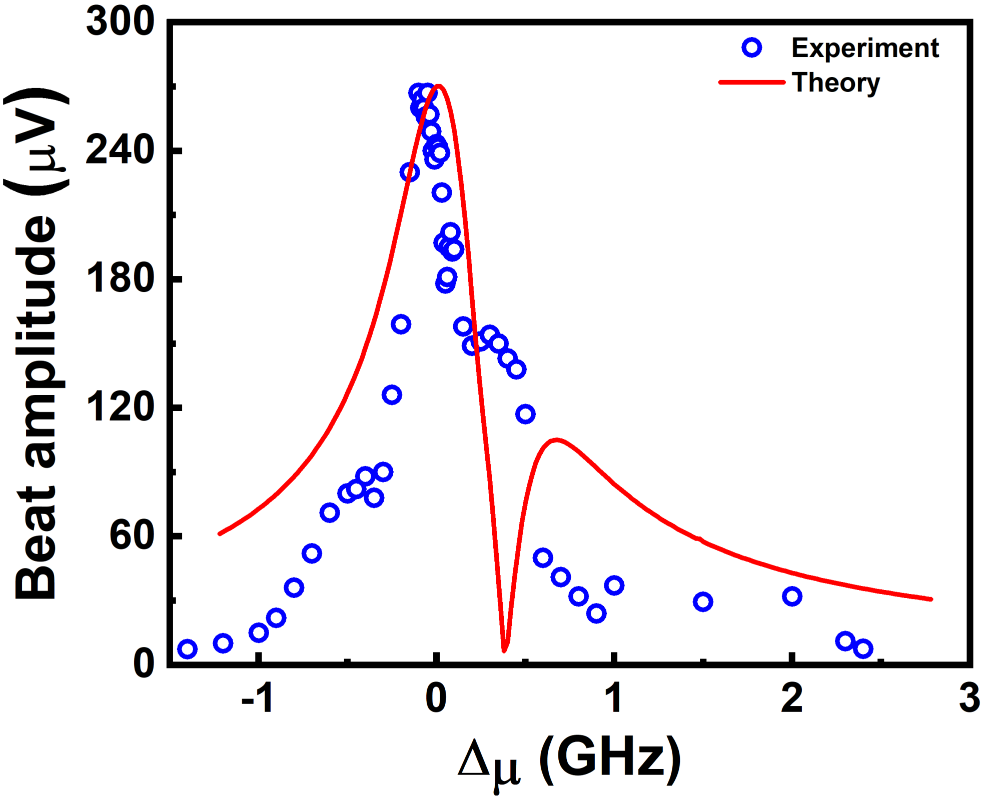

Figure 4.10: Beat signal amplitude with varying Δ_μ for fixed $\delta = 5$ MHz. Other experimental parameters used are: $\Omega_p = 283$ MHz, $\Omega_c = 2$ MHz, $\Omega_{\mu_1} = 80$ MHz and $\Omega_{\mu_2} = 40$ MHz, $\Delta_p = 1.2$ GHz, and $\Delta_c = -1.2$ GHz.

between the microwave fields fixed at $\delta = 5$ MHz. We observe the generation of the new optical field in a wide frequency band with an FWHM of nearly 400 MHz, as shown in Fig. 4.10. The experimental plot and the theoretically generated data qualitatively agree with each other. The extra features in the experimental plot are due to the nearby fine structure Rydberg state $|52D_{\frac{3}{2}}\rangle$ lying nearby, which have not been accounted for in the theoretical model. In all these experiments, we have ignored the reflections of the microwave from the surface of the optical table and from the surface of the vapor cell.

4.7.5 E-field strength of weak microwave field in free space

When the microwave field is radiated from the horn antenna, it travels in free space to interact with the atomic medium. To understand the dependence of beat strength on the power of the weak microwave field, its electric field strength in free space is needed to be known. This calculation is valid for a far-field region where the wave is assumed to be a spherical wave. Let P_o be the power output from the microwave source. A horn antenna radiates this power with a gain of G in dB. As the waves travel in free space, they spread out like spheres of increasing radius. At distances far away from the antenna, i.e., in the far-field region, the wavefronts are approximated to be spheres, and the source is considered a point source. The radius of the sphere increases with the square of the distance d^2. The total power carried by the wave doesn't change but keeps on spreading on larger surfaces. Hence, the power density has $\frac{1}{d^2}$ dependence. The power density at a given distance d is

$$S = g\frac{P_o}{4\pi d^2} \tag{4.48}$$

where g is the gain that gives the measure of the antenna's ability to give direction to the radiated power. g is found from the relation $G = 10\log_{10}(g)$. S is also called the Poynting vector. The relation between the Poynting vector and the strength of the electric field is given by

$$S = \frac{E^2}{Z_0} \tag{4.49}$$

where Z_0=377 Ω is the characteristic impedance of the vacuum. The above relation is used to find out the electric field strength of the weak microwave field.

4.7.6 Dependence of the beat strength on weak microwave power

The dependence of the beat strength on the power of the weak microwave field is studied by increasing the power of the weak microwave field and recording the amplitude of the beat signal. From the microwave source's output power, the weak microwave field's electric field strength is calculated as discussed in the previous section. Here, the antennas are placed at a distance of 32 cm from the atomic vapor cell; hence, the calculation is done considering the far-field regime. A linear

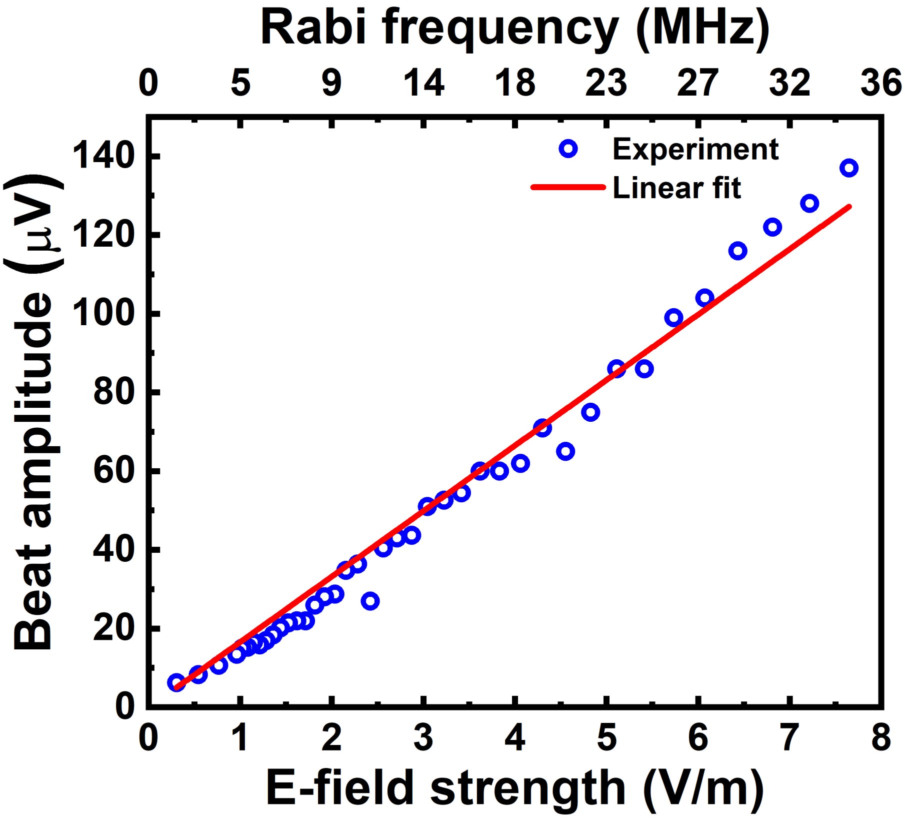

Figure 4.11: Beat signal amplitude with increasing weak microwave field strength at $\delta = 10$ MHz. Other experimental parameters used are: $\Omega_p = 283$ MHz, $\Omega_c = 2$ MHz, $\Omega_{\mu_1} = 80$ MHz, $\Delta_p = 1.2$ GHz, $\Delta_c = -1.2$ GHz and $\Delta_\mu = 0$.

increase is observed in the beat strength with increasing microwave field strength, as shown in Fig. 4.11. This linear increase is expected from the wave propagation equations where $E_{\pm 1} \propto \kappa_{\pm 1} \propto E_{\mu_2}$. The experimental data is fitted with a straight line equation $y = a * E_{\mu_2}$ where $a = 16.64 \pm 0.22$ acts as a gain in the system. The antenna gain (G) is around 15 dB. Here, the antenna gain G includes any losses from the antenna.

4.8 Temporal response of the system

Rydberg EIT-based microwave field sensing techniques have been exploited to find the data transfer rate in atomic systems. The requirement is larger modulation bandwidth. As discussed in the previous chapter, the system can have a data transfer rate of a few Mbit/s, as the modulation bandwidth is limited only to a few MHz by the optical pumping rate to the EIT dark state. Since the six-wave mixing process in the thermal vapor system is a parametric generation process, it is expected to be faster than the on resonant EIT-based sensing techniques.

The temporal response is investigated through amplitude modulation of the generated optical fields. A message signal encoded into a carrier wave is similar to the amplitude modulation of the carrier wave. Consider the modulation wave to be $m(t) = A_0 cos(\nu t)$, where A_0 is the amplitude of the modulation wave, and ν is the modulation frequency. The carrier wave is represented as $c(t)$ with complex amplitude A. After amplitude modulation, the modulated wave is expressed as $(1 + \frac{m(t)}{A})c(t) = (1 + mcos(\nu t))c(t)$ where $m = \frac{A_0}{A}$ is the modulation index with $m \leq 1$.

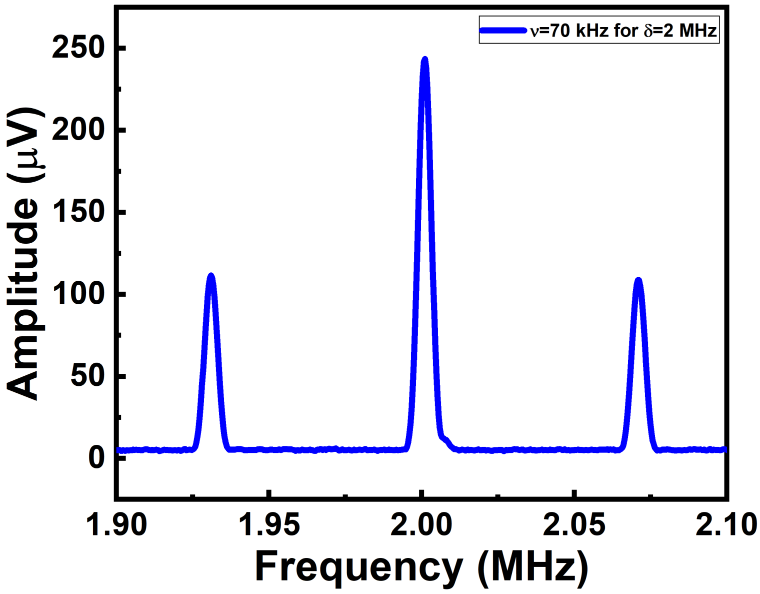

Figure 4.12: Amplitude modulated signal with side bands for $\delta = 2$ MHz and $\nu = 70$ kHz. Other experimental parameters are: $\Omega_p = 283$ MHz, $\Omega_c = 2$ MHz, $\Omega_{\mu_1} = 80$ MHz and $\Omega_{\mu_2} = 40$ MHz, $\Delta_p = 1.2$ GHz, $\Delta_c = -1.2$ GHz, and $\Delta_\mu = 0$.

Amplitude modulation of the weak microwave field results in amplitude modulation of the generated optical field due to the six-wave mixing process inside the atomic medium. The generated field acts as a carrier wave for the modulation wave. After amplitude modulation, the generated fields are written as

$(1+mcos(\nu t))E_{\pm 1}e^{i(\omega_p \pm \delta)t}$. Amplitude modulation results in the generation of sidebands around the carrier wave at frequencies $(\omega_p \pm \delta) \pm \nu$. As we know, the generated field interferes with the probe field to give the beat signal at δ and hence, the generated sidebands are observed at $(\delta \pm \nu)$ as shown in Fig. 4.12 where $\delta = 2$ MHz and $\nu = 70$ kHz. The total intensity after the amplitude modulation is given by the interference of the probe field, and the amplitude modulated generated fields. This total intensity is found to be:

$$\begin{aligned}
&|\vec{E}_p e^{i\omega_p t} + (1+mcos(\nu t))\vec{E}_{+1}e^{i(\omega_p+\delta)t}|^2 + |\vec{E}_p e^{i\omega_p t} + (1+mcos(\nu t))\vec{E}_{-1}e^{-i(\omega_p-\delta)t}|^2 \\
&= 2|E_p|^2 + |E_{+1}|^2 + |E_{-1}|^2 + m^2(|E_{+1}|^2 + |E_{-1}|^2) + \frac{m^2}{2}(|E_{+1}|^2 + |E_{-1}|^2)\cos(2\nu t) + \\
&\qquad 2m(|E_{+1}|^2 + |E_{-1}|^2)cos(\nu t) + 2|E_p|(|E_{+1}| + |E_{-1}|)\cos(\delta t) + \\
&\qquad m|E_p|(|E_{+1}| + |E_{-1}|)(\cos(\delta+\nu)t + \cos(\delta-\nu)t).
\end{aligned} \tag{4.50}$$

The first term is a d.c. term corresponding to the intensity due to the probe field. The second, third, and fourth terms are also d.c. terms that correspond to the intensities due to the generated fields. The sixth term represents the modulation wave at frequency ν, and the fifth term denotes the higher orders generated due to the modulation wave. The seventh term corresponds to the carrier wave at frequency δ, and the last two terms represent the sidebands due to the amplitude modulation of the carrier signal generated at frequencies $(\delta + \nu)$ and $(\delta - \nu)$.

Taking the ratio of the amplitudes of generated sidebands to the amplitude of the carrier signal gives

$$R = \frac{m \mid E_p \mid (\mid E_{+1} \mid + \mid E_{-1} \mid)}{2 \mid E_p \mid (\mid E_{+1} \mid + \mid E_{-1} \mid)} = \frac{m}{2} \tag{4.51}$$

Experimentally, the ratio of the amplitude of the generated sidebands to the amplitude of the un-modulated carrier signal is found out for a given δ. For example, in Fig. 4.12, the amplitude of the generated side bands along with the modulated car-

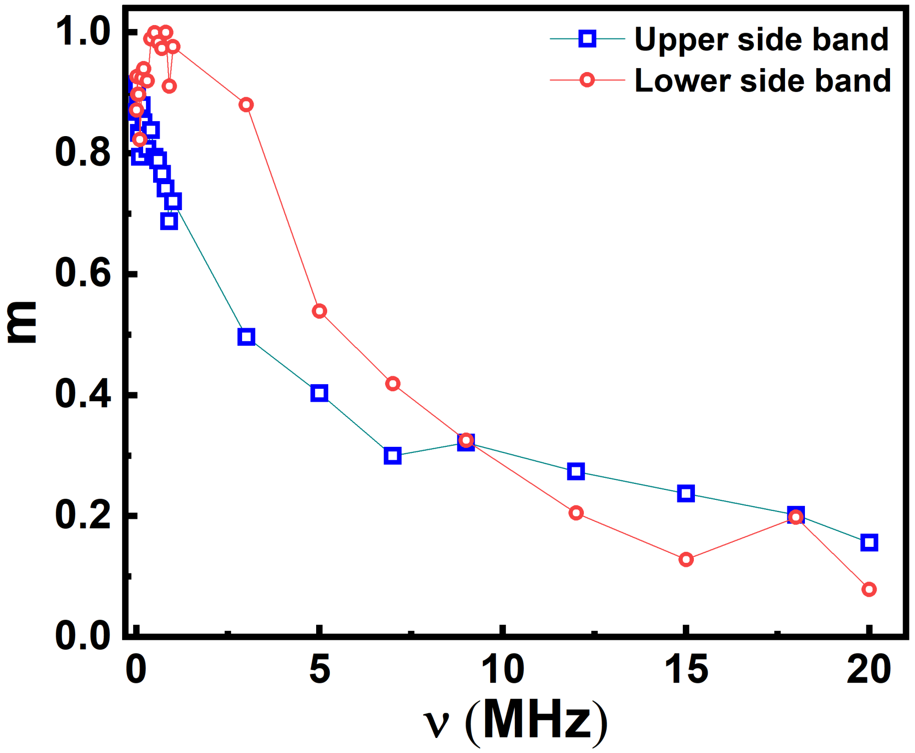

Figure 4.13: m with varying modulation frequency ν at $\delta = 2$ MHz for the upper sideband at $(\delta + \nu)$ and lower sideband at $(\delta - \nu)$. The experimental parameters are: $\Omega_p = 283$ MHz, $\Omega_c = 2$ MHz, $\Omega_{\mu_1} = 80$ MHz and $\Omega_{\mu_2} = 40$ MHz, $\Delta_p = 1.2$ GHz, $\Delta_c = -1.2$ GHz and $\Delta_\mu = 0$.

rier wave for $\delta = 2$ MHz and $\nu = 70$ KHz is observed. With the modulation signal not switched on, the amplitude of the un-modulated carrier wave is measured. The base offset is subtracted from the peak value, and the amplitude of the peak-to-peak is calculated. By taking the ratio as discussed, the value of the modulation index is calculated. By comparing the experimentally found value with eqn. 4.51, the modulation index m is determined as a function of modulation frequency ν. The value of m is calculated for both the upper and lower sidebands as a function of the modulation frequency represented by Fig. 4.13.

4.8.1 Modulation bandwidth

The generation of sidebands is observed up to a certain modulation frequency for the given experimental parameters. For given $\delta = 2$ MHz, the bandwidth of the mod-

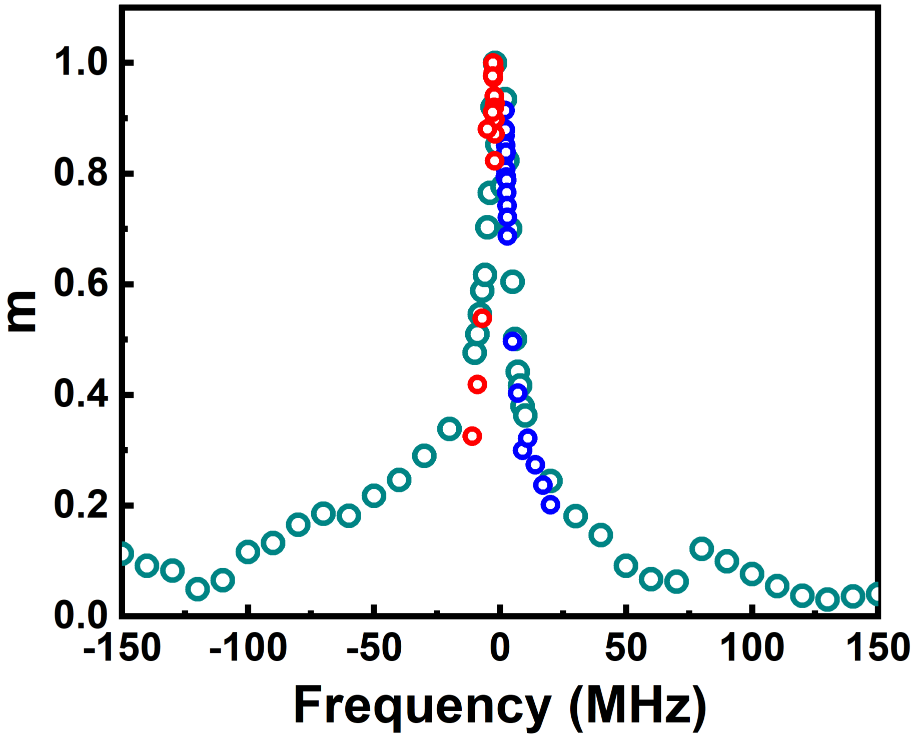

Figure 4.14: Comparison of the modulation spectrum with the normalized beat spectrum due to the six-wave mixing process. Cyan open circles represent the beat spectrum given by Fig. 4.7. Blue and red open circles represent m for the upper and lower sideband of the modulated signal, respectively, at $\delta = 2$ MHz. The other experimental parameters are: $\Omega_p = 283$ MHz, $\Omega_c = 2$ MHz, $\Omega_{\mu_1} = 80$ MHz and $\Omega_{\mu_2} = 40$ MHz, $\Delta_p = 1.2$ GHz, $\Delta_c = -1.2$ GHz, and $\Delta_\mu = 0$.

ulation spectrum is observed to be $\sim$ 17 MHz. The bandwidth of the modulation spectrum determines the system's data transfer rate. This bandwidth is limited by the available coupling power. To verify that, the bandwidth of the modulation spectrum is compared with the normalized beat generation spectrum as shown in Fig. 4.14. Since the beat frequency is fixed at $\delta = 2$ MHz, the m value for the sidebands is plotted by adding 2 MHz to the modulation frequency (x-axis of modulation spectrum) for comparison with the x-axis of the beat spectrum. The bandwidth of both spectrums is in good match with each other. In this system, a parametric six-wave mixing process is observed, which is faster than the EIT systems. As discussed earlier, it has been demonstrated that the two-photon Rydberg EIT system can have a data transfer rate of 8.2 Mbit/s with a signal bandwidth of nearly 1 MHz [40].

The bandwidth in EIT systems can be increased with an increase in coupling Rabi frequency leading to a decrease in the sensitivity of the detected microwave field, which is limited by the EIT bandwidth. The limitation to the bandwidth in the parametric system discussed in this chapter and hence, the limit to the data transfer rate is because of less coupling Rabi frequency. An increase in the coupling Rabi frequency does not compromise the sensitivity of the detected field in such parametric processes. Hence, a faster data transfer rate can be achieved with a higher available coupling Rabi frequency, which has been theoretically demonstrated in the next section.

4.9 Effect of large coupling Rabi frequency on beat spectrum

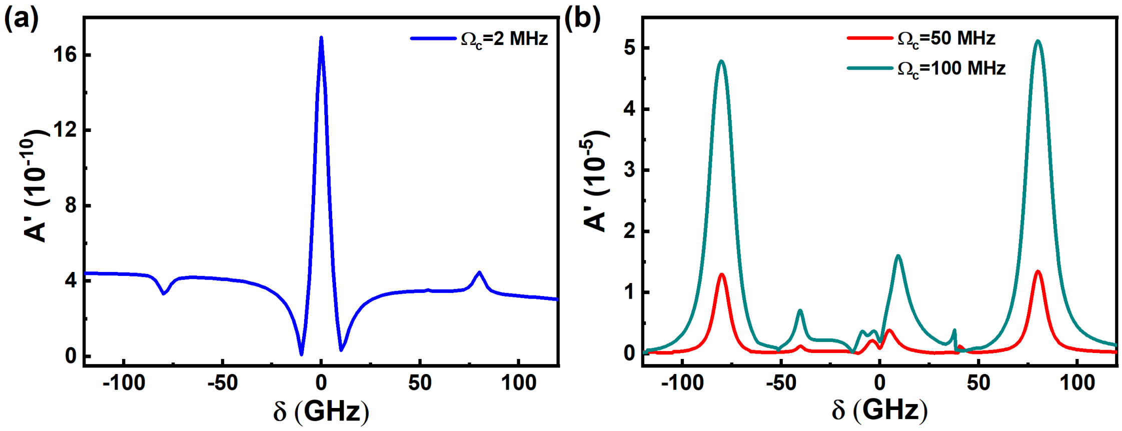

Figure 4.15: Theoretically generated spectrum for A' as a function of δ for (a) $\Omega_c = 2$ MHz and (b) $\Omega_c = 50, 100$ MHz. Other parameters used are: $\Omega_p = 300$ MHz, $\Omega_{\mu_1} = 80$ MHz and $\Omega_{\mu_2} = 1$ MHz, $\Delta_p = 1.2$ GHz, $\Delta_c = -1.2$ GHz and $\Delta_\mu = 0$.

In order to determine the signal bandwidth that can be achieved with this system, a theoretical study is performed to understand the effect of coupling Rabi frequency on the beat generation spectrum $A' = \frac{\sin(\phi_+ + \phi_-)}{\sin(\phi + \phi_-)} \int_{-\infty}^{+\infty} \rho_{eg}^{(+1)} e^{-v^2/2v_p^2} dv$. For the resonance condition discussed in the above sections with $\Delta_p = 1.2$ GHz, $\Delta_c = -1.2$

GHz, and $\Delta_\mu = 0$, an increase in coupling Rabi frequency results in extra peaks due to formation of dressed states and also the bandwidth of the spectrum does not increase as shown in Fig. 4.15. So the system is investigated at off-resonance condition i.e., $\Delta_p = 1.2$ GHz, $\Delta_c = -0.6$ GHz and $\Delta_\mu = 0.2$ GHz as shown in Fig. 4.16(a). To be able to understand the observations in the thermal vapor system, first, the system is studied considering the atoms to be at rest.

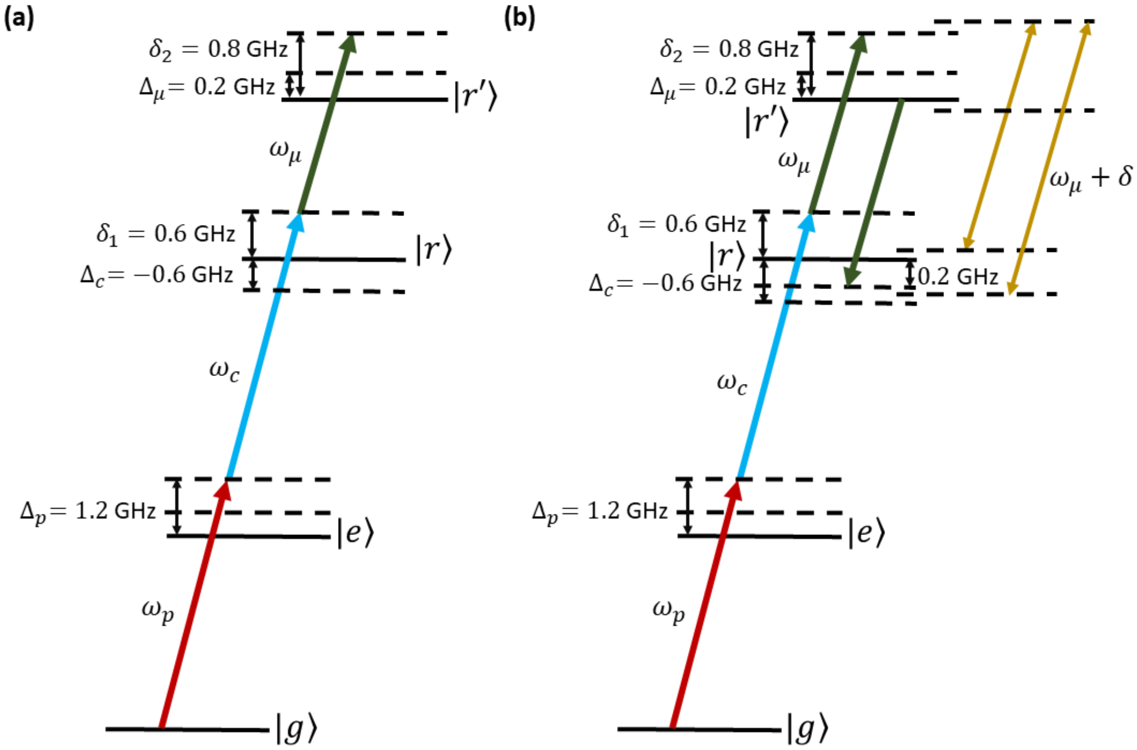
(a)
$\delta_2 = 0.8$ GHz
$\Delta_\mu = 0.2$ GHz
$|r'\rangle$
ω_μ
$\delta_1 = 0.6$ GHz
$|r\rangle$
$\Delta_c = -0.6$ GHz
ω_c
$\Delta_p = 1.2$ GHz
$|e\rangle$
ω_p
$|g\rangle$
(b)
$\delta_2 = 0.8$ GHz
$\Delta_\mu = 0.2$ GHz
$|r'\rangle$
ω_μ
$\omega_\mu + \delta$
$\delta_1 = 0.6$ GHz
$|r\rangle$
0.2 GHz
$\Delta_c = -0.6$ GHz
ω_c
$\Delta_p = 1.2$ GHz
$|e\rangle$
ω_p
$|g\rangle$

Figure 4.16: Schematic of energy levels: (a) for off-resonant condition with two-photon detuning $\delta_1 = 0.6$ GHz and three-photon detuning $\delta_2 = 0.8$ GHz and (b) weak microwave transitions (yellow lines) corresponding to the two peaks at $\delta = 0.6$ GHz and $\delta = 0.8$ GHz.

4.9.1 Investigation in a system with atoms at rest

First, the A' spectrum is studied for low Rabi frequencies, i.e., $\Omega_p = 10$ MHz, $\Omega_c = 2$ MHz, $\Omega_{\mu_1} = 10$ MHz and $\Omega_{\mu_2} = 1$ MHz, which is shown as an inset in Fig. 4.17(a). Application of a strong microwave field at the off-resonant conditions leads to the formation of dressed states, leading to many possible peaks while scanning

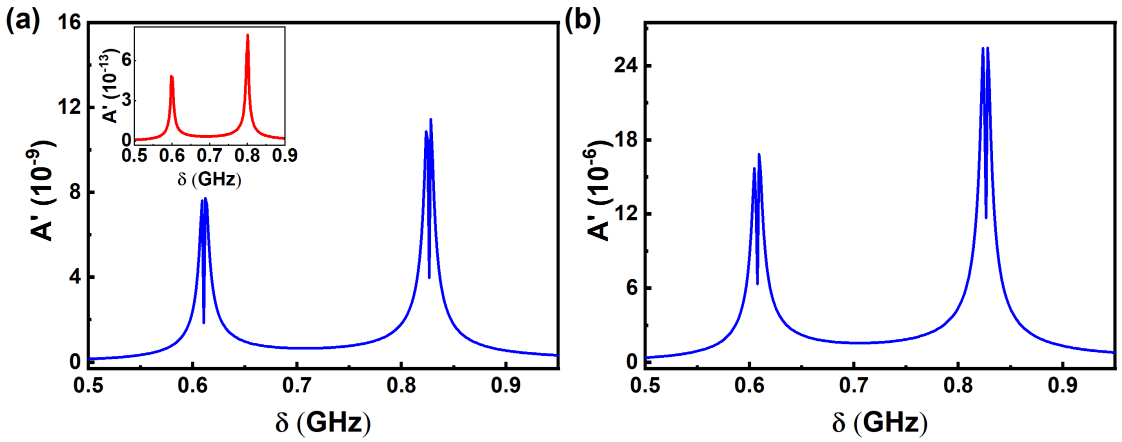

Figure 4.17: Theoretically generated spectrum for A' with atoms at rest as a function of δ for: (a) Ω_p = 300 MHz, Ω_c = 2 MHz, Ω_{μ_1} = 80 MHz and Ω_{μ_2} = 1 MHz. Inset shows the spectrum for Ω_p = 10 MHz, Ω_c = 2 MHz, Ω_{μ_1} = 10 MHz and Ω_{μ_2} = 1 MHz. (b) Ω_p = 300 MHz, Ω_c = 100 MHz, Ω_{μ_1} = 80 MHz and Ω_{μ_2} = 1 MHz. Other parameters used are: Δ_p = 1.2 GHz, $\Delta_c = -0.6$ GHz and Δ_μ = 0.2 GHz.

the weak microwave field. But the stronger contribution comes from two possible weak microwave field transitions. These transitions are represented by yellow lines, as shown in Fig. 4.16(b). Two peaks are observed at δ = 600 MHz and δ = 800 MHz. With the increase in the laser Rabi frequencies to Ω_p = 300 MHz, Ω_c = 2 MHz, Ω_{μ_1} = 80 MHz, and Ω_{μ_2} = 1 MHz, the peaks are shifted due to light shifts introduced into the system by the laser fields as shown in Fig. 4.17. Also, the two peaks split because of the formation of dressed states due to high probe Rabi frequency. An increase of coupling Rabi frequency to Ω_c = 100 MHz leads to an increase in the strength of A' whereas the spectrum bandwidth remains the same, which can be observed in Fig. 4.17(b).

4.9.2 Effect of large coupling Rabi frequency in thermal system

In the thermal vapor system, along with the light shift factors of the laser fields, there is a wave-vector mismatch between the probe and the coupling field. At low

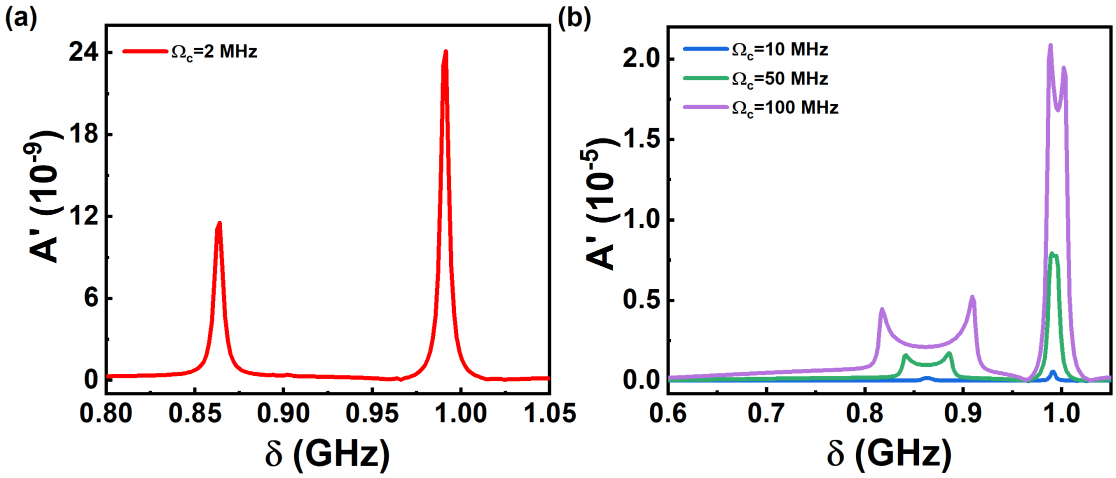

Figure 4.18: Theoretically generated spectrum for A' as a function of δ for (a) $\Omega_c = 2$ MHz and (b) $\Omega_c = 10, 50, 100$ MHz. Other parameters used are: $\Omega_p = 300$ MHz, $\Omega_{\mu_1} = 80$ MHz and $\Omega_{\mu_2} = 1$ MHz, $\Delta_p = 1.2$ GHz, $\Delta_c = -0.6$ GHz and $\Delta_\mu = 0.2$ GHz.

coupling Rabi frequency of $\Omega_c = 2$ MHz, the two peaks are observed as shown in Fig. 4.18(a). The peaks are shifted from $\delta = 600$ MHz and $\delta = 800$ MHz due to wave-vector mismatch as well as the light shift factors and the frequency difference between the peaks is $\sim \Delta_\mu \frac{k_p}{k_c}$. An increase in coupling Rabi frequency leads to the broadening of the A' spectrum, as shown in Fig. 4.18. For the left side peak, it is observed that the width of the spectrum is equal to the coupling Rabi frequency. Hence, the bandwidth of the modulation spectrum will also increase with the increase in coupling Rabi frequency. If the coupling Rabi frequency can be increased to 100 MHz, a beat spectrum with a bandwidth of 100 MHz can be achieved. The power requirement for achieving such coupling Rabi frequency is nearly 27 Watt with $1/e$ beam radius of 50 μm. In the current scenario, achieving such large power is difficult. 27 Watt is a quantitative estimate of the power required to achieve such larger bandwidth. The observation clearly indicates that this system is advantageous for a faster data transfer rate.

4.10 Conclusion

The six-wave mixing of optical and microwave fields in thermal rubidium vapor results in the parametric generation of a new optical field. The frequency of the generated field depends on the frequency difference between the two microwave fields, and the direction is along the probe field. The system has a generation bandwidth of 17 MHz limited by the available coupling Rabi frequency. A theoretical investigation demonstrates that a larger coupling Rabi frequency of 100 MHz can lead to a generation bandwidth of 100 MHz. This study in thermal vapor systems provides a robust platform for larger bandwidth of microwave-to-optical conversion and hence, a faster data transfer rate.

Chapter 5

Study of electromagnetically induced transparency (EIT) using four-photon excitation to the Rydberg state in thermal atomic vapor

Microwave field sensing with Rydberg atoms is performed with a two-photon excitation [68] process to the Rydberg state [12] under the conditions of EIT. The two-photon excitation processes to the Rydberg state in thermal atomic vapor have a large wave-vector mismatch. This leads to significant motion-induced dephasing in the system. There are studies that propose achieving Doppler-free conditions for EIT with three-photon excitation processes using suitable beam geometry [86]. Also, there are proposals for eliminating the motion-induced dephasing using four-photon excitation to the Rydberg state [87, 88]. Still, the four-photon excitation process has not been discussed in detail. This chapter provides an atomic model of a five-level system to study EIT using the four-photon excitation to the Rydberg state in thermal atomic vapor [89]. The system achieves EIT using an effective probe and coupling transition where the variation of EIT peak transmission with wave-vector mismatch is studied. The method of adiabatic elimination is discussed, which reduces the five-level system to an effective three-level system. Finally, an experimental proposal is provided where motion-induced dephasing can be eliminated using suitable beam geometry.

5.1 Five-level atomic model for four-photon excitation to the Rydberg state

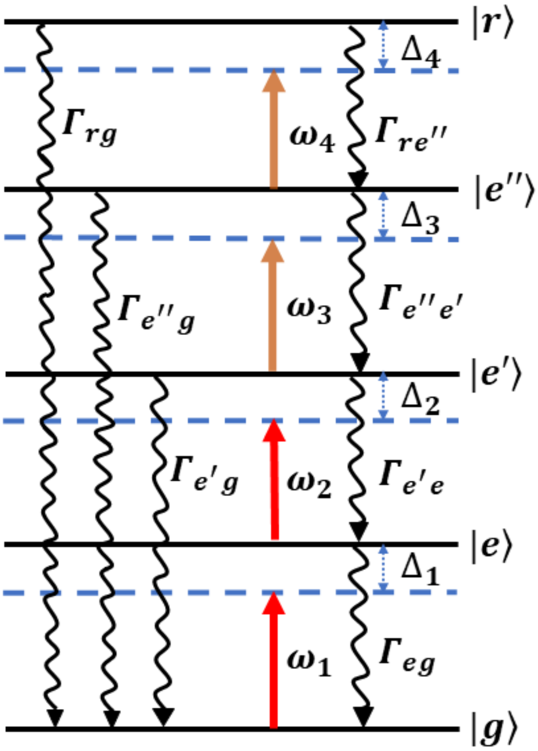
$|r\rangle$
Δ_4
Γ_{rg}
ω_4
$\Gamma_{re''}$
$|e''\rangle$
Δ_3
$\Gamma_{e''g}$
ω_3
$\Gamma_{e''e'}$
$|e'\rangle$
Δ_2
$\Gamma_{e'g}$
ω_2
$\Gamma_{e'e}$
$|e\rangle$
Δ_1
ω_1
Γ_{eg}
$|g\rangle$

Figure 5.1: Energy level scheme of a five-level system in the ladder configuration.

Consider an atomic system of five energy levels represented by Fig. 5.1. The ground state is represented by $|g\rangle$, first excited state or intermediate state by $|e\rangle$, second excited state or second intermediate state by $|e'\rangle$, third excited state or third intermediate state by $|e''\rangle$ and final excited state or Rydberg state by $|r\rangle$. Excitation from $|g\rangle \rightarrow |e\rangle$, $|e\rangle \rightarrow |e'\rangle$, $|e'\rangle \rightarrow |e''\rangle$ and $|e''\rangle \rightarrow |r\rangle$ are dipole allowed with ω_{01}, ω_{02}, ω_{03} and ω_{04} being the corresponding atomic transition frequencies. The excitation from $|g\rangle \rightarrow |e'\rangle$ and $|e'\rangle \rightarrow |r\rangle$ are dipole forbidden. A probe field at frequency ω_1 drives the transition $|g\rangle \rightarrow |e\rangle$. Fields at frequencies ω_2, ω_3 and ω_4 drive the transition between the states $|e\rangle \rightarrow |e'\rangle$, $|e'\rangle \rightarrow |e''\rangle$ and $|e''\rangle \rightarrow |r\rangle$, respectively. The laser electric fields are represented as $\vec{E'}_1 = \vec{E}_1 e^{-i\omega_1 t} + c.c$, $\vec{E'}_2 = \vec{E}_2 e^{-i\omega_2 t} + c.c$, $\vec{E'}_3 = \vec{E}_3 e^{-i\omega_3 t} + c.c$ and $\vec{E'}_4 = \vec{E}_4 e^{-i\omega_4 t} + c.c$. The detunings of the various fields from the corresponding atomic resonances are given by $\Delta_1 = \omega_1 - \omega_{01}$, $\Delta_2 = \omega_2 - \omega_{02}$, $\Delta_3 = \omega_3 - \omega_{03}$ and $\Delta_4 = \omega_4 - \omega_{04}$. The two-photon, three-photon and four-photon detuning are defined respectively as $\delta_2 = (\Delta_1 + \Delta_2)$, $\delta_3 = (\Delta_1 + \Delta_2 + \Delta_3)$, and $\delta_4 = (\Delta_1 + \Delta_2 + \Delta_3 + \Delta_4)$. Two other detunings are defined as $\delta_5 = (\Delta_2 + \Delta_3)$, $\delta_6 = (\Delta_2 + \Delta_3 + \Delta_4)$, and $\delta_7 = (\Delta_3 + \Delta_4)$. The Rabi frequency of the four laser fields are given by $\Omega_1 = \frac{2\mu_{ge}E_1}{\hbar}$, $\Omega_2 = \frac{2\mu_{ee'}E_2}{\hbar}$, $\Omega_3 = \frac{2\mu_{e'e''}E_3}{\hbar}$ and $\Omega_4 = \frac{2\mu_{e''r}E_4}{\hbar}$. μ_{ge}, $\mu_{ee'}$, $\mu_{e'e''}$ and $\mu_{e''r}$ denote the transition dipole moments. E_1, E_2, E_2 and E_4 denote the electric field amplitude of the four laser fields with frequency ω_1, ω_2, ω_3 and ω_4 respectively.

The total Hamiltonian for the five-level system is represented as $\tilde{H} = H_0 + H_{int}$ where $H_0 = \hbar\omega_1|e\rangle\langle e| + \hbar(\omega_1 + \omega_2)|e'\rangle\langle e'| + \hbar(\omega_1 + \omega_2 + \omega_3)|e''\rangle\langle e''| + \hbar(\omega_1 + \omega_2 + \omega_3 + \omega_4)|r\rangle\langle r|$ is the bare atomic Hamiltonian and $H_{int} = -\vec{\mu} \cdot \vec{E} = -E_1(\mu_{ge}|g\rangle\langle e| + \mu_{eg}|e\rangle\langle g|) - E_2(\mu_{ee'}|e\rangle\langle e'| + \mu_{e'e}|e'\rangle\langle e|) - E_3(\mu_{e'e''}|e'\rangle\langle e''| + \mu_{e''e'}|e''\rangle\langle e'|) - E_4(\mu_{e''r}|e''\rangle\langle r| + \mu_{re''}|r\rangle\langle e''|)$ is the interaction Hamiltonian which represents the atom-light interaction taking place. The use of rotating wave approximation in a suitable rotating frame makes the total Hamiltonian time-independent and is represented as

$$H = -\frac{\hbar}{2}\begin{pmatrix} 0 & \Omega_1 & 0 & 0 & 0 \\ \Omega_1^* & 2\Delta_1 & \Omega_2 & 0 & 0 \\ 0 & \Omega_2^* & 2\delta_2 & \Omega_3 & 0 \\ 0 & 0 & \Omega_3^* & 2\delta_3 & \Omega_4 \\ 0 & 0 & 0 & \Omega_4^* & 2\delta_4 \end{pmatrix}.$$

5.2 Construction of the master equation

The master equation which leads us to the equations of motions is

$$\dot{\rho} = \frac{i}{\hbar}[\rho, H] + \mathcal{L}_{\mathcal{D}}(\rho). \tag{5.1}$$

The density matrix ρ is a 5×5 matrix and is represented as $\rho_{i,j}$ with $i, j = g, e, e', e'', r$. The Lindblad operator representing the decay and decoherence terms is given by

$$\mathcal{L}_{\mathcal{D}}(\rho) = \begin{pmatrix} L_{D_{gg}} & L_{D_{ge}} & L_{D_{ge'}} & L_{D_{ge''}} & L_{D_{gr}} \\ L_{D_{eg}} & L_{D_{ee}} & L_{D_{ee'}} & L_{D_{ee''}} & L_{D_{er}} \\ L_{D_{e'g}} & L_{D_{e'e}} & L_{D_{e'e'}} & L_{D_{e'e''}} & L_{D_{e'r}} \\ L_{D_{e''g}} & L_{D_{e''e}} & L_{D_{e''e'}} & L_{D_{e''e''}} & L_{D_{e''r}} \\ L_{D_{rg}} & L_{D_{re}} & L_{D_{re'}} & L_{D_{re''}} & L_{D_{rr}} \end{pmatrix}$$

where the different matrix elements are given as below:

$L_{D_{gg}} = \Gamma_{eg}\rho_{ee} + \Gamma_{e'g}\rho_{e'e'} + \Gamma_{e''g}\rho_{e''e''} + \Gamma_{rg}\rho_{rr}$

$L_{D_{ge}} = -\frac{1}{2}\Gamma_{eg}\rho_{ge}$

$L_{D_{ge'}} = -\frac{1}{2}(\Gamma_{e'g} + \Gamma_{e'e})\rho_{ge'}$

$L_{D_{ge''}} = -\frac{1}{2}(\Gamma_{e''g} + \Gamma_{e''e'})\rho_{ge''}$

$L_{D_{gr}} = -\frac{1}{2}(\Gamma_{rg} + \Gamma_{re''})\rho_{gr}$

$L_{D_{eg}} = -\frac{1}{2}\Gamma_{eg}\rho_{eg}$

$L_{D_{ee}} = \Gamma_{e'e}\rho_{e'e'} - \Gamma_{eg}\rho_{ee}$

$L_{D_{ee'}} = -\frac{1}{2}(\Gamma_{e'g} + \Gamma_{e'e} + \Gamma_{eg})\rho_{ee'}$

$L_{D_{ee''}} = -\frac{1}{2}(\Gamma_{e''g} + \Gamma_{e''e'} + \Gamma_{eg})\rho_{ee''}$

$L_{D_{er}} = -\frac{1}{2}(\Gamma_{rg} + \Gamma_{re''} + \Gamma_{eg})\rho_{er}$

$L_{D_{e'g}} = -\frac{1}{2}(\Gamma_{e'g} + \Gamma_{e'e})\rho_{e'g}$

$L_{D_{e'e}} = -\frac{1}{2}(\Gamma_{e'g} + \Gamma_{e'e} + \Gamma_{eg})\rho_{e'e}$

$L_{D_{e'e'}} = \Gamma_{e''e'}\rho_{e''e''} - (\Gamma_{e'g} + \Gamma_{e'e})\rho_{e'e'}$

$L_{D_{e'e''}} = -\frac{1}{2}(\Gamma_{e'e} + \Gamma_{e'g} + \Gamma_{e''e'} + \Gamma_{e''g})\rho_{e'e''}$

$L_{D_{e'r}} = -\frac{1}{2}(\Gamma_{e'e} + \Gamma_{e'g} + \Gamma_{re''} + \Gamma_{rg})\rho_{e'r}$

$L_{D_{e''g}} = -\frac{1}{2}(\Gamma_{e''g} + \Gamma_{e''e'})\rho_{e''g}$

$L_{D_{e''e'}} = -\frac{1}{2}(\Gamma_{e''g} + \Gamma_{e''e'} + \Gamma_{eg})\rho_{e''e'}$

$L_{D_{e''e'}} = -\frac{1}{2}(\Gamma_{e'e} + \Gamma_{e'g} + \Gamma_{e''e'} + \Gamma_{e''g})\rho_{e''e'}$

$L_{D_{e''e''}} = \Gamma_{re''}\rho_{rr} - (\Gamma_{e''g} + \Gamma_{e''e'})\rho_{e''e''}$

$L_{D_{e''r}} = -\frac{1}{2}(\Gamma_{e''e'} + \Gamma_{e''g} + \Gamma_{re''} + \Gamma_{rg})\rho_{e''r}$

$L_{D_{rg}} = -\frac{1}{2}(\Gamma_{rg} + \Gamma_{re''})\rho_{rg}$

$L_{D_{re}} = -\frac{1}{2}(\Gamma_{rg} + \Gamma_{re''} + \Gamma_{eg})\rho_{re}$

$L_{D_{re'}} = -\frac{1}{2}(\Gamma_{e'e} + \Gamma_{e'g} + \Gamma_{re''} + \Gamma_{rg})\rho_{re'}$

$L_{D_{re''}} = -\frac{1}{2}(\Gamma_{e''e'} + \Gamma_{e''g} + \Gamma_{re''} + \Gamma_{rg})\rho_{re''}$

$L_{D_{rr}} = -(\Gamma_{rg} + \Gamma_{re''})\rho_{rr}$

Γ_{eg}, $\Gamma_{e'e}$, $\Gamma_{e''e'}$ and $\Gamma_{re''}$ are the population decay rates through the dipole allowed decay channels. The transit time decays of the excited states through the transverse direction of the beam are Γ_{rg}, $\Gamma_{e''g}$, and $\Gamma_{e'g}$. The decay values used in the model for calculation are $\Gamma_{eg} = 6$ MHz, $\Gamma_{e'e} = 0.65$ MHz, $\Gamma_{e''e'} = 0.3$ MHz and $\Gamma_{re''} = 0.01$ MHz. The transit time decay rates are 0.2 MHz.

5.3 Optical Bloch equations

The optical Bloch equations are solved for the steady state, i.e., $\dot{\rho} = 0$ to get the density matrix equations as

$$\frac{i}{2}(\Omega_1\rho_{eg} - \Omega_1^*\rho_{ge}) + \Gamma_{eg}\rho_{ee} + \Gamma_{e'g}\rho_{e'e'} + \Gamma_{e''g}\rho_{e''e''} + \Gamma_{rg}\rho_{rr} = 0 \tag{5.2}$$

$$\frac{i}{2}[-2\Delta_1\rho_{ge} + \Omega_1(2\rho_{ee} + \rho_{e'e'} + \rho_{e''e''} + \rho_{rr}) - \Omega_1 - \Omega_2^*\rho_{ge'}] - \frac{\Gamma_{eg}}{2}\rho_{ge} = 0 \tag{5.3}$$

$$\frac{i}{2}[-2\delta_2\rho_{ge'} - \Omega_3^*\rho_{ge''} + \Omega_1\rho_{ee'} - \Omega_2\rho_{ge}] - \frac{(\Gamma_{e'g} + \Gamma_{e'e})}{2}\rho_{ge'} = 0 \tag{5.4}$$

$$\frac{i}{2}[-2\delta_3\rho_{ge''} - \Omega_3\rho_{ge'} + \Omega_1\rho_{er'} - \Omega_4\rho_{gr}] - \frac{(\Gamma_{e''g} + \Gamma_{e''e'})}{2}\rho_{ge''} = 0 \tag{5.5}$$

$$\frac{i}{2}[-2\delta_4\rho_{gr} - \Omega_4\rho_{ge''} + \Omega_1\rho_{er}] - \frac{(\Gamma_{rg} + \Gamma_{re''})}{2}\rho_{gr} = 0 \tag{5.6}$$

$$\frac{i}{2}[\Omega_1^*\rho_{ge} - \Omega_1\rho_{eg} + \Omega_2\rho_{e'e} - \Omega_2^*\rho_{ee'}] + \Gamma_{e'e}\rho_{e'e'} + \Gamma_{re}\rho_{rr} - \Gamma_{eg}\rho_{ee} = 0 \tag{5.7}$$

$$\frac{i}{2}[\Omega_1^*\rho_{ge'} - 2\Delta_2\rho_{ee'} - \Omega_3^*\rho_{ee''} + \Omega_2(\rho_{e'e'} - \rho_{ee})] - \frac{(\Gamma_{eg} + \Gamma_{e'e} + \Gamma_{e'g})}{2}\rho_{ee'} = 0 \tag{5.8}$$

$$\frac{i}{2}[-\Omega_3\rho_{ee'} - 2\delta_5\rho_{ee''} - \Omega_4\rho_{er} + \Omega_1^*\rho_{ge''} + \Omega_2\rho_{e'e''}] - \frac{(\Gamma_{eg} + \Gamma_{e''g} + \Gamma_{e''e'})}{2}\rho_{ee''} = 0 \tag{5.9}$$

$$\frac{i}{2}[-2\delta_6\rho_{er} - \Omega_4\rho_{ee''} + \Omega_1^*\rho_{gr} + \Omega_2\rho_{e'r}] - \frac{(\Gamma_{eg} + \Gamma_{rg} + \Gamma_{re''})}{2}\rho_{er} = 0 \tag{5.10}$$

$$\frac{i}{2}[\Omega_2^*\rho_{ee'} - \Omega_2\rho_{e'e} + \Omega_3\rho_{e''e'} - \Omega_3^*\rho_{e'e''}] - (\Gamma_{e'e} + \Gamma_{e'g})\rho_{e'e'} + \Gamma_{e''e'}\rho_{e''e''} = 0 \tag{5.11}$$

$$\frac{i}{2}[\Omega_2^*\rho_{ee''} - 2\Delta_3\rho_{e'e''} - \Omega_3(\rho_{e'e'} - \rho_{e''e''})] - \frac{(\Gamma_{e'e} + \Gamma_{e'g} + \Gamma_{e''e'} + \Gamma_{e''g})}{2}\rho_{e'e''} = 0 \tag{5.12}$$

$$\frac{i}{2}[\Omega_2\rho_{er} - 2\delta_7\rho_{e'r} + \Omega_3\rho_{e''r} - \Omega_4\rho_{e'e''}] - \frac{(\Gamma_{e'e} + \Gamma_{e'g} + \Gamma_{re''} + \Gamma_{rg})}{2}\rho_{e'r} = 0 \tag{5.13}$$

$$\frac{i}{2}[\Omega_3^*\rho_{e'e''} - \Omega_3\rho_{e''e'} + \Omega_4^*\rho_{re''} - \Omega_4\rho_{e''r}] - (\Gamma_{e''e'} + \Gamma_{e''g})\rho_{e''e''} + \Gamma_{re''}\rho_{rr} = 0 \tag{5.14}$$

$$\frac{i}{2}[\Omega_3\rho_{e'r} - 2\Delta_4\rho_{e''r} + \Omega_4\rho_{rr} - \Omega_4\rho_{e''e''}] - \frac{(\Gamma_{e''e'} + \Gamma_{e''g} + \Gamma_{re''} + \Gamma_{rg})}{2}\rho_{e''r} = 0 \tag{5.15}$$

$$\frac{i}{2}[\Omega_4^*\rho_{e''r} - \Omega_4\rho_{re''}] - (\Gamma_{rg} + \Gamma_{re''})\rho_{rr} = 0 \tag{5.16}$$

Numerical methods are used to solve the density matrix equations and find out the ground to excited state coherence ρ_{eg}.

5.4 EIT in a four-photon excitation process

To observe the EIT using the four-photon excitation process to the Rydberg state, as described in the above section, a few concepts that are needed to be understood are described below.

5.4.1 Geometry of the laser beams

The laser beam geometry is shown in Fig. 5.2, where all the beams propagate co-linearly through the atomic vapor medium. Laser field with frequency ω_2 counter-propagates the field with frequency ω_1 and field with frequency ω_4 counter-propagates

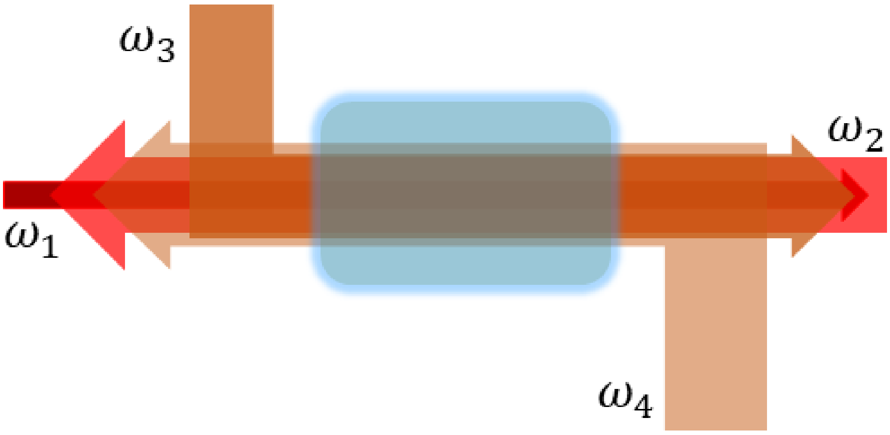

Figure 5.2: Schematic of the laser geometry through a Rb vapor cell consisting of four laser fields of frequencies ω_1, ω_2, ω_3, and ω_4.

the field with frequency ω_3. Fields with frequency ω_1 (ω_2) and ω_3 (ω_4) co-propagate with each other. The magnitude of the wave vectors of the four fields are given by k_1, k_2, k_3 and k_4.

5.4.2 Energy level scheme for EIT

The five-level system is coupled by four laser fields, and the details have been discussed in Sec. 5.1. Here, none of the lasers satisfy the single photon resonance. But the excitation from the ground state ($|g\rangle$) to the second excited state ($|e'\rangle$) satisfies the two-photon resonance. Similarly, the excitation from the second excited state ($|e'\rangle$) to the Rydberg state ($|r\rangle$) satisfies the two-photon resonance. The laser beam with frequency ω_1 is kept largely detuned from resonance by detuning Δ_1. Laser beam with frequency ω_2 and detuning Δ_2 is scanned around Δ_1 such that the two-photon resonance condition is satisfied by the $|g\rangle \rightarrow |e'\rangle$ transition. Transition from $|g\rangle \rightarrow |e'\rangle$ is called as the effective probe transition. Similarly, the laser beam with frequency ω_3 is kept largely detuned from resonance with detuning Δ_3. The detuning Δ_4 of beam with frequency ω_4 is adjusted around Δ_3 such that the two-photon resonance is satisfied by $|e'\rangle \rightarrow |r\rangle$ transition. Transition from $|e'\rangle \rightarrow |r\rangle$ is called as the effective coupling transition. The effective probe and coupling transition satisfy

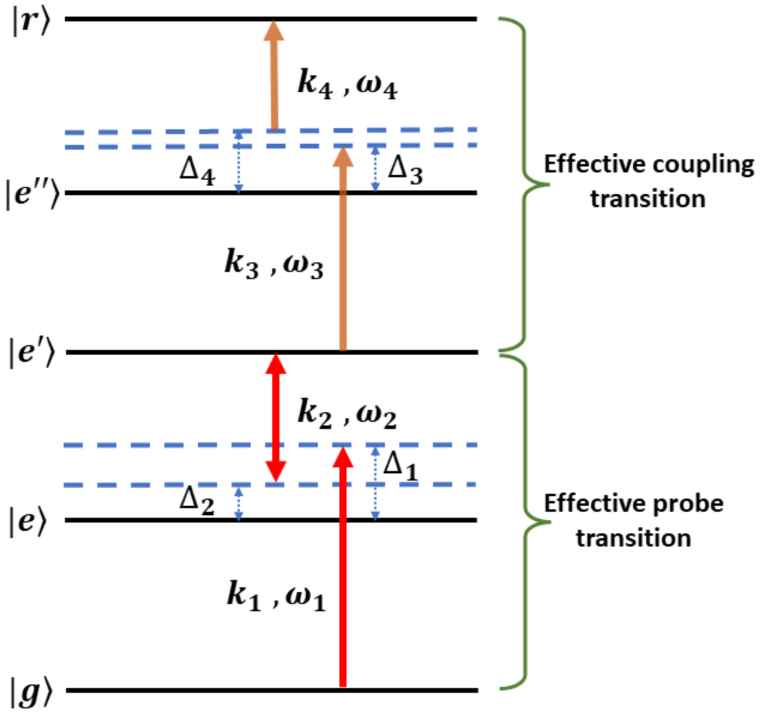
$|r\rangle$
k_4, ω_4
Δ_4
Δ_3
$|e''\rangle$
Effective coupling transition
k_3, ω_3
$|e'\rangle$
k_2, ω_2
Δ_1
Δ_2
$|e\rangle$
Effective probe transition
k_1, ω_1
$|g\rangle$

Figure 5.3: Energy level scheme of the five-level system representing the conditions to satisfy EIT.

the conditions of EIT even though single photon resonances are not satisfied by the individual laser fields.

5.4.3 Doppler averaging

Since the study is based on a thermal vapor system, we need to consider the thermal motion of the atoms and the beam geometry presented in Fig. 5.2. For the thermal atomic medium, the detunings are modified as $\Delta_1 \rightarrow \Delta_1 - k_1 v$, $\Delta_2 \rightarrow \Delta_2 + k_2 v$, $\Delta_3 \rightarrow \Delta_3 - k_3 v$ and $\Delta_4 \rightarrow \Delta_4 + k_4 v$, where v is the velocity of the atoms in the vapor. k_2 is considered to be greater than k_1, i.e. $k_2 > k_1$ and k_3 is considered to be greater than k_4, i.e. $k_3 > k_4$. Hence, the effective wave vector of the effective probe transition is defined as $k_p = k_2 - k_1$ and the effective wave vector of the effective coupling transition is defined as $k_c = k_3 - k_4$. The residual wave vector of the system is found as $\Delta k = k_c - k_p$.

The susceptibility of the probe field coupling the transition from $|g\rangle \rightarrow |e\rangle$ is calculated as

$$\chi(\Delta_2, v)f(v)dv = \frac{2N|\ \mu_{ge}\ |^2}{\hbar\epsilon_0\Omega_1}\frac{1}{\sqrt{\pi}v_p}\rho_{eg}(\Delta_2, v)e^{-\frac{v^2}{v_p^2}}dv \tag{5.17}$$

where μ_{ge} is the dipole moment of $|g\rangle \rightarrow |e\rangle$ transition, N is the density of the atoms inside the atomic vapor medium, and v_p is the most probable speed of the atoms. The transmission of the probe beam is given by $T = (\frac{I}{I_0}) = e^{(-\alpha l)}$ where α is the absorption coefficient and is given by $\alpha = \Im(\chi)k_1 l$. l is the length of the vapor cell medium.

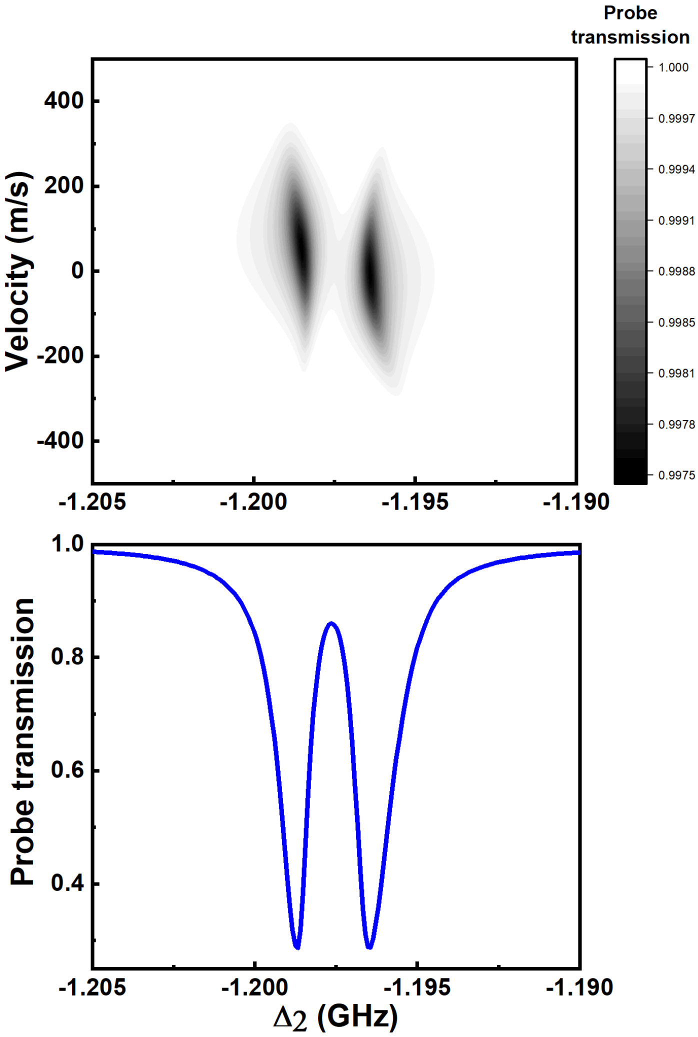

Figure 5.4: Up: Two-dimensional density plots for probe transmission as a function of Δ_2 and velocity for $\Delta k = 0$. Down: Doppler averaged probe transmission for the same.

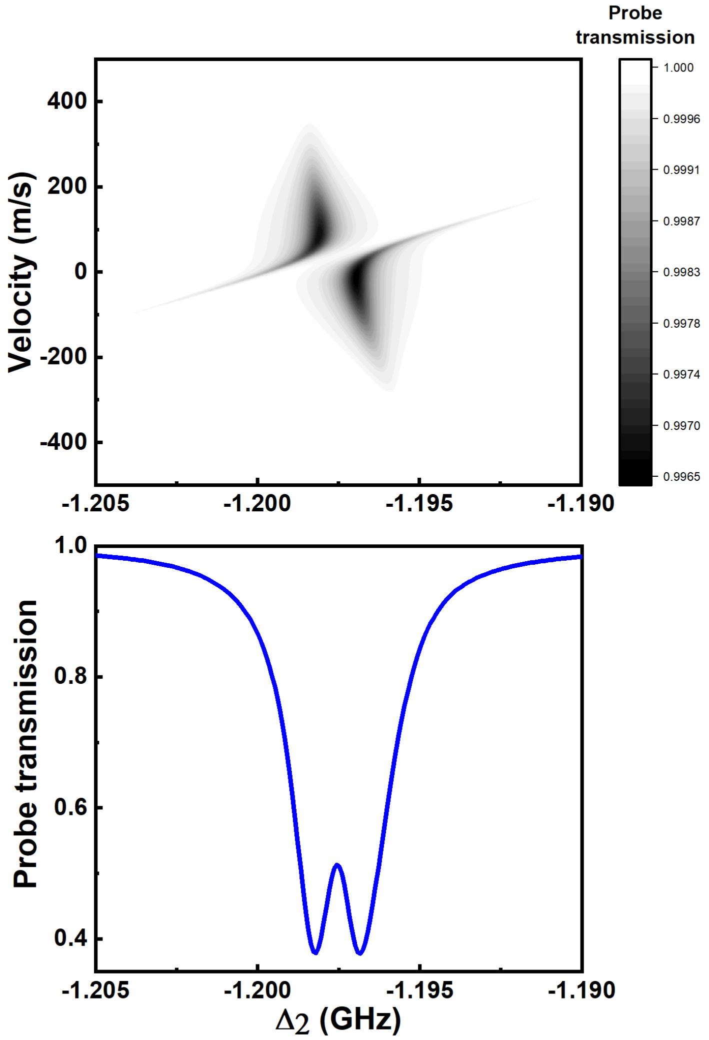

Figure 5.5: Up: Two-dimensional density plots for probe transmission as a function of Δ_2 and velocity for $\Delta k = 0.043 \times 10^6$ m^{-1}. Down: Doppler averaged probe transmission for the same.

Fig. 5.4 represents the two-dimensional density plots for probe transmission as a function of Δ_2 and velocity for $\Delta k = 0$ (Up) and its comparison with the probe transmission by Doppler averaging over all the velocity range (Down). It can be observed that for a fixed detuning towards the center at nearly $\Delta_2 = -1.197$ GHz, averaging over all the velocity range gives the maximum EIT transparency of $\sim$ 0.9. Fig. 5.5 represents the two-dimensional density plots for probe transmission as a function of Δ_2 and velocity for $\Delta k = 0.043 \times 10^6$ m^{-1} (Up) and its comparison with the probe transmission by Doppler averaging over all the velocity range

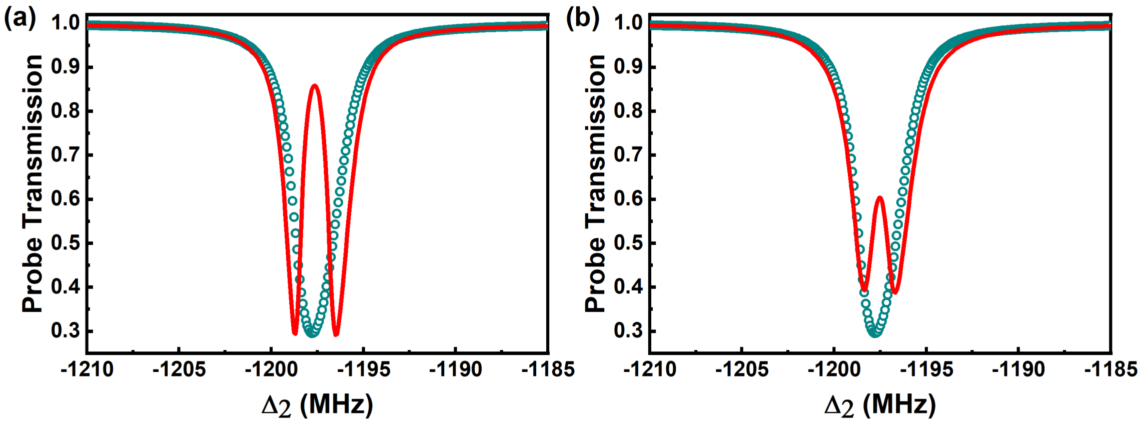

Figure 5.6: Probe transmission in the absence of the coupling fields while scanning Δ_2 (cyan open circles) and in the presence of the coupling fields (solid red line) for (a) $\Delta k = 0$ and for (b) $\Delta k = 0.023 \times 10^6$ m^{-1}. The laser parameters used in the model are $\Omega_1 = 10$ MHz, $\Omega_2 = 110$ MHz, $\Omega_3 = 25$ MHz, $\Omega_4 = 160$ MHz, $\Delta_1 = 1200$ MHz, $\Delta_3 = 1000$ MHz and Δ_4 is adjusted around Δ_3 to make the transmission symmetric. Here, the value of the effective probe transition wave vector is taken to be $k_p = 0.007 \times 10^6$ m^{-1}.

(Down). Averaging over all the velocities at $\Delta_2 = -1.197$ GHz gives a reduced EIT transparency of ~ 0.5 due to the presence of large absorption components along with transmission components. Similarly at other detunings within the absorption window, the transparency reduces as the light gets absorbed.

Averaging over all the velocity components of the atoms, the susceptibility of the probe is given by

$$\chi(\omega_1) = \frac{2N|\ \mu_{ge}\ |^2}{\hbar\epsilon_0\Omega_1}\frac{1}{\sqrt{2\pi}v_p}\int_{-\infty}^{+\infty}\rho_{eg}e^{-\frac{v^2}{2v_p^2}}dv \tag{5.18}$$

The vapor density is taken to be 4.5×10^{10} cm^{-3}, and the length of the vapor cell is 5 cm. The transmission of the probe calculated from the model in the EIT regime is shown in Fig.5.6. For $\Delta k = 0$, the peak transmission of the EIT signal is observed to be ~ 0.9, as shown in the Fig. 5.6(a). If $\Delta k = 0.023 \times 10^6$ m^{-1}, the peak EIT transmission is found to be ~ 0.6, as shown in the Fig. 5.6(b). Hence, EIT transmission of nearly 100% is achieved if the residual wave vector is reduced to zero, i.e., achieve a Doppler-free condition. This thermal vapor system behaves like a cold atomic system when the wave-vector mismatch is eliminated. The usual two-photon excitation processes in a thermal vapor system does not allow a Doppler-free condition [68]. There are certain conditions under which Doppler-free conditions for the three-photon excitation process can be achieved with suitable beam geometry, which has been discussed in [86]. This study aims to achieve a Doppler-free condition with the four-photon excitation process to the Rydberg state leading to a narrow EIT width.

5.5 Variation of EIT peak transmission with k_c

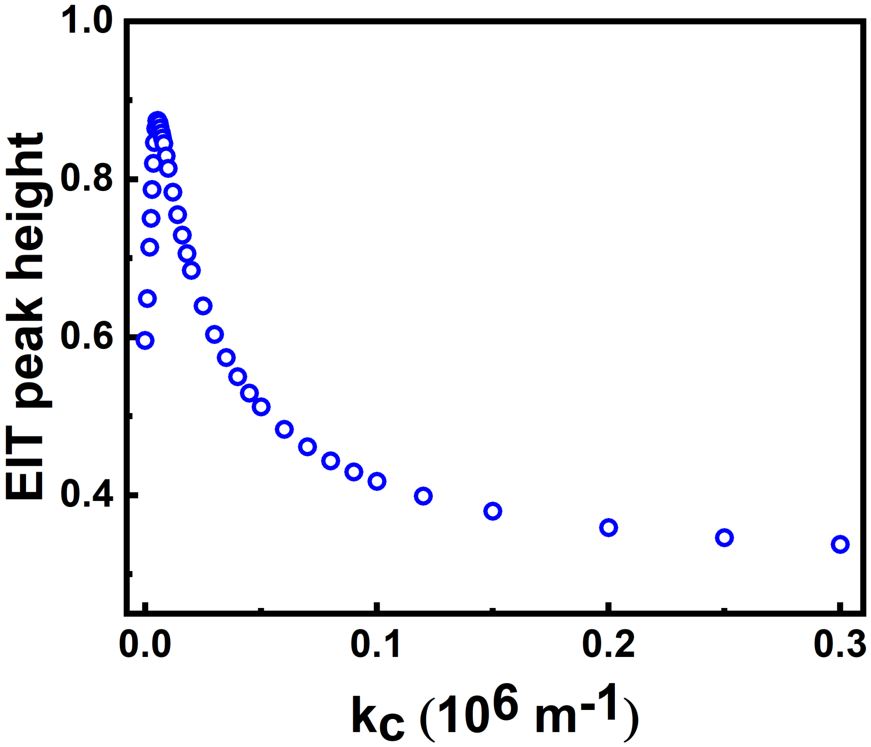

Figure 5.7: EIT transmission peak height as a function of k_c. The laser parameters used in the model are $\Omega_1 = 10$ MHz, $\Omega_2 = 110$ MHz, $\Omega_3 = 25$ MHz, $\Omega_4 = 160$ MHz, $\Delta_1 = 1200$ MHz, $\Delta_3 = 1000$ MHz and Δ_4 is adjusted around Δ_3 to make the transmission symmetric.

To have a proper understanding of the EIT in the four-photon process, the variation of peak EIT transmission with the residual wave vector is studied. The effective probe transition wave vector is kept fixed at $k_p = 0.007 \times 10^6$ m^{-1} and the effective coupling wave vector k_c is changed to vary the residual wave vector Δk. The variation of peak EIT transmission with k_c is shown in Fig. 5.7. Maximum EIT transmission is observed at $\Delta k \approx 0$. The EIT transmission decreases as k_c is varied away from $\Delta k \approx 0$. This is because when $\Delta k = 0$, all the atoms can be resonant to the probe and coupling lasers. Irrespective of the velocity of the atoms in the thermal vapor, all the atoms contribute to the dark state formation and hence, contribute to maximum EIT transmission. When $\Delta k \neq 0$, only a certain velocity class of atoms contribute to the dark state formation. The effective number of atoms participating in the dark state formation reduces compared to $\Delta k \approx 0$. This results in a decrease in the peak EIT transmission as we go away from $\Delta k \approx 0$.

5.6 Reduction of five-level system to an effective three-level system: Adiabatic elimination method

The five-level system involves a 5×5 Hamiltonian, which makes the system complex for various studies. Hence, the method of adiabatic elimination is used to reduce the five-level system to a simpler, effective three-level system. This method involves the elimination of the intermediate states assuming that the change in the population of such states is zero under certain conditions, which has been discussed in Sec. 2.2.5.

5.6.1 Formation of the effective three-level system

The five-level system is reduced to an effective three-level system by eliminating the intermediate states $|e\rangle$ and $|e''\rangle$ as shown in Fig. 5.8. The conditions required for such an elimination are $\Delta_1 \gg \Omega_1, \Gamma_{eg}$ and $\Delta_3 \gg \Omega_3, \Gamma_{e''e'}$. Under these conditions the change in population of the states $|e\rangle$ and $|e''\rangle$ is zero. If the initial population in these states is zero, then there will not be any population transfer to these states, and hence, these states can be neglected or eliminated. The effective-three level system is represented by states $|g\rangle$, $|e'\rangle$ and $|r\rangle$ with effective Rabi frequencies,

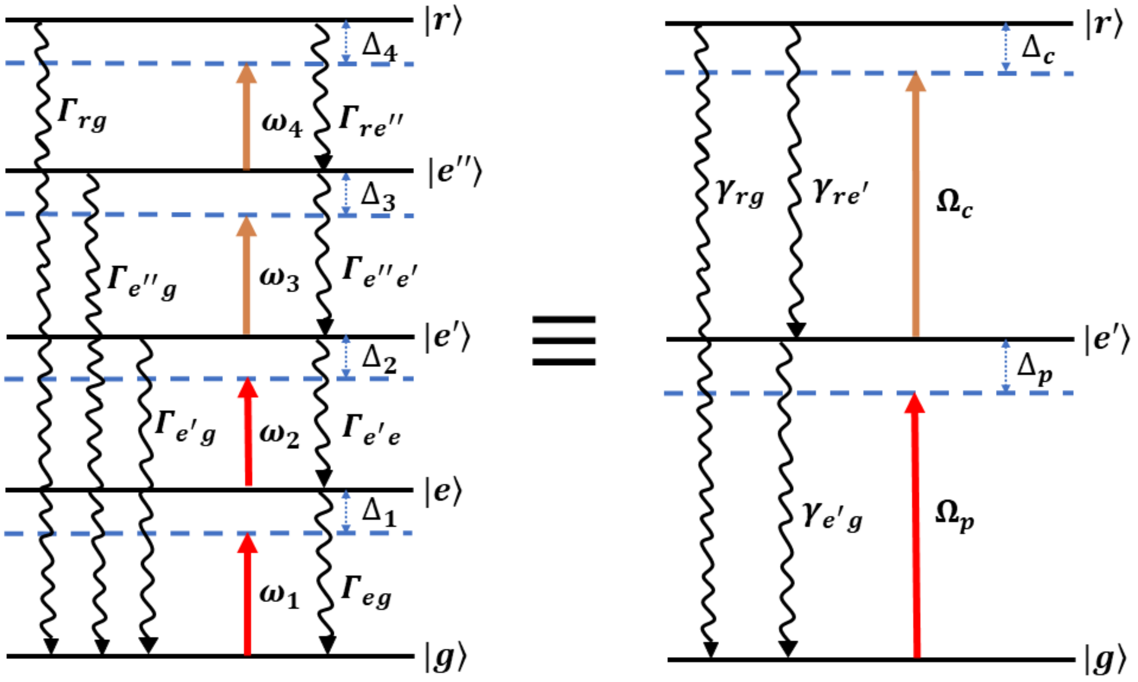
$|r\rangle$
Δ_4
Γ_{rg}
ω_4
$\Gamma_{re''}$
$|e''\rangle$
Δ_3
$\Gamma_{e''g}$
ω_3
$\Gamma_{e''e'}$
$|e'\rangle$
Δ_2
$\Gamma_{e'g}$
ω_2
$\Gamma_{e'e}$
$|e\rangle$
Δ_1
ω_1
Γ_{eg}
$|g\rangle$
$\equiv$
$|r\rangle$
Δ_c
γ_{rg}
$\gamma_{re'}$
Ω_c
$|e'\rangle$
Δ_p
$\gamma_{e'g}$
Ω_p
$|g\rangle$

Figure 5.8: Schematic of reduction of a five-level system (left) to an effective three-level system (right).

effective detunings and effective decay rates. The effective probe and coupling Rabi frequencies are represented by Ω_p and Ω_c, respectively. The effective probe and coupling detunings are represented by Δ_p and Δ_c, respectively.

Using the translation to the Hamiltonian H of the five-level system $\rightarrow H + \frac{\delta_4}{2}I$, the new Hamiltonian is written as

$$H' = \frac{\hbar}{2}\begin{pmatrix} \delta_4 & -\Omega_1 & 0 & 0 & 0 \\ -\Omega_1^* & \delta_4 - 2\delta_1 & -\Omega_2 & 0 & 0 \\ 0 & -\Omega_2^* & \delta_4 - 2\delta_2 & -\Omega_3 & 0 \\ 0 & 0 & -\Omega_3^* & \delta_4 - 2\delta_3 & -\Omega_4 \\ 0 & 0 & 0 & -\Omega_4^* & -\delta_4 \end{pmatrix}$$

The time-dependent schrödinger equation is represented as:

$$i\hbar\frac{\partial}{\partial t}|\psi(t)\rangle = H'|\psi(t)\rangle \tag{5.19}$$

where

$$|\psi(t)\rangle = \begin{pmatrix} C_1(t) \\ C_2(t) \\ C_3(t) \\ C_4(t) \\ C_5(t) \end{pmatrix}.$$

$C_1(t)$, $C_2(t)$, $C_3(t)$, $C_4(t)$ and $C_5(t)$ are the probability amplitudes of the respective components of $|\psi(t)\rangle$. Since $\Delta_1 >> \Omega_1, \Gamma_{eg}$ and $\Delta_3 >> \Omega_3, \Gamma_{e''e'}$, considering the initial population of the states $|e\rangle$ and $|e''\rangle$ to be zero, these states barely get populated. So the change in the population of these states is approximated to zero, i.e. $\frac{\partial}{\partial t}C_2(t) = 0$ and $\frac{\partial}{\partial t}C_4(t) = 0$. These two equations are solved to get $C_2(t)$ and $C_4(t)$ as a linear combination of $C_1(t)$, $C_3(t)$ and $C_5(t)$. These values are then substituted in the equations of motions for $C_1(t)$, $C_3(t)$ and $C_5(t)$ to eliminate $C_2(t)$ and $C_4(t)$. The effective Hamiltonian of the effective three-level system is written as :

$$H_{eff} = \frac{\hbar}{2} \begin{pmatrix} \delta_4 - \frac{|\Omega_1|^2}{\delta_4 - 2\delta_1} & -\frac{\Omega_1\Omega_2}{\delta_4 - 2\delta_1} & 0 \\ -\frac{\Omega_1\Omega_2}{\delta_4 - 2\delta_1} & \delta_4 - 2\delta_2 - \frac{|\Omega_2|^2}{\delta_4 - 2\delta_1} - \frac{|\Omega_3|^2}{\delta_4 - 2\delta_3} & -\frac{\Omega_3\Omega_4}{\delta_4 - 2\delta_3} \\ 0 & -\frac{\Omega_3\Omega_4}{\delta_4 - 2\delta_3} & -\delta_4 - \frac{|\Omega_4|^2}{\delta_4 - 2\delta_3} \end{pmatrix}$$

The effective three-level system is used to study EIT, and hence, the system satisfies four-photon resonance under EIT, i.e., $\delta_4 = 0$ and $\delta_2 = 0$. The Hamiltonian is simplified and written as:

$$H_{eff} = -\frac{\hbar}{2} \begin{pmatrix} 0 & \Omega_p & 0 \\ \Omega_p^* & 2\Delta_p & \Omega_c \\ 0 & \Omega_c^* & 2(\Delta_p + \Delta_c) \end{pmatrix}.$$

Comparing the effective three-level system with an exact three-level system, we observe that the Hamiltonian of the effective system is similar to that of the three-level system with the Rabi frequencies and detunings modified as

$$\Omega_p = \frac{\Omega_1 \Omega_2}{2\Delta_1} \tag{5.20}$$

$$\Omega_c = \frac{\Omega_3 \Omega_4}{2\Delta_3} \tag{5.21}$$

$$\Delta_p = (\Delta_1 + \Delta_2) + \frac{\mid \Omega_1 \mid^2}{4\Delta_1} - \frac{\mid \Omega_2 \mid^2}{4\Delta_1} - \frac{\mid \Omega_3 \mid^2}{4\Delta_3} \tag{5.22}$$

$$\Delta_c = (\Delta_3 + \Delta_4) + \frac{\mid \Omega_2 \mid^2}{4\Delta_1} + \frac{\mid \Omega_3 \mid^2}{4\Delta_3} - \frac{\mid \Omega_4 \mid^2}{4\Delta_3} \tag{5.23}$$

The laser fields will shift the atomic levels by factors known as light shifts. These factors have to be added carefully to the detunings of the effective system such that it includes all the light shifts of the atomic levels induced by the individual laser fields, i.e. $\frac{|\Omega_1|^2}{4\Delta_1}$, $\frac{|\Omega_2|^2}{4\Delta_1}$, $\frac{|\Omega_3|^2}{4\Delta_3}$ and $\frac{|\Omega_4|^2}{4\Delta_3}$. The density matrix of the effective three-level system is a 3×3 matrix ρ_{ij} with $i, j = g, e', r$. The decay and decoherence processes for the effective system are also modified. As discussed earlier, the transition from state $|g\rangle \rightarrow |e'\rangle$, $|e\rangle \rightarrow |e''\rangle$ and $|e'\rangle \rightarrow |r\rangle$ are dipole forbidden. The decay process from state $|e\rangle$ to state $|g\rangle$ has a faster rate as compared to the decay process from state $|e'\rangle$ to state $|e\rangle$, i.e. $\Gamma_{eg} \gg \Gamma_{e'e}$. So the atoms in state $|e'\rangle$ are considered to decay directly to state $|g\rangle$ at a rate $\Gamma_{e'e}$ as there will not be any population inversion in $|e\rangle$. Similarly, the decay process from state $|e''\rangle$ to state $|e'\rangle$ has a faster rate as compared to the decay process from state $|r\rangle$ to state $|e''\rangle$, i.e. $\Gamma_{e''e'} \gg \Gamma_{re''}$. The atoms in state $|r\rangle$ directly decay to state $|e'\rangle$ at a rate $\Gamma_{re''}$. There are also decay terms that take care of the transit time decay rates. So the effective decay rate of the channel $|e'\rangle \rightarrow |g\rangle$ is given by $\gamma_{e'g} \approx \Gamma_{e'e} + \Gamma_{e'g}$. Similarly, the effective decay rate for the channel $|r\rangle \rightarrow |g\rangle$ is $\gamma_{rg} \approx \Gamma_{rg}$ and for $|r\rangle \rightarrow |e'\rangle$ is $\gamma_{re'} \approx \Gamma_{re'}$. These decay rates form the Lindblad operator for the effective system.

5.6.2 Optical Bloch equations

The master equation is solved in the steady state to obtain the optical Bloch equations as:

$$\frac{i}{2}[-2\Delta_p\rho_{ge'} + \Omega_p(2\rho_{e'e'} + \rho_{rr}) - \Omega_p - \Omega_c^*\rho_{gr}] - \frac{\gamma_{e'g}}{2}\rho_{ge'} = 0 \tag{5.24}$$

$$\frac{i}{2}[-2\delta\rho_{gr} + \Omega_p\rho_{e'r} - \Omega_c\rho_{ge'}] - \frac{(\gamma_{rg} + \gamma_{re'})}{2}\rho_{gr} = 0 \tag{5.25}$$

$$\frac{i}{2}[\Omega_p^*\rho_{ge'} - \Omega_p\rho_{e'g} + \Omega_c\rho_{re'} - \Omega_c^*\rho_{e'r}] + \gamma_{re'}\rho_{rr} - \gamma_{e'g}\rho_{e'e'} = 0 \tag{5.26}$$

$$\frac{i}{2}[\Omega_p^*\rho_{gr} - 2\Delta_c\rho_{e'r} + \Omega_c(\rho_{rr} - \rho_{e'e'})] - \frac{(\gamma_{rg} + \gamma_{re'} + \gamma_{e'g})}{2}\rho_{e'r} = 0 \tag{5.27}$$

$$\frac{i}{2}[\Omega_c^*\rho_{e'r} - \Omega_c\rho_{re'}] - (\gamma_{rg} + \gamma_{re'})\rho_{rr} = 0 \tag{5.28}$$

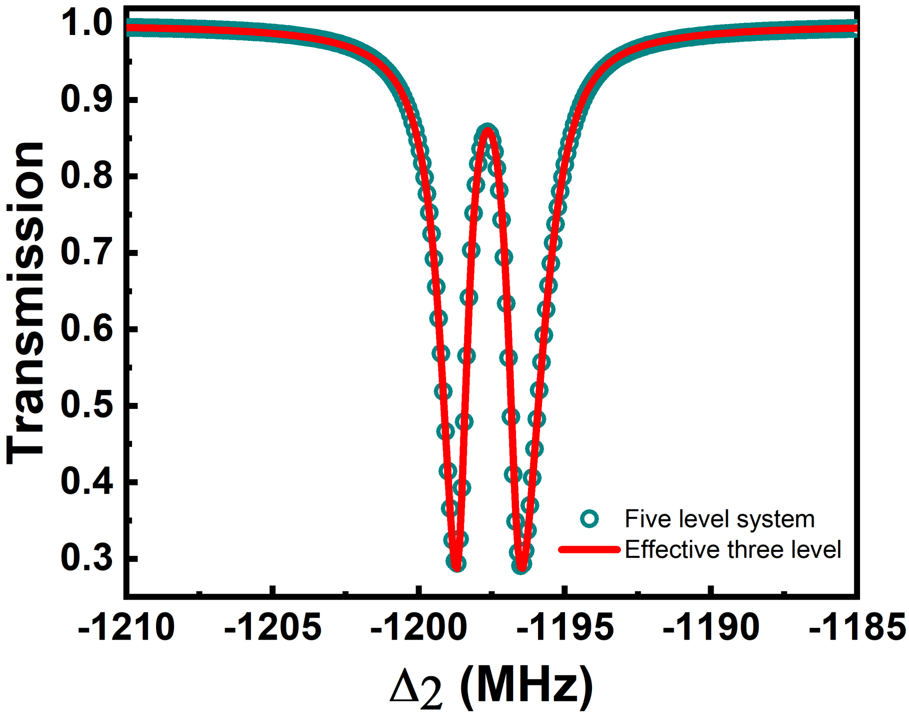

Figure 5.9: Comparison of probe transmission of effective three-level system with a five-level system.

The above equations are solved to evaluate $\rho_{e'e'}$ and $\rho_{e'g}$. The ground to excited state coherence ρ_{eg} is evaluated [68] by substituting $\rho_{e'e'}$ and $\rho_{e'g}$ in the equation given below:

$$\rho_{eg} = \frac{\Omega_1(\rho_{e'e'} - 1) - \Omega_2\rho_{e'g}}{2\Delta_1 + i\Gamma_{eg}}. \tag{5.29}$$

The transmission of the probe for the effective three-level system is evaluated for a thermal atomic medium, and it is compared with the transmission of the probe in a five-level system as shown in Fig. 5.9. It is observed that the probe transmission of an effective three-level system matches perfectly with that of the five-level system. Using the method of adiabatic elimination, a complex system can be reduced to a simpler effective system, and the effective system can be used for the purpose of various studies.

5.7 Experimental proposal

The four-photon excitation to the Rydberg state can be performed experimentally with a real thermal vapor system, i.e., rubidium atomic vapor, as shown in Fig. 5.10. The different available transitions of the rubidium atomic system can be accessed using lasers of available wavelength. The transitions that can be accessed to form the five-level system are $|5S_{\frac{1}{2}}\rangle \rightarrow |5P_{\frac{3}{2}}\rangle$, $|5P_{\frac{3}{2}}\rangle \rightarrow |5D_{\frac{3}{2}}\rangle$, $|5D_{\frac{3}{2}}\rangle \rightarrow |8P_{\frac{1}{2}}\rangle$ and $|8P_{\frac{1}{2}}\rangle \rightarrow |nS_{\frac{1}{2}}\rangle$. The $|5S_{\frac{1}{2}}\rangle \rightarrow |5P_{\frac{3}{2}}\rangle$ excitation can be carried out by a laser of wavelength 780.24 nm, $|5P_{\frac{3}{2}}\rangle \rightarrow |5D_{\frac{3}{2}}\rangle$ excitation can be carried out by a laser of wavelength 776.2 nm, $|5D_{\frac{3}{2}}\rangle \rightarrow |8P_{\frac{1}{2}}\rangle$ excitation can be carried out by a laser of wavelength 2.41 μm, $|8P_{\frac{1}{2}}\rangle \rightarrow |nS_{\frac{1}{2}}\rangle$ excitation can be carried out by a laser of wavelength 2.67 μm. The wave vectors of the laser beams are $k_1 = 1.281655\times10^6$ m^{-1}, $k_2 = 1.288328\times10^6$ m^{-1}, $k_3 = 0.414938 \times 10^6$ m^{-1} and $k_4 = 0.374532 \times 10^6$ m^{-1} respectively. For the rubidium system, the decay rates are $\Gamma_{eg} = 6$ MHz, $\Gamma_{e'e} = 0.65$ MHz, $\Gamma_{e''e'} = 0.3$ MHz and $\Gamma_{re''} = 0.01$ MHz. The transit time decay rates for the system are Γ_{rg}, $\Gamma_{e''g}$, $\Gamma_{e'g}$. The transit time decay rates are taken to be 0.2 MHz. The transition from $|5S_{\frac{1}{2}}\rangle \rightarrow |5D_{\frac{3}{2}}\rangle$, $|5P_{\frac{3}{2}}\rangle \rightarrow |8P_{\frac{1}{2}}\rangle$ and $|5D_{\frac{3}{2}}\rangle \rightarrow |nS_{\frac{1}{2}}\rangle$ are dipole forbidden transitions.

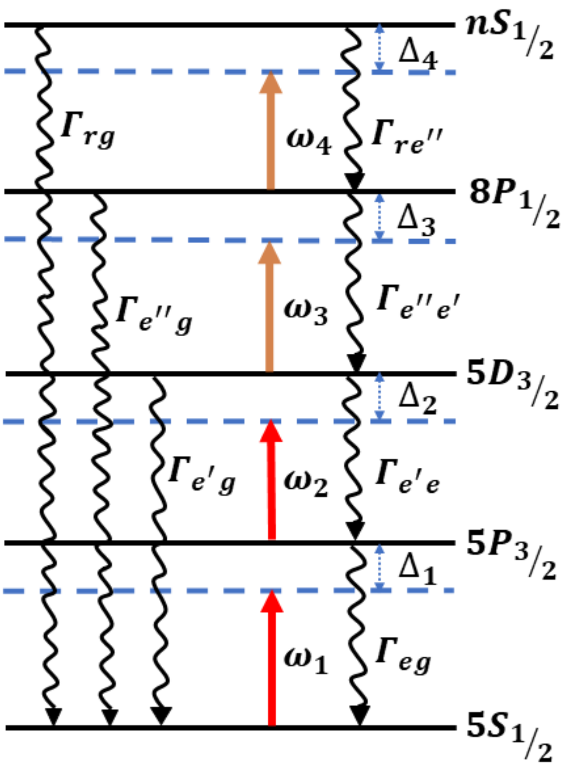
$nS_{1/2}$
Δ_4
Γ_{rg}
ω_4
$\Gamma_{re''}$
$8P_{1/2}$
Δ_3
$\Gamma_{e''g}$
ω_3
$\Gamma_{e''e'}$
$5D_{3/2}$
Δ_2
$\Gamma_{e'g}$
ω_2
$\Gamma_{e'e}$
$5P_{3/2}$
Δ_1
ω_1
Γ_{eg}
$5S_{1/2}$

Figure 5.10: Rubidium energy levels in ladder configuration for four-photon excitation to the Rydberg state.

5.8 Elimination of the residual wave vector using suitable beam geometry

The motion-induced dephasing can be eliminated with the proper choice of wavelength and suitable beam geometry. The transitions are chosen such that the first two excitations have nearly equal wave vectors with the laser beams counter-propagating each other. Also, the third and fourth excitation have nearly equal wave vectors with the respective laser fields counter-propagating each other. This will result in the cancellation of the wave vectors and, in turn, reduced residual wave vector. With the laser configuration as shown in Fig. 5.2, $k_2 > k_1$ and $k_3 > k_4$, therefore $\Delta k = 0.033 \times 10^6$ m^{-1}. This residual wave vector is very large, which leads to a reduction in EIT transparency. Hence, the achieved EIT transparency is very low for such laser configuration, which can be observed from Fig. 5.7. The effective

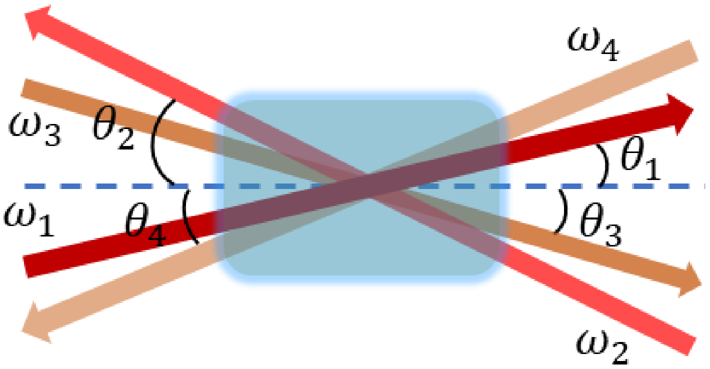

Figure 5.11: Laser beam geometry through rubidium vapor cell.

wave-vector mismatch can be reduced to zero with a suitable choice of beam geometry, i.e., by applying the laser fields at some angles with respect to the horizontal axis of the atomic vapor cell as shown in Fig. 5.11. Let's say the laser field with frequency ω_1 is applied at an angle θ_1, field with frequency ω_2 at an angle θ_2, field with frequency ω_3 at an angle θ_3 and field with frequency ω_4 at an angle θ_4 with respect to the horizontal axis of the vapor cell. In order to completely cancel out the wave vector mismatch, both the vertical and horizontal components of the wave vectors need to be canceled out. This leads to the following two equations:

$$k_1 \cos\theta_1 + k_3 \cos\theta_3 - k_2 \cos\theta_2 - k_4 \cos\theta_4 = 0 \tag{5.30}$$

$$k_1 \sin\theta_1 + k_2 \sin\theta_2 - k_3 \sin\theta_3 - k_4 \sin\theta_4 = 0. \tag{5.31}$$

By solving the two equations, the angles are found out to be $\theta_1 = 6°$, $\theta_2 = 6°$, $\theta_3 = 3°$ and $\theta_4 = 3°$. The angle through which the beams will propagate is very small. This will result in overlapping of the beams in a large optical path length.

5.9 Conclusion

The four-photon excitation to the Rydberg state is performed to study EIT in thermal atomic vapor. The system uses four laser fields where the two pairs of laser fields have a nearly equal wavelength. Proper choice of laser wavelength and suitable beam geometry results in the elimination of motion-induced dephasing in the system. The reduced wave-vector mismatch provides an opportunity to achieve 100 % EIT transparency. Even though it is a thermal vapor system, the system behaves similar to a cold atomic system with the elimination of the residual wave-vector to zero. Instead of a complex cold atomic system, the thermal vapor system provides a better platform for building quantum devices due to its simplicity as compared to the cold atomic system. Such a four-photon system has huge technological applications as the Rydberg atomic systems have been paving the way for quantum technology [90].

Chapter 6

Outlook: Microwave field sensing using four-photon excitation to the Rydberg state in thermal rubidium vapor

The four-photon excitation process can achieve a narrow EIT transition, resulting in better sensitivity of the electric field. The electric field sensitivity of a two-photon Rydberg EIT-based sensor in a thermal atomic medium is reported to be 30 μVcm^{-1}Hz$^{-1/2}$ [7]. This sensitivity was improved to 5 μVcm^{-1}Hz$^{-1/2}$ using a homodyne detection method [26]. As discussed in chapter 3, measured electric field sensitivity is given by $\frac{E_{min}}{\sqrt{Hz}} = \frac{h}{\mu\sqrt{T_2 N}}$ [12] where E_{min} is the minimum detectable electric field limited by the line-width of the EIT spectrum γ_{EIT} [43], T_2 is the dephasing time of the EIT process and N is the number of atoms participating in the detection process. The minimum detectable field can be improved with the help of the four-photon excitation method, where the motion-induced dephasing in the system is eliminated through the proper choice of laser wavelengths and suitable beam geometry. The details of the four-photon excitation method have been discussed in the chapter 5. As an outlook to the thesis, this chapter provides a theoretical study on microwave field sensing using the four-photon Rydberg EIT in a thermal vapor system. A comparison of the field sensing using two-photon excitation and four-photon excitation process is provided. Using suitable laser parameters, a narrow linewidth EIT is achieved, which results in higher sensitivity of the detected electric field. Finally, the chapter discusses the experimental plan to perform microwave field sensing with a four-photon excitation process to the Rydberg state.

6.1 Theoretical model for microwave field sensing with four-photon excitation process

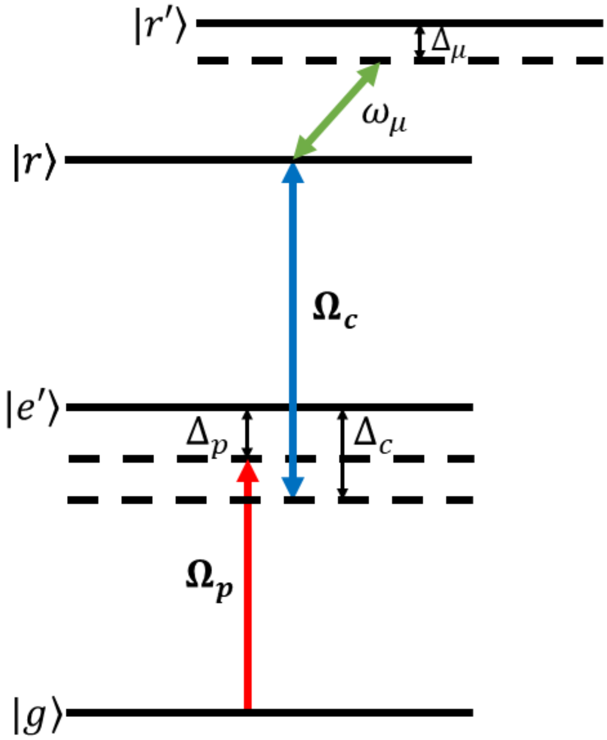

Figure 6.1: Schematic of energy levels in ladder configuration.

The four-photon excitation process can be used to achieve Rydberg EIT using a five-level system. Application of a microwave field, results in coupling of two neighboring Rydberg states. The microwave field sensing with a four-photon excitation process involves another Rydberg state along with the five-level system, which makes the system complex. Hence, the method of adiabatic elimination is used to reduce the five-level system to a simpler, effective three-level system which has been discussed in Sec. 5.6. So, the atomic model consists of a four-level system with states $|g\rangle$, $|e'\rangle$, $|r\rangle$ and $|r'\rangle$ where the lower three levels $|g\rangle$, $|e'\rangle$ and $|r\rangle$ correspond to the effective three-level system with $|r\rangle$ being the Rydberg state and the fourth level $|r'\rangle$ is another nearby Rydberg state. As discussed in the previous chapter, the effective probe and coupling Rabi frequency are given by $\Omega_p = \frac{\Omega_1\Omega_2}{2\Delta_1}$ and $\Omega_c = \frac{\Omega_3\Omega_4}{2\Delta_3}$ respectively. The effective probe and coupling detunings are given by $\Delta_p = \Delta_1 + \Delta_2 + \frac{|\Omega_1|^2}{4\Delta_1} - \frac{|\Omega_2|^2}{4\Delta_1} - \frac{|\Omega_3|^2}{4\Delta_3}$ and $\Delta_c = \Delta_3 + \Delta_4 + \frac{|\Omega_2|^2}{4\Delta_1} + \frac{|\Omega_3|^2}{4\Delta_3} - \frac{|\Omega_4|^2}{4\Delta_3}$. The effective probe transition has effective wave-vector magnitude to be $k_p = k_2 - k_1$ and the effective coupling transition has effective wave-vector magnitude as $k_c = k_3 - k_4$. The residual wave-vector for the system is defined as $\Delta k = k_c - k_p$. The Rabi frequency (detuning) of the microwave field is Ω_μ (Δ_μ), and the magnitude of the wave vector of the microwave field is k_μ which is very small as compared to the optical fields. The energy level of the system is represented by Fig. 6.1.

The total Hamiltonian for the given system, in a suitable rotating frame, is written as

$$H = -\frac{\hbar}{2}\begin{pmatrix} 0 & \Omega_p & 0 & 0 \\ \Omega_p^* & 2\Delta_p - k_p v & \Omega_c & 0 \\ 0 & \Omega_c^* & 2(\Delta_p + \Delta_c) & \Omega_\mu \\ 0 & 0 & \Omega_\mu^* & 2(\Delta_p + \Delta_c + \Delta_\mu) \end{pmatrix}.$$

For the thermal vapor system, the detunings are modified as $\Delta_1 \rightarrow \Delta_1 - k_1 v$, $\Delta_2 \rightarrow \Delta_2 + k_2 v$, $\Delta_3 \rightarrow \Delta_3 - k_3 v$ and $\Delta_4 \rightarrow \Delta_4 + k_4 v$. The Master equation for the system is written as $\dot{\rho} = \frac{i}{\hbar}[\rho, H] + \mathcal{L}_{\mathcal{D}}(\rho)$ where ρ is the 4×4 density matrix of the system and $\mathcal{L}_{\mathcal{D}}(\rho)$ is the Lindblad operator which includes the decay and decoherence processes occurring in the system. The decay rates in the system are $\gamma_{re'} \approx \Gamma_{re''}$, $\gamma_{rg} \approx \Gamma_{rg}$, $\gamma_{e'g} \approx \Gamma_{e'e} + \Gamma_{e'g}$, $\Gamma_{r'r}$ and $\Gamma_{r'g}$ where the population decay rates are given by $\Gamma_{e'e} = 0.65$ MHz, $\Gamma_{re''} = 1$ kHz and $\Gamma_{r'r} = 0.5$ kHz and the transit time decay rates are $\Gamma_{e'g} = \Gamma_{rg} = \Gamma_{r'g} = 0.2$ MHz. The optical Bloch equations are similar to the four-level system discussed in the chapter. 3, which are solved to evaluate $\rho_{e'e'}$ and $\rho_{e'g}$.

The ground to excited state coherence ρ_{eg} is evaluated as [68]:

$$\rho_{eg} = \frac{\Omega_1(\rho_{e'e'} - 1) - \Omega_2\rho_{e'g}}{2\Delta_1 + i\Gamma_{eg}}. \tag{6.1}$$

The Doppler averaged probe susceptibility coupling the $|g\rangle \rightarrow |e\rangle$ transition is given by

$$\chi(\omega_1) = \frac{2N|\ \mu_{ge}\ |^2}{\hbar\epsilon_0\Omega_1}\frac{1}{\sqrt{\pi}v_p}\int_{-\infty}^{\infty}\rho_{eg}e^{-\frac{v^2}{v_p^2}}dv \tag{6.2}$$

where μ_{ge} is the transition dipole moment, N is the density of the atomic vapor, and v_p is the most probable speed of the atoms. The transmission of the probe beam is $T = e^{-\Im(\chi)k_1 l}$ where l is the length of the atomic medium. The vapor density is taken to be 4.5×10^{10} cm^{-3}, and the length of the vapor cell is 5 cm.

6.2 Effect of a microwave field on four-photon EIT

The probe transmission in the case of the four-photon excitation process is represented by Fig. 6.2, where the solid red line and solid blue line represent the transmission of the probe field in the absence and presence of a microwave field, respectively. We observe an EIT linewidth of 1.8 MHz. The application of microwave field results in splitting of the EIT peak where the frequency difference between the AT splitted peak depends on the microwave field Rabi frequency. Before providing an estimate of how the sensitivity of electric field measurement can be improved using this system, first, the microwave field sensitivity in the case of the two-photon Rydberg EIT system is needed to be understood.

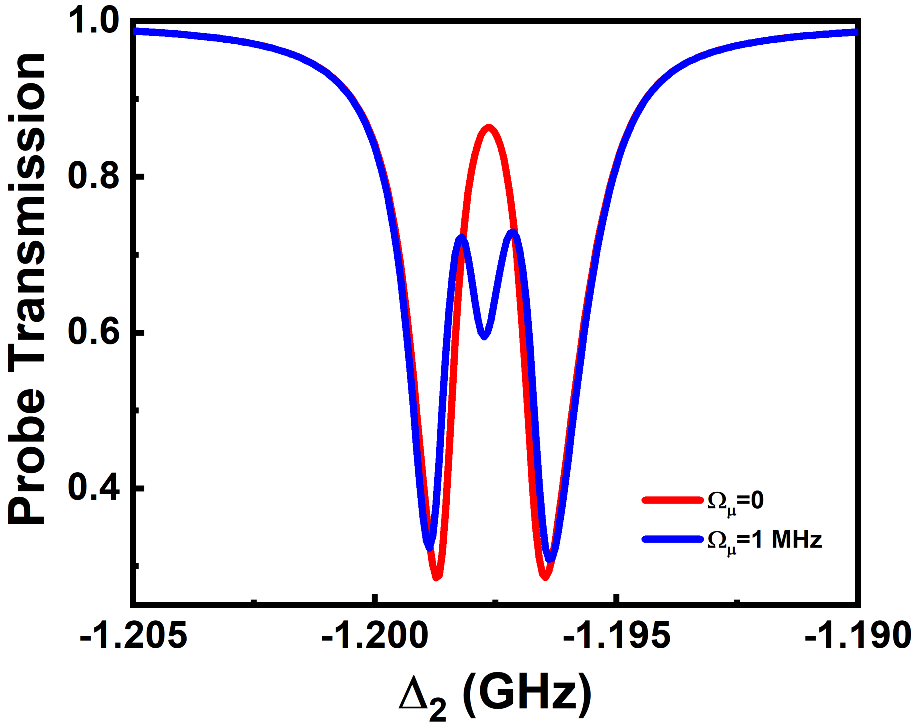

Figure 6.2: Probe transmission: (a) in absence of microwave field ($\Omega_\mu = 0$) and (b) in presence of microwave field ($\Omega_\mu = 1$ MHz). $k_p = k_c = 0.007 \times 10^6\ \mathrm{m}^{-1}$ and $k_\mu = 0.00005 \times 10^6\ \mathrm{m}^{-1}$. The laser parameters used in the model are $\Omega_1 = 10$ MHz, $\Omega_2 = 110$ MHz, $\Omega_3 = 25$ MHz, $\Omega_4 = 160$ MHz, $\Delta_1 = 1200$ MHz, $\Delta_3 = 1000$ MHz, $\Delta_\mu = 0$ and Δ_4 is adjusted around Δ_3 to make the transmission symmetric.

6.3 Microwave field sensing with two-photon Rydberg EIT system

There has been a study on microwave field sensing with the two-photon Rydberg EIT process where the atoms are excited to the Rydberg state $53D_{5/2}$ using a 780 nm probe and a 480 nm coupling field. A microwave field couples $53D_{5/2}$ state to $54P_{3/2}$ state with transition dipole moment of 3611 ea_0. The study reports the minimum detectable microwave electric field to be 8 μV/cm which produces a change of 0.02% in probe transmission [7]. This section describes the effect of microwave field in a two-photon Rydberg EIT system which is used to find the minimum detectable field. The schematic of microwave field sensing with the two-photon Rydberg EIT

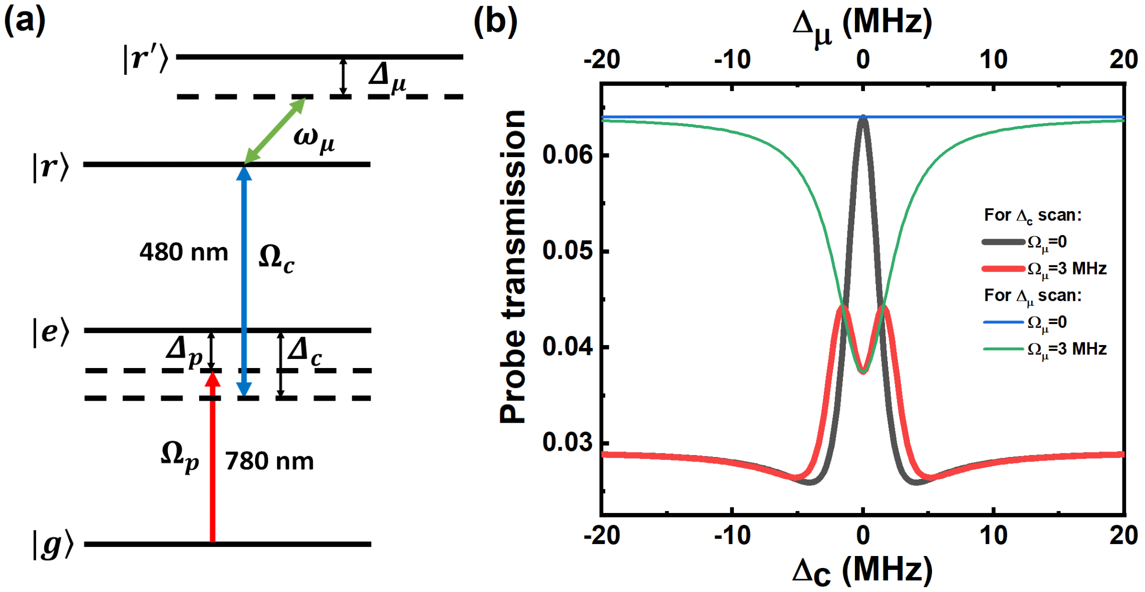

Figure 6.3: (a) Schematic of a four-level system for microwave field sensing with a two-photon excitation process. (b) Probe transmission as a function of Δ_c and Δ_μ in the absence ($\Omega_\mu = 0$) and presence of microwave field ($\Omega_\mu = 3$ MHz). The laser parameters are: $\Omega_p = 0.5$ MHz, $\Omega_c = 2$ MHz, $\Delta_p = 0$, $\Gamma_{eg} = 6$ MHz, $\Gamma_{re} = 1$ kHz, $\Gamma_{r'r} = 0.5$ kHz, $\Gamma_{rg} = 0.2$ MHz, $\Gamma_{r'g} = 0.2$ MHz, $k_p = 1.28166 \times 10^6$ m^{-1}, $k_c = 2.08333 \times 10^6$ m^{-1} and $k_\mu = 0.00005 \times 10^6$ m^{-1}.

process is shown in Fig. 6.3(a). In the absence of a microwave field, an EIT peak is observed (black line) as a function of coupling field detuning as shown in 6.3(b). If the microwave field detuning is scanned, a constant peak EIT transmission (blue line) is observed. Application of microwave field results in splitting of the EIT peak (red line), which can be observed as a function of coupling detuning. With the microwave field scan, the decrease in probe transmission around the resonance is observed as a function of microwave detuning (green line). If the microwave field is very weak, such that the splitting of the EIT peak is less than the EIT linewidth, then it becomes difficult to differentiate the splitting and estimate the strength of the microwave field. In such cases, observing the change in probe transmission as a function of microwave detuning gives an estimate of the strength of the microwave field. Fig. 6.4 shows the percentage of reduction in probe transmission as a function of microwave field strength calculated using Eq. 3.19. It is observed that a microwave field strength of 8 μV/cm produces a change of 0.02%, similar to that reported in

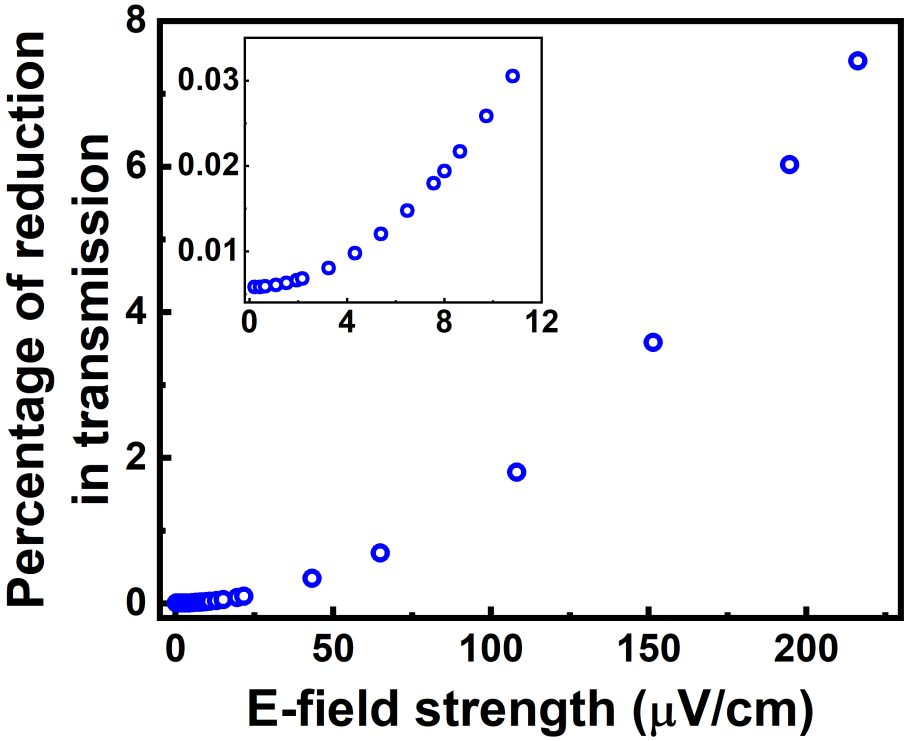

Figure 6.4: Percentage of reduction in probe transmission as a function of microwave E-field strength. The laser parameters are: $\Omega_p = 0.5$ MHz, $\Omega_c = 2$ MHz, $\Delta_p = 0$, $\Delta_c = 0$, $\Gamma_{eg} = 6$ MHz, $\Gamma_{re} = 1$ kHz, $\Gamma_{r'r} = 0.5$ kHz, $\Gamma_{rg} = 0.2$ MHz, $\Gamma_{r'g} = 0.2$ MHz, $k_p = 1.28166 \times 10^6$ m^{-1}, $k_c = 2.08333 \times 10^6$ m^{-1} and $k_\mu = 0.00005 \times 10^6$ m^{-1}.

Ref. [7].

6.4 Microwave field sensing with four-photon Rydberg EIT system

To compare microwave sensing using in a four-photon Rydberg EIT system with a two-photon system, the percentage of reduction in probe transmission as a function of microwave Rabi frequency and microwave field strength for the four-photon system is also studied. This is represented in Fig. 6.5. In order to produce a change of 0.02%, similar to that of a two-photon excitation process, a microwave field strength of 4 μV/cm is needed, which is two times smaller than the minimum field detected using a two-photon Rydberg EIT method. The four-photon excitation process is

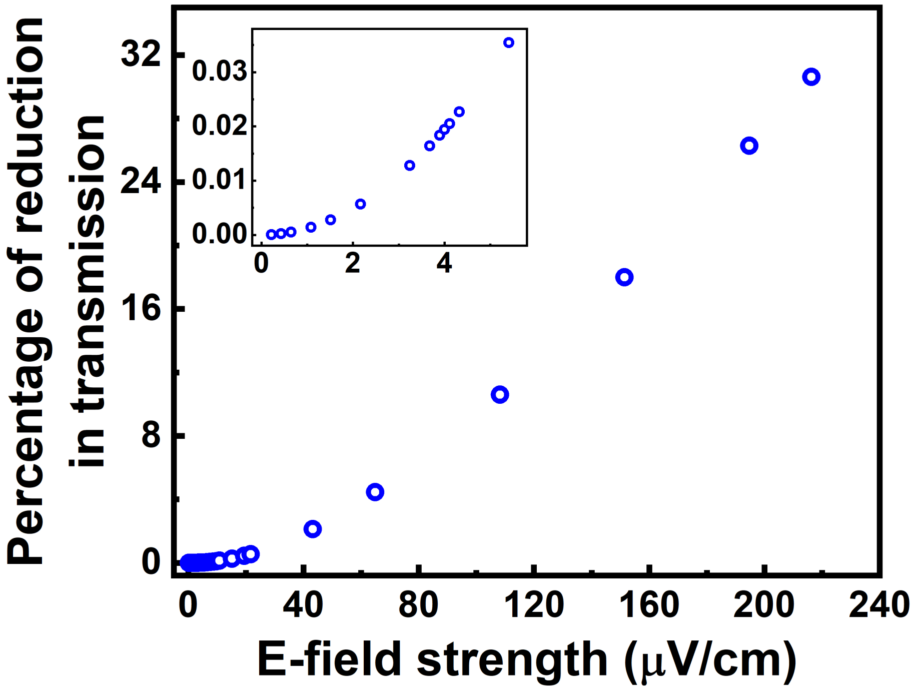

Figure 6.5: Percentage of reduction in probe transmission with varying microwave E-field strength. $k_p = k_c = 0.007 \times 10^6$ m^{-1} and $k_\mu = 0.00005 \times 10^6$ m^{-1}. The laser parameters used in the model are $\Omega_1 = 10$ MHz, $\Omega_2 = 110$ MHz, $\Omega_3 = 25$ MHz, $\Omega_4 = 160$ MHz, $\Delta_1 = 1200$ MHz, $\Delta_3 = 1000$ MHz, $\Delta_\mu = 0$ and Δ_4 is adjusted around Δ_3 to make the transmission symmetric.

used to achieve higher sensitivity, as discussed in the following sections.

6.5 Achieving a narrow EIT line-width

It is known that the minimum detectable field depends on the EIT linewidth γ_{EIT}. To achieve a narrow linewidth EIT, suitable laser parameters are needed to be used, and the wave-vector mismatch has to be reduced to zero. The laser parameters considered for this study are $\Omega_1 = 1$ MHz, $\Omega_2 = 30$ MHz, $\Omega_3 = 20$ MHz, $\Omega_4 = 50$ MHz, $\Delta_1 = 1200$ MHz and $\Delta_3 = 1000$ MHz. The population decay rates considered in the calculation remain the same as discussed in Sec. 6.1. The transit time decay rate is considered to be 10 kHz. Such a small transit time decay rate can be achieved by expanding the beam diameter to 2 cm with the help of lenses. The magnitude of effective wave-vectors is considered to be $k_p = k_c = 0.00005 \times 10^6$ m^{-1} which are

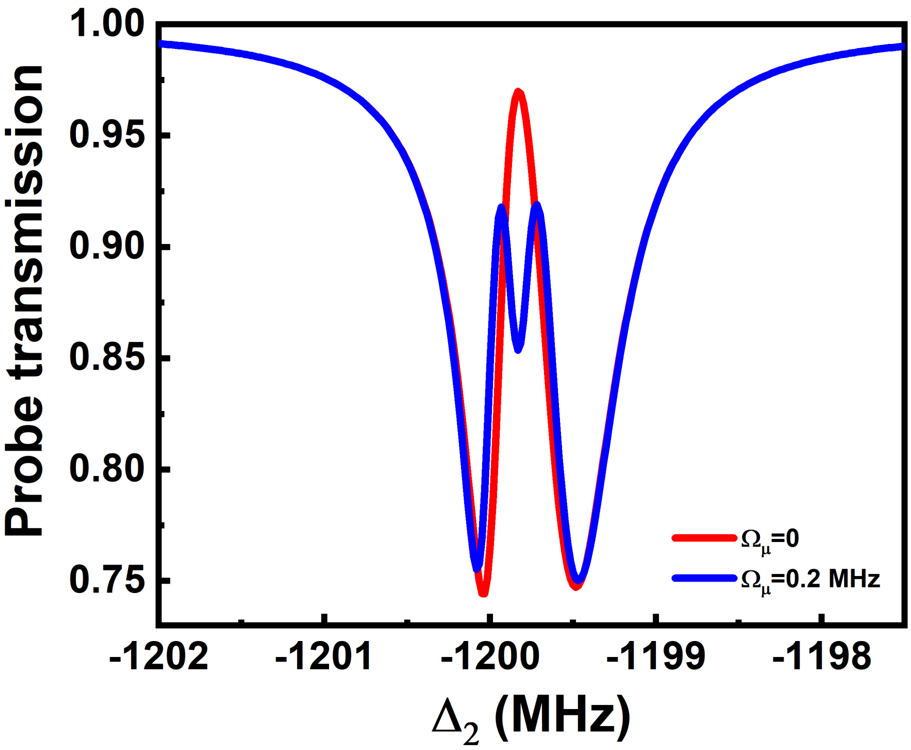

Figure 6.6: Probe transmission: (a) in the absence of microwave field ($\Omega_\mu = 0$) and (b) in presence of microwave field ($\Omega_\mu = 0.2$ MHz). $k_p = k_c = k_\mu = 0.00005 \times 10^6$ m^{-1}. The laser parameters used in the model are $\Omega_1 = 1$ MHz, $\Omega_2 = 30$ MHz, $\Omega_3 = 20$ MHz, $\Omega_4 = 50$ MHz, $\Delta_1 = 1200$ MHz, $\Delta_3 = 1000$ MHz, $\Delta_\mu = 0$ and Δ_4 is adjusted around Δ_3 to make the transmission symmetric.

same as the magnitude of the microwave field wave-vector. The probe transmission is represented by Fig. 6.6 where the red line represents the EIT linewidth of 230 kHz, and the blue line represents the splitting in the EIT signal in the presence of the microwave field.

The change in probe transmission is studied while scanning the microwave detuning. Fig. 6.7 represents the percentage of reduction in probe transmission with varying microwave field strength. It is observed that a 0.02 % reduction in probe transmission can be seen for a microwave field of 1.36 μV/cm with the help of a narrow four-photon Rydberg EIT. This is the same achievable experimental condition as has been reported in [7]. This minimum field observed is 5.88 times smaller as compared to the microwave field detected using a two-photon Rydberg EIT system, which will result in better sensitivity of the measured electric field.

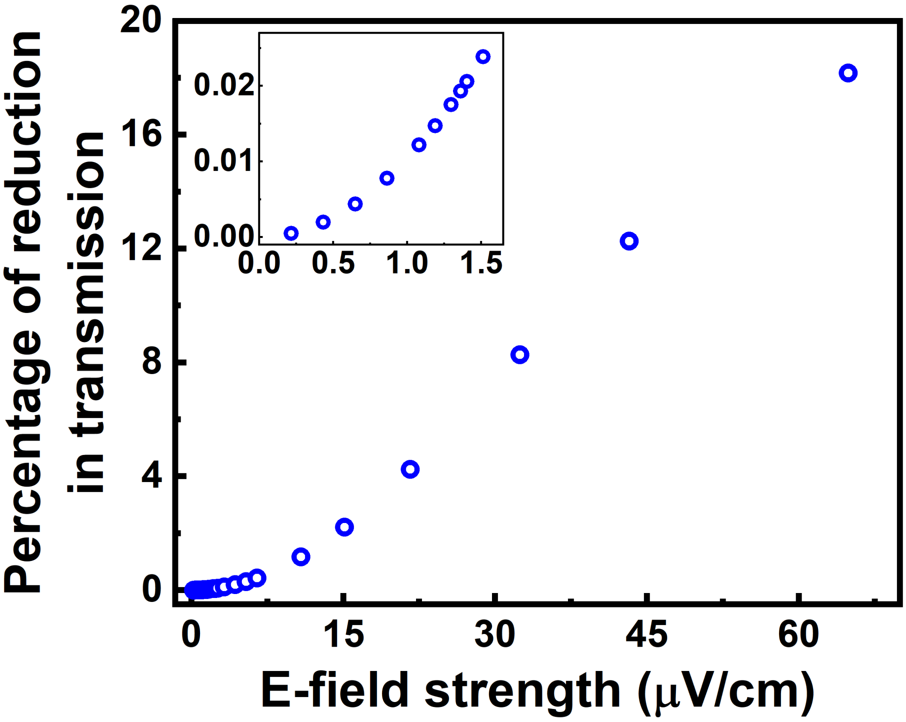

Figure 6.7: Percentage of reduction in probe transmission with varying microwave E-field strength. $k_p = k_c = k_\mu = 0.00005 \times 10^6$ m^{-1}. The laser parameters used in the model are $\Omega_1 = 1$ MHz, $\Omega_2 = 30$ MHz, $\Omega_3 = 20$ MHz, $\Omega_4 = 50$ MHz, $\Delta_1 = 1200$ MHz, $\Delta_3 = 1000$ MHz, $\Delta_\mu = 0$ and Δ_4 is adjusted around Δ_3 to make the transmission symmetric.

6.6 Sensitivity of electric field

The sensitivity of detected electric field is given by $\frac{E_{min}}{\sqrt{Hz}} = \frac{h}{\mu\sqrt{T_2 N}}$ [12] and is reported to be 30 μVcm^{-1}Hz$^{-1/2}$ for a two-photon Rydberg EIT system [7] with $T_2 \sim 5$ μs. If the residual wave vector is non-zero, which is the case in a two-photon Rydberg EIT system, then all the atoms do not participate in the EIT process. Only a certain class of atoms become resonant to the probe and coupling field. Elimination of residual wave-vector makes all the atoms resonant to the probe and coupling field, hence allowing participation of all the atoms in the EIT process. The effective number of atoms participating in the detection of the electric field in the two-photon EIT process is $\sim \frac{1}{400}$ times the density of atoms inside the atomic vapor cell. As discussed earlier, the minimum detectable electric field improves nearly six times using the four-photon Rydberg EIT process. Considering the increase in the effective number of atoms participating in the EIT process, minimum detectable field, and transit time decay of 10 kHz, the improvement in total sensitivity is $\sim \frac{1}{6\sqrt{400*20}} = \frac{1}{540}$ times where $T_2 = 100\ \mu$s. Using this method, an electric field sensitivity of $\frac{30}{540}\ \mu\text{Vcm}^{-1}\text{Hz}^{-1/2} \sim 55\ \text{nVcm}^{-1}\text{Hz}^{-1/2}$ can be achieved. This estimate is made considering the experiment is performed in free space to measure the electric field strength. The actual plan for the experiment is to work with a microwave waveguide inside a vacuum chamber.

6.7 Experimental plan

6.7.1 Beam geometry

As discussed earlier, the residual wave-vector is eliminated with the help of a proper choice of the wavelength of laser fields and selecting beam geometry at suitable angles, aligned with respect to the horizontal axis of the vapor cell [89]. Small effective wave-vectors of $k_p = k_c = 0.00005 \times 10^6\ \text{m}^{-1}$ can be achieved with non-collinear beam geometry. The laser fields ω_1, ω_2, ω_3 and ω_4 need to be oriented with an angle of $\theta_1 = 6°$, $\theta_2 = 6°$, $\theta_3 = 2.8°$ and $\theta_4 = 2.8°$ respectively.

6.7.2 Using a microwave waveguide

A co-planar microwave waveguide has been designed to apply the microwave field shown in Fig. 6.8. The waveguide has dimensions of 72 mm × 35 mm. It is made up of a dielectric substrate where the conductor is situated on one side of the substrate. It consists of a conducting region represented by the thick red-colored line at the center. The conductor is separated from the two sides by two slots represented by blue lines. The back side of the dielectric is grounded. SMA connectors are fitted to the waveguide for electrical connections. These will also be used for mounting the waveguide to the vacuum chamber designed for the experiment. In a co-planar

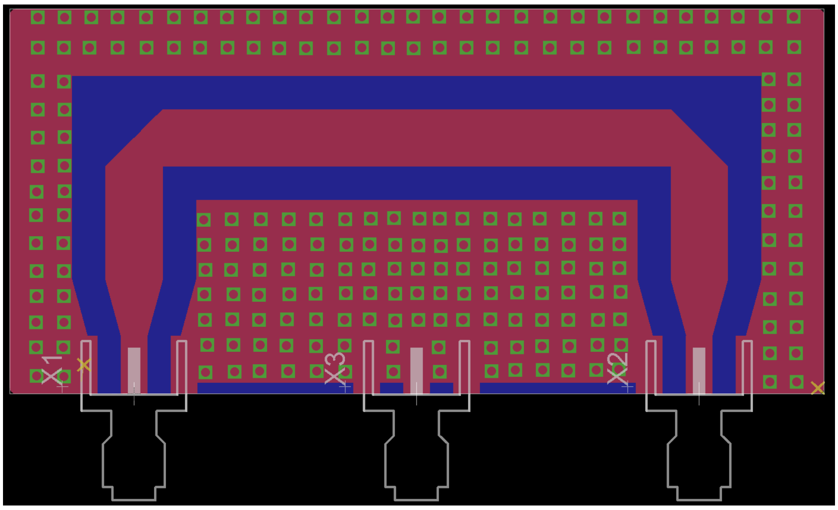

Figure 6.8: Microwave wave-guide.

waveguide, the central conductor has a positive potential with respect to the two adjacent ground planes. The co-planar waveguide propagates quasi-TEM modes where electromagnetic wave exists partly in the air and partly above it. The evanescent waves are concentrated in a few square millimeters region. The laser fields will interact with the evanescent waves of the microwave waveguide as they will be made to pass nearly 1mm above the surface of the waveguide. A beam diameter of 2 cm cannot be achieved inside the chamber to have a smaller transit time decay rate which enhances the sensitivity. However, coupling the optical field to the evanescent waves of the microwave waveguide greatly improves the sensor sensitivity [91].

6.7.3 Design of the vacuum chamber for four-photon excitation experiment

A schematic of the vacuum chamber has been designed using SOLIDWORKS to carry out the four-photon excitation experiment, as shown in Fig. 6.9. One face of the chamber of 63 CF will be used to mount the chamber on the optical table, which is the back face of the shown figure. As shown in the figure, the front face of the chamber, with a 63 CF flange, will be used for mounting the waveguide through the SMA connectors. The 63 CF flange is shown in Fig. 6.10, which is also designed

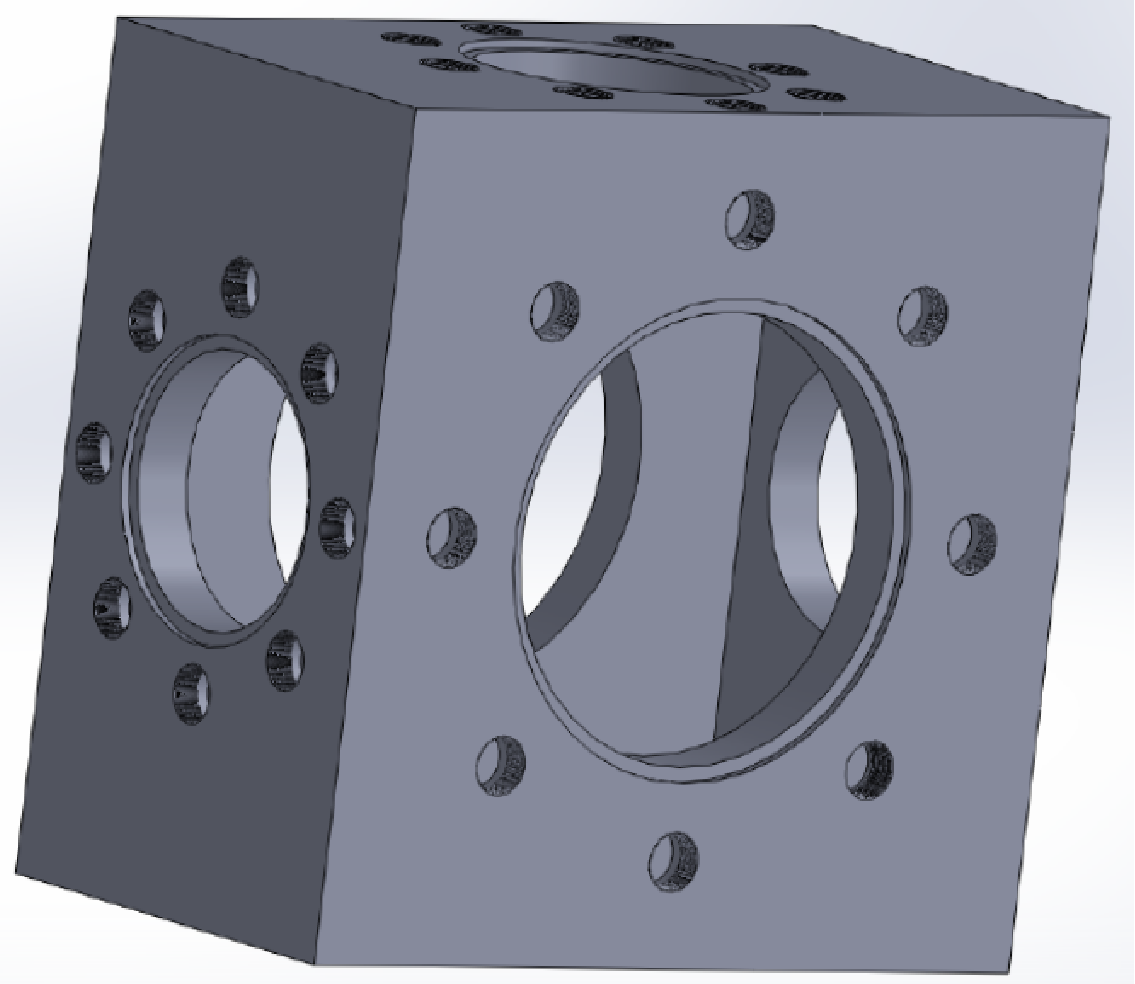

Figure 6.9: Design of vacuum chamber for four-photon experiment.

using SOLIDWORKS. The two 40 CF flange designs at the two side faces will be used to mount two MgF_2 glass windows. These are special windows that will allow the light of all four wavelengths, 780.24 nm, 776.2 nm, 2.41 μm, and 2.67 μm (NIR and MIR) to pass through the chamber. One of the faces with a 40 CF flange design, which is the top face, will be used to mount the turbo pump. Another face with a 40 CF flange design, the down face, will be used to mount the ion pump, rubidium source, and a vacuum gauge using a four-way cross connector. Inside the vacuum chamber, the pressure maintained will be of the order of 10^{-7}-10^{-8} torr using the turbo pump and ion pump.

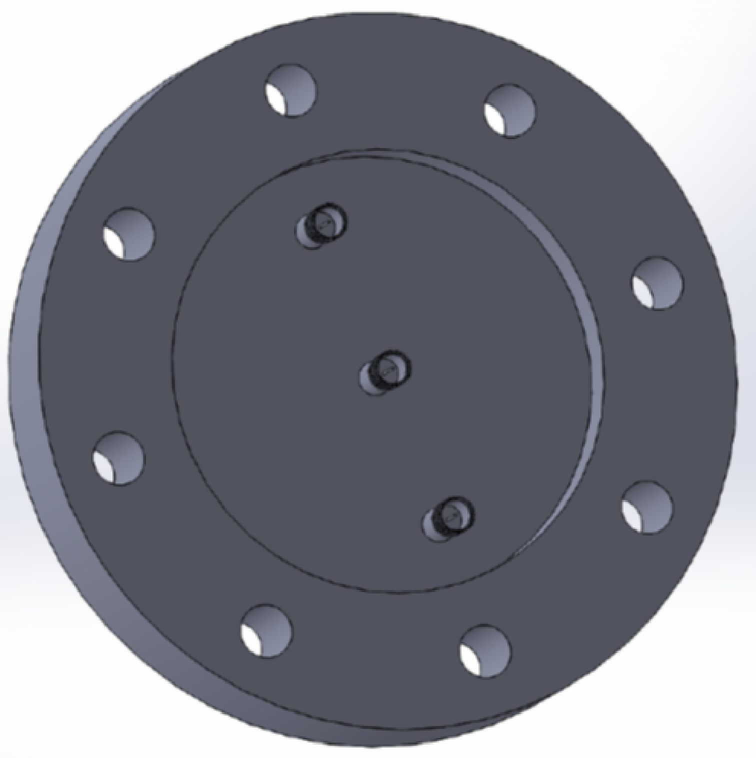

Figure 6.10: 63 CF flange design for mounting the wave-guide.

6.8 Conclusion

The microwave field sensing using a two-photon excitation process has limited sensitivity. This limitation is primarily because of the significant wave-vector mismatch. This leads to a broad EIT linewidth, and also, the effective number of atoms participating in the detection process is less. Using the four-photon excitation to the Rydberg state, a narrow linewidth EIT of 230 kHz can be achieved. The effective number of atoms participating in the detection can be increased due to the elimination of motion-induced dephasing in the system with suitable beam geometry. Also, the transit time decay rate can be reduced with the use of larger diameter beams. All these factors can result in achieving a higher sensitivity of ~ 55 nVcm^{-1}Hz$^{-1/2}$ for free space experiments.

Appendix A

Electromagnetically induced transparency (EIT) in the strong blockade regime using four-photon excitation to the Rydberg state in thermal atomic vapor

Electromagnetically induced transparency (EIT) using the four-photon excitation to the Rydberg state has been discussed in detail in chapter 5 [89]. The four-photon excitation process to the Rydberg state has also been explored to investigate the phenomenon of Rydberg blockade using two interacting Rydberg atoms. The study of EIT will be discussed in the strong blockade regime in thermal atomic vapor in this appendix. The atomic model of a five-level system has been discussed in chapter 5, and it has been shown that the five-level system can be reduced to an effective three-level system using an adiabatic elimination method. Using the five-level system to study the Rydberg blockade phenomenon leads us to a Hamiltonian of order 25×25. The effective three-level system is very useful for developing the two-atom model as it leads to a simpler Hamiltonian for the system of order 9×9. Hence, further studies are based on the model developed using an effective three-level system.

A.1 Development of two-atom model

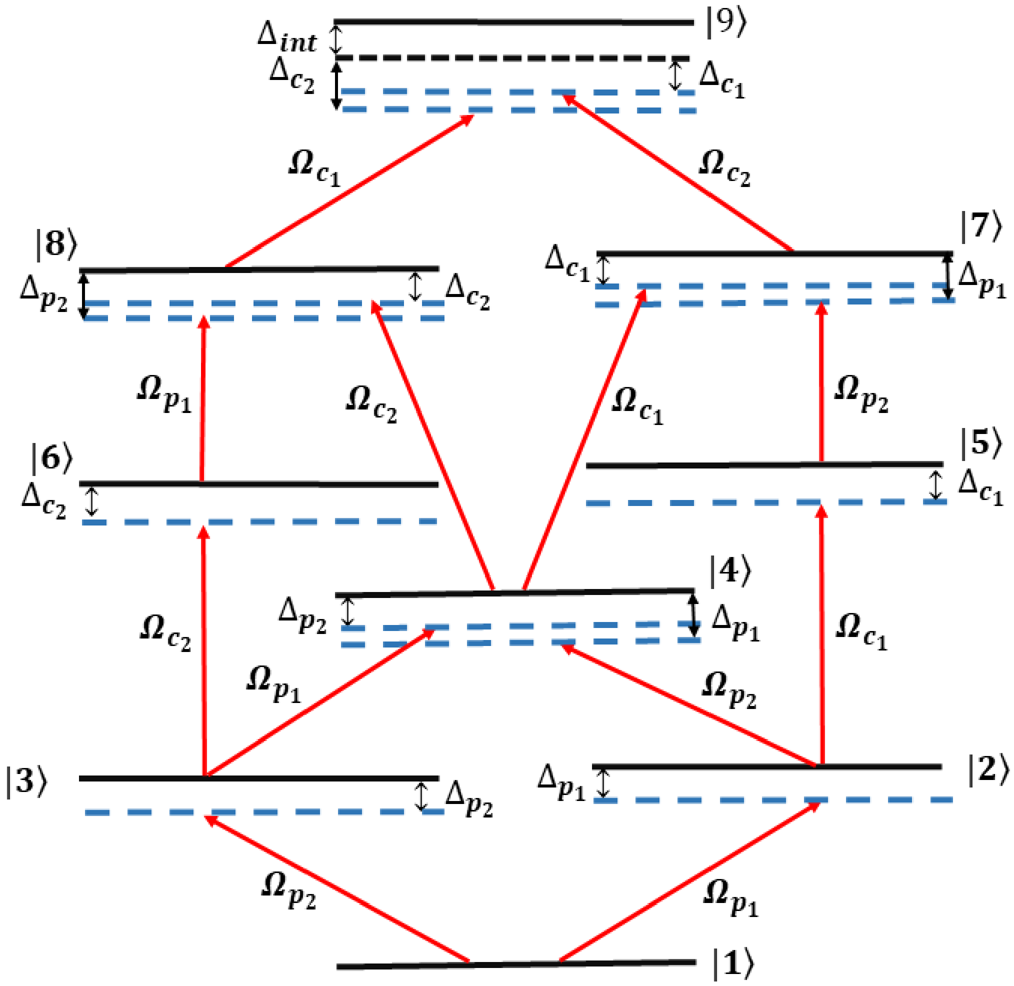
Δ_{int}
$|9\rangle$
Δ_{c_2}
Δ_{c_1}
Ω_{c_1}
Ω_{c_2}
$|8\rangle$
$|7\rangle$
Δ_{p_2}
Δ_{c_2}
Δ_{c_1}
Δ_{p_1}
Ω_{p_1}
Ω_{c_2}
Ω_{c_1}
Ω_{p_2}
$|6\rangle$
$|5\rangle$
Δ_{c_2}
Δ_{c_1}
$|4\rangle$
Δ_{p_2}
Δ_{p_1}
Ω_{c_2}
Ω_{p_1}
Ω_{p_2}
Ω_{c_1}
$|3\rangle$
Δ_{p_2}
Δ_{p_1}
$|2\rangle$
Ω_{p_2}
Ω_{p_1}
$|1\rangle$

Figure A.1: Energy level scheme for the two-atom system. Each atom is in an effective three-level system in a ladder configuration.

The energy level diagram for the composite two-atom system is represented in Fig. A.1. Each atom lies in an effective three-level system consisting of states$|g\rangle$, $|e'\rangle$ and $|r\rangle$. When both the atoms are in the ground state $|g\rangle$, the energy level of the two-atom system is represented as $|1\rangle$. Similarly, energy levels $|4\rangle$ and $|9\rangle$ of the composite system represent the case when both the atoms are in states $|e'\rangle$ and $|r\rangle$, respectively. Energy levels $|2\rangle$ and $|3\rangle$ represent the case when one atom is in state $|g\rangle$, and the other atom is in state $|e'\rangle$ and vice-versa. Similarly, energy levels $|5\rangle$ and $|6\rangle$ ($|7\rangle$ and $|8\rangle$) represent the case when one atom is in state $|g\rangle$ ($|e'\rangle$) and the other atom is in state $|r\rangle$ and vice-versa. For the composite two-atom system, the states are expressed as $|1\rangle \equiv |g\rangle \otimes \langle g|$, $|2\rangle \equiv |g\rangle \otimes \langle e'|$, $|3\rangle \equiv |e'\rangle \otimes \langle g|$, $|4\rangle \equiv |e'\rangle \otimes \langle e'|$, $|5\rangle \equiv |g\rangle \otimes \langle r|$, $|6\rangle \equiv |r\rangle \otimes \langle g|$, $|7\rangle \equiv |e'\rangle \otimes \langle r|$, $|8\rangle \equiv |r\rangle \otimes \langle e'|$, and $|9\rangle \equiv |r\rangle \otimes \langle r|$. Both the atoms are considered to be moving with different velocities v_1 and v_2 in the thermal vapor system. Let the probe (coupling) Rabi frequency for both the atoms be represented as Ω_{p_1} (Ω_{c_1}) and Ω_{p_2} (Ω_{c_2}). The probe (coupling) detuning for both the atoms are Δ_{p_1} (Δ_{c_1}) and Δ_{p_2} (Δ_{c_2}). When the inter-atomic distance is less than the blockade radius, the atoms undergo strong repulsive van der Waals interaction. Due to this strong interaction, the energy level $|9\rangle$ state is shifted out of resonance leading to the phenomena of Rydberg blockade. The interaction strength is given by Δ_{int}. For the composite system, the interacting Hamiltonian is written as

$$H = H^{(1)} \otimes I + I \otimes H^{(2)} + \Delta_{int}|9\rangle\langle 9| \tag{A.1}$$

where $H^{(1)}$, $H^{(2)}$ are the Hamiltonian of the individual atoms in the effective three-level system, and I is an identity matrix. The total Hamiltonian H is given as

$$H = -\frac{\hbar}{2}\begin{pmatrix}
0 & \Omega_{p_2} & 0 & \Omega_{p_1} & 0 & 0 & 0 & 0 & 0 \\
\Omega^*_{p_2} & 2\Delta_{p_2} & \Omega_{c_2} & 0 & \Omega_{p_1} & 0 & 0 & 0 & 0 \\
0 & \Omega^*_{c_2} & 2\delta_1 & 0 & 0 & \Omega_{p_1} & 0 & 0 & 0 \\
\Omega^*_{p_1} & 0 & 0 & 2\Delta_{p_1} & \Omega_{p_2} & 0 & \Omega_{c_1} & 0 & 0 \\
0 & \Omega^*_{p_1} & 0 & \Omega^*_{p_2} & 2\delta_2 & \Omega_{c_2} & 0 & \Omega_{c_1} & 0 \\
0 & 0 & \Omega^*_{p_1} & 0 & \Omega^*_{c_2} & 2\delta_3 & 0 & 0 & \Omega_{c_1} \\
0 & 0 & 0 & \Omega^*_{c_1} & 0 & 0 & 2\delta_4 & \Omega_{p_2} & 0 \\
0 & 0 & 0 & 0 & \Omega^*_{c_1} & 0 & \Omega^*_{p_2} & 2\delta_5 & \Omega_{c_2} \\
0 & 0 & 0 & 0 & 0 & \Omega^*_{c_1} & 0 & \Omega^*_{c_2} & 2\delta_6 + \Delta_{int}
\end{pmatrix}$$

where $\delta_1 = (\Delta_{p_2} + \Delta_{c_2})$, $\delta_2 = (\Delta_{p_1} + \Delta_{p_2})$, $\delta_3 = (\Delta_{p_1} + \Delta_{p_2} + \Delta_{c_2})$, $\delta_4 = (\Delta_{p_1} + \Delta_{c_1})$, $\delta_5 = (\Delta_{p_1} + \Delta_{p_2} + \Delta_{c_1})$ and $\delta_6 = (\Delta_{p_1} + \Delta_{p_2} + \Delta_{c_1} + \Delta_{c_2})$. The Lindblad operator for the system is written as $L_D(\rho) = L_{D_1}(\rho^{(1)}) \otimes \rho^{(2)} + \rho^{(1)} \otimes L_{D_2}(\rho^{(2)})$ where $L_{D_1}(\rho^{(1)})$, $L_{D_2}(\rho^{(2)})$ are the Lindblad operators and $\rho^{(1)}$, $\rho^{(2)}$ are the density matrices for the two individual atoms. The total density matrix for a non-interacting system is given by $\rho = \rho^{(1)} \otimes \rho^{(2)}$ which is chosen as a basis to write the density matrix for the interacting two-atom system. The density matrix is given by a 9×9 matrix where each element is given by ρ_{ij} with $i, j = 1, 9$.

A.1.1 Optical Bloch equations

The Master equation is given by $\dot{\rho} = \frac{i}{\hbar}[\rho, H] + \mathcal{L}_{\mathcal{D}}(\rho)$, which is solved in steady state to get the following 45 independent optical Bloch equations.

$$\frac{i}{2}(\Omega_{p_2}\rho_{21} + \Omega_{p_1}\rho_{41} - \Omega_{p_2}\rho_{12} - \Omega_{p_1}\rho_{14}) + \Gamma_{21}(\rho_{22} + \rho_{44}) + \Gamma_{31}(\rho_{33} + \rho_{77}) = 0 \tag{A.2}$$

$$\begin{aligned} -\frac{i}{2}(2\Delta_{p2}\rho_{12} + \Omega_{c_2}\rho_{13} + \Omega_{p_2}\rho_{11} + \Omega_{p_1}\rho_{15} - \Omega_{p_2}\rho_{22} - \Omega_{p_1}\rho_{42}) \\ -\Gamma_{21}(\frac{1}{2}\rho_{12} - \rho_{45}) + \Gamma_{31}\rho_{78} = 0 \end{aligned} \tag{A.3}$$

$$\begin{aligned} -\frac{i}{2}(\Omega_{c_2}\rho_{12} + 2(\Delta_{p2} + \Delta_{c2})\rho_{13} + \Omega_{p_1}\rho_{16} - \Omega_{p_2}\rho_{23} - \Omega_{p_1}\rho_{43}) + \Gamma_{21}\rho_{46} \\ +\Gamma_{31}\rho_{79} - \frac{1}{2}(\Gamma_{31} + \Gamma_{32})\rho_{13} = 0 \end{aligned} \tag{A.4}$$

$$\begin{aligned} -\frac{i}{2}(\Omega_{c_1}\rho_{17} + 2\Delta_{p1}\rho_{14} + \Omega_{p_1}\rho_{11} + \Omega_{p_2}\rho_{15} - \Omega_{p_2}\rho_{24} - \Omega_{p_1}\rho_{44}) - \frac{1}{2}\Gamma_{21}\rho_{14} \\ +\Gamma_{21}\rho_{25} + \Gamma_{31}\rho_{36} = 0 \end{aligned} \tag{A.5}$$

$$\begin{aligned} -\frac{i}{2}(2(\Delta_{p1} + \Delta_{p2})\rho_{15} + \Omega_{c_2}\rho_{16} + \Omega_{c_1}\rho_{18} + \Omega_{p_1}\rho_{12} + \Omega_{p_2}\rho_{14} - \Omega_{p_2}\rho_{25} \\ -\Omega_{p_1}\rho_{45}) - \Gamma_{21}\rho_{15} = 0 \end{aligned} \tag{A.6}$$

$$\begin{aligned} -\frac{i}{2}(\Omega_{c_2}\rho_{15} + \Omega_{c_1}\rho_{19} + 2(\Delta_{p1} + \Delta_{p2} + \Delta_{c2})\rho_{16} + \Omega_{p_1}\rho_{13} - \Omega_{p_2}\rho_{26} - \Omega_{p_1}\rho_{46}) \\ -\frac{1}{2}(\Gamma_{21} + \Gamma_{31} + \Gamma_{32})\rho_{16} = 0 \end{aligned} \tag{A.7}$$

$$\begin{aligned}-\frac{i}{2}(\Omega_{c_1}\rho_{14} + 2(\Delta_{c1}+\Delta_{p1})\rho_{17} + \Omega_{p_2}\rho_{18} - \Omega_{p_2}\rho_{27} - \Omega_{p_1}\rho_{47}) + \Gamma_{21}\rho_{28} \\ -\frac{1}{2}(\Gamma_{31}+\Gamma_{32})\rho_{17} + \Gamma_{31}\rho_{39} = 0\end{aligned}\tag{A.8}$$

$$\begin{aligned}-\frac{i}{2}(\Omega_{c_1}\rho_{15} + \Omega_{c_2}\rho_{1,9} + 2(\Delta_{p1}+\Delta_{p2}+\Delta_{c1})\rho_{18} + \Omega_{p_2}\rho_{17} - \Omega_{p_2}\rho_{28} - \Omega_{p_1}\rho_{48}) \\ -\frac{1}{2}(\Gamma_{21}+\Gamma_{31}+\Gamma_{32})\rho_{18} = 0\end{aligned}\tag{A.9}$$

$$\begin{aligned}-\frac{i}{2}(\Omega_{c_1}\rho_{16} + \Omega_{c_2}\rho_{18} + 2(\Delta_{p1}+\Delta_{p2}+\Delta_{c1}+\Delta_{c2}+2V)\rho_{19} - \Omega_{p_2}\rho_{29} \\ -\Omega_{p_1}\rho_{49}) - (\Gamma_{31}+\Gamma_{32})\rho_{19} = 0\end{aligned}\tag{A.10}$$

$$\begin{aligned}\frac{i}{2}(\Omega_{c_2}\rho_{32} - \Omega_{c_2}\rho_{23} + \Omega_{p_2}\rho_{12} - \Omega_{p_2}\rho_{21} + \Omega_{p_1}\rho_{52} - \Omega_{p_1}\rho_{25}) - \Gamma_{21}\rho_{22} + \Gamma_{21}\rho_{55} \\ +\Gamma_{31}\rho_{88} + \Gamma_{32}\rho_{33} = 0\end{aligned}\tag{A.11}$$

$$\begin{aligned}\frac{i}{2}(-2\Delta_{c2}\rho_{23} + \Omega_{c_2}\rho_{33} - \Omega_{c_2}\rho_{22} + \Omega_{p_2}\rho_{13} - \Omega_{p_1}\rho_{26} + \Omega_{p_1}\rho_{53}) + \Gamma_{21}\rho_{56} \\ +\Gamma_{31}\rho_{89} - \frac{1}{2}(\Gamma_{21}+\Gamma_{31}+\Gamma_{32})\rho_{23} = 0\end{aligned}\tag{A.12}$$

$$\begin{aligned}\frac{i}{2}(2(-\Delta_{p1}+\Delta_{p2})\rho_{24} + \Omega_{c_2}\rho_{34} - \Omega_{c_1}\rho_{27} + \Omega_{p_2}\rho_{14} - \Omega_{p_1}\rho_{21} - \Omega_{p_2}\rho_{25} \\ +\Omega_{p_1}\rho_{54}) - \Gamma_{21}\rho_{24} = 0\end{aligned}\tag{A.13}$$

$$\begin{aligned}-\frac{i}{2}(2\Delta_{p1}\rho_{25} + \Omega_{c_2}\rho_{26} + \Omega_{c_1}\rho_{28} - \Omega_{c_2}\rho_{35} + \Omega_{p_1}\rho_{22} - \Omega_{p_2}\rho_{15} + \Omega_{p_2}\rho_{24} \\ -\Omega_{p_1}\rho_{55}) - \frac{3}{2}\Gamma_{21}\rho_{25} + \Gamma_{32}\rho_{36} = 0\end{aligned}\tag{A.14}$$

$$\begin{aligned}\frac{i}{2}(-2(\Delta_{p1}+\Delta_{c2})\rho_{26} - \Omega_{c_2}\rho_{25} - \Omega_{c_1}\rho_{29} + \Omega_{c_2}\rho_{36} + \Omega_{p_2}\rho_{16} - \Omega_{p_1}\rho_{23} \\ +\Omega_{p_1}\rho_{56}) - \frac{1}{2}(2\Gamma_{21}+\Gamma_{31}+\Gamma_{32})\rho_{26} = 0\end{aligned}\tag{A.15}$$

$$\begin{aligned}\frac{i}{2}(-2(\Delta_{c1}+\Delta_{p1}-\Delta_{p2})\rho_{27} - \Omega_{c_1}\rho_{24} + \Omega_{c_2}\rho_{37} + \Omega_{p_2}\rho_{17} - \Omega_{p_2}\rho_{28} + \Omega_{p_1}\rho_{57}) \\ -\frac{1}{2}(\Gamma_{21}+\Gamma_{31}+\Gamma_{32})\rho_{27} = 0\end{aligned}\tag{A.16}$$

$$\begin{aligned}\frac{i}{2}(-2(\Delta_{c1}+\Delta_{p1})\rho_{28} - \Omega_{c_1}\rho_{25} - \Omega_{c_2}\rho_{29} + \Omega_{c_2}\rho_{38} + \Omega_{p_2}\rho_{18} - \Omega_{p_2}\rho_{27} \\ +\Omega_{p_1}\rho_{58}) - \frac{1}{2}(2\Gamma_{21}+\Gamma_{31}+\Gamma_{32})\rho_{28} + \Gamma_{32}\rho_{39} = 0\end{aligned}\tag{A.17}$$

$$\begin{aligned}&\frac{i}{2}(-2(\Delta_{c1}+\Delta_{c2}+\Delta_{p1}+2V)\rho_{29}-\Omega_{c_1}\rho_{2,6}-\Omega_{c_2}\rho_{28}+\Omega_{c_2}\rho_{39}+\Omega_{p_2}\rho_{19}\\&\qquad+\Omega_{p_1}\rho_{59})-\frac{1}{2}(\Gamma_{21}+2\Gamma_{31}+2\Gamma_{32})\rho_{29}=0\end{aligned}\tag{A.18}$$

$$\frac{i}{2}(\Omega_{c_2}\rho_{23}-\Omega_{c_2}\rho_{32}+\Omega_{p_1}\rho_{63}-\Omega_{p_1}\rho_{36})+\Gamma_{21}\rho_{66}+\Gamma_{31}\rho_{99}-(\Gamma_{31}+\Gamma_{32})\rho_{33}=0\tag{A.19}$$

$$\begin{aligned}&\frac{i}{2}(2(\Delta_{c2}-\Delta_{p1}+\Delta_{p2})\rho_{34}+\Omega_{c_2}\rho_{24}-\Omega_{c_1}\rho_{37}-\Omega_{p_1}\rho_{31}-\Omega_{p_2}\rho_{35}+\Omega_{p_1}\rho_{64})\\&\qquad-\frac{1}{2}(\Gamma_{21}+\Gamma_{31}+\Gamma_{32})\rho_{34}=0\end{aligned}\tag{A.20}$$

$$\begin{aligned}&\frac{i}{2}(2(\Delta_{c2}-\Delta_{p1})\rho_{35}+\Omega_{c_2}\rho_{25}-\Omega_{c_1}\rho_{38}-\Omega_{c_2}\rho_{36}-\Omega_{p_1}\rho_{32}-\Omega_{p_2}\rho_{34}\\&\qquad+\Omega_{p_1}\rho_{6,5})-\frac{1}{2}(2\Gamma_{21}+\Gamma_{31}+\Gamma_{32})\rho_{35}=0\end{aligned}\tag{A.21}$$

$$\begin{aligned}&-\frac{i}{2}(2\Delta_{p1}\rho_{36}-\Omega_{c_2}\rho_{26}+\Omega_{c_1}\rho_{39}+\Omega_{c_2}\rho_{35}+\Omega_{p_1}\rho_{33}-\Omega_{p_1}\rho_{66})\\&\qquad-\frac{1}{2}(\Gamma_{21}+2\Gamma_{31}+2\Gamma_{32})\rho_{36}=0\end{aligned}\tag{A.22}$$

$$\begin{aligned}&\frac{i}{2}(\Omega_{c_2}\rho_{27}-\Omega_{c_1}\rho_{34}+2(-\Delta_{c1}+\Delta_{c2}-\Delta_{p1}+\Delta_{p2})\rho_{37}+\Omega_{p_1}\rho_{67}-\Omega_{p_2}\rho_{38})\\&\qquad-(\Gamma_{31}+\Gamma_{32})\rho_{37}=0\end{aligned}\tag{A.23}$$

$$\begin{aligned}&-\frac{i}{2}(2(\Delta_{c1}-\Delta_{c2}+\Delta_{p1})\rho_{38}-\Omega_{c_2}\rho_{28}+\Omega_{c_2}\rho_{39}+\Omega_{c_1}\rho_{35}+\Omega_{p_2}\rho_{37}-\Omega_{p_1}\rho_{68})\\&\qquad-\frac{1}{2}(\Gamma_{21}+2\Gamma_{31}+2\Gamma_{32})\rho_{38}=0\end{aligned}\tag{A.24}$$

$$\begin{aligned}&\frac{i}{2}(\Omega_{p_1}\rho_{69}-2(\Delta_{p1}+\Delta_{c1}+2V)\rho_{39}+\Omega_{c_2}\rho_{29}-\Omega_{c_1}\rho_{36}-\Omega_{c_2}\rho_{38})\\&\qquad-\frac{3}{2}(\Gamma_{31}+\Gamma_{32})\rho_{39}=0\end{aligned}\tag{A.25}$$

$$\begin{aligned}&\frac{i}{2}(\Omega_{c_1}\rho_{74}-\Omega_{c_1}\rho_{47}+\Omega_{p_1}\rho_{14}-\Omega_{p_1}\rho_{41}-\Omega_{p_2}\rho_{45}+\Omega_{p_2}\rho_{54})-\Gamma_{21}\rho_{44}\\&\qquad+\Gamma_{32}\rho_{77}+\Gamma_{21}\rho_{55}+\Gamma_{31}\rho_{66}=0\end{aligned}\tag{A.26}$$

$$\begin{aligned}&-\frac{i}{2}(2\Delta_{p2}\rho_{45}+\Omega_{c_2}\rho_{46}+\Omega_{c_1}\rho_{48}-\Omega_{c_1}\rho_{75}+\Omega_{p_1}\rho_{42}+\Omega_{p_2}\rho_{44}-\Omega_{p_1}\rho_{15}\\&\qquad-\Omega_{p_2}\rho_{55})-\Gamma_{21}\rho_{45}+\Gamma_{32}\rho_{78}-\frac{1}{2}\Gamma_{21}\rho_{45}=0\end{aligned}\tag{A.27}$$

$$\begin{split}\frac{i}{2}(-2(\Delta_{p2}+\Delta_{c2})\rho_{46}-\Omega_{c_2}\rho_{45}-\Omega_{c_1}\rho_{49}+\Omega_{c_1}\rho_{76}+\Omega_{p_1}\rho_{16}-\Omega_{p_1}\rho_{43}\\+\Omega_{p_2}\rho_{56})-\Gamma_{21}\rho_{46}+\Gamma_{32}\rho_{79}-\frac{1}{2}(\Gamma_{31}+\Gamma_{32})\rho_{46}=0\end{split}\tag{A.28}$$

$$\begin{split}\frac{i}{2}(-2\Delta_{c1}\rho_{47}-\Omega_{c_1}\rho_{44}+\Omega_{c_1}\rho_{77}+\Omega_{p_1}\rho_{17}-\Omega_{p_2}\rho_{48}+\Omega_{p_2}\rho_{57})+\Gamma_{21}\rho_{58}\\-\frac{1}{2}(\Gamma_{21}+\Gamma_{31}+\Gamma_{32})\rho_{47}+\Gamma_{31}\rho_{69}=0\end{split}\tag{A.29}$$

$$\begin{split}\frac{i}{2}(-2(\Delta_{p2}+\Delta_{c1})\rho_{48}-\Omega_{c_1}\rho_{45}-\Omega_{c_2}\rho_{49}+\Omega_{c_1}\rho_{78}+\Omega_{p_1}\rho_{18}-\Omega_{p_2}\rho_{47}\\+\Omega_{p_2}\rho_{58})-\frac{1}{2}(\Gamma_{21}+\Gamma_{31}+\Gamma_{32})\rho_{48}-\frac{1}{2}\Gamma_{21}\rho_{48}=0\end{split}\tag{A.30}$$

$$\begin{split}\frac{i}{2}(-2(\Delta_{p2}+\Delta_{c1}+\Delta_{c2}+4V)\rho_{49}-\Omega_{c_1}\rho_{46}-\Omega_{c_2}\rho_{48}+\Omega_{c_1}\rho_{79}+\Omega_{p_1}\rho_{19}\\+\Omega_{p_2}\rho_{59})-\frac{1}{2}(\Gamma_{21}+2\Gamma_{31}+2\Gamma_{32})\rho_{49}=0\end{split}\tag{A.31}$$

$$\begin{split}\frac{i}{2}(\Omega_{c_2}\rho_{65}+\Omega_{c_1}\rho_{85}-\Omega_{c_2}\rho_{56}-\Omega_{c_1}\rho_{58}+\Omega_{p_1}\rho_{25}+\Omega_{p_2}\rho_{45}-\Omega_{p_1}\rho_{52}-\Omega_{p_2}\rho_{54})\\-2\Gamma_{21}\rho_{55}+\Gamma_{32}(\rho_{88}+\rho_{66})=0\end{split}\tag{A.32}$$

$$\begin{split}\frac{i}{2}(\Omega_{p_1}\rho_{26}+\Omega_{p_2}\rho_{46}-\Omega_{p_1}\rho_{53}-2\Delta_{c2}\rho_{56}+\Omega_{c_2}\rho_{66}+\Omega_{c_1}\rho_{86}-\Omega_{c_2}\rho_{55}\\-\Omega_{c_1}\rho_{59})-\Gamma_{21}\rho_{56}+\Gamma_{32}\rho_{89}-\frac{1}{2}(\Gamma_{21}+\Gamma_{31}+\Gamma_{32})\rho_{56}=0\end{split}\tag{A.33}$$

$$\begin{split}\frac{i}{2}(2(\Delta_{p2}-\Delta_{c1})\rho_{57}-\Omega_{c_1}\rho_{54}+\Omega_{c_2}\rho_{67}+\Omega_{c_1}\rho_{87}+\Omega_{p_1}\rho_{27}+\Omega_{p_2}\rho_{47}-\Omega_{p_2}\rho_{58})\\-\frac{1}{2}(2\Gamma_{21}+\Gamma_{31}+\Gamma_{32})\rho_{57}=0\end{split}\tag{A.34}$$

$$\begin{split}\frac{i}{2}(\Omega_{p_1}\rho_{28}+\Omega_{p_2}\rho_{48}-\Omega_{p_2}\rho_{57}-2\Delta_{c1}\rho_{58}+\Omega_{c_2}\rho_{68}+\Omega_{c_1}\rho_{88}-\Omega_{c_1}\rho_{55}\\-\Omega_{c_2}\rho_{59})-\frac{1}{2}(\Gamma_{21}+\Gamma_{31}+\Gamma_{32})\rho_{58}-\Gamma_{21}\rho_{58}+\Gamma_{32}\rho_{69}=0\end{split}\tag{A.35}$$

$$\begin{split}\frac{i}{2}(\Omega_{p_1}\rho_{29}+\Omega_{p_2}\rho_{49}-2(\Delta_{c1}+\Delta_{c2}+2V)\rho_{59}+\Omega_{c_2}\rho_{69}+\Omega_{c_1}\rho_{89}-\Omega_{c_1}\rho_{56}\\-\Omega_{c_2}\rho_{58})-(\Gamma_{21}+\Gamma_{31}+\Gamma_{32})\rho_{59}=0\end{split}\tag{A.36}$$

$$\begin{split}\frac{i}{2}(\Omega_{p_1}\rho_{36}-\Omega_{p_1}\rho_{63}+\Omega_{c_2}\rho_{56}+\Omega_{c_1}\rho_{96}-\Omega_{c_2}\rho_{65}-\Omega_{c_1}\rho_{69})\\-(\Gamma_{21}+\Gamma_{31}+\Gamma_{32})\rho_{66}+\Gamma_{32}\rho_{99}=0\end{split}\tag{A.37}$$

$$\frac{i}{2}(2(-\Delta_{c1}+\Delta_{c2}+\Delta_{p2})\rho_{67}+\Omega_{c_2}\rho_{57}-\Omega_{c_1}\rho_{64}+\Omega_{c_1}\rho_{97}+\Omega_{p_1}\rho_{37}-\Omega_{p_2}\rho_{68}) \\ -\frac{1}{2}(\Gamma_{21}+2\Gamma_{31}+2\Gamma_{32})\rho_{67}=0 \tag{A.38}$$

$$\frac{i}{2}(\Omega_{p_1}\rho_{38}-\Omega_{p_2}\rho_{67}+2(-\Delta_{c1}+\Delta_{c2})\rho_{68}+\Omega_{c_2}\rho_{58}+\Omega_{c_1}\rho_{98}-\Omega_{c_1}\rho_{65} \\ -\Omega_{c_2}\rho_{69})-(\Gamma_{21}+\Gamma_{31}+\Gamma_{32})\rho_{68}=0 \tag{A.39}$$

$$\frac{i}{2}(\Omega_{p_1}\rho_{39}-2(\Delta_{c1}+2V)\rho_{69}+\Omega_{c_2}\rho_{59}-\Omega_{c_1}\rho_{66}-\Omega_{c_2}\rho_{68}+\Omega_{c_1}\rho_{99}) \\ -\frac{1}{2}\Gamma_{21}\rho_{69}-\frac{3}{2}(\Gamma_{31}+\Gamma_{32})\rho_{69}=0 \tag{A.40}$$

$$\frac{i}{2}(\Omega_{p_2}\rho_{87}-\Omega_{p_2}\rho_{78}+\Omega_{c_1}\rho_{47}-\Omega_{c_1}\rho_{74})-(\Gamma_{31}+\Gamma_{32})\rho_{77}+\Gamma_{21}\rho_{8,8} \\ +\Gamma_{31}\rho_{99}=0 \tag{A.41}$$

$$\frac{i}{2}(2\Delta_{p2}\rho_{78}+\Omega_{c_1}\rho_{75}-\Omega_{c_1}\rho_{48}+\Omega_{c_2}\rho_{79}+\Omega_{p_2}\rho_{77}-\Omega_{p_2}\rho_{88}) \\ -\frac{1}{2}(\Gamma_{21}+2\Gamma_{31}+2\Gamma_{32})\rho_{78}=0 \tag{A.42}$$

$$\frac{i}{2}(\Omega_{p_2}\rho_{89}-2(\Delta_{p2}+\Delta_{c2}+2V)\rho_{79}+\Omega_{c_1}\rho_{49}-\Omega_{c_1}\rho_{76}-\Omega_{c_2}\rho_{78}) \\ -\frac{3}{2}(\Gamma_{31}+\Gamma_{32})\rho_{79}=0 \tag{A.43}$$

$$\frac{i}{2}(\Omega_{p_2}\rho_{78}-\Omega_{p_2}\rho_{87}+\Omega_{c_1}\rho_{58}+\Omega_{c_2}\rho_{98}-\Omega_{c_1}\rho_{85}-\Omega_{c_2}\rho_{89})+\Gamma_{32}\rho_{99} \\ -(\Gamma_{21}+\Gamma_{31}+\Gamma_{32})\rho_{88}=0 \tag{A.44}$$

$$\frac{i}{2}(\Omega_{p_2}\rho_{79}-2(\Delta_{c2}+2V)\rho_{89}+\Omega_{c_1}\rho_{59}-\Omega_{c_1}\rho_{86}-\Omega_{c_2}\rho_{88}+\Omega_{c_2}\rho_{99}) \\ -\frac{1}{2}(\Gamma_{21}+3\Gamma_{31}+3\Gamma_{32})\rho_{89}=0 \tag{A.45}$$

$$\frac{i}{2}(\Omega_{c_2}\rho_{89}-\Omega_{c_1}\rho_{96}+\Omega_{c_1}\rho_{69}-\Omega_{c_2}\rho_{98})-2(\Gamma_{31}+\Gamma_{32})\rho_{99}=0 \tag{A.46}$$

In this system, there are two atoms with different velocities v_1 and v_2. The contribution of each atom is added up to find $\rho_{e'e'}$ and $\rho_{e'g}$ from the optical Bloch equations as

$$\rho_{e'e'}=\rho_{44}+\frac{1}{2}(\rho_{22}+\rho_{33}+\rho_{77}+\rho_{88}) \tag{A.47}$$

$$\rho_{e'g} = \frac{1}{2}(\rho_{21} + \rho_{31} + \rho_{42} + \rho_{43} + \rho_{75} + \rho_{86}). \tag{A.48}$$

$\rho_{e'e'}$ is the effective population in the excited state. The Rabi frequencies are considered to be real without the loss of generality. The ground to excited state coherence is calculated by substituting $\rho_{e'e'}$ and $\rho_{e'g}$ in the equation provided below [68]:

$$\rho_{eg} = \frac{\Omega_1(\rho_{e'e'} - 1) - \Omega_2\rho_{e'g}}{2\Delta_1 + i\Gamma_{eg}}. \tag{A.49}$$

The Doppler averaged susceptibility of the probe is found as

$$\chi = \frac{2N|\ \mu_{ge}\ |^2}{\hbar\epsilon_0\Omega_1}\frac{1}{\pi v_p^2}\int_{-\infty}^{+\infty}\int_{-\infty}^{+\infty}\rho_{eg}e^{-\frac{(v_1^2+v_2^2)}{v_p^2}}dv_1 dv_2 \tag{A.50}$$

where μ_{ge} is the transition dipole moment of $|g\rangle \rightarrow |e\rangle$ transition, N is the density of the atomic vapor and v_p is the most probable speed of the atoms. The integral is solved using the Monte Carlo simulation technique. The transmission of the probe beam is $T = e^{-\Im(\chi)k_1 l}$ where l is the length of the atomic medium and k_1 is the magnitude of the wave-vector of the probe beam. The vapor density is taken to be 4.5×10^{10} cm^{-3}, and the length of the vapor cell is 5 cm.

A.1.2 Monte Carlo simulation technique

The above integral for calculating the probe susceptibility follows a Gaussian distribution. It is solved using the Monte Carlo simulation technique. The Monte-Carlo technique utilizes the Box-Muller algorithm, where two sets of random numbers are generated between the closed interval [-1,1]. Let the two random numbers be x and y. They are independent and uniformly distributed between the closed interval such that the square root of the sum of their individual squares lies between (0,1). If not, then the random number pairs are discarded, and another pair of random numbers are tried. The generated random numbers follow a Gaussian distribution as shown in Fig. A.2. For each data point, the code is run over for N (10,000-50,000) random numbers. The larger the value of N, the better the generated result. After the ran-

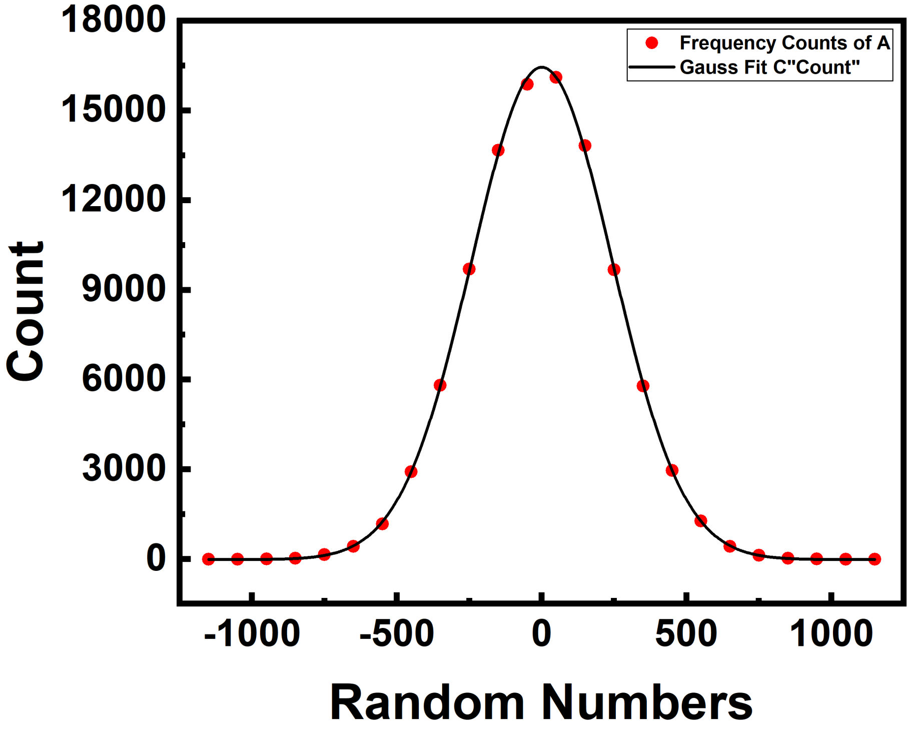

Figure A.2: Gaussian distribution of random numbers.

dom numbers are generated, they are fed into the velocity of each atom multiplied with a factor of the most probable velocity (v_p) of an atom and a normalization factor. The velocities are represented as $v_1 = x * v_p * f$ and $v_2 = y * v_p * f$ where $f = \sqrt{\frac{-2\ln(s)}{s}}$ and $s = x^2 + y^2$. Then the integration is performed by summing over all the generated values of the observable quantity, and it is averaged over N to get the result.

A.2 Comparison of non-interacting two-atom system with a single-atom system

The probe EIT transmission is calculated for a single-atom system using the effective three-level calculation as described in Sec. 5.6 and is represented in Fig. A.3 by the solid black line. The EIT transmission for a non-interacting two-atom system is calculated from the two-atom model and is represented using open red circles. The

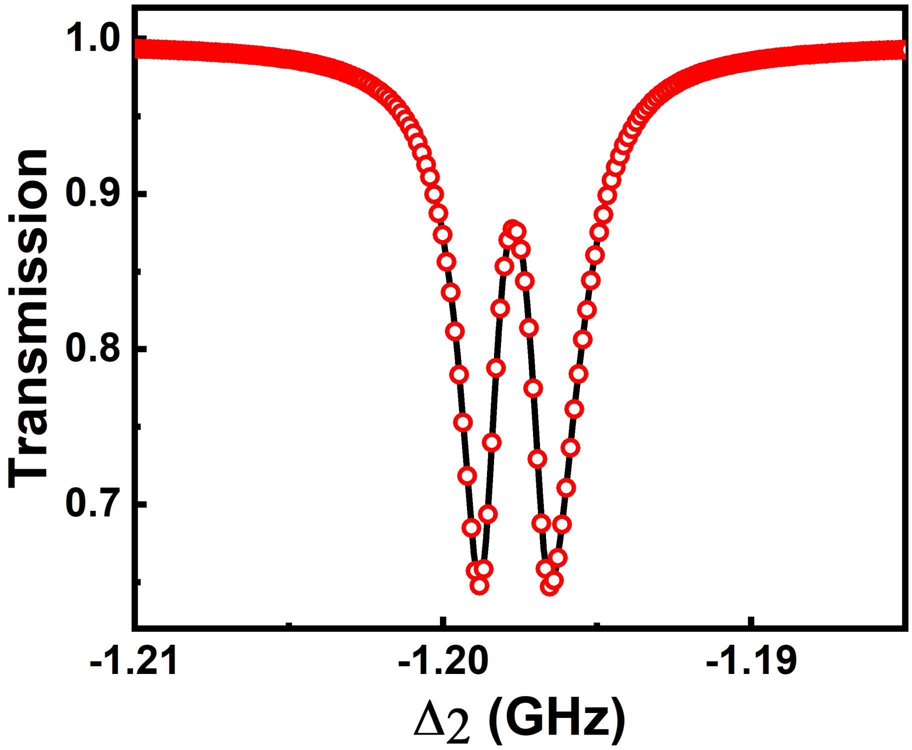

Figure A.3: Comparison of probe transmission calculated using single-atom system (solid black line) and non-interacting two-atom system (open red circles) for $\Delta k = 0$. Here, $k_p = 0.007 \times 10^6$ m^{-1}. The laser parameters used in the model are $\Omega_1 = 25$ MHz, $\Omega_2 = 110$ MHz, $\Omega_3 = 25$ MHz and $\Omega_4 = 160$ MHz, $\Delta_1 = 1200$ MHz, $\Delta_3 = 1000$ MHz and Δ_4 is adjusted around Δ_3 such that the transmission is symmetric.

EIT transmission for a non-interacting two-atom system matches perfectly with that for a single-atom system. As discussed in chapter 5, the motion-induced dephasing can be eliminated in this system. The absence of residual wave-vector ($\Delta k = 0$) leads to transparency of the EIT signal to be nearly 90%, which has been discussed in detail in chapter 5.

A.3 Observation of Rydberg blockade phenomenon

Fig. A.4(a) shows the comparison of EIT transmission for non-interacting two-atom system with two-atom interacting system for $\Delta k = 0$. The strong interaction between Rydberg atoms leads to the phenomenon known as Rydberg blockade [50]. Due to the blockade phenomenon, the EIT transmission is suppressed. In the ab-

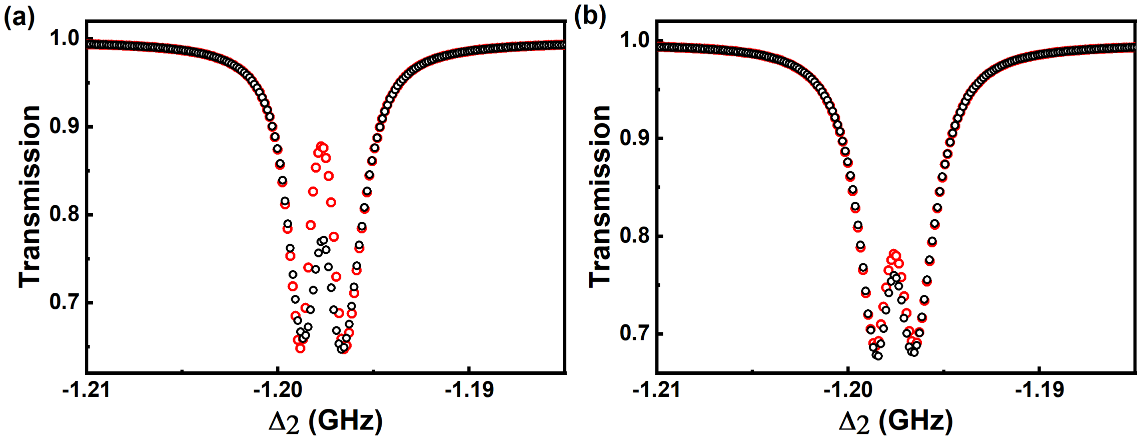

Figure A.4: Comparison of probe transmission calculated for non-interacting two-atom system (open red circles) and interacting two-atom system with $\Delta_{int} = 100$ MHz (open black circles) for (a) $\Delta k = 0$ and (b) $\Delta k = 0.013 \times 10^6$ m^{-1}. Here, $k_p = 0.007 \times 10^6$ m^{-1}. The laser parameters used in the model are $\Omega_1 = 25$ MHz, $\Omega_2 = 110$ MHz, $\Omega_3 = 25$ MHz and $\Omega_4 = 160$ MHz, $\Delta_1 = 1200$ MHz, $\Delta_3 = 1000$ MHz and Δ_4 is adjusted around Δ_3 such that the transmission is symmetric.

sence of a blockade, the light gets completely transmitted under EIT. But in the presence of Rydberg blockade, only one of the atoms is excited to the Rydberg state and the second atom is not, leading to the absorption of the light by the second atom and hence reduction in EIT transparency. The observed suppression in EIT transmission because of the strong interaction between Rydberg atoms is similar to that observed in ultra-cold atoms [57]. The reason for similar suppression is the elimination of motion-induced dephasing in the system. If $\Delta k = 0.013 \times 10^6$ m^{-1}, as shown in Fig. A.4(b), the EIT transmission reduces for two-atom non-interacting system. Also, the suppression in EIT transmission is reduced for the two-atom interacting system with non-zero Δk.

A.3.1 Dependence of Rydberg blockade on k_c

Fig. A.5 shows the normalized blockaded transmission as a function of k_c. Normalized blockaded transmission is defined as the ratio of blockaded probe transmission to probe transmission for a non-interacting system. An increase in k_c leads to a reduction in the blockade effect. This effect is understood as a reduction in the

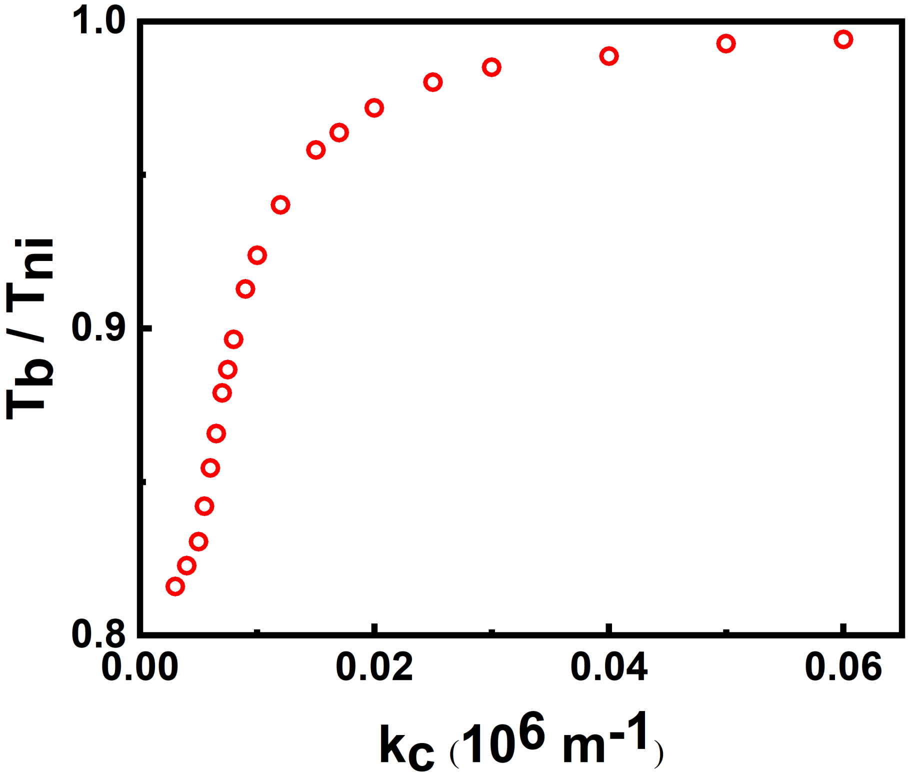

Figure A.5: Normalized blockaded transmission as a function of k_c with $k_p = 0.007 \times 10^6$ m^{-1} for $\Delta_{int} = 100$ MHz. The laser parameters used in the model are $\Omega_1 = 25$ MHz, $\Omega_2 = 110$ MHz, $\Omega_3 = 25$ MHz and $\Omega_4 = 160$ MHz, $\Delta_1 = 1200$ MHz, $\Delta_3 = 1000$ MHz and Δ_4 is adjusted around Δ_3 such that the transmission is symmetric.

effective number of atoms participating in the blockade process. With a non-zero residual wave vector, only a certain velocity class of atoms are resonant to the probe and coupling field. This means that only a certain velocity class of atoms is resonant to the EIT process. An increase in the residual wave vector has a significant effect on the suppression of the Rydberg blockade phenomenon.

A.3.2 Variation of Rydberg blockade with super-atom dephasing

There is another dephasing mechanism, called the super-atom dephasing (Γ_s), which occurs due to the transverse velocity of the atoms in the thermal vapor system [92].

This happens when an atom moves out of the blockade sphere and another atom enters the blockade sphere, leading to the dephasing of the multi-atom coherence due to the Rydberg blockade. Super-atom dephasing can be understood as the dephasing of the coherence between the singly excited Rydberg states. It is introduced into the $\mathcal{L}_{\mathcal{D}}$ matrix by hand for the singly excited Rydberg states, i.e., ρ_{56} and ρ_{78}. If $2r_b\Delta k > 1$, then Γ_s is given by the transit time of the atoms through the blockade sphere, where r_b is the blockade radius. If $2r_b\Delta k < 1$, then the super-atom dephasing is given by $\Delta k v_{avg}$, where v_{avg} is the average velocity of the atoms [92]. If the residual wave-vector is eliminated in the system, i.e., $\Delta k = 0$, then the decoherence in the system is dominated by the transit time decay rate of the atoms. The transit time decay rate can be 100 kHz for a beam diameter of 1 mm.

A.3.3 Effect of Δ_{int} on Rydberg blockade

If $\Delta_{int} \gg \gamma_{EIT}$, then the blockade effect does not depend on the interaction shift of the Rydberg state [57] where γ_{EIT} is the linewidth of the EIT signal. This has been verified with the codes for this system. In the analysis, $\Delta_{int} = 100$ MHz, much larger than the typical EIT width of 2 MHz.

The study presented here is a proof of principle for observation of blockade phenomenon in thermal vapor systems. This cannot be directly applied to model the experimental results. In a typical experimental situation, the number of atoms inside the blockade sphere is $N_b = N\frac{4}{3}\pi r_b^3$. The blockade radius is defined as $r_b = \sqrt[6]{\frac{C_6}{\gamma_{EIT}}}$ where C_6 is the coefficient of van der Waals interaction. For the vapor density used for the simulation, if the lasers are tuned to $35S_{\frac{1}{2}}$ state, then on average, there are two atoms inside the blockade sphere. If the lasers are tuned to a different Rydberg state or the vapor density is changed, then the number of atoms inside the blockade sphere can be varied. For n atoms inside the blockade sphere, a model with n interacting atoms is needed to understand the effect of the blockade phenomenon. All the atoms inside the blockade sphere will be collectively excited and behave like a single super-atom. The absorption of the probe laser beam will be given by an ensemble average of all the super-atoms present within the interaction volume of the laser field interacting with the atomic vapor. The analysis presented here is a theoretical demonstration of the Rydberg blockade for two interacting atoms.

References

[1] Hans G. Dehmelt, *IEEE Transactions on Instrumentation and Measurement*, **IM-31**, 83–87 (1982).

[2] D. J. Wineland et al., *Phys. Rev. A*, **36**, 2220–2232 (1987).

[3] T. Rosenband et al., *Science*, **319**, 1808–1812 (2008).

[4] N. Hinkley et al., *Science*, **341**, 1215–1218 (2013).

[5] E. A. Burt et al., *Nature*, **595**, 43–47 (2021).

[6] L.R. Pendrill and L Robertsson. “Atomic Physics and the Laser Metrology of Time and Length”. In: ed. by Per-Olov Löwdin. Vol. 30. Advances in Quantum Chemistry. Academic Press, 1998, 445–468.

[7] Jonathon A. Sedlacek et al., *Nature Physics*, **8**, 819–824 (2012).

[8] J. A. Sedlacek et al., *Phys. Rev. Lett.*, **111**, 063001 (2013).

[9] Joshua A. Gordon et al. “Quantum-based SI traceable electric-field probe”. In: *2010 IEEE International Symposium on Electromagnetic Compatibility*. 2010, 321–324.

[10] M G Bason et al., *New Journal of Physics*, **12**, 065015 (2010).

[11] John Kitching, Svenja Knappe, and Elizabeth A. Donley, *IEEE Sensors Journal*, **11**, 1749–1758 (2011).

[12] Haoquan Fan et al., *Journal of Physics B: Atomic, Molecular and Optical Physics*, **48**, 202001 (2015).

[13] I. M. Savukov et al., *Phys. Rev. Lett.*, **95**, 063004 (2005).

[14] M. Koschorreck et al., *Phys. Rev. Lett.*, **104**, 093602 (2010).

[15] W. Clark Griffith, Svenja Knappe, and John Kitching, *Opt. Express*, **18**, 27167–27172 (2010).

[16] D. Sheng et al., *Phys. Rev. Lett.*, **110**, 160802 (2013).

[17] Yuval Cohen et al., *Applied Physics Letters*, **114**, 073505 (2019).

[18] Sushree S. Sahoo et al., *Phys. Rev. A*, **105**, 063509 (2022).

[19] Peter W. Graham et al., *Phys. Rev. Lett.*, **110**, 171102 (2013).

[20] M. Kanda and L.D. Driver, *IEEE Transactions on Microwave Theory and Techniques*, **35**, 124–130 (1987).

[21] K. Matloubi. "A broadband, isotropic, electric-field probe with tapered resistive dipoles". In: *1993 IEEE Instrumentation and Measurement Technology Conference*. 1993, 183–184.

[22] J. Randa, M. Kanda, and R.D. Orr. "Resistively-tapered-dipole electric-field probes up to 40 GHz". In: *IEEE 1991 International Symposium on Electromagnetic Compatibility*. 1991, 265–266.

[23] Christopher L. Holloway et al., *IEEE Transactions on Antennas and Propagation*, **62**, 6169–6182 (2014).

[24] Motohisa Kanda, *IEEE Transactions on Electromagnetic Compatibility*, **36**, 261–273 (1994).

[25] Christopher L. Holloway et al., *Journal of Applied Physics*, **121**, 233106 (2017).

[26] Santosh Kumar et al., *Scientific Reports*, **7**, 42981 (2017).

[27] Thomas F. Gallagher. *Rydberg Atoms*. Cambridge Monographs on Atomic, Molecular and Chemical Physics. Cambridge University Press, 1994.

[28] K.-J. Boller, A. Imamoğlu, and S. E. Harris, *Physical Review Letters*, **66**, 2593–2596 (1991).

[29] Stephen E. Harris, *Physics Today*, **50**, 36–42 (1997).

[30] Ashok K. Mohapatra et al., *Nature Physics*, **4**, 890–894 (2008).

[31] C. G. Wade et al., *Nature Photonics*, **11**, 40–43 (2017).

[32] Alfredo Rueda et al., *Optica*, **3**, 597–604 (2016).

[33] R. W. Andrews et al., *Nature Physics*, **10**, 321–326 (2014).

[34] D. V. Strekalov et al., *Phys. Rev. A*, **80**, 033810 (2009).

[35] H. Q. Fan et al., *Opt. Lett.*, **39**, 3030–3033 (2014).

[36] Christopher L. Holloway et al., *Applied Physics Letters*, **104**, 244102 (2014).

[37] Joshua A. Gordon et al., *Applied Physics Letters*, **105**, 024104 (2014).

[38] M. Hafezi et al., *Phys. Rev. A*, **85**, 020302 (2012).

[39] Jingshan Han et al., *Phys. Rev. Lett.*, **120**, 093201 (2018).

[40] David H. Meyer et al., *Applied Physics Letters*, **112**, 211108 (2018).

[41] Zhenfei Song et al., *Opt. Express*, **27**, 8848–8857 (2019).

[42] Yuechun Jiao et al., *Applied Physics Express*, **12**, 126002 (2019).

[43] Joshua A. Gordon et al., *AIP Advances*, **9**, 045030 (2019).

[44] Robert W. Boyd. *Nonlinear Optics, Third Edition*. 3rd. USA: Academic Press, Inc., 2008. ISBN: 0123694701.

[45] A. K. Mohapatra, T. R. Jackson, and C. S. Adams, *Phys. Rev. Lett.*, **98**, 113003 (2007).

[46] R. P. Abel et al., *Applied Physics Letters*, **94**, 071107 (2009).

[47] A. Osterwalder and F. Merkt, *Phys. Rev. Lett.*, **82**, 1831–1834 (1999).

[48] M. Saffman, T. G. Walker, and K. Mølmer, *Rev. Mod. Phys.*, **82**, 2313–2363 (2010).

[49] M. D. Lukin et al., *Phys. Rev. Lett.*, **87**, 037901 (2001).

[50] E. Urban et al., *Nature Physics*, **5**, 110–114 (2009).

[51] Alpha Gaëtan et al., *Nature Physics*, **5**, 115–118 (2009).

[52] Arup Bhowmick, Dushmanta Kara, and Ashok K. Mohapatra. *Study of Rydberg blockade in thermal vapor*. 2018.

[53] Georg Günter et al., *Physical review letters*, **108**, 013002 (2012).

[54] Myron L Zimmerman et al., *Physical Review A*, **20**, 2251 (1979).

[55] T Baluktsian et al., *Physical review letters*, **110**, 123001 (2013).

[56] Matthieu Viteau et al., *Physical Review Letters*, **109**, 053002 (2012).

[57] Jonathan D Pritchard et al., *Physical review letters*, **105**, 193603 (2010).

[58] N. Šibalić et al., *Computer Physics Communications*, **220**, 319–331 (2017).

[59] Richard R Freeman and Daniel Kleppner, *Physical Review A*, **14**, 1614 (1976).

[60] Wenhui Li et al., *Physical Review A*, **67**, 052502 (2003).

[61] G. Lindblad, *Communications in Mathematical Physics*, **48**, 119–130 (1976).

[62] Michael Fleischhauer, Atac Imamoglu, and Jonathan P. Marangos, *Rev. Mod. Phys.*, **77**, 633–673 (2005).

[63] Lene Vestergaard Hau et al., *Nature*, **397**, 594–598 (1999).

[64] J. E. Field, K. H. Hahn, and S. E. Harris, *Phys. Rev. Lett.*, **67**, 3062–3065 (1991).

[65] Lene Vestergaard Hau et al., *Nature*, **397**, 594–598 (1999).

[66] Klemens Hammerer, Anders S. Sørensen, and Eugene S. Polzik, *Rev. Mod. Phys.*, **82**, 1041–1093 (2010).

[67] Rui Han, Hui Khoon Ng, and Berthold-Georg Englert, *Journal of Modern Optics*, **60**, 255–265 (2013).

[68] Arup Bhowmick, Dushmanta Kara, and Ashok K. Mohapatra, *Pramana*, **92**, 76 (2019).

[69] Zhangli Lai et al., *Phys. Rev. A*, **98**, 052503 (2018).

[70] M J Piotrowicz et al., *New Journal of Physics*, **13**, 093012 (2011).

[71] Manuel Kaiser et al., *Phys. Rev. A*, **96**, 043401 (2017).

[72] Christopher L. Holloway et al., *IEEE Transactions on Electromagnetic Compatibility*, **59**, 717–728 (2017).

[73] Matt T. Simons, Joshua A. Gordon, and Christopher L. Holloway, *Journal of Applied Physics*, **120**, 123103 (2016).

[74] H. S. Rawat et al. "E-Field Strength Measurement using Rydberg Atom Based sensor for Microwave Metrology". In: *2020 XXXIIIrd General Assembly and Scientific Symposium of the International Union of Radio Science*. 2020, 1–4.

[75] Lucy A. Downes et al., *Phys. Rev. X*, **10**, 011027 (2020).

[76] Christopher L. Holloway et al., *AIP Advances*, **9**, 065110 (2019).

[77] Haoquan Fan et al., *Phys. Rev. Applied*, **4**, 044015 (2015).

[78] Hao Zhang et al., *Phys. Rev. A*, **90**, 043849 (2014).

[79] Graham Thomas Purves, *Doctoral Thesis*, **Chap. 3.** (2006).

[80] Matt T. Simons et al., *Applied Physics Letters*, **108**, 174101 (2016).

[81] David Alexander Anderson, Rachel Elizabeth Sapiro, and Georg Raithel, *IEEE Transactions on Antennas and Propagation*, **69**, 2455–2462 (2021).

[82] Jingshan Han et al., *Phys. Rev. Lett.*, **120**, 093201 (2018).

[83] Thibault Vogt et al., *Phys. Rev. A*, **99**, 023832 (2019).

[84] Tanim Firdoshi et al. *Six-wave mixing of optical and microwave fields using Rydberg excitations in thermal atomic vapor*. 2022.

[85] Robert W. Boyd. "Chapter 6 - Nonlinear Optics in the Two-Level Approximation". In: *Nonlinear Optics (Third Edition)*. Ed. by Robert W. Boyd. Third Edition. Burlington: Academic Press, 2008, 277–328. ISBN: 978-0-12-369470-6.

[86] Nikola Šibalić et al., *Physical Review A*, **94**, 033840 (2016).

[87] F. Bariani et al., *Phys. Rev. Lett.*, **108**, 030501 (2012).

[88] R. Finkelstein et al., *Phys. Rev. X*, **11**, 011008 (2021).

[89] Tanim Firdoshi et al., *Phys. Rev. A*, **104**, 013711 (2021).

[90] C S Adams, J D Pritchard, and J P Shaffer, *Journal of Physics B: Atomic, Molecular and Optical Physics*, **53**, 012002 (2019).

[91] David H. Meyer, Paul D. Kunz, and Kevin C. Cox, *Phys. Rev. Applied*, **15**, 014053 (2021).

[92] Dushmanta Kara and Ashok K Mohapatra, *Journal of Physics B: Atomic, Molecular and Optical Physics*, **53**, 245301 (2020).